THERMAL AND EXTRUSION PROCESSING OF ALUMINIUM-LITHIUM BASED ALLOYS

by

Ashim Kumar Mukhopadhyay

A thesis submitted for the degree of
Doctor of Philosophy in the University of London

Department of Materials
Imperial College of Science and Technology
London, SW7 2BP

April, 1988

TO

SHOBHANA

AND MY PARENTS

ABSTRACT

The present investigation is concerned with the development of microstructure and mechanical properties in Al-Li-Cu-Mg-(Zr) alloys within the AA 8090 specification. Microstructural development has been followed through homogenisation and extrusion employing a range of temperatures, extrusion ratios, ram speeds and subsequent heat treatment. Mechanical properties are related to the microstructural changes involved.

Detailed studies of the effects of variation in solution treatment temperature combined with natural ageing treatment upon the precipitation reactions have been studied in sheet LITAL A alloy which also lies within the AA 8090 specification. The microstructural changes have been investigated by transmission electron microscopy (TEM) and the age hardening characteristics have been characterised by hardness measurements. The results suggest that the vacancies play a major role in controlling the precipitation reactions in lithium containing Al alloys. The precipitation reactions in Al-Li based alloys have also been characterised by differential scanning calorimetry. The results detail the precipitation reactions which occur and confirm the effective role of vacancies in the development of appropriate precipitate phases in the material.

The cast material received in the form of DC cast billets for extrusion work has been characterised microstructurally by a combination of light microscopy, scanning electron microscopy (SEM) and TEM; additional phase and particle chemical analysis has been carried out using X-ray EDS micro-analysis and secondary ion mass spectrometry (SIMS). An optimum homogenisation schedule has also been established based on the thermal analysis data of the cast material.

The homogenised billets have been extruded over a wide range of extrusion processing variables. The as extruded material has been examined microstructurally by a combination of light microscopy (using polarised light techniques on anodised surfaces) and TEM. The as extruded mechanical properties have been evaluated by hardness measurements and longitudinal tensile tests; the mechanical properties have been correlated with the extrusion processing conditions.

The microstructures of the heat treated extrudates have been examined by TEM. The corresponding mechanical properties have been evaluated by hardness measurements, longitudinal tensile tests and transverse fracture toughness tests. The fracture surfaces of the tensile and fracture toughness test specimens have been characterised by SEM. The tensile properties have been correlated with the extrusion processing conditions. The tensile failure modes, however, change only with ageing conditions and such changes have been correlated with the development of typical phases in the matrix and at the grain boundaries. Variation in extrusion temperature has not found to have any effect on the toughness. Toughness, however, changes both with ageing times, and with variation in preageing treatments, viz. a preageing stretch, and a prior natural age. The beneficial effect associated with a prior natural age on the mechanical properties of the material has been correlated with the modification in the matrix precipitation characteristics.

LIST OF CONTENTS

	PAGE
ABSTRACT	2
LIST OF TABLES	8
LIST OF FIGURES	9
CHAPTER ONE INTRODUCTION	18
CHAPTER TWO LITERATURE REVIEW	22
2.1. The Physical Metallurgy of Al-Li Alloys	22
2.1.1. Phase Transformations in Al-Li Alloys	22
2.1.1.1. Binary Al-Li system	22
2.1.1.2. Ternary Al-Li-Mg system	28
2.1.1.3. Ternary Al-Li-Cu system	30
2.1.1.4. Al-Li-Cu-Mg system	34
2.1.2. The role of grain refining additions and impurities on the grain structure and the precipitation reactions in Al-Li alloys.	38
2.1.2.1. Grain Refining Additions	38
2.1.2.2. Impurities	40
2.1.3. Grain Boundary Precipitation Within the Heat Treated Al-Li Alloys	41
2.2. Physical and Mechanical Properties of Al-Li Alloys	43
2.2.1. Density	43
2.2.2. Modulus	43
2.2.3. Strength and Deformation Mechanisms	45
2.2.4. Ductility and Fracture Toughness	47
2.2.4.1. Role of slip coplanarity, precipitate free zones and associated grain structure	47
2.2.4.2. Role of matrix precipitation	49
2.2.4.3. Role of Grain Boundary Precipitation	51
2.3. Extrusion Processing and Recrystallisation in Al-Li Alloys	53
2.3.1. Hot Deformation via Extrusion	53
2.3.1.1. Introduction	53
2.3.1.2. The Hot Working Equations	54
2.3.1.3. Restoration Processes	56
2.3.1.4. Substructure strengthening	59
2.3.2. Extrusion Processing of Aluminium-Lithium Alloys	60
2.3.3. Recrystallisation in Aluminium-Lithium Alloys	62

CHAPTER THREE EXPERIMENTAL PROCEDURE 65
3.1. Introduction 65
3.2. Materials 67
3.3. Alloy Deformation Routes 67
3.3.1. Introduction 67
3.3.2. Extrusion 67
3.3.3. Torsion 68
3.4. Heat Treatments 68
3.5. Thermal Analysis Study 69
3.6. Microstructural Characterisation 70
3.6.1. Light Microscopy 70
3.6.2. Scanning Electron Microscopy (SEM) 70
3.6.3. Transmission Electron Microscopy (TEM) 70
3.6.4. Quantitative Chemical Analysis 71
3.6.5. Secondary Ion Mass Spectrometry (SIMS) 71
3.7. Mechanical Testing 72
3.7.1. Hardness Tests 72
3.7.2. Tensile Tests 72
3.7.3. Fracture Toughness Tests 72

CHAPTER FOUR DEVELOPMENT OF MICROSTRUCTURE AND PROPERTIES THROUGH SUITABLE CONTROL OF HEAT TREATMENT CONDITIONS. 75
4.1. Introduction 75
4.2. Results 75
4.2.1. Age Hardening Behaviour 75
4.2.2. Microstructure of the Alloy Without Natural Ageing Treatment 77
4.2.2.1. As Quenched Microstructure 77
4.2.2.2. Artifically Aged Microstructure 81
4.2.3. Effect of Natural Ageing 86
4.2.3.1 Quenched Microstructure 86
4.2.3.2. Artifically Aged Microstructure 86
4.2.4. Effect of Quench Bath Temperature 91
4.3. Discussion 96
4.3.1. Ageing Curves 96
4.3.2. Effect of Natural Ageing, Solution Treatment Temperature and Quench Bath Temperature 100
4.4. Summary 103

CHAPTER FIVE THERMAL ANALYSIS STUDY OF THE PRECIPITATION REACTIONS IN Al-Li-Cu-Mg-Zr ALLOY 106
5.1. Introduction 106
5.2. Results 106
5.2.1. Aluminium-Lithium (Alloy A3) 106
5.2.2. Aluminium-Lithium-Zirconium (Alloy A4) 109
5.2.3. Aluminium-Copper-Magnesium (Alloy A5 & A6) 110
5.2.4. Aluminium-Lithium-Copper-Magnesium-Zirconium (Alloy A2) 110
5.3. Discussion 115
5.3.1. Al-Li System 115
5.3.2. Al-Li-Zr system 117
5.3.3. Al-Cu-Mg system 117
5.3.4. Al-Li-Cu-Mg-Zr system 117

5.3.5. Natural Ageing Response of Al-Li-Cu-Mg-Zr Alloy 119
5.4. Summary 120

CHAPTER SIX AS CAST MICROSTRUCTURE AND HOMOGENISATION 122
6.1. Introduction 122
6.2. Results 123
6.2.1. Characterisation of As Cast Microstructure 123
6.2.1.1. Grain Boundary Phases 123
6.2.1.2. Matrix Phases 135
6.2.1.3. Homogenisation 139
6.3. Discussion 140
6.3.1. Grain Boundary Phases 140
6.3.2. Matrix Phase 149
6.3.3. Homogenisation 150
6.4. Summary 151

CHAPTER SEVEN CHARACTERISATION OF THE AS EXTRUDED MICROSTRUCTURE AND MECHANICAL PROPERTIES 154
7.1. Introduction 154
7.2. Results 154
7.2.1. Extrusion Processing 154
7.2.2. Extrudate Grain Structure 156
7.2.2.1. Effect of Extrusion Processing Variables 156
7.2.2.2. Effect of Isothermal Annealing 159
7.2.2.3. Effect of Variations in Cooling Rate Post Deformation 159
7.2.3. Grain Structure Produced in Torsion 162
7.2.4. Development of Subgrain Structure 162
7.2.5. Recrystallisation Mechanisms 167
7.2.6. Precipitation Within the As Extruded Microstructure 175
7.2.7. As Extruded Mechanical Properties 178
7.2.7.1. Tensile Properties
7.2.7.2. Hardness Data
7.2.7.3. Artificial Ageing Response
7.3. Discussion 183
7.3.1. As Extruded Mechanical Properties 183
7.3.2. Natural and Artificial Ageing Response 184
7.3.3. Recrystallisation 185
7.4. Summary 187

CHAPTER EIGHT HEAT TREATED EXTRUDATES - THEIR MICROSTRUCTURE AND MECHANICAL PROPERTIES 190
8.1. Introduction 190
8.2. Results 190
8.2.1. Ageing Response 190
8.2.1.1. Microstructure of the Alloy without Natural Ageing 195
8.2.1.2. Effect of Natural Ageing 195
8.2.2. The Effect of a Preaging Stretch, and Combination of Natural Ageing and a Preaging Stretch on S Phase Precipitation. 198

8.2.3. Coarse Grain Boundary Precipitates in the Heat Treated Material 201
8.2.4. Mechanical Properties of Heat Treated Material 204
8.2.4.1. Tensile Properites 204
8.2.4.2. Fracture Toughness 209
8.2.5. Fractorgraphy 213
8.2.5.1. Tensile samples 213
8.2.5.2. Fracture Toughness Samples 220
8.3. Discussion 220
8.3.1. Ageing Curves 220
8.3.2. Heat Treated Microstructures 223
8.3.2.1. Microstructure of the Alloy without Natural Ageing 223
8.3.2.2. Effect of Natural Ageing 223
8.3.3. Coarse Grain Boundary Precipitates 224
8.3.4. Tensile Properties 227
8.3.5. Serrated Yielding 228
8.3.6. Fractography 231
8.3.6.1. Tensile Samples 231
8.3.6.2. Fracture Toughness Samples 232
8.3.7. Fracture Toughness 233
8.4. Summary 236

CHAPTER NINE CONCLUSIONS AND SUGGESTIONS FOR FURTHER WORK 239
9.1. Conclusions 239
9.2. Suggestions for Further Work 244

ACKNOWLEDGEMENTS 246

REFERENCES 247

LIST OF TABLES

		PAGE
Table 3.1.	Composition of the alloys used in the present investigation.	66
Table 4.1.	Average δ' particle diameter and homogeneous S precipitate density in the heat treated alloy A2 as functions of varying heat treatment schedules.	97
Table 6.1.	Phases detected in the cast material A1.	145
Table 6.2.	A summary of iron bearing phases formed in the cast and homogenised Al based alloys as functions of the cooling rate and the alloy composition.	148
Table 7.1.	As extruded tensile properties (longitudinal) as functions of varying extrusion temperatures and extrusion ratios.	180
Table 7.2.	As extruded hardness data as functions of varying extrusion temperatures and extrusion ratios.	180
Table 8.1.	Longitudinal tensile properties of the heat treated extrudates (produced at 400°C) as functions of varying extrusion ratios, and ageing hours at 190°C.	206
Table 8.2.	Longitudinal tensile properties of the heat treated extrudates (produced at 500°C) as functions of varying extrusion ratios, and ageing hours at 190°C.	208
Table 8.3.	Transverse fracture toughness properties of the heat treated extrudates as functions of varying extrusion temperatures, preaging treatments, and ageing hours at 190°C.	212
Table 8.4.	A summary of grain boundary phases detected in various heat treated Al-Li-Cu-Mg alloys.	225
Table 8.5.	Effect of varying heat treatment cycle on the longitudinal tensile properties of the extrudates produced at 500°C.	235

LIST OF FIGURES

		PAGE
Figure 1.1.	Composition ranges for commercially registered Al-Li-Cu-Mg-(Zr) alloys.	20
Figure 2.1.	(a) The equilibrium Al-Li phase diagram (after McAlister(4)) and (b) experimentally determined solvus lines for both δ and δ' (8, 9, 10, 11).	23
Figure 2.2.	Phase diagram of Al-Li showing the δ solvus, and the apparent and coherent δ' solvus lines (8, 11, 13).	26
Figure 2.3.	The metastable α-δ' system (a) as proposed by Gayle and Vander Sande (14) (b) as predicted by Sigli and Sanchez (16)	26
Figure 2.4.	Isothermal section of the Al-Li-Mg system at 200°C (after Schurmann and Geissler (31)).	29
Figure 2.5.	Isothermal sections of the Al-Li-Cu system (a) phases identified at 350°C (after Hardy and Silcock (39)). (b) phases identified after 16 hours at 165°C (after Silcock (5)).	31
Figure 2.6.	Isothermal sections of the Al-Cu-Mg system (after Silcock and Parsons (58)).	36
Figure 2.7.	Variation of tensile properties with lithium content. (a) Young's modulus of solution treated, and solution treated and aged material (b) Contribution of different strengthening mechanisms after ageing to near peak strength (after Noble and co-workers (98, 99).	44
Figure 2.8.	A summary of notch tensile strength/yield strength ratio as a function of yield strength for ternary and quaternary Al-Li based alloys (L-T orientation) as compared with 7000 series commercial aircraft alloys (after Gregson (52)).	50
Figure 3.1.	Fracture toughness test piece dimensions; all dimensions in inches.	73
Figure 4.1.	Effect of variation in solution treatment temperature on the artificial ageing response of alloy A2 at 190°C.	76
Figure 4.2.	The natural ageing response of alloy A2 after solution treatment at 530°C and water quench at room temperature (RT).	76

Figure 4.3. Effect of variation in solution treatment temperature, and 24 hours natural ageing on subsequent artificial ageing response of alloy A2 at 190°C. 78

Figure 4.4. TEM micrographs of the as quenched material 80
(a)-(c) BF images showing variation in subgrain size due to variation in solution treatment temperature viz. 540, 560 and 580°C respectively.
(d) DF image showing δ' precipitation; imaged using (100) superlattice reflection; <100> Al orientation.
(e) DF image showing superdislocations; g = 222. <112>Al orientation.
(f) BF image showing inhomogeneous distribution of β' precipitates; close to <100>Al orientation.

Figure 4.5. TEM micrographs showing precipitate phases in the peakaged material. Material treatment: ST 530°C, WQ(RT), and AA 24 hours at 190°C; 83
(a) DF image showing δ' precipitation; imaged using (100) superlattice reflection
(b) BF image showing heterogeneous T_1 and S precipitation; <110> Al orientation
(c) BF image showing heterogeneous S (and a few T_1) precipitation; <110> Al orientation.

Figure 4.6. TEM BF micrographs showing homogeneous S precipitation. Material treatment: solution treated (ST) at 580[(a) and (d)], 560 [(b) and (e)] and 540°C[(c) and (f)], water quenched (WQ) at room temperature (RT) and artificially aged (AA) 72 hours at 190°C. (a) -(c) <110> Al orientation and (d) - (f) <100> Al orientation. 85

Figure 4.7. TEM BF micrographs showing precipitation of dislocation loops and helices; <110>Al orientation. Material treatment: 88
(a) ST 580°C, WQ(RT), NA 24 hours
(b) ST 580°C, WQ(RT), NA 120 hours
(c) ST 580°C, WQ(RT), NA 1440 hours
(d) ST 580°C, WQ(RT), NA 24 hours and AA 24 hours at 190°C.

Figure 4.8. TEM BF micrographs showing homogeneous S precipitation; <100>Al orientation. Material treatment: 90
(a) ST 580°C, WQ(RT), naturally aged (NA) for 24 hours and AA 24 hours at 190°C.
(b) ST 580°C, WQ(RT), NA 24 hours and AA 72 hours at 190°C.
(c) ST 580°C, WQ(RT), NA 1440 hours and AA 24 hours at 190°C.

Figure 4.9. TEM BF micrographs; <110>Al orientation. 93
(a) Distribution of dislocation loops
(b) Homogeneous S precipitation
(c) Heterogeneous S precipitation upon dislocation loops
Material treatment: ST 580°C [ST 560°C for 4.9(b) and (c)], WQ(RT), NA 1440 hours and AA 24 hours at 190°C.

Figure 4.10. TEM BF micrographs showing homogeneous S precipitation; <100> Al orientation. Material treatment: 95
(a) ST 580°C, WQ (60°C for 1 minute), WQ(RT) and AA 24 hours at 190°C.
(b) ST 580°C, Oil quenched (100°C for 14 hours), WQ(RT) and AA 24 hours at 190°C.
(c) ST 580°C, WQ (100°C for 1 minute), WQ (RT) and AA 24 hours at 190°C.

Figure 4.11. Details of heat treatments carried out. 99

Figure 5.1. Specific heat capacity vs. Temperature curves for binary Al-Li system (alloy A3). 108

Figure 5.2. Specific heat capacity vs. Temperature curves for ternary Al-Li-Zr system (alloy A4). 108

Figure 5.3. Specific heat capacity vs. Temperature curves for ternary Al-Cu-Mg system (alloy A5). 111

Figure 5.4. (a) TEM DF micrograph showing precipitation of dislocation loops in alloy A5. Material treatment: ST 540°C and WQ(RT). 112
(b) TEM BF micrograph showing heterogeneous S precipitation in alloy A5; <110> Al orientation. Material treatment: ST 540°C, WQ(RT), NA 1 month and AA 24 hours at 190°C.

Figure 5.5. Specific heat capacity vs. Temperature curves for quaternary Al-Li-Cu-Mg-(Zr) system (alloy A2). 114

Figure 6.1. Microstructures of the as cast material (alloy A1) 125
(a) Light micrograph
(b) An SEM micrograph imaged in the secondary electron mode
(c) An SEM micrograph imaged in the back scattered mode.

Figure 6.2. (a) An SEM micrograph in the back scattered mode showing the phases at the grain boundary triple point junctions. 127
(b) - (e) Element X-ray maps of 6.2(a); (b) Aluminium (the count level is adjusted to show only the matrix aluminium distribution, (c) copper (d) magnesium and (e) iron.

Figure 6.3. Secondary Ion Mass Spectrometry (SIMS). Line scan traces showing the distribution of elements at the grain boundaries of the cast material A1. 129

Figure 6.4. Element SIMS maps of the grain boundary phases in cast material A1. All images are from the same area. 131
(a) Copper, 63 Cu^+
(b) Lithium, 7 Li^+
(c) Magnesium, 24 Mg^+
(d) Iron, 56 Fe^+

Figure 6.5. TEM micrographs of the grain boundary phases in cast material A1 134
(a) BF micrograph showing grain boundary particles (labelled G_1 and G_2)
(b) SADP from particle G_1; close to [013] FCC. $L\lambda$ = 42.44 mm Å.
(c) BF micrograph showing grain boundary particles (labelled G_3).
(d) SADP from G_3; close to [100]FCC. $L\lambda$ = 398 mm Å.
(e) BF micrograph showing lamellar eutectic and silicon rich phase, P3 (shown by arrows) at the grain boundary triple point junctions.

Figure 6.6. Details of matrix phases in cast material A1. 137
(a) BF micrograph showing distribution of matrix phases.
(b) BF micrograph showing a typical rhombohedral shaped particle.
(c) High resolution image revealing modulation of planar defects normal to the length of a particle.
(d) SADP of 6.6 (c); streaking about the diffraction spots due to planar defect structure.

Figure 6.7. DSC trace of the cast material A1. 139

Figure 6.8. Light micrographs showing the effect of annealing temperatures and times on the cast material A1. The heat treated materials were air cooled. Material Treatment: 142
(a) 8 hours at 550°C
(b) 10 hours at 525°C
(c) 8 hours at 537°C
(d) 24 hours at 537°C

Figure 6.9. (a) BF micrograph of the homogenised material 144
(b) BF micrograph showing an Al-Fe-Cu based particle at the grain boundary of the wrought structure.
(c) SADP from the Al-Fe-Cu based particle of 6.9(b); close to [001] orthorhombic; $L\lambda = 47.75$ mm Å.
(d) BF micrograph showing matrix particles in cast material A2.
(e) SADP from particle M3 of 6.9(d); close to [034] orthorhombic. $L\lambda = 42.24$ mm Å.
(f) SADP from particle M3 of 6.9(d); close to [001] orthorhombic; $L\lambda = 42.24$ mm Å.

Figure 7.1. Variation in peak pressure as functions of initial billet temperature and extrusion ratio. 155

Figure 7.2. Variation in peak pressure as a function of ram speed. 155

Figure 7.3. Light micrographs of the as extruded grain structure (Longitudinal section); 159
(a) Near surface; 500°C (initial billet temperature), 20:1 (extrusion ratio), 3 mm/sec (ram speed).
(b) Near surface; 400°C, 20:1, 3 mm/sec.
(c) Core, 500°C, 20:1, 3 mm/sec.
(d) Mid-radius, 500°C, 80:1, 3 mm/sec.
(e) Core, 500°C, 80:1, 3 mm/sec.
(f) Core, 400°C, 50:1, 3 mm/sec.

Figure 7.4. Light micrographs of the extruded material (Longitudinal sections) 161
(a) Mid-radius; 450°C, 20:1, 3 mm/sec; annealed at 530°C for 5 hours under argon atmosphere.
(b) Core; 450°C, 20:1, 3 mm/sec; annealed at 530°C for 5 hours under argon atmosphere.
(c) Mid-radius; 400°C, 20:1, 3 mm/sec; annealed at 530°C for 5 hours under argon atmosphere.
(d) Mid-radius; 500°C, 20:1, 15 mm/sec.
(e) Core; 500°C, 20:1, 15 mm/sec.
(f) Core structure of an air cooled extrudate; 500°C, 20:1, 3 mm/sec.

Figure 7.5. Light micrographs showing grain structure produced in torsion (deformed at 500°C; total strain = 2.5). 164
(a) Near surface
(b) Near surface
(c) Mid-radius
(d) core

Figure 7.6. BF micrographs showing development of subgrain structures at the core of the as extruded material. 166
(a) 500°C, 20:1.
(b) 450°C, 20:1.
(c) 400°C, 20:1.
(d) 500°C, 50:1.
(e) 500°C, 80:1.
Ram speed being 3 mm/sec. TEM micrographs of longitudinal sections.

Figure 7.7. BF(a,b) & DF(c) micographs showing development of subgrain structures, in the as extruded material. 169
(a) Mid-radius 500°C, 20:1, 3 mm/sec.
(b) Mid-radius 400°C, 50:1, 3 mm/sec.
(c) Mid-radius, 500°C, 50:1, 3 mm/sec.

Figure 7.8. (a) TEM BF micrograph illustrating recrystallisation by grain boundary bulging mechanism in the as extruded material; 500°C, 20:1, 3 mm/sec. 172
(b) TEM BF micrograph illustrating recrystallisation by grain boundary bulging mechanism in the as extruded material; 500°C, 20:1, 3 mm/sec.

Figure 7.9. (a) TEM BF micrograph illustrating development of highly misoriented subgrains adjacent to the original boundaries; 500°C, 50:1, 15 mm/sec. 174
(b) TEM BF micrograph showing a large subgrain (labelled A) in the as extruded material; 500°C, 50:1, 15 mm/sec.

Figure 7.10. TEM BF micrographs showing 177
(a) precipitation of second phase particles in the as extruded material; 400°C, 20:1, 3 mm/sec.
(b) Precipitation of helices in the material extruded at 500°C and NA 1 month; <112> Al orientation.
(c) Heterogeneous S (and T_1) precipitation in the material extruded at 500°C, NA 2 months, AA 24 hours at 190°C.
(d) Homogeneous, and heterogeneous (on dislocation loops) S precipitation in the material extruded at 500°C, NA 2 months, AA 24 hours at 190°C.

Figure 7.11. Variation in as extruded tensile (longitudinal) properties as functions of extrusion temperatures and extrusion ratios. 179

Figure 7.12. Artificial ageing response at 190°C of the extrudates produced at 400 and 500°C, 20:1, 3 mm/sec and NA 2 months. 182

Figure 8.1. Ageing response of the extrudates (produced at 400°C and 500°C, 20:1, 3 mm/sec) at 190°C with prior solution treatment at 530°C for 20 minutes. 191

Figure 8.2. Ageing response of the extrudates (produced at 400°C and 500°C, 20:1, 3 mm/sec) at 190°C with prior solution treatment at 530°C for 40 minutes. 191

Figure 8.3. Ageing response of the extrudates (produced at 400 and 500°C, 20:1, 3 mm/sec). at 170°C (T6 temper). 193

Figure 8.4. Ageing response of the extrudates (produced at 500°C, 50:1 and 80:1, and 3 mm/sec) at 190°C (T6 temper). 194

Figure 8.5. Ageing response of the extrudates (produced at 400 and 500°C, 20:1, 3 mm/sec) at 190°C with a prior natural age of 24 hours. 194

Figure 8.6. (a) TEM DF image showing δ' precipitation imaged using (100) superlattice reflection; <110> Al orientation. Material treatment: ST 530°C, WQ, AA 5 hours at 190°C. 197

(b) BF image showing subgrain boundaries free of any S and T_1 precipitate. The arrows show precipitation of coarse grain boundary precipitates. Material treatment: ST 530°C, WQ and AA 5 hours at 190°C.

(c) BF image showing heterogeneous S and T_1 precipitation; close to <112> Al orientation. Material treatment: ST 530°C, WQ, AA 24 hours at 190°C.

(d) BF image showing homogeneous S precipitation; <100> Al orientation. Material treatment: ST 530°C, WQ, AA 24 hours at 190°C.

(e) BF image showing precipitation of dislocation loops; Close to <112> Al orientation. Material treatment: ST 530°C, WQ, NA 1 month.

(f) BF image showing homogeneous S precipitation; <100> Al orientation. Material treatment: ST 530°C, WQ, NA 24 hours and AA 24 hours at 190°C.

Figure 8.7. TEM BF images showing 200
(a) Homogeneous S precipitation; <100> Al orientation.
Material Treatment: ST 530°C, WQ, NA 1 month,
AA 24 hours at 190°C.
(b) Heterogeneous S precipitation, <100> Al orientation.
Material Treatment: ST 530°C, WQ, NA 1 month,
2 % stretch and AA 24 hours at 190°C.
(c) Heterogeneous S precipitation; <100> Al orientation.
Material treatment: ST 530°C, WQ, 2% stretch, and
AA 24 hours at 190°C.

Figure 8.8. (a) BF image showing coarse grain boundary precipitates; <110> Al orientation. 203
Material treatment: ST 530°C, WQ, AA
24 hours at 190°C.
(b) DF image of 8.8(a) showing δ' PFZs;
imaged using (100) superlattice reflection.
(c) BF image showing coarse grain boundary precipitates.
Material treatment: ST 530°C, WQ, AA 24 hours at 190°C.
The micrograph also shows an intragranular Al-Fe-Cu based particle.
(d) BF image showing coarse grain boundary precipitates associated with dislocation structures.
Material treatment: ST 530°C, WQ, AA 24 hours at 190°C.

Figure 8.9. Longitudinal tensile properties of the heat treated extrudates (T6 condition) extruded at 400°C. 205

Figure 8.10. Longitudinal tensile properties of the heat treated (T6 condition) extrudates produced at 500°C. 207

Figure 8.11. Traces of load-extension curves obtained from longitudinal tensile tests made on the solution treated, underaged and peakaged material. 210

Figure 8.12. Transverse fracture toughness properties of the heat treated extrudates produced at 500°C, 20:1, 3 mm/sec. 211
Details of treatments prior to artificial ageing at 190°C are included in the figure.

Figure 8.13. SEM micrographs of fracture surfaces (a, c and d) and accompanying light micrograph (b) of longitudinal tensile profile in the underaged condition (5 hours at 190°C). 215

Figure 8.14. SEM micrographs of fracture surface (a and c) and accompanying light micrograph of longitudinal tensile profile (b) in the peakaged condition (24 hours at 190°C); Figure 8.14(c) shows the fracture surfaces in the overaged condition (100 hours at 190°C). 217

Figure 8.15. SEM micrographs showing the fracture surfaces of the failed tensile specimens. Material treatment: (a) ST 530°C, WQ, NA 1 month, AA 24 hours at 190°C; (b)& (c) ST 530°C, WQ, NA 1 month, 2 % stretch and AA 24 hours at 190°C. 219

Figure 8.16. SEM micrographs showing the fracture surfaces of the transverse fracture toughness specimens. Material treatment: (a) underaged (5 hours at 190°C), (b) peakaged (24 hours at 190°C), (c) overaged (100 hours at 190°C) (d) ST 530°C, WQ(RT), NA 1 month and AA 5 hours at 190°C; (e) and (f) ST 530°C; WQ(RT), NA 1 month, and AA 24 hours at 190°C. 222

Figure 8.17. Traces of load-extension curves obtained from tensile tests made on the solution treated binary Al--2.8 wt % Li and Al-1.2 wt % Li alloys. 229

CHAPTER ONE

INTRODUCTION

Lithium is the lightest metallic element and the only one which when alloyed with aluminium increases the elastic modulus and significantly decreases the density. For every weight percent lithium added to aluminium, the density is reduced approximately 3 % and the elastic modulus is increased about 6 % (1). Therefore, aluminium alloys that contain lithium as a primary alloying constituent offer great potential for improving the structural efficiency of aircraft components.

The attempts to realise the potential benefits of increased modulus and reduced density of Al-Li alloy date back over sixty years; although, it was not until the 1950's when the Al-Cu-Li alloy, AA 2020 was developed in the USA by the Aluminium Company of America (ALCOA). Compared to 7075, AA 2020 has had approximately 3 % lower density and a 7 % higher elastic modulus; commercial application of this alloy was found and it was used in a Mach-2 fighter and the RA-5C 'vigilante' by the U.S. Navy. However, further research revealed that the alloy was notch sensitive and had a lower fracture toughness than 7075; new U.S. airplane damage tolerance requirements could not be met and the result was the withdrawal of AA 2020 from commercial production, although it continued to fly successfully in existing aircraft.

In the U.S.S.R., at about the same time, VAD 23, an alloy similar in composition to AA 2020 was developed. Later the Soviets investigated and developed a series of Al-Mg-Li alloys referred to as 01420. However, these alloys too exhibited poor ductility and fracture toughness properties. Attempts to improve the mechanical properties were made, but, without any success. It is now understood that the development work was carried out in those days without a proper understanding of the strengthening and deformation mechanisms in lithium - containing aluminium alloys.

In the early 70's, several important factors combined to accelerate activity in the Al-Li technology area. They included mainly the increased importance for

improved aircraft materials, the changing economics of commercial and military aircraft fleet operation costs and the advent of carbon fibre composities. The total combined effects have been catalytic and the development work on Al-Li alloys was promoted in the U.S. by ALCOA and simultaneously in Great Britain by the British Aluminium Company (later absorbed within British ALCAN) and the Royal Aircraft Establishment (RAE). The emphasis of those investigations was to improve the commercially unacceptable low ductility and fracture toughness of Al-Li alloys (2).

In the mid and late 70's, the deformation mechanisms and the primary technical factors responsible for the brittle behaviour of Al-Li alloys were identified. This very substantial technical progress together with continuing large scale development programme inspired the aluminium producers to examine and produce more complex Al-Li alloys via both ingot and powder metallurgy routes. In 1983, British ALCAN international in association with RAE developed via ingot metallurgy route the first of the new generation of Al-Li alloys referred to as DTD XXXA (Aluminium Association designation being AA 8090). This XXXA alloy was designed to replace medium strength 2014-T6 and 2024-T3 plate and sheet in aircraft. In the following years, a higher strength alloy DTD XXXB was also developed in UK to substitute for 7000 series aluminium alloys. Since the introduction of these two alloys, several other Al-Li alloys of varying compositions have been developed by other leading aluminium producers in US and France. The chemical composition of current commercial 'ingot route' Al-Li alloys together with their trade names and the associated other details are described (3) in Figure 1.1.

Recently, commercial production of the new generation quaternary Al-Li alloys has begun, although, the problems associated with poor ductility and fracture toughness properties of these alloys have only been partially overcome. However, the fundamental metallurgical concepts which are responsible for the strength and ductility characteristics of these alloys are more clearly understood today and they suggest that both the alloy composition and hence control of heat treatment conditions to develop appropriate precipitate phase distributions as well as a control over the materials' grain structure are of extreme importance.

The current industry assessment is that for a large modern transport aircraft the extrusion product form may be as high as 28 wt.% of the total product form (1). So, studies in detail on the extrusion processing of Al-Li alloys are

Figure 1.1. Composition Ranges for Commercially Registered Al-Li-Cu-Mg-(Zr) Alloys

Aluminium Association designation	Company of origin	Trade Names/ other designations	Chemical Composition (weight per cent) Li	Cu	Mg	Zr	Si	Fe	Cr	Ti	Zn	Mn	Al	Substitute for
8090	Alcan/Pechiney	F92 (RAE) DTD --- A (RAE) LITAL 'A' (Alcan) CP271 (Pechiney)	2.20 to 2.70	1.00 to 1.60	0.60 to 1.30	0.04 to 0.16	0.00 to 0.20	0.00 to 0.30	0.00 to 0.10	0.00 to 0.10	0.00 to 0.25	0.00 to 0.10	Bal.	2014-T3 & T851 2024-T4 7475-T73 7075-T73
X8090A	Alcoa	Alithalite A	2.10 to 2.70	1.10 to 1.60	0.80 to 1.40	0.08 to 0.15	0.00 to 0.10	0.00 to 0.15	0.00 to 0.05	0.00 to 0.15	0.00 to 0.10	0.00 to 0.05	Bal.	2024-T3 & T351
8091	Alcan	DTD --- B (RAE) LITAL 'B' (Alcan)	2.40 to 2.80	1.60 to 2.20	0.50 to 1.20	0.08 to 0.16	0.00 to 0.20	0.00 to 0.30	0.00 to 0.10	0.00 to 0.10	0.00 to 0.25	0.00 to 0.10	Bal.	7075-T76 7475-T76 7050-T7651 7010-T7651
X8192	Alcoa	Alithalite C	2.30 to 2.90	0.40 to 0.70	0.90 to 1.40	0.08 to 0.15	0.00 to 0.10	0.00 to 0.15	0.00 to 0.05	0.00 to 0.15	0.00 to 0.10	0.00 to 0.05	Bal.	Low density Medium strength
X8092	Alcoa	Alithalite D	2.10 to 2.70	0.50 to 0.80	0.90 to 1.40	0.08 to 0.15	0.00 to 0.10	0.00 to 0.15	0.00 to 0.05	0.00 to 0.15	0.00 to 0.10	0.00 to 0.05	Bal.	7075-T73
2090	Alcoa	Alithalite B	1.90 to 2.60	2.40 to 3.00	0.00 to 0.25	0.08 to 0.15	0.00 to 0.10	0.00 to 0.12	0.00 to 0.40	0.00 to 0.15	0.00 to 0.10	0.00 to 0.05	Bal.	7075-T6 7075-T73 (forgings)
2091	Pechiney	CP274	1.70 to 2.30	1.80 to 2.50	1.10 to 1.90	0.04 to 0.16	0.00 to 0.20	0.00 to 0.30	0.00 to 0.10	0.00 to 0.25	0.00 to 0.10	0.00 to	Bal.	2024-T351 7475-T7351 7175-T731
	Pechiney	CP276	1.90 to 2.60	2.50 to 3.30	0.20 to 0.80	0.04 to 0.16	0.00 to 0.20	0.00 to 0.30	0.00 to 0.10	0.00 to 0.10	0.00 to 0.25	0.00 to 0.10	Bal.	7050-T6 & T851 7010-T6 & T851

necessary. An additional advantage in using extrusion processing route is that a variety of grain structures may be produced through varying the extrusion processing variables such that optimisation of the processing conditions can lead to improved microstructures and properties.

The present research study concerns AA 8090 Al-Li all oys and the aim is to design initially a series of suitable heat treatment conditions to develop typical phases within the microstructure, investigate the effect of extrusion processing variables on the variation in structure and properties of the material and finally to investigate the combined effects of the use of suitable heat treatment and optimum processing conditions upon the strength, ductility and the fracture toughness characteristics of the material.

CHAPTER TWO

LITERATURE REVIEW

2.1. THE PHYSICAL METALLURGY OF Al-Li ALLOYS

2.1.1. Phase Transformations in Al-Li Alloys

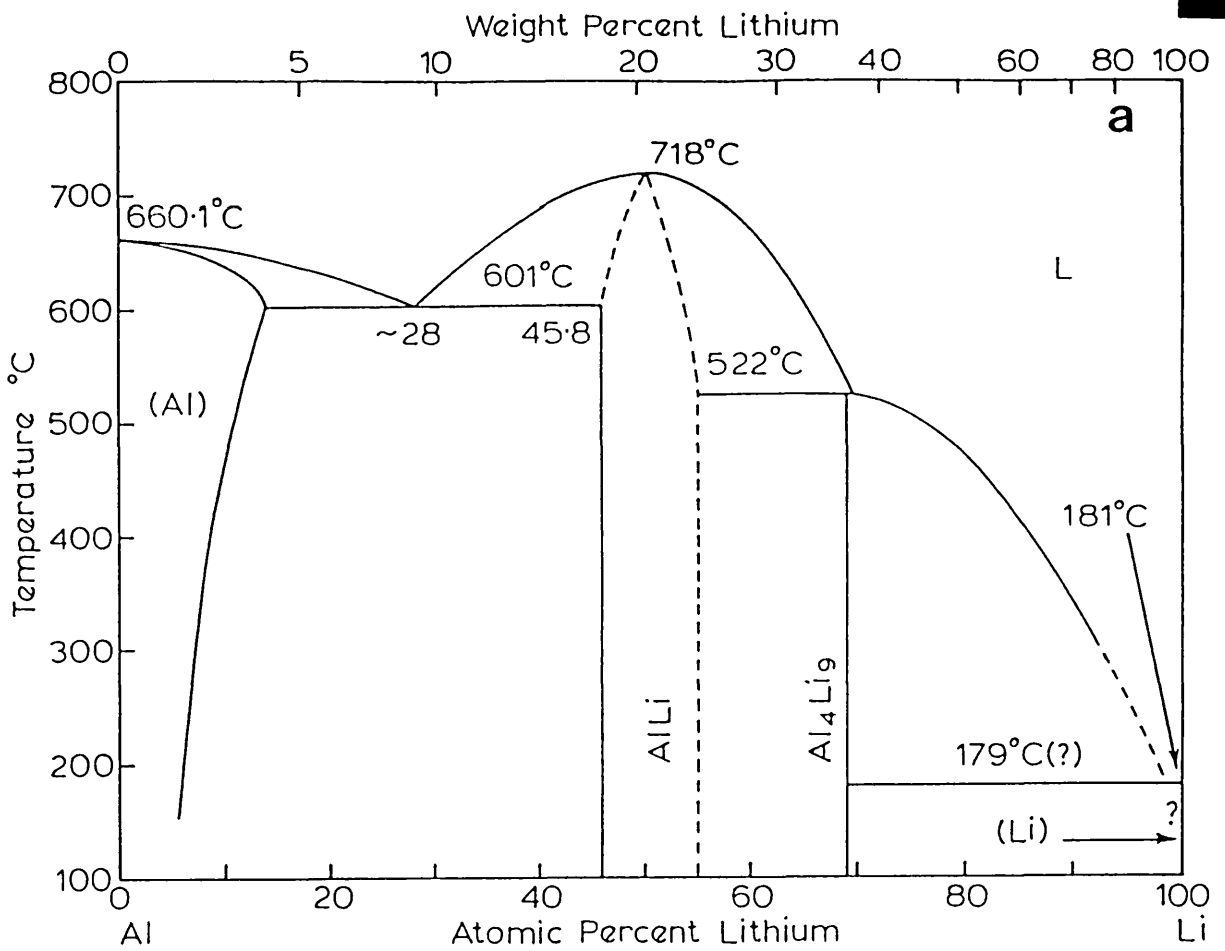
2.1.1.1. Binary Al-Li system

In common with conventional heat-treatable aluminum alloys e.g. Al-Cu-Mg, Al-Zn-Mg-Cu, Al-Mg-Si etc., Al-Li alloys rely upon the ageing heat treatments producing precipitation hardening behaviour for increased strength. The aluminum rich corner of the equilibrium Al-Li phase diagram reviewed in detail by McAlister (4) is presented in Figure 2.1(a). The figure shows that a simple eutectic reaction liquid $\rightarrow \alpha$(Al) + δ(AlLi) takes place at about 600^{o}C; additionally, the solubility of lithium in aluminum decreases rapidly with decrease in temperature such that an alloy containing more than about 6 at % lithium may be quenched from the single phase field and aged in the two phase field to obtain the whole amount of excess lithium available in the form of precipitates.

In the early 1960's Silcock (5) detected the presence of δ(AlLi) phase in Al-9 at % Li alloys aged at 240^{o}C. Silcock confirmed that δ has a B_{32} (NaTl) type of structure with lattice parameter a = 6.37 ± 0.01 Å and maintains an orientation relationship with the matrix as follows:

$(100)_{\delta} \| (110)_{Al}$; $(0\bar{1}1)_{\delta} \| (1\bar{1}2)_{Al}$; $(011)_{\delta} \| (\bar{1}11)_{Al}$, a {111} matrix habit plane was also suggested. At a lower ageing temperature of 165^{o}C, a simple Ll_2 superlattice of the face centered cubic matrix occurred; it was identified to be due to $\delta'(Al_3Li)$ phase with lattice parameter a = 4.038 Å. This precipitate is spherical and yields a very low α/δ' mismatch value ~ -0.3 % (6). It is coherent with the matrix and is responsible for age hardening in the binary Al-Li system.

Although δ' was extensively studied by both x-ray diffraction (5) and Transmission Electron Microscopy (6,7) for several years after its discovery, it was not until 1971 that the δ' solvus was first defined by Noble and Thompson (8) using transmission electron microscopy and resistivity measurements. Their (8) work



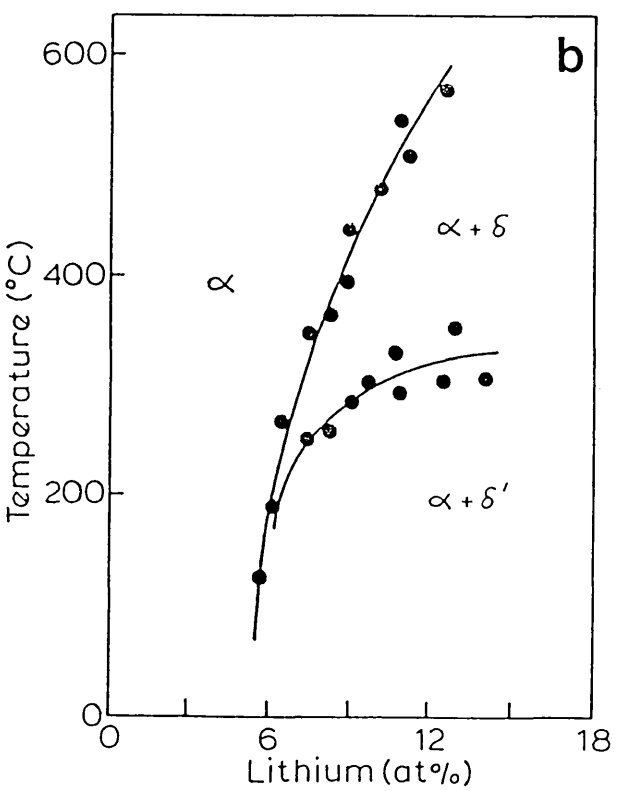


Figure 2.1. (a) The equilibrium Al-Li phase diagram (after McAlister(4)) and (b) experimentally determined solvus lines for both δ and δ' (8, 9, 10, 11).

together with that of Costas and Marshall (9), Nozato and Nakai (10) and Williams and Edington (11) is included in Figure 2.1 (b) showing the solvus lines for both δ and δ'. In addition to the metastable solvus line, Williams and Edington (11) inferred the presence of a coherent solvus line just below the δ' solvus from the heterogeneous precipitation of δ' on dislocations and the absence of homogeneously precipitated matrix δ'. Further work by Ceresara et al (12) using small angle x-ray scattering (SAXS) to define the δ' coherent solvus agreed well with that due to Williams and Edington (11). This line was termed the thermodynamic solvus, to distinguish it from the apparent solvus lines shown in Figure 2.1 (b). Additional SAXS work by Cocco et al (13) extended the thermodynamic δ' solvus line to define the coherent miscibility gap over the full range of the δ' phase field to ~25 at % lithium. Extrapolation of this line agrees closely with the apparent solvus lines of Williams and Edington (11) indicating that the difference between the coherent and incoherent solvus lines is very small over the entire phase field. This is well understood in view of the small amount of lattice strain generated by δ' formation. The full Al-Li phase diagram showing the δ solvus and the apparent coherent δ' solvus lines as determined by TEM (8,11) and SAXS (12,13) is shown in Figure 2.2. The metastable α + δ' solvus plays a significant role ensuring that heat treatment of alloys of commercial interest involves compositions and temperatures lying within it. A simple miscibility gap, produced by connecting the experimentally determined α and δ' solvi, (Figure 2.2) was generally accepted until recently. However, Gayle and Vandersande (14) pointed out that such a miscibility gap involving two distinct crystal structures (disordered α and $L1_2$ ordered δ') violates thermodynamic restrictions: since $L1_2$ ordering is a first order transformation it is necessary that the two phase regions be bordered by the two single phase fields. These authors have proposed several possible forms of metastable phase diagrams (14, 15), the latest being shown in Figure 2.3(a). A theoretical model concerning the stable and metastable Al-Li phase diagram has been recently developed by Sigli and Sanchez (16). The developed metastable diagram is shown in Figure 2.3(b). The α-δ' relationship is similar to that proposed by Gayle and Vandersande but the diagram additionally predicts another miscibility gap viz. ($\alpha_1 + \alpha_2$) within the (α + δ') phase field. The presence of such second level of metastability within the (α + δ') phase field has been claimed through the interpretation of data from differential scanning calorimetry which shows low temperature endotherms and exotherms consistent with GP zones formation and dissolution (10, 17). Microstructural investigations, however, have been unable to confirm the existence of such zones.

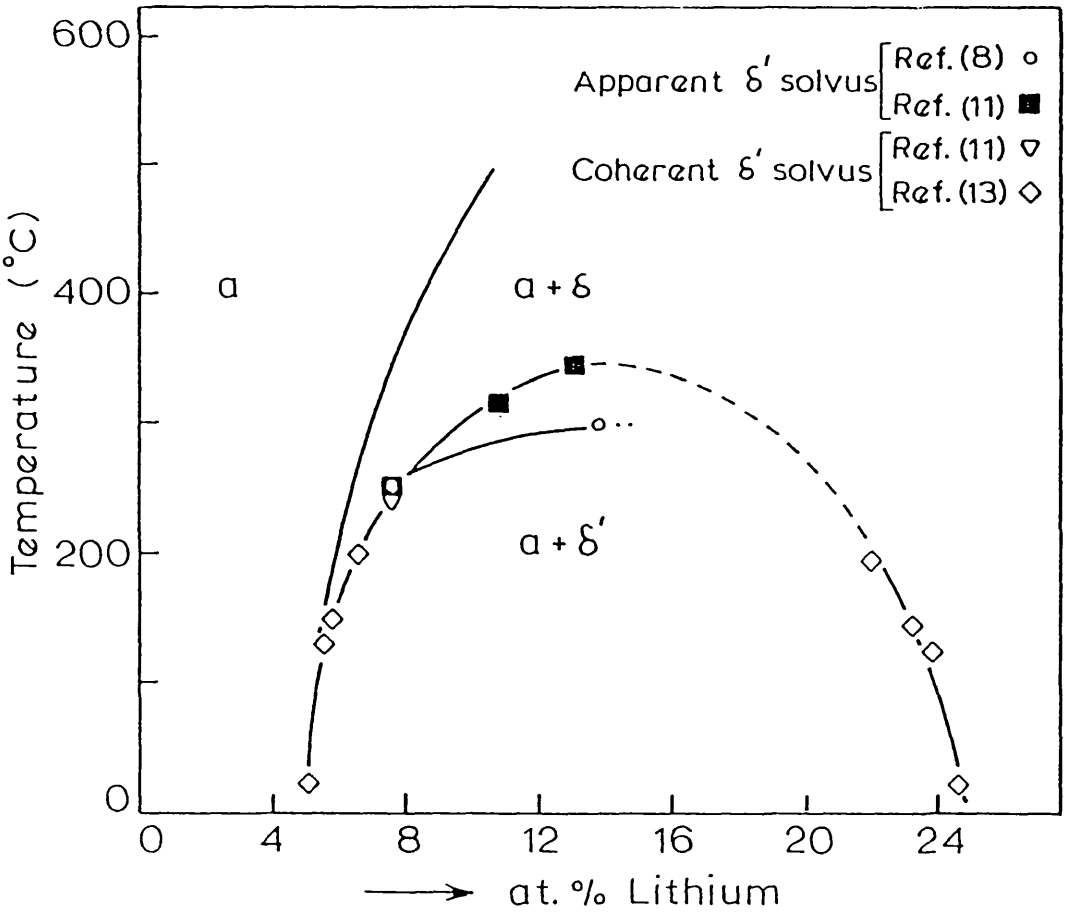


Figure 2.2. Phase diagram of Al-Li showing the δ solvus, and the apparent and coherent δ' solvus lines (8, 11, 13).

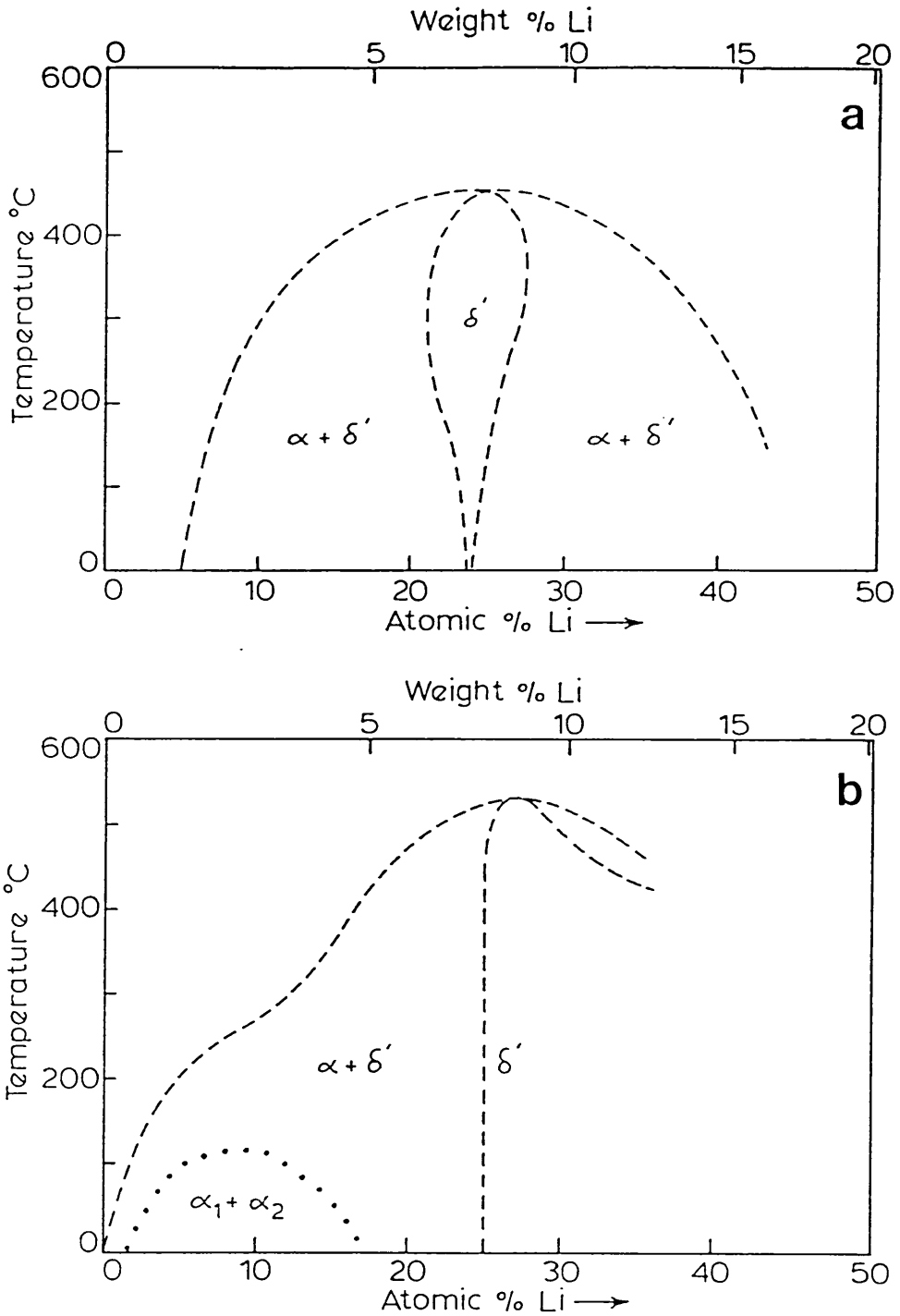


Figure 2.3. The metastable α-δ' system
(a) as proposed by Gayle and Vander Sande (14)
(b) as predicted by Sigli and Sanchez (16)

Balmuth (18) also observed low temperature dissolution peaks in thermal analysis experiments but has attributed these to the reversion of fine δ' produced on quenching.

The nucleation of δ' has been studied intensively by numerous investigators (8, 11, 19, 20). The authors (2) showed that because of the small coherency strains, the particles tend to be spherical and the particles precipitate by homogeneous nucleation because of very low interfacial energy between δ' and the matrix, resulting in a uniform distribution of δ' with most of the decomposition occurring apparently during the quench. Even the nucleation could not be prevented by step quenching above the δ' solvus, to remove excess vacancies (11), although, Suzuki et al (21) observed that the excess vacancies exert an important role on δ' nuclei formation. In all cases, the alloy strengthening was found to be due to the very great precipitation of δ'. The strengthening fades off sharply at ageing temperatures above $200^{o}C$; this is attributed to the decrease in δ' volume fraction and rapid coarsening of δ' particles in accordance with the Lifshitz-Wagner kinetics showing a classical change in average size γ with $(time)^{1/3}$ (8, 11, 22). Additionally, preferential coarsening has been observed at dislocations (11) and grain boundaries (23); the former effect can be accounted for by rapid pipe diffusion at dislocations whilst the latter case is a good example of a discontinuous coarsening reaction, providing the lamellar α + δ' to grow at the expense of fine homogeneous δ'-dispersion. The driving force for such a discontinuous reaction would be expected to be small in view of reported small surface energy values (e.g. 0.24 Jm^{-2} (8), 0.18 Jm^{-2} (6)). The reaction was shown to terminate rapidly as δ formed.

The exact mechanism of δ formation has been the subject of great debate. Nozato and Nakai (10) proposed that δ forms from the metastable δ'. A similar mechanism due to Schegoleva and Rybalko (24) was that the formation of δ phase consists in the rearrangement of f.c.c. to NaTl type structure by collective shears of groups of {111} f.c.c. planes similar to the martensitic transformation process. However, failure to produce diffraction evidence to support such a process weakened the argument for the proposed mechanism. Niskanen et al (25) suggested that the formation of δ on the grain boundaries is as a result of preferential coarsening of δ' such that the boundaries provide the energy required to overcome the interfacial energy barrier of the δ' - δ transformation. However, Williams (26), Sanders et al

(27) and Jha et al (28) showed evidence in favour of the δ nucleation independent of δ' and growth of δ-phase particles accompanied by dissolution of surrounding metastable δ'.

2.1.1.2. Ternary Al-Li-Mg system

In the early stages of the development of lithium containing aluminium alloys, basically ternary additions e.g. copper and magnesium by Jones and Das (29) were made with the aim of increasing the strength without sacrificing much ductility and density; promising results were obtained, though, it is now apparent that those developments were carried out with an incomplete understanding of the strengthening mechanism and the role of metastable δ' phase.

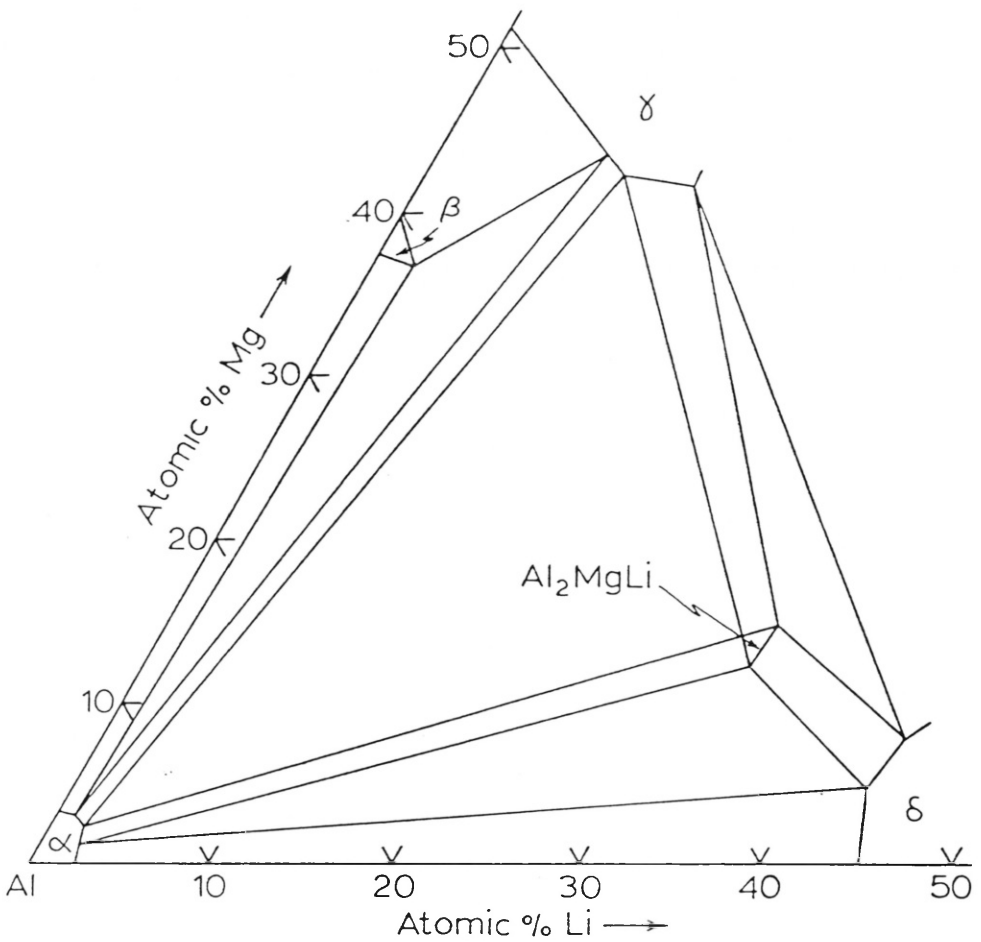
A detailed study on the equilibrium phase relations in the Al-Li-Mg system was initially carried out by Levinson and McPherson (30). The isothermal phase section of the Al-Li-Mg system for a typical ageing temperature of 200^{o}C (31) is presented in Figure 2.4. At the same time I.N. Fridylander et al (32) studied the phase equilibria and mechanical properties of Al-Mg-Li alloys and finally their work resulted in an alloy designated 01420 in the mid 1960's with a nominal composition of Al-5Mg-2Li-0.5 Mn. The authors explained the precipitation sequence of the following type:

supersaturated solution (ss)→GP zones→Al_2LiMg

Little strengthening was associated with the zone formation but ageing at 160 - 180^{o}C produced a substantial increase in strength. Al_2LiMg phase was claimed to be the major strengthening phase in this alloy system. The exact precipitation reactions in this alloy system were not known until Thomson and Noble (33) examined in detail the precipitation characteristics of Al - (1.5 - 2.0 wt %) Li - (1-6 wt %) Mg alloys and showed the precipitation sequence to be

α_{ss}→δ' (Al_3Li)→Al_2LiMg

The authors (33) suggested that the δ'(Al_3Li) phase is the major strengthening phase in these ternary alloys and the equilibrium Al_2LiMg phase appears in alloys with a high magnesium content (greater that 2 wt %) when aged at temperatures above



β : Al_3Mg_2 , γ : $Al_{12}Mg_{17}$, δ : AlLi

Figure 2.4. Isothermal section of the Al-Li-Mg system at 200°C (after Schurmann and Geissler (31)).

170^{o}C; Al_2LiMg phase is coarsely dispersed producing little strengthening and occurs as rods with <110> growth directions and maintains an orientation relationship of the following type:

$$(1\bar{1}0)_{ppt.} \| (\bar{1}10)_{Al};\ [110]_{ppt.} \| [111]_{Al}.$$

The equilibrium Al_2LiMg phase possesses a f.c.c. structure with lattice parameter a = 19.9 Å (20.2 Å according to Levinson and McPherson (30)). Schegoleva and Rybalko (34) suggested that the formation of equilibrium precipitate Al_2LiMg, which they misleadingly termed S, was prece ded by that of an intermediate metastable phase S'; S' was found to have a face centered monoclinic lattice with lattice parameters a=c=20.004 Å, b= 19.797 Å, β = 88^{o}50' and an orientation relationship with the matrix of the following type:

$$(101)_{S'} \| (\bar{1}10)_{Al};\ (10\bar{1})_{S'} \| (\bar{1}\bar{1}1)_{Al}.$$

However, no other literature is available in support of the existence of any such metastable precursor to Al_2LiMg phase.

Thompson and Noble (33) suggested that the primary contribution of magnesium to strength is in its solid solution hardening. Also, it has been suggested (35, 36) that magnesium reduces the solubility of lithium, thereby increasing the volume fraction of δ' for a given lithium content. Additional strengthening involving possible incorporation of magnesium into δ' has also been suggested (36, 37, 38).

2.1.1.3. Ternary Al-Li-Cu system

Addition of copper to binary Al-Li alloys produces phases which are partly related to the Al-Cu system and partly to the Al-Li system; also, formation of several ternary phases is feasible depending on the alloy composition. In the early stages of the development of these alloys, the studies by Hardy and Silcock (39) concerning phase relationships in Al rich Al-Cu-Li alloys were most encouraging. An isothermal phase section at 350^{o}C of the Al-Li-Cu system (39) is shown in Figure 2.5(a). The figure shows the presence of three ternary phases (viz. T_B, T_1 and T_2) in addition to the binary δ(AlLi) and θ(Al_2Cu) phases.

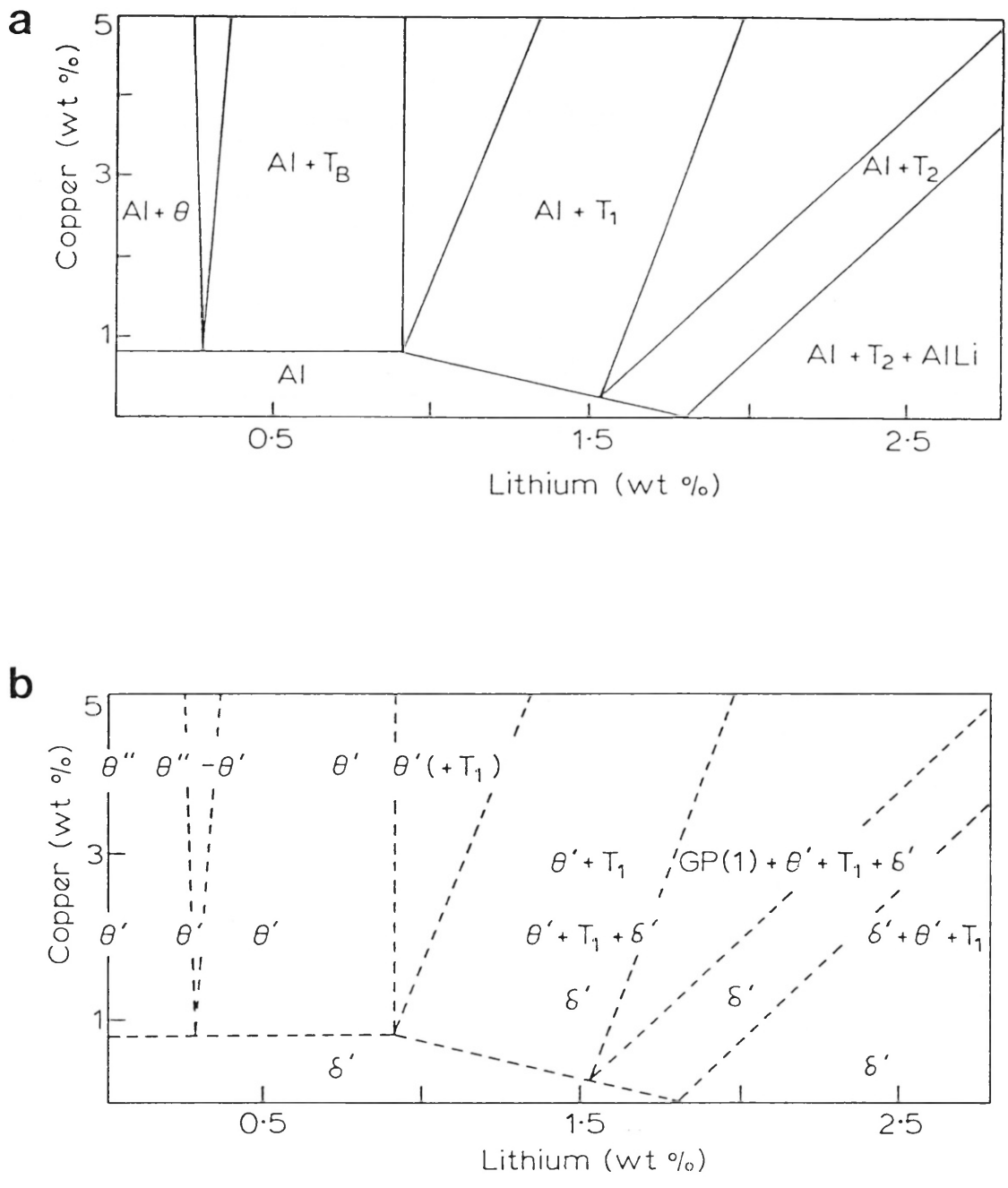


Figure 2.5. Isothermal sections of the Al-Li-Cu system

(a) phases identified at 350°C (after Hardy and Silcock (39)).

(b) phases identified after 16 hours at 165°C (after Silcock (5)).

The crystallographic data of these ternary phases were evaluated as follows: $T_B = Al_{7.5}Cu_4Li$, cubic, CaF_2 structure; a=5.83 Å; the orientation relationship being, $(100)_{T_B} \parallel (110)_{Al}$; $[001]_{T_B} \parallel [001]_{Al}$; $T_1 = Al_2CuLi$, hexagonal; a = 4.97, c = 9.35 Å; the orientation relationship being $(0001)_{T_1} \parallel (111)Al$; $[10\bar{1}0]_{T_1} \parallel [\bar{1}10]_{Al}$; $T_2 = Al_6CuLi_3$, structure undetermined. [The structure of T_2 phase was found later (40) to be icosahedral exhibiting point group symmetry M35. Cassada et al (41) also observed the icosahedral phase and found that at 190°C the majority of T_2 particles were b.c.c. with a lattice parameter of 13.9 Å;this is consistent with the structure of T_2 determined by Cherkashim et al (42).]. Later, using x-ray techniques, Silcock (5) investigated the structural ageing characteristics of these alloys. The phases observed in Al-Cu-Li alloys after ageing at 165°C for 16 hours are shown in Figure 2.5(b); the precipitates observed in alloys containing up to 2.5 wt % Li and 5 wt % Cu were, therefore, δ' (Al_3Li) , θ($CuAl_2$) and its precursors, and T_1 (Al_2CuLi) phase.

In the U.S.A., a commercial alloy 2020 of the Al-Cu-Li alloy series was developed following Silcocks' work with a composition Al-4.5 wt % Cu - 1.1 wt % Li - 0.5 wt % Mn - 0.2 wt % Cd. The precipitation sequences in these alloys described by Sanders et al (27, 43) are as follows:

$$\alpha_{SS} \nearrow \text{GP zones} \rightarrow \theta'' \rightarrow \theta' \rightarrow \theta\ (CuAl_2)$$

$$\alpha_{SS} \searrow \delta'\ (Al_3Li) \rightarrow \delta\ (AlLi)$$

Peak strength in this series of alloys has been attributed to the formation of θ" and δ'.

In the U.S.S.R., the commercial alloy VAD 23 based on the Al-Cu-Li system was developed at the same time but with increased copper and lithium content. The phases present within these alloys were found to be similar to those found by Silcock (5), but, the major strengthening of VAD 23 was attributed to the phases T_B and T_1. Schegoleva and Rybalko (44) reported in contrast to Silcock (5) that T_1 precipitation is possible in Al-Cu-Li alloys with high copper content (~5.07 wt %) and held T_1 and T_B phases responsible for the major strengthening in these alloys.

Meanwhile, Gayle (45) examined Al-Li-Cu alloys with increased lithium (2.22 wt %) and decreased copper (2.01 wt %) and reported significantly greater precipitation of δ' together with the existence of T_1 (Al_2CuLi) precipitation. Gayle also suggested that this ternary phase may form either from solid solution or from a transformation of θ' after diffusion of lithium into the Al-Cu phase had taken place. The effects of lithium additions (0.4 - 1.5 wt % Li) to an Al- 4.5 wt % copper alloy were systematically studied by Noble et al (46). The authors have shown that lithium additions modify the structure of the homogeneously nucleated GP zones. The presence of GP zones (Cu-Li) additionally, suggested that the precipitation reactions of the binary Al-Li and Al-Cu systems are very much inter-related in the Al-Li-Cu system.

Recently, Jo and Hirano (47) have summarised the precipitation sequences of Al-Cu-Li alloys as a function of copper: lithium concentration (wt %) as investigated by several investigations (5, 19, 39, 46, 48) and being shown as follows:

Cu/Li > 4; supersaturated solid solution (SSS) → GP zones →
→ θ'' → θ'

Cu/Li = 2.5~4; SSS → GP zones
→ (GP zones + δ') → (θ'' + δ') → (θ' + δ')
→ (δ' + T_1) → T_1

Cu/Li = 1~2.5; S.S.S. → (GP zones + δ')
→ (θ' + δ') → (δ' + T_1) → T_1

Cu/Li < 1: S.S.S. → (δ' + T_1) → T_1

A detailed study on the mechanism of T_1 precipitation as a function of alloy composition was carried out by Noble and Thompson (19). The authors showed that in the alloy containing high copper (3.5 wt %) and low lithium (1.5 wt %) T_1 phase was homogeneously distributed in the matrix; the nucleating sites being the homogeneously nucleated GP zones. Whereas,in the alloy containing low copper (2.5 wt %) and high lithium (2.0 wt %) T_1 phase formed heterogeneously at the matrix dislocations; the enrichment of intrinsic stacking faults (produced due to

the dissociation of 1/2 <110> dislocations into 1/6 <211> Shockley partials) by copper and lithium produced a thin layer of the T_1 phase on a {111} habit plane.

Until recently, there was no reference of any metastable precursors to T_1 and T_2 phases in the literature. Rioja and Ludwickzak (49) have proposed on the basis of diffraction evidence the existence of additional intermediate metastable phases viz. T_1' and T_2'. T_1' phase has been proposed to have a similar morphology and identical habit plane to T_1 but unlike T_1 it possesses an orthorhombic structure; whilst, T_2' has been proposed to form by the incorporation of lithium into θ' (Al_2Cu). However, these observations are controversial and the interpretation of the diffraction data had been criticised by other workers (40, 50, 51).

The influence of additional phases from the ternary Al-Li-Cu system on the δ' precipitation has been studied by several investigators. Tosten et al (40, 51) and Huang and Ardell (50) have shown that δ' can grow on the faces of θ' - plates. Tosten et al have also shown that at low Li:Cu ratio, T_1 can compete with δ' for available lithium such that heterogeneous precipitation of T_1 phase at the grain boundaries resulted in a δ' precipitation free zone within the Al-2 % Li - 3 wt % Cu alloy whereas no such PFZ's were observed within the alloy containing 2.6 wt % lithium and 1 wt % copper. The formation of PFZ in this manner has been shown to be related to the copper: lithium ratio of the Al-Li-Cu alloys.

2.1.1.4. Al-Li-Cu-Mg system

Magnesium addition to ternary Al-Li-Cu system forms the basis for todays commercial Li containing Al based alloys. The precipitation reactions within the Al-Li-Cu-Mg system are complex and also the phase diagram of the quaternary system has not been determined. However, recent studies (52-57) have shown that the phases present within the quaternary Al-Li-Cu-Mg system are similar to those present within the ternary Al-Li-Cu, Al-Li-Mg and Al-Cu-Mg systems and the choice of phases may be obtained via optimisation of the alloy composition and the ageing conditions.

The beneficial effect of Mg addition is primarily two fold: firstly, it can replace some percentage of copper which is advantageous from density consideration and secondly precipitation of additional phases viz. Al_2CuMg based

S phase and Al_6CuMg_4 based T phase in the Al-Cu-Mg system are feasible. Precipitation of T phase requires a high supersaturation of magnesium and so to allow it to form would also simultaneously encourage formation of Al_2LiMg phase in the Al-Li-Mg system; formation of coarse and intergranular Al_2LiMg phase was shown (33,36) to produce deleterious effects on the mechanical properties of the Al-Li-Mg alloys and hence the formation of T phase cannot be encouraged in the Al-Li-Cu-Mg system. However, formation of Al_2CuMg based on S phase requires relatively less magnesium for its formation. An isothermal section of the ternary Al-Cu-Mg system (57, 58) is shown in Figure 2.6. It is the ternary S (Al_2CuMg) phase which exists over much of the ternary section. Precipitation in the Al-Cu-Mg system was initially investigated by Bagaryatsky (59) and the precipitation sequence after his work is as follows:

$$\alpha_{SS} \rightarrow \text{GP zones} \rightarrow S'' \rightarrow S' \rightarrow S\ (Al_2CuMg)$$

The intermediate S" and S' are similar to S in structure and orientation but have different lattice parameters; Bagaryatsky showed that the S phase has an orthorhombic structure and its orientation relationship with the matrix as follows:

$$[100]_{S'} \,||\, [100]_{Al};\ [010]_{S'} \,||\, [021]_{Al};\ [001]_{S'} \,||\, [012]_{Al}.$$

S phase grows as rods along <1 1 0> directions; the rods widen and form laths on {2 1 0} planes. The lattice parameters of S' were found to be, a = 4.04 Å, b = 9.25 Å, and c = 7.18 Å, whereas the equilibrium S was reported (60) to have the following unit cell dimensions viz. a = 4.04 Å, b = 9.23 Å, and c = 7.14 Å.

Later studies by Lorimer (61) reconfirmed the precipitation sequence and the S'/α orientation relationship except the author did not find any metastable precursor to S' phase. Only recently the existence of such precursors (viz.S") has received support from Cuisiat et al (62). Unlike the established correlation between the GP zones and formation of other metastable and stable phases in the Al-Cu system, the connection between the GP zones and the S phase is questionable (63). Even, to date, no microstructural evidence is available to justify the transition from S' to S phase. In lithium containing Al-Cu-Mg alloys, at the typical ageing temperatures, the Al_2CuMg based precipitate is generally termed S' phase;

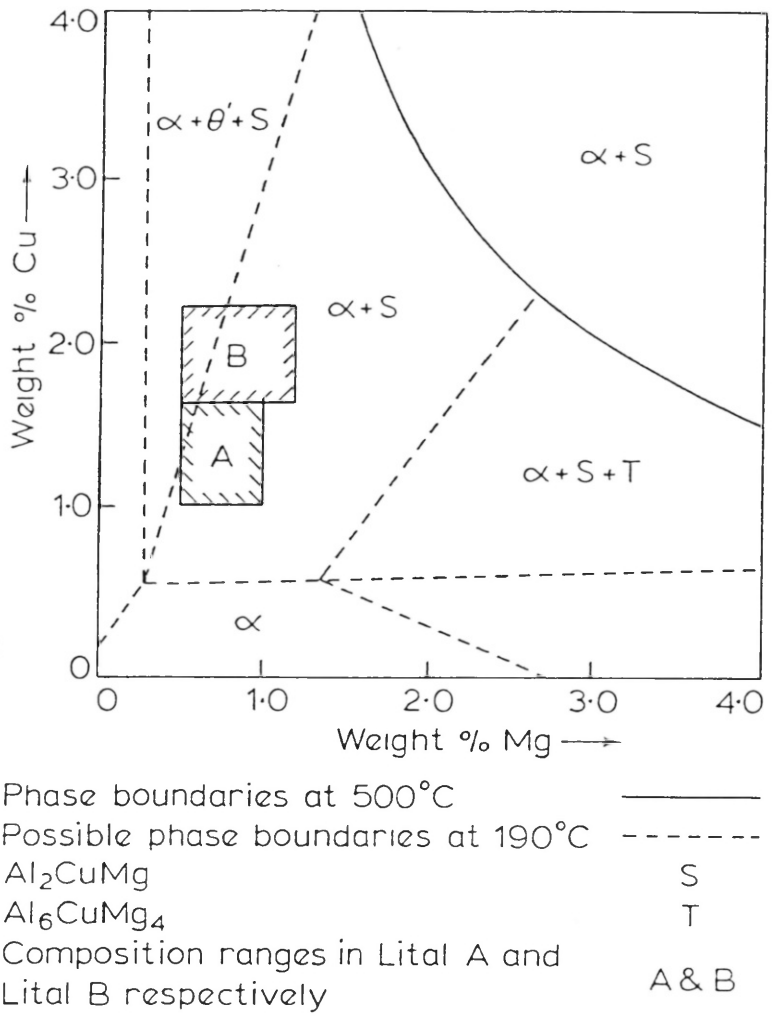


Figure 2.6. Isothermal sections of the Al-Cu-Mg system (after Silcock and Parsons (58)).

formation of Al-Cu-Mg GP zones has not been reported and the possibility of lithium incorporation into these precipitates has not been evaluated. Additionally, no precise lattice parameter measurements of the precipitates have been carried out. Under these circumstances, it is unwise to distinguish between S' and S precipitates in quaternary Al-Li-Cu-Mg alloys.

At the typical ageing temperatures, precipitation of S' phase in the Al-Cu-Mg alloys takes place heterogeneously upon the quenched in defects (viz. dislocation loops and helices) which are present in high density within the as quenched microstructure. Whilst, in the lithium containing alloys the extent of such precipitation is limited by the low density of such defects and the only available heterogeneous nucleation sites are grain and subgrain boundaries. Ceresara et al (64) attributed this phenomenon to the high lithium-vacancy binding energy which inhibits vacancy condensation upon quenching. However, Wilson and Partridge (65) suggested that in the absence of such defects, homogeneous nucleation of S phase is promoted; but, in a recent investigation by Gregson and Flower (66) no trace of homogeneous nucleation of S phase was detected even after ageing at 120^{o}C ensuring that GP zones solvus was not exceeded. They suggested that homogeneous nucleation might be substantially delayed or even prevented by low diffusion rates arising from the lithium-vacancy binding energy. The authors also suggested that extended heat-treatment to allow for this would not be commercially viable. So, they introduced a pre-ageing stretch in order to increase the dislocation density and hence encourage the widespread heterogeneous precipitation of S phase. Futhermore, a finer and uniform S phase precipitation was obtained by using a two step ageing process.

In commercial Al-Li-Cu-Mg alloys, the major matrix precipitates observed are δ' (Al_3Li), T_1(Al_2CuLi) and S (Al_2CuMg). Since, both T_1 and S phases involve copper, a critical balance between copper and magnesium concentration has been found to be a deciding factor as to optimisation of a particular phase within the aged microstructure. Peel et al (**54**) suggested that the balance between T_1 and S phases depends upon the Cu:Mg ratio and from commercial point of view it is important to maintain a Mg content of 0.7 wt % in order to ensure the optimum distribution of S phase, may be produced during thermomechanical processing. In the alloys containing 2.6 wt % Li, 1.20 wt % Cu, 0.5 wt % Mg and 0.13 wt % Zr, the authors showed that a slight reduction in the Mg content limits S precipitation and allows

for T_1 precipitation. Gregson and Flower (62) additionally suggested that a Cu:Mg ratio of 2.6:1 (composition of S phase being 44.8 wt % Cu, 17.1 wt % Mg, balance Al (53)) would maximise S precipitation providing all Cu and Mg is available for the formation of the ternary phase.

With due consideration of the role of Cu and Mg on the resultant microstructure together with the knowledge of the practical limit (from ductility consideration) of lithium content (< 3 wt %), a series of Al-Li alloys have been developed in recent years. Compositional details of these commercial Al-Li alloys have been summarised by Smith (63) and are included in Figure 1.1.

2.1.2. The role of grain refining additions and impurities on the grain structure and the precipitation reactions in Al-Li alloys.

2.1.2.1. Grain Refining Additions

Superlattice alloys with a coarse grain size do exhibit a low ductility as a result of work hardening and stress concentrations at the grain boundaries. Al-Li alloys are no exception. Also, despite the choice of various thermomechanical processing routes, which themselves may vary the grain structure considerably, the final Al-Li alloy product was always recrystallised. Under commercial development of Al-Li alloys, therefore, control of grain structure via grain refining additions was an immediate task.

Chromium additions were strictly limited since it was proved to be highly ineffective in inhibiting recrystallisation in Al-Li alloys (53). Whilst, manganese additions were studied by many investigators (22, 67, 68) as a possible grain refiner via the Al_6Mn dispersoid which forms on solidification and in the solid state. However, the result was a fully recrystallised structure in the solution soaked material. This was attributed to the dissolution of fine incoherent Al_6Mn during solutionising treatment together with the loss of manganese towards formation of coarse intermetallics like $Al_{12}(FeMn)_3Si$, Al_9MnSi etc. during solidification (69). Furthermore, promotion of unwanted δ(AlLi) formation by the dispersoids was also reported (70). Consequently, Mn additions received little attention in the later stages of commercial development of Al-Li alloys.

In recent years, the effectiveness of zirconium in Al-Li alloys as a potent grain refiner and recrystallisation inhibitor has been widely recognised (71). Such behaviour is associated with the presence of fine, but uneven, dispersions of spherical, coherent and ordered ($L1_2$ structure) Al_3Zr (β') particles (72). The dispersions are very stable at the solution treatment temperature mainly due to the small a/β' misfit value and sluggish diffusivity of zirconium (73, 74). During the migration of a grain boundary, the Al_3Zr particles must change from coherent to incoherent and the energy involved in this process would account for the very high recrystallisation temperature associated with zirconium additions to aluminium (71, 75).

The coherent Al_3Zr particles, additionally, provide heterogeneous nucleation sites for δ' (Al_3Li) precipitation (76, 77, 78). This results in an apparent acceleration of the ageing process as δ'- coated Al_3Zr behave as a population of large δ' particles. The characteristic appearance of the composite precipitates has recently led to a great deal of research to understand the exact nature of these precipitates. Gayle and Vandersande (76) have proposed that lithium is incorporated into the β' implying a core composition of the type $Al_3(LiZr)$. Unfortunately, it is not possible to analyse lithium using TEM techniques and hence conflicting results have been reported (79, 80). However, recent studies (81, 82, 83) using atom-probe field-ion microscopy, lithium incorporation into the β' has been clearly established, though quantification of lithium present in each phase on an absolute scale was not possible.

There is no evidence that coherent β' particles influence δ phase formation, although, Miller et al (84) recently reported that incoherent β' particles act as the principal nucleating sites for matrix δ precipitation in recrystallised structures. Unfortunately, the authors provided insufficient evidence in support of their observations. However, increased δ formation in the recrystallised structures may be interpreted on the basis of more heterogeneous sites (in terms of high angle grain boundaries) available for δ formation compared to the unrecrystallised material.

Finally, Gayle et al (85) have shown that larger and more uniform β' dispersions inhibit dislocation cutting of particles in the matrix as a consequence of the high antiphase boundary (APB) energy associated with β'. β' also results in strengthening of δ' precipitate free zones by β' particles. This results in improved combination of strength and toughness in Al-Li alloys.

2.1.2.2. Impurities

The chief source of the majority of the impurities (e.g. sodium, potassium, calcium, iron, silicon) which are commonly found in Al-Li alloys are those which are already present in the raw material. This was partly attributed to the very reactive nature of lithium (71). Depending on the chemical nature and solid solubility in aluminium the impurities may form aluminium rich dispersoids and coarse intermetallics (iron, silicon) or grain boundary films (e.g. sodium, potassium).

Impurities like iron and silicon often combine with other alloying elements (e.g copper and magnesium) from the melt early during the solidification process and precipitate as insoluble constituent phases along the high angle grain boundaries. Also, in the presence of manganese as an alloying element, iron and silicon often combine with this element to form insoluble dispersoids (69). Depending on the size of these coarse intermetallics and dispersoids, particle induced recrystallisation may well occur giving rise to formation of unwanted high angle grain boundaries (69). Also, reduction in the solute (viz. copper, magnesium and manganese) concentration in solution due to their formation reduces the necessary driving force for the formation of age hardening phases and grain refining dispersoids. Attempts are made, therefore, to keep the iron and silicon levels low within the material; although, it has been reported (71) that the presence of small amounts of iron and silicon is often desirable as they soak up harmful elements like sodium and potassium preventing formation of embrittling grain boundary films.

Segregation of alkali-impurities like sodium, potassium and calcium has been demonstrated to reduce toughness of Al-Li alloys (86). Due to their insoluble nature, they are present as grain boundary films and liquid phase embrittlement may be occurring. Webster et al (87, 88) examined in detail the effect of these impurities and concluded that the presence of these impurities is not the major cause of poor toughness in Al-Li alloys. The presence of any of these impurities does not affect the grain structure and neither of the precipitation reactions within the alloy system is affected. However, the presence of these impurities is undesirable since they only affect the mechanical properties (viz. ductility and fracture toughness) of the material adversely.

2.1.3. Grain Boundary Precipitation Within the Heat treated Al-Li alloys

The grain boundary precipitates observed within the heat treated Al-Li alloys may be grouped into two categories: firstly, the coarse iron and silicon bearing constituent particles which form early in the solidification process, survive the practical homogenizing annealing treatment (and remain at the grain boundaries of the homogenised material) and secondly, the precipitates which form during the artificial ageing heat treatment. Whilst formation of the former types of precipitates are controlled by the impurity content of the original cast material, formation of the latter types of precipitates depends on the ageing temperatures, ageing times, alloy composition and to an extent the preageing treatments the material receives (89, 90, 91). Information on the former types of precipitates has been provided in section 2.1.2.2. The present section will consider only the other types of precipitates. Additionally, the age hardening phases like T_1 and S which form at the low angle grain boundaries will not be discussed.

In binary Al-Li alloys, formation of the equilibrium δ(AlLi) phase at the grain boundaries has been documented by many investigators (11, 92, 93). Due to its reactive nature, retention of δ during the preparation of thin foils for TEM is difficult and hence only a few investigators (89, 94) have been able to provide electron diffraction evidence of its presence; it is usually identified by x-ray diffraction methods (5, 11).

In magnesium containing Al-Li alloys, Harris et al (95) identified coarse Al_2LiMg precipitates at the grain boundaries; the authors also noted an increase in its concentration with increasing magnesium content. Sanders (96) also reported formation of such phase within Al-Li-Mg alloys, but the formation of δ phase was not reported. Grain boundary precipitation in Al-Li-Cu alloys was investigated initially by Starke et al (71) & Lin et al (89). The authors reported the presence of mainly two coarse precipitates viz. T_2 and δ phase at the grain boundaries of the alloys in the peak aged condition. Low ductility in the alloys was correlated with the presence of these precipitates together with the strain localisation in PFZs. Tosten et al (51) recently investigated grain boundary precipitation in Al-Li-Cu alloys; the authors suggested that δ' PFZs were always associated with boundaries containing δ particles. The authors additionally noted an increase in δ' PFZ

formation together with the grain boundary precipitation due to an increase in the copper content in the alloy. Unfortunately, the authors did not provide any electron diffraction evidence to prove that the major grain boundary precipitate was the equilibrium δ phase; rather the major grain boundary precipitate in their alloys was assumed to be δ mainly because of its striking resemblence to δ phase of binary Al-Li alloys both in appearance (i.e. surrounded by misfit dislocations) and its occurrence in association with δ' PFZs. Recently, Cassada et al (41) using electron microdiffraction techniques showed that in Al-Li-Cu alloys aged at 190^{o}C or higher, δ phase particles were not observed at grain boundaries; rather the grain boundary precipitates were recognised to be a T_2 (Al_6 Cu Li_3) phase and an icosahedral phase (I phase). The authors concluded that when Al-Li alloys are further alloyed with elements such as Cu and Mg the grain boundary precipitates formed during typical ageing heat treatments must not be misinterpreted in terms of δ phase-particles.

Grain boundary precipitation in commercial Al-Li-Cu-Mg alloys has been recently investigated by several workers. Miller et al (91) and Peters et al (97) reported the presence of δ phase particles at the grain boundaries associated with δ' PFZ in the peak and overaged AA 8090 alloys; but, again their observations were not supported by electron diffraction evidence. Recently, Owen (90) carried out a detailed investigation of the grain boundary precipitation within the AA 8090 alloys. Using quantitative x-ray EDS analysis together with the electron diffraction techniques the author found no evidence of stable δ phase particles at the grain boundaries in the peak and overaged conditions; it was concluded that an icosahedral phase similar to I phase reported by Cassada et al (41) is the major grain boundary precipitate and responsible for δ' PFZ formation. The author also noted a decrease in grain boundary precipitation when the material was given a preageing stretch. This observation was explained on the basis of promotion of matrix precipitation which reduced the solute available for formation of grain boundary precipitation. Such observations seem very logical and parallel those by Lin et al (89) earlier in Al-Li-Cu alloys and more recently by Miller et al (91) in Al-Li-Cu-Mg alloys. However, definite quantitative information is clearly required to strengthen these observations.

2.2. Physical and Mechanical Properties of Al-Li Alloys

2.2.1. Density

Lithium is the lightest metallic element and has a significant effect on density when alloyed with aluminium. For every weight percent lithium added to aluminium (up to the limit of solid solubility) the density is reduced 3 %(56). Al-Li alloys are, therefore, recognised to be potentially very useful materials for aircraft structures. Recently , Peel et al (54) derived a formula of following type:

$$\text{Density (gm/c.c.)} = 2.71 + 0.024\,Cu + 0.018\,Zn + 0.022\,Mn - 0.079\,Li - 0.01\,Mg - 0.004\,(wt\,\%)\,Si$$

in order to predict the density from known compositions of the alloys: the negative contribution of lithium is appreciable.

2.2.2. Modulus

Coincident with decreasing density, for each weight percent of lithium added to aluminium (up to a lithium content of about 4 %) the elastic modulus is also increased about 6 % (56). However, the explanation for the increased stiffness observed in these alloys is not so straightforward. Sankaran & Grant (56) initially misinterpreted and attributed such high stiffness to the high elastic modulus of the δ' particles due to its ordered nature. Noble et al (98) also found a high value (~96 GPa) for the elastic modulus of δ', but, for the range of alloys of commercial importance they showed that the major contribution to the modulus arises from the lithium in solid solution, not due to the short range ordering or strain energy effects. Accordingly they successfully explained the observed decrease in stiffness during ageing in terms of the precipitation of lithium out of solid solution during age hardening. Figure 2.7(a) shows the effect of lithium content on the modulus of alloys in the solution treated, and in the solution treated and aged conditions; a much greater contribution of the solid solution relative to δ' towards the observed modulus is clearly depicted. Noble et al (98) reported that lithium in solid solution modifies the electronic structure of the alloy and constitutes the basis for the large increase in modulus.

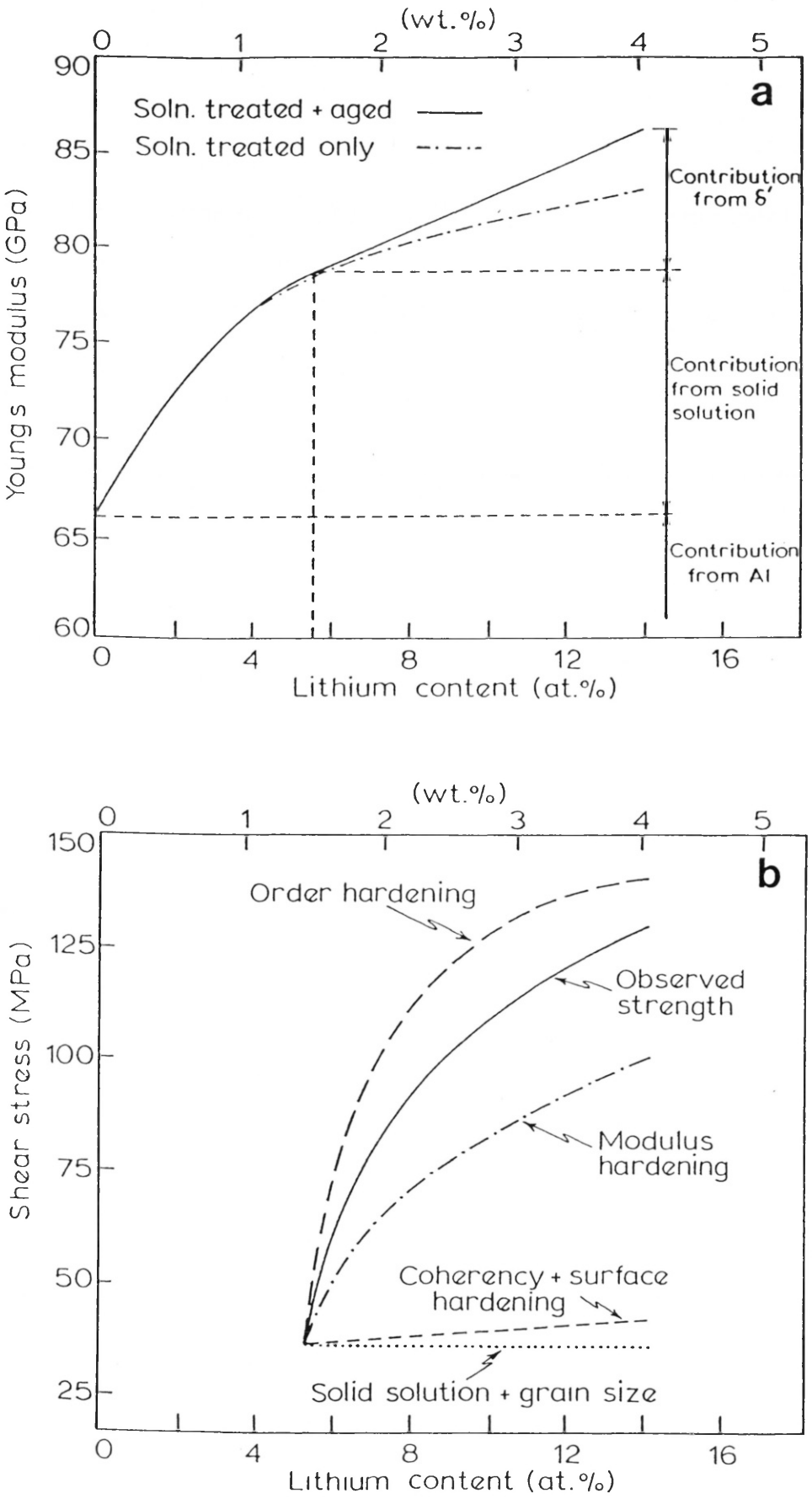


Figure 2.7. Variation of tensile properties with lithium content.
(a) Young's modulus of solution treated, and solution treated and aged material
(b) Contribution of different strengthening mechanisms after ageing to near peak strength (after Noble and co-workers (98, 99).

2.2.3. Strength and Deformation Mechanisms

Interaction between precipitates and moving dislocations constitutes the basis for strengthening in any precipitation hardened system. In Al-Li alloys (containing more than ~1.6 wt % lithium), the major strength increment is afforded by δ' precipitation. Since, the slip planes of coherent δ' particles and the matrix are identical, the particles are sheared by the moving dislocations. Where, the dislocations cut and deform the particles, the strengthening mechanisms, as suggested by Decker (100) are as follows: (a) order hardening (b) lattice mismatch (c) modulus hardening and (d) Peirls force mismatch. Noble et al (99) examined each of these strengthening mechanisms and concluded that strengthening in Al-Li alloys is caused by a combination of (i) order hardening such that antiphase boundary energy is significant (ii) modulus hardening which arises from the difference in elastic modulus between precpitate and matrix. The increment in strength associated with lattice mismatch between δ' and the matrix is small due to low coherency strains associated with δ'; also the energy required to create new surface when the particles are sheared by the dislocations is small due to low α/δ' interfacial energy. Sanders et al (22) explained the strengthening mechanisms in these alloys in terms of δ' precipitate size and spacing as a function of artificial ageing conditions. The authors (22) showed that the dislocations shear the particles in the early stages of ageing when the particles are small and closely spaced, whereas, as the precipitates grow and their spacings increase with ageing, less force is required for the dislocations to bow and loop around the precipitates. Competition between shearing and looping results in the classical ageing curve, where, the strength initially increases with increasing particle size as the particles are sheared and then decreases as the particles are looped.

The possibility of additional strengthening due to lithium in solid solution was investigated by Noble et al (99); however, the authors reported very little solid solution strengthening and attributed this to the low atomic size factor that exists between an aluminium atom and a lithium atom (considering solid solution of lithium in aluminium). Also, recently, Furukawa et al (100) and Miura et al (101) have suggested that besides order hardening, the main contribution to critical resolved shear stress in the cutting stage comes from the frictional stresses resisting dislocation motions in the δ' particles. However, no direct evidence for such a mechanism has been put forward.

Plastic deformation in precipitation hardened Al-Li alloys occurs through the motion of dislocations on close packed {111} planes in closed packed directions. The strength and micro deformation characteristics of such an alloy, therefore, are dominated by the interaction of mobile dislocations and the coherent, ordered δ' particles. The strengthening effect associated with δ' particles and the associated work-softening that can result when they are destroyed by intensive slip, can be estimated as follows: the motion of a unit dislocation through the ordered lattice of the δ' precipitate will not recreate the structure in its wake, but creates disorder in the form of an antiphase boundary. To eliminate the extra energy necessary to create an antiphase boundary, dislocations in Al-Li alloys (6, 22, 109) have been found normally to move in pairs connected by a strip of an antiphase boundary such that the passage of a second dislocation recreates the order disturbed by the first. The separation of two unit dislocations is determined by a balance between the force imposed by the structure to maintain its order and the repulsive force between the two dislocations of same sign. When order hardening is the dominating mechanism, increase in shear stress may be written in the following form (109),

$$\tau_{CRSS} \alpha \gamma_{APB}^{3/2}. r^{1/2}. f^{1/2}$$

where, γ_{APB} is the APB (antiphase boundary) energy of the particle, r is the mean particle radius and f is the volume fraction of the particles. When, n dislocations of Burgers vector b shear a given particle, the cross section of the particle in the slip plane is reduced by an amount nb; assuming, particles are sheared across their diameter, the shear stress required for further shear becomes (103)

$$\tau \alpha \gamma_{APB}^{3/2} . f^{1/2} (\gamma - nb)^{1/2}$$

such that once slip occurs on a particular slip plane further slip/deformation is encouraged along the same slip plane. Slip becomes coplanar and the slip plane becomes thus work softened. Up to the peak aged condition, where dislocation motion occurs by particle shearing mechanism, such planar deformation is typically observed in Al-Li alloys (66, 99, 104). After examining each of the possible strengthening mechanisms Sanders (22) and Noble (99) concluded that order and modulus hardening were the main strengthening mechanisms in binary Al-Li

alloys. However, Noble (99) in agreement with later workers (100, 101, 105, 106) concluded that order hardening is the dominant strengthening mechanism (Figure 2.7(b)).

2.2.4. Ductility and Fracture Toughness

2.2.4.1. Role of slip coplanarity, precipitate free zones and associated grain structure

Evidence of coplanar slip within Al-Li alloys has been presented by numerous investigations (66, 99, 104). As a result of planar deformation, described in earlier section, dislocations pile up at the grain boundaries. Since the number of dislocations which are piled up at the boundary is proportional to the slip length, an increase either in the number of particles or the grain size will also increase the number of dislocations on the glide plane; the result is increasing stress concentrations at the boundary. Crack nucleation can occur at slip band - grain boundary intersections (107) and subsequent propagation can occur resulting finally in intergranular failure (96). Planar deformation has also been observed in other aluminium alloys (e.g. Al-Cu, Al-Zn, etc.) where the shearing mechanism occurs (108); however, the propensity towards planar slip in these alloys is reduced because the dislocations can cross slip. In Al-Li alloys, cross slip is not a viable process for the superdislocations (96); additionally, the coherency strains around the particles are low (19). Gregson and Flower (66), Sanders and Starke (104) and Noble et al (99) have suggested that such slip co-planarity is the major cause of poor ductility and fracture toughness in Al-Li alloys.

Depending on the age hardening conditions (especially in the peakaged conditions), the existence of precipitate free zones (PFZ) along grain boundaries of Al-Li alloys has been also documented (22, 96). Sanders et al (22) proposed that PFZs occurs in these alloys as a result of preferential ripening of δ' precipitates in the grain boundaries by enhanced diffusion in these regions. The authors also showed that the PFZ developed and grew with ageing time. In binary Al-Li alloys, such PFZs are always present in association with equilibrium δ (AlLi) phase formation at the grain boundaries. The PFZ is softer compared to the neighbouring matrix and, therefore, the local deformation in the PFZ can be high enough to initiate a crack at a grain boundary or at a grain boundary triple point before

substantial macroscopic deformation can occur. The result is a microstructure with low macroscopic ductility (104, 108).

Several approaches have been made to reduce the propensity towards coplanar slip. These include, primarily, modification of δ'/α misfit through ternary additions; so that dislocations will cross slip around the particles rather than shear them. Baumann and Williams (37) showed that ternary additions of silver and zinc cause a significant increase in δ'/α misfit. However, these elements besides being relatively heavy, were also found to lower the solubility of lithium in the matrix; these factors in turn counteracted the beneficial effects of lithium additions. Encouragement of cross slip using combination of various alloying additions to produce a fine dispersions of nonshearable particles was attempted by Palmer et al (109) and Sankaran et al (56). Palmer et al (109) obtained lower yield strength in their alloys without any improvement in ductility; whilst, in the latter case, an increase in elongations in the alloys was obtained but at the cost of a significant reduction in yield strength. Though, limited microstructural evidence was put forward in favour of reduced planar slip, it is anticipated that this might be due to the reduced δ' - precipitation as a result of substitution of lithium for dispersoid forming elements.

Since planar deformation is more pronounced at large grain sizes, Al-Li alloys contain small additions of zirconium (see Section 2.1.2.1) in order to refine the ingot grain size and control the recrystallisation in wrought products. Dinsdale et al (36) added zirconium as a grain refiner to an alloy Al-2 Li-2 wt % Mg. They noted that the amount of grain boundary failure was decreased as a result of formation of subgrain structures. However, the essential fracture mode in these alloys still remained severely intergranular with some alteration of the fracture surface following a change in grain shape. Later, Starke and Lin (110) used thermomechanical processing to study the influence of grain structure on the ductility of 2020 plate. They observed significant improvement in ductility in the unrecrystallised materials associated with the transgranular ductile type fracture mode compared to that of recrystallised materials which again failed via a predominantly intergranular fracture mode. Such a change in fracture mode was attributed to the sharp texture observed in the unrecrystallised materials, which, in turn prevents the build up of localised stress concentrations and enhances slip across grain boundaries. The authors suggested the use of zirconium in preference

to manganese as a grain refining addition in order to retain a pro nounced texture; the presence of such strong texture, however, results in severely anisotropic properties.

2.2.4.2. Role of matrix precipitation

In the present generation of Al-Li alloys, besides the δ', the major strengthening phase, close control of alloy composition enables formation of several matrix age hardening phases (see section 2.1.1.4.). Considerable research interest has been shown in recent years to evaluate the effectiveness of each of these phases in dispersing coplanar slip.

Formation of θ' phase which occurs only in copper rich alloys, has not proven beneficial in exerting a controlling influence on slip behaviour (111, 112). At other composition levels, formation of additional precipitates viz. S and T_1 is possible.

The thin plates of hexagonal T_1 (Al_2CuLi) phase,which form on the {111} slip planes, are not effective in dispersing slip (66). Also, a recent investigation by Sainfort and Guyot (106) revealed that T_1 phase is unshearable by dislocations and may, therefore, lead to slip localisation by deformation channelling in regions where T_1 phase is absent. Such heterogeneous deformation would otherwise counteract the beneficial effect of slip homogenisation due to dislocation bypassing of the T_1 precipitate. However, Gregson and Flower (66) have shown that unlike T_1, S phase is an effective slip dispersing agent. The authors noted that since there are no uniform densely packed potential slip planes within the S phase which lie parallel to the matrix slip planes, the laths of S phase are unlikely to be penetrated by dislocations. Bowing around S phase, will, therefore, increase the local work hardening rate and prevent development of bands of coplanar slip. A uniform dispersion of S phase throughout the microstructure is however, therefore necessary. Gregson and Flower (66) encouraged the widespread uniform heterogeneous precipitation of fine laths of S phase via a preageing stretch combined with a two step ageing heat treatment. They obtained an appreciable improvement in ductility and toughness properties together with a comparable yield strength value (see Figure 2.8). An important change in failure mechanism

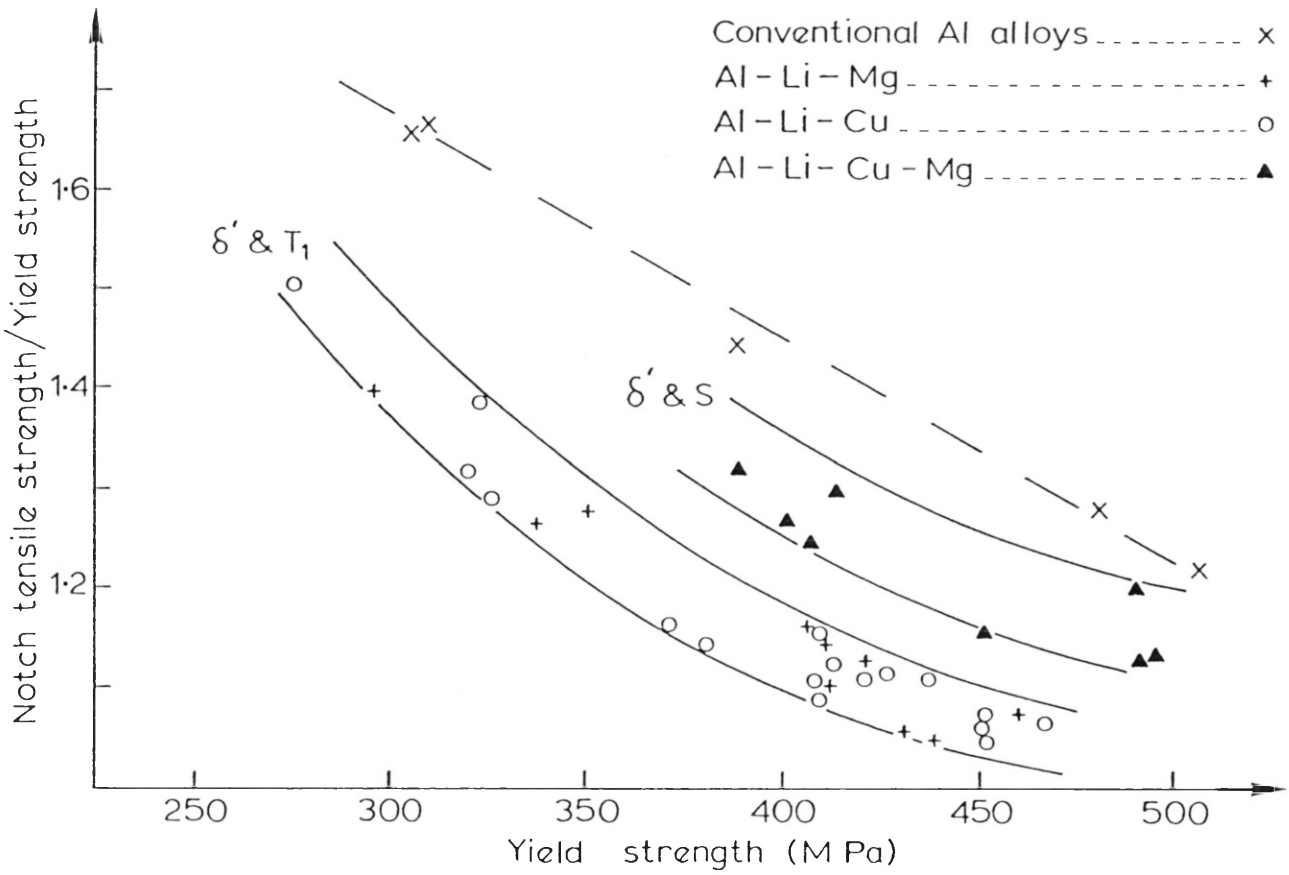


Figure 2.8. A summary of notch tensile strength/yield strength ratio as a function of yield strength for ternary and quaternary Al-Li based alloys (L-T orientation) as compared with 7000 series commercial aircraft alloys (after Gregson (52)).

from one of the long range planar shear observed in both underaged and peakaged conditions to one consistent with intersubgranular type fracture mode in the overaged condition was also noted. Such a change in failure mechanism has been attributed to the homogeneous deformation induced by the ternary Al_2CuMg(S) phase. A uniform deformation within the substructure caused by S phase also enabled the materials to display isotropic properties even though the presence of a strong texture is typical of a zirconium refined sheet product. However, although the development of such an alloy is a significant step towards the development of Al-Li alloys, the utilisation of a preageing stretch in achieving them is not a commercially viable route, where various other forming operations are concerned such that control of the distribution of deformation becomes questionable and also, the products might need resolution treatment. Additionally, in the unstretched material (e.g. in AA 8090 alloys) the sluggish precipitation kinetics of the S phase in Al-Li alloys imply that this mechanism cannot be exploited.

2.2.4.3. Role of Grain Boundary Precipitation

The major grain boundary precipitates which form within the commercial Al-Li alloys have been described in detail in section 2.1.3. Recent studies have shown that besides the inherent problem associated with slip coplanarity the grain boundary precipitates are additionally responsible for the premature intergranular failure and low ductility and toughness of these alloys.

The effect of coarse iron bearing constituent phases on the mechanical properties of Al-Li alloys has been characterised recently by Owen et al (113). The authors concluded that these intermetallic particles are responsible for reducing grain boundary toughness at all ageing conditions, such that, these particles are fractured by coplanar slip impingement and early void initiation occurs at these causing premature intergranular failure. Additionally, during fabrication the coarse intermetallics are aligned to form stringers in the direction of metal flow; this causes anisotropy in mechanical properties such that in the short transverse direction in which stress acts normal to the stringers of intermetallics, the tensile ductility is least. The deleterious effects of these particles on the fracture toughness of other aluminium alloys were documented before (114,115) and a good correlation was obtained between decreasing plane strain fracture toughness values and

increasing (Fe + Si) level within the Al-Cu-Mg alloys (116). In commercial Al-Li alloys, therefore, attempts are made to keep the Fe + Si level a minimum.

Precipitation of δ phase particles at the grain boundaries of binary Al-Li alloys has been documented by many investigators (see section 2.1.3). Vasudévan and Doherty (93) in a recent investigation, concluded that the lower ductility in binary Al-Li alloys is due to the formation of δ particles of much larger size and quantity at the grain boundaries. The authors noticed a change in fracture behaviour from classical ductile transgranular failure in the as quenched condition to a predominantly intergranular failure in the δ' reverted sample from the overaged condition; such a change was attributed to the absence of any grain boundary δ preciptates in the as quenched condition to initiate grain boundary fracture and the presence of mainly grain boundary δ precipitation with no shearable δ' particles within the matrix in the latter case. Whilst these two microstructures revealed almost the same yield strength, the authors showed that the latter microstructure was accompanied by a toughness value lower by more than 50 % compared to that due to the former microstructure.

In Al-Li-Mg alloys, formation of δ phase at the grain boundaries has not been reported but Harris et al (95) showed that formation of coarse and brittle Al_2LiMg phase particles at the grain boundaries encourages the intergranular fracture process. The authors also showed that the toughness value decreases with increasing amount of these coarse grain boundary particles.

In Al-Li-Cu alloys, the observed low ductility in the peak aged condition was explained on the basis of strain localization in PFZs and around coarse grain boundary precipitates like T_2 ($Al_6Cu\ Li_3$) and δ(AlLi) (89, 71). The authors (89) also noted a decrease in grain boundary precipitation when a preageing stretch was employed but this did not result in any increase in ductility. The deleterious effect of grain boundary precipitates on the ductility of these alloys was not, therefore, correlated. Tosten et al (51) recently studied the grain boundary precipitation in Al-Li-Cu alloys but the ductility and toughness of these alloys were not correlated with the grain boundary precipitates.

Information on the grain boundary precipitation and its correlation with the ductility and toughness of Al-Li-Cu-Mg-Zr is so far limited. Owen (90) recently

examined the grain boundary precipitation in Al-Li-Cu-Mg alloys and concluded that the dramatic change in fracture mode with ageing is primarily associated with the increase in grain boundary precipitation of the I-phase which causes embrittlement of the grain and subgrain boundary structures. The authors also observed that the mechanical properties improved when the material was stretched prior to artificial ageing; this was attributed to the reduction in grain boundary precipitation due to stretching. Ashton et al (117) also reported reduction in grain boundary precipitation and the associated PFZs in Al-Li-Cu-Mg alloys with increasing levels (3-7 %) of preageing stretch; the authors obtained a combination of higher strength and toughness in their alloys due to the use of higher levels (7 %) of stretch together with the use of lower ageing temperatures. The use of such duplex treatment minimised the grain boundary precipitation but at the same time refined the matrix precipitation (viz. S phase dispersion) to a greater extent; this particular situation is, therefore, unlikely to demonstrate exclusively the deleterious effect of grain boundary precipitation on the fracture toughness of Al-Li-Cu-Mg alloys.

Since, the grain boundary precipitates in Al-Li alloys are almost always accompanied by the soft PFZ, it is difficult to quantify the effect due to each of them individually. However, since voids at grain boundary particles appear to be formed by stress concentrations even in the absence of a PFZ (118) and have also been reported in a sample showing homogeneous strain (119), the phenomenon of grain boundary ductile failure may still occur in the absence of a soft PFZ. It seems reasonable to predict, therefore, that an alloy with the grain boundary precipitates but no PFZ, though capable of showing grain boundary failure should be tougher and more ductile than a similar alloy with a finite PFZ.

2.3. Extrusion processing and recrystallisation in Al-Li alloys

2.3.1. Hot Deformation via Extrusion

2.3.1.1. Introduction

High temperature thermomechanical treatment of structural aluminum alloys via extrusion processing is most widely carried out. It is primarily because extrusion is simple in operation and a variety of complex shapes may be produced

easily; also, control over the temperature, rate and degree of straining during the process enables the formation of a range of structures at the end of hot deformation which may have a recovered (polygonised), recrystallised or a mixed type (partially recovered and partially recrystallised) structure. Moreover, often when the optimum temperature range of hot deformation is the same as that of solutionising treatment, the hot deformed material may be press quenched and directly aged. Such a process, which combines hot deformation with solution treatment is undoubtedly profitable. However, when the deformation temperature is low, the material requires solution treatment before ageing. The recovered structure at the end of hot deformation provides a driving force for static recrystallisation during such solution treatment; to avoid this, recrystallisation inhibitors such as manganese and zirconium are often added to the alloy. Such elements also promote the formation of unrecrystallised structures on hot deformation.

High strength-low density, aluminium-lithium alloys containing zirconium are being currently developed as a major substitute for conventional 2000 and 7000 series aluminium aircraft alloys. In a typical modern transport aircraft, the use of extruded product may be as high as 28 % of total product forms (1). Also, the hot deformed material may be press quenched and directly aged without involving a separate solution heat treatment; in lithium containing aluminium alloys such a step is significant in preventing the formation of lithium depleted layers in the product by oxidation during high temperature annealing treatments. (120). Of more importance, the development of an unrecrystallised structure on extrusion and its retention during subsequent ageing heat treatments would be expected to affect significantly the ductility and toughness of these alloys; because it has been shown earlier that a reduction in slip length by reducing grain size (121, 122) or by processes that result in unrecrystallised structures improve the ductility and toughness of a material (110).

2.3.1.2. The Hot Working Equations

Most aluminum alloys are extruded at homologous temperatures of over 0.55 since the stress to deform a material at a given strain rate decreases owing to the increased ease of dislocation motion. The most important feature of the flow stress is its temperature and strain rate dependency, where for a given temperature, the higher the strain rate, the greater is the flow stress developed.

The interdependence of the steady state flow stress, strain rate and temperature in hot deformation has been reviewed (123-125) extensively. Available hot working data consists mostly of compression and torsion results and the following relationships have been established using these data.

At low stress levels and constant temperatures the steady state flow stress can be described by:

$\dot{\varepsilon} = A_1 \sigma^{n'}$ where, n' and A_1 are assumed to be temperature independent constants.

At high stress levels and constant temperature

$\dot{\varepsilon} = A_2 \exp(\beta\sigma)$, where, A_2 and β are assumed to be temperature independent constants.

Expressions of this form have also been applied to creep phenomena and the similarity between steady state creep and steady state hot working led Sellars and Tegart (125) to propose a relationship of the following form:

$\dot{\varepsilon} = A [\sinh(\alpha\sigma)]^n \exp(-\Delta H/RT)$, where, A, α and n were described as temperature independent constants and ΔH as the activation energy of the hot working process. At high and low stresses this equation reduces to the respective power and exponential functions. The same equation can be rewritten in the form of a temperature compensated strain rate, originally proposed by Zener and Hollomon (127):

$$Z = \dot{\varepsilon} \exp[\Delta H/RT] = A [\sinh(\alpha\sigma)]^n,$$

where, Z is the Zener-Hollomon parameter.

The dependence of σ on temperature indicates that hot working is a thermally activated process with ΔH equal to the activation energy of the rate controlling process.

2.3.1.3. Restoration Processes

Hot deformation increases the density of dislocations and produces a hot strain hardening effect which can be partially or fully removed owing to the development of the restoration mechanisms viz. dynamic recovery and dynamic recrystallisation. The structural characteristics of a hot worked material depend primarily on the stacking fault energy of a material; such that, in high stacking fault energy (S.F.E.) materials the steady state structures are usually characterised by subgrains of low misorientations (127) whilst in low S.F.E. materials a steady state structure comprising of recrystallised grains is found (128). Aluminium is characterised by a high S.F.E. so that in aluminium and its alloys recovery can occur quite easily. The extrusion process, therefore, results in a very well recovered structure in aluminium alloys. The formation of a recovered structure is additionally favoured by an increased temperature, reduced rate and degree of deformation. Dynamic recovery reduces the driving force for dynamic recrystallisation which is consequently limited.

During steady state deformation the subgrain size and the dislocation density remain constant (127). The mean subgrain size increases with increase in temperature and decrease in strain rate (125, 129, 130). In aluminium alloys, the subgrains are reported to consist of very sharp boundaries. The misorientation between them is small ranging from less than 1^{o} to 7^{o} (127, 129-131). In extrudates processed below 0.5 T_m (where, T_m is the melting point of the metal or alloy) the subgrains tend to be elongated in the extrusion direction whilst above this temperature the subgrains are equiaxed although the grains in which they are embedded are elongated in accordance with the imposed macroscopic strain (123, 124). Recently, the effect of strain on the subgrain morphology has been recognised (132) such that with increasing strain the subgrains become more elongated in the extrusion direction.

The effects of alloying additions on the restoration mechanisms have been reported recently by many investigators. In general, an increase in alloying additions increases the strain usually required to establish the steady state substructure, which is usually less recovered than the unalloyed metal (127). In solution an increase in the solute content has also been reported (133) to decrease the S.F.E. in low S.F.E. materials, although there is no real evidence to suggest that this

is the case for high S.F.E. materials. Also, solute additions can hamper climb process through the binding energies that tie vacancies to solute atoms (139). In materials of low S.F.E., the rate of dynamic recovery is low and steady state deformation results in dynamic recrystallisation (125). However, in recent years many investigators have reported dynamic recystallisation to occur in Al-Mg alloys. Truszkowski et al (135), Tensi et al (136) and, Gardner and Grimes (137) reported that magnesium additions reduce the S.F.E. of aluminium such that dynamic recrystallisation may be expected. However, the measurements of S.F.E. taken by the authors were based on the measurement of texture intensity ratios and since the relationship between S.F.E. and texture can not be substantiated fully, their results are not considered to be reliable. Moreover, the authors did not report observations of extended dislocations in this alloy system (using TEM) which are otherwise observed in materials of low S.F.E.. Sheppard et al (138, 139) examined the hot deformation behaviour of Al-Mg alloys and showed that the degree of dynamic recrystallisation increases with increasing magnesium content. The authors suggested that the high solute content hinders the motion of dislocations and recrystallisation nuclei form when a large number of dislocations cluster at obstacles formed by other dislocations or at small submicrometre size intermetallics, producing tangles of dislocations, leading to the establishment of a high angle grain boundary. Kalu and Humphreys (140) took due consideration of the second phase particle sizes and the deformation conditions quoted by Sheppard et al (138, 139) and McQueen et al (141) showed that those particles cannot be held responsible for nucleation of new grains during hot deformation of Al-Mg alloys. It is a prerequisite that the particles must be associated with lattice rotations in order for recrystallisation nucleation to occur at a particle (142) and the particle sizes are too small for this to occur in the Al-Mg alloys. Later, Humphreys and Drury (143) studied the deformation and restoration mechanisms in Al-Mg alloys at elevated temperatures. The authors carried out detailed microstructural and lattice misorientation studies and concluded that the mechanisms responsible for recrystallisation during hot deformation of Al-Mg alloys do not resemble the conventional model of dynamic recrystallisation such as have been proposed for copper. The authors (143), proposed that the new grains and high angle boundaries are formed by several mechanisms viz. formation of high angle grain boundaries due to deformation bands, triple point folds, progressive lattice rotation and, by grain impingement. The authors suggested that nucleation of new grains adjacent

to the original grain boundaries occurs by progressive lattice rotations. Rotation recrystallisation may be attributed to the low grain boundary mobility in this material: this contrasts with pure aluminium in which the grain boundaries will migrate rapidly and consume the adjacent regions of high dislocation density and thus prevent the build up of inhomogeneous deformation in the grain boundary regions. A magnesium solute drag mechanism seems to be responsible for decreasing boundary mobility. Thus it appears that the recrystallisation processes described by Humphreys and co-workers are more realistic than those which rely on unsubstantiated low stacking fault energy in Al-Mg alloys.

The as quenched hot worked structures are examined with a basic assumption that little or no change in the structure occurs before or during quenching. However, as soon as the hot deformation ceases, the release of stored energy in the form of substructure introduced during working acts as the driving force for static restoration processes viz. static recovery and static recrystallisation. If the critical strain for recrystallisation is not reached or the deformation temperature is not high enough, the static recovery process which does not require any incubation period (unlike static recrystallisation) will be the only softening mechanism after deformation, although, full softening is never achieved by static recovery alone (145). The effect of alloying additions on the occurrence of static recovery is not fully understood. However, the solutes or precipitates tend to pin dislocations thereby making static recovery more difficult (146). On the other hand, inhibition of static recrystallisation due to the presence of solutes or fine precipitates is clearly understood such that, in their presence the motion of high angle grain boundaries or the rearrangement of the sub-boundaries leading to the formation of boundaries of higher misorientation become extremely difficult.

Within the as quenched material hot deformed via extrusion, both statically recrystallised and dynamically recrystallised grains may be present. The formation of dynamically recrystallised grains depends on the nature of the alloy, whilst the presence of statically recrystallised grains may be attributed to the fact that the hot deformed extrudates cannot be press quenched immediately without avoiding a delay of about a few seconds such that static recrystallisation could always occur during this period under appropriate deformation conditions. Using TEM, the distinction between the statically recrystallised grains and dynamically

recrystallised grains is carried out as follows. The statically recrystallised grains are ideally free of any dislocations whilst within the dynamically recrystallised grains an intense dislocation activity may always be observed; this is because the dynamically recrystallised grains, once nucleated, get repeatedly deformed during the deformation cycle. This is the reason why the dynamically recrystallised grains are always much smaller in size than the statically recrystallised grains. In order to avoid delay before quenching, alternative deformation processes such as hot torsion testing is often carried out. In this process, deformation may be stopped with immediate quenching; alternatively, the material may be quenched first and then the deformation may be stopped. In the latter case, there is no time available for the static recrystallisation to occur; this particular test is often carried out in order to check the tendency of a material to undergo dynamic recrystallisation.

2.3.1.4. Substructure strengthening

Aluminium and its alloys have usually been considered to be high stacking fault energy materials in which high temperature deformation involves, principally, dynamic recovery. In such materials the room temperature structure consists of equiaxed subgrains providing that deformation conditions, alloy composition and cooling are controlled so that static recrystallisation is prevented. The balance between dislocation generation and annihilation in the deforming material results in larger subgrains at higher temperatures and, since these subgrains are retained in the final structure, they may have considerable influence on properties. Relationships for substructural strengthening have been established (127, 146) and may be written in the form of a modified Hall-Petch equation:

$$\sigma_y = \sigma_A + kd^{-m} \qquad (1)$$

where, σ_y is the room temperature yield or proof stress, d is the subgrain size, σ_A is the yield strength of the coarse grained material in the absence of sub-boundaries, k is a constant and the exponent has been reported to have a value in the range 1-2 (131). It is also established (127) that the relationship between the subgrain diameter and the high temperature flow stress σ is of the form

$$d^{-1} = a + b \ln (\sinh \alpha\sigma) \qquad (2)$$

where, a and b are constants and α is reported to be a constant equal to the reciprocal stress at which the temperature compensated strain rate Z change from power to exponential stress dependence.

Since the Z is also a function of the hyperbolic stress, subgrain size can be related to Z by a relationship (148, 149) of the form

$$d^{-m} = a + b \ln Z \qquad (3)$$

considerations of equation (1) and (3) suggest that mechanical properties can be related to the extruded substructure and this in turn can be related to the Z parameter. Sheppard (149) has shown that the relationship takes the form:

$\sigma_y = c' + e' \ln Z$, where c' and e' are constants such that processing conditions are important in the control of structure and properties of aluminium alloys. Later work by Sheppard et al (150) showed that such simple relationships between properties and processing parameters can not be established in materials such as Al-Mg alloys which exhibit duplex deformation mechanisms (i.e. both dynamic recovery and recrystallisation) during high temperature deformation.

2.3.2. Extrusion Processing of Aluminium-Lithium Alloys

Reported work on the extrusion processing of lithium containing aluminium alloys was initially due to Parson and Sheppard (151, 152). The authors investigated in detail the effect of processing variables on the as extruded and heat treated mechanical properties of ternary Al-(3.5 - 3.8) Mg - (2.1 - 2.3) wt % Li alloys and quaternary Al - 3.4 Mg - 2.4 Li - 0.8 wt % Cu alloys; zirconium (~0.15 wt %) was used in these alloys as a grain refining addition.

In Al-Mg-Li alloys, the authors (151, 152) showed that the substructures produced on hot deformation can be retained in the fully heat treated condition. Accordingly, the as extruded and the heat treated proof stress values were related to the processing parameters; at lower extrusion ratios where the recrystallisation was less the proof stress increased with increasing Z values (lower extrudate temperatures) such that substructural strengthening was predominant. At higher

ratios, the strength was found to decrease with both increasing Z parameter as well as extrusion ratios. The authors also showed that the maximum permissible temperature of hot deformation was adequate to avoid a separate solution soak so that the material may be press quenched and directly aged. However, the variation in subgrain size was found to have only a weak effect on the ductility. In copper containing Al-Mg-Li alloys, correlation between the processing variables and the mechanical properties was not so straightforward. At lower extrusion ratios, the as extruded strength showed only a weak response to the variation in Z values, although, the volume fraction recrystallised throughout the working temperature range was small. In the heat treated conditions, it was shown that for higher extrusion ratios the proof stress increased with increasing extrusion temperatures. It was realised that such an effect could not be associated with the variation in subgrain size or volume fraction recrystallised. The authors anticipated that process heating solutionised a proportion of the cast S phase (Al_2CuMg) particles remaining after homogenisation such that higher temperature combined with the higher stress (due to higher extrusion ratio) allowed more copper and magnesium to go into solution and thus a greater ageing response was produced. The quaternary alloys exhibited higher strength compared to the ternary alloys but over the range of various processing variables investigated the ductility and the notch tensile values (in the extrusion direction) of the heat treated material did not show any variation.

In Al-Mg-Li alloys, the notch tensile values decreased with decreasing extrusion temperatures and it was attributed to the increasing level of recrystallisation observed at the lower temperatures. Relatively lower notch tensile values observed in the quaternary alloys were attributed to the increased yield stress and inclusion (iron and silicon) content of the alloys. The authors concluded that these alloys contain a fundamental grain boundary weakness and variation in subgrain size cannot be utilised to improve the ductility and toughness of these alloys.

Although Parson and Sheppard (151, 142) examined in detail the effect of range of variables (encountered in commercial practice) on the structure and properties of Al-Mg-Li-Cu alloys, those alloys had a composition quite different from those currently being pursued commercially (see section 2.2.1.4). Recently Reynolds and Creed (153) studied extrusion processing of AA 8090 (Al - 2.5 Li - 1.12

Cu - 0.78 Mg - 0.11 Zr) and AA 8091 (Al - 2.5 Li - 1.64 Cu - 0.75 Mg - 0.14 wt % Zr) alloys. The authors discussed the effect of processing variables only on the heat treated structure and properties of the material. It was shown that in both alloys the heat treated proof stress increased linearly with decreasing extrusion temperatures; however, at higher extrusion ratios there was a smaller change in strength with extrusion conditions. This was attributed to the increase in volume percent recrystallised with increasing extrusion ratios. It was shown that little or no improvement in fracture toughness values w obtained due to a change in extrusion conditions; however, deformation conditions which promote or result in a recrystallised structure always caused a significant loss in toughness.

2.3.3. Recrystallisation In Aluminium-Lithium Alloys

Control of grain structure, size and shape in aluminium-lithium alloys is of extreme importance as direct correlations between variation in these parameters with the materials' strength, toughness and isotropy have been well documented (91, 110, 154). Todays commercial Al-Li alloys, therefore, always contain zirconium as a strong recrystallisation inhibitor and also as a potent grain refiner (see also section 2.1.2.1). Under suitable deformation and heat treatment conditions zirconium additions accordingly help to preserve an unrecrystallised microstructure or provide superplastic properties in a fully recrystallised material via. inhibiting grain growth and thereby maintaining a fine grain size (156).

Detailed fundamental studies on the recrystallisation behaviour of binary Al-Li alloys containing zirconium were initially due to Makin and Stobbs (157). The authors showed that the reason why recrystallisation is greatly inhibited in the ternary Al-Li-Zr alloys is the fact that the energy required for nucleation increases due to the combined effects of the solute drag effect of lithium on the boundaries and pinning of the boundaries by coherent Al_3Zr precipitates; when one of these two effects was absent e.g. in Al-Li or Al-Zr alloys, recrystallisation occurred. The observation of recrystallised annuli formed on the surfaces of the hot deformed Al-Li-Zr alloy was, therefore, explained on the basis of loss of lithium from the surface by oxidation. However, formation of such recrystallised annuli on the surfaces is also observed during hot deformation of other aluminium alloys and it is attributed to the high strain and strain rate the surface material experiences during

processing. Hence, it is unlikely that in lithium containing Al alloys, mere loss of lithium from the surface (by oxidation) can be held responsible for the recrystallised annuli observed on the surfaces. The authors also showed that the bulk of the hot deformed microstructure does not recrystallise during conventional furnace annealing treatments despite the use of a very high temperatures and long annealing times; this has been attributed to the tendency of the material to undergo recovery processes. However, it was shown that static recrystallisation within the hot deformed microstructure could be induced using a faster heat up rate; this has been attributed to reduced recovery taking place during rapid heating to the annealing temperature.

The factors affecting the recrystallisation characteristics of commercial Al-Li-Cu-Mg-Zr alloys have been studied recently by Palmer et al (154). The authors showed that a complete change in the grain structure within the commercially produced sheet material may be brought about by varying three significant parameters viz. zirconium content in the alloy, percentage cold work before solution heat treatment and the heat up rate during solutionising heat treatment, such that a transition from unrecrystallised to a fully recrystallised structure occurs due to a decrease in the zirconium content of the alloy from 0.16 to 0.05 wt % or an increase in the pre-solutionising percentage cold work from 37.5 to 87.5 % or an increase in the heat up rate from 3^{o}C to 3000^{o}C/minute. The authors showed that more isotropic properties of the material could be obtained as a result of the fraction of a fine recrystallised grain structure.

Although several other approaches involving an overage practice (154, 155), modifications of alloy composition (viz. increasing copper content over a certain minimum level) to develop coarse second phase particles (155), etc. have been proposed to date to induce recrystallisation in these alloys, fundamental studies on the mechanisms responsible for recrystallisation in Al-Li alloys are so far limited. In hot rolled Al-Li-Zr alloys, Makin and Stobbs (156) induced recrystallisation using faster heat up rates to the solution heat treatment temperature and observed that new grains were always nucleated along or in the vicinity of original high angle grain boundaries and the grains were often elongated along the rolling direction. It was proposed that grain boundary bulging and subgrain coalescence were the two principal mechanisms responsible for their formation; the authors, however, suggested that formation of recrystallisation nuclei via a subgrain coalescence

process which necessarily involves dislocation rearrangements, is extremely difficult in Zr containing Al-Li alloys. Using conventional furnace annealing treatment Parson et al (152) also observed that the hot deformed extruded material is extremely resistant to static recrystallisation. While the periphery of the extrudates was recrystallised under all imposed process conditions (and it was attributed to the high strain and strain rate the surface material experiences as it traverses the deformation zone) the authors also observed presence of recrystallised grains within the bulk of the press quenched extrudates and showed that the degree of recrystallisation observed within the bulk material is directly related to the extrusion parameters (see section 2.4.2); such correlation together with the reluctance of the material to undergo recrystallisation during solutionising treatment led the authors to propose that the recrystallisation took place during the deformation process. In agreement with the observations made by Makin and Stobbs (156), Parson and Sheppard (152) also noted that the new grains were always nucleated in regions adjacent to the original high angle boundaries and the recrystallisation appeared as a banded structure corresponding to the extrusion direction; however, the authors did not discuss the possible nucleation mechanisms and provided no evidence to confirm that those grains nucleated dynamically.

In Al-Li alloys, recrystallisation due to coarse second phase particles has been reported recently by several investigators. Particle induced recrystallisation in Al alloys is well understood (142) and in agreement with this theory, it has been shown by Srivatsan (69) and Lin et al (89) that the coarse constituent phases like $Al_{12}(FeMn)_3Si$ and Al_7Cu_2Fe particles in AA 2020 alloys and Al_7Cu_2Fe paricles in Al - 3 Li - 2 Cu - 0.2 wt % Zr alloys act as nucleating sites for recrystallisation. Also, the practical homogenisation treatment recommended for commercial Al-Li alloys of low copper and magnesium is inadequate for similar alloys having higher copper and magnesium (157), such that as a result of incomplete homogenisation, the copper rich particles remain in the material and these have been reported (90) to encourage recrystallisation in the wrought structure.

CHAPTER THREE

EXPERIMENTAL PROCEDURE

3.1. Introduction

Initially in this investigation the microstructure and property changes within an Al-Li-Cu-Mg-Zr alloy in the sheet form were studied as a function of heat treatment; thermal analysis studies were also carried out to characterise, in general, the precipitation reactions in aluminium-lithium alloys. Later studies concerned evaluation of structure-property relationships within an Al-Li-Cu-Mg-Zr alloy in the extrusion form as a function of a wide range of extrusion processing variables and modified heat treatment conditions developed in the first part of this investigation.

Microstrucutral characterisation was made using a combination of light microscopy, scanning and transmission electron microscopy. Thermal analysis studies were carried out using differential scanning calorimetry and additional phase and particle analysis were carried out using x-ray micro-analysis and secondary ion mass spectrometry.

Mechanical property studies using hardness, tensile and fracture toughness tests were carried out to assess the effects of extrusion processing parameters and variable heat treatment conditions on the strength and fracture toughness of the material.

3.2. Materials

The compositions of the alloys used in this investigation are included in Table 3.1. Alloy A1 was the material for the extrusion work and was supplied by the Aluminium Company of America in the form of 75 mm diameter billets machined out of DC (Direct Chill) cast ingots. Alloy A2 was DC cast and hot rolled to 3 mm sheet by British ALCAN; this alloy was used extensively for the phase transformations and thermal analysis studies in the first part of the present investigation. Alloys A3 to A5 were also DC cast and hot rolled to 1.6 mm sheet by

Table 3.1. Composition of the Alloys Used in the Present Investigation

Alloy Code	Elements, wt % (balance aluminium)							(Cu + Mg)	Cu : Mg
	Li	Cu	Mg	Zr	Fe	Si	Ti		
A1	2.50	1.04	1.11	0.12	0.04	0.04	0.01	2.14	0.93
A2	2.57	1.24	0.68	0.13	0.06	0.06	0.015	1.92	1.82
A3	2.80	-	-	-	-	-	-	-	-
A4	2.60	-	-	0.1	-	-	-	-	-
A5	-	2.0	0.80	-	-	-	-	2.80	2.50
A6	-	1.24	0.68	-	-	-	-	1.92	1.82
A7	1.2	-	-	-	-	-	-	-	-

British ALCAN and alloys A6 and A7 were cast under argon from high purity metals and were hot rolled to 1 mm sheet. Alloy A7 was used for solute (lithium) - dislocation interaction studies.

3.3. Alloy Deformation Routes

3.3.1. Introduction

The principal production route was extrusion. However, there is inevitably a short delay between the end of deformation and the quenching of the material. To check if this delay affects the microstructure additional hot torsion tests were carried out at equivalent strain rates and strains; in this case quenching in very rapid post deformation. Microstructures were compared with the equivalent extruded material. In the following subsections the range of processing parameters used in each deformation route together with a brief description on the preheating and quenching facilities of the material related to each deformation practice are described. Full details of extrusion press design and operation, and information on the torsion machine design and operation can be found in reference 158.

3.3.2. Extrusion

The extrusion press used in this investigation was an ENEFCO vertical acting 5MN press with fast ram approach facility. A 75 mm diameter container liner was used for the experimental work with a billet length of 100 mm. The ram speeds used were in the range of 3-15 mm/sec. and the extrusion ratio was varied from 20:1 to 80:1. Initial billet temperatures were varied from 400 to 500^{o}C. Heating for extrusion was by induction giving a heat up rate of 125^{o}C/minute and on reaching it the material was given a 5 minute soak. The electrically heated container was maintained at 30^{o}C below the initial billet temperature to prevent excessive heating at the die face whilst avoiding significant heat loss from the billet prior to extrusion. All the extrusions were of round bar section and unless specified as air cooled all the extruded products were press quenched in order to retain the hot worked structure. Extrusion data in the form of load-displacement curves were recorded using an IBM microcomputer linked through a digital analogue interface.

3.3.3. Torsion

Specimen for torsion testing were machined from homogenised billets. The testing machine was capable of surface shear strain rates of up to 50 sec^{-1} on the specimens used which had a 10 mm gauge length and 5 mm gauge radius (see reference 158 for the specimen geometry details). The specimens were clamped in the machine and an induction coil around the gauge section heated the specimens to the test temperature controlled by a Eurotherm programme controller. On reaching the test temperature, the material was given a 5 minute soak and uniformity in temperature to within ± $2^{o}C$ along the gauge length was thereby maintained. Testing conditions involved only one deformation temperature viz. $500^{o}C$ and two surface shear strains rates viz. 0.1 and 0.3 sec^{-1}. Tests were stopped and the hot deformed materials were immediately quenched within the processing chamber to retain the hot worked structure. Some tests were also stopped after the material was quenched; in all cases tests were stopped well after the steady state deformation was achieved.

3.4. Heat Treatments

In extrusion work, all the high temperature treatments such as homogenisation, solution heat treatments were carried out in a large air circulating furna ce. After homogenisation the billets were scalped to remove the oxidised layers. Low temperature artificial ageing heat treatments were carried out in smaller fan driven air circulating ovens. A standard solution heat treatment temperature of $530^{o}C$ was used throughout. Extrudates made at $500^{o}C$ were solutionised for 20 minutes while 40 minutes was employed for the products of lower temperature extrusion. All the ageing treatments were performed at $190^{o}C$.

During phase transformation studies a much smaller specimen size was used and all high temperature solution treatments and low temperature ageing treatments were carried out in the resistance heated tube furnaces. Three different solution treatment temperatures viz. 540, 560 and $580^{o}C$ were used using a recommended solution treatment time of 20 minutes for this alloy (viz. alloy A2) following a constant low temperature ageing treatment at $190^{o}C$. Keeping in mind the presence of lithium depleted surface layers, both sides of the test pieces were

mechanically polished to an equal level finally to be left with 0.3 mm of material of the central portion of the original heat treated pieces.

For thermal analysis studies, specimens were also heat treated in the similar environment but samples were solution heat treated at 540^{o}C for 20 minutes (except alloy A2 which was solution heat treated at 580^{o}C) and quenched into water. Thermal analysis was undertaken immediately after quenching (AQ), after natural ageing for 3 months at room temperature (NA) and after an artificial ageing treatment at 185^{o}C for 8 hours (AA).

3.5. Thermal Analysis Study

The specimens for the thermal anlaysis studies were produced by the spark erosion of 5 mm diameter discs from the 1 mm thick heat treated specimens. The spark erosion technique was used to ensure that no ill-defined mechanically deformed region of the alloy was present in any specimen. The discs were lightly polished on silicon carbide paper to remove the oxide surface layers produced during heat treatment, washed in methanol and weighed to an accuracy of ±0.01 mg. Such heat treated samples weighing 60 mg were used for each alloy.

A Perkin Elmer DSC-2 calorimeter was used in all experiments at a scanning rate of 10^{o}C/minute and sensitivity of 10 mcal/sec.. Temperature calibration of the calorimeter was carried out using standard indium sample.

For each sample the baseline over the temperature range 50-400^{o}C was first defined with the cell containing an empty aluminium sample pan; a sapphire standard was then inserted into one cell of the DSC and scanned against the empty pan. Finally, the alloy specimen was scanned against the same empty pan after removal of the sapphire standard. Before performing each scan the system was allowed to equilibriate at 40^{o}C for 45 seconds. From the experimental data three displacements could be measured for baseline, sapphire reference, and alloy specimen, D1, D2 and D3 respectively over the entire temperature range. Specific heat capacity data were then measured using the following equation:

$$c_p(\text{alloy}) = w(\text{sapphire})/w(\text{alloy}) \times (D3-D1)/(D2-D1) \times c_p(\text{sapphire})$$

c_p(alloy) and c_p(sapphire) are the specific heat capacities of the alloy sample and sapphire standard respectively at a given temperature; w(alloy) and w(sapphire) are the weights of specimen and standard respectively. The relationships between c_p and temperature were plotted with the aid of a second programme.

3.6. Microstructural Characterisation

3.6.1. Light Microscopy

For the undeformed material specimens for light microscopy were prepared using standard metallographic techniques viz. the surface was ground flat on 800 and 1200 grit silicon carbide papers, polished on 3 μm and 1 μm diamond paste and etched in Kellers reagent. For examination of the deformed structure, the specimens were not etched in Kellers reagent; instead, the specimens were electropolished using a solution of 30 % nitric acid and 70 % methanol (by volume) at -20^{o}C and 20 V and were then anodised using Barker's reagent (3.5 gm H_3BO_3 + 23 ml HBF_3 + 485 ml H_20 for 500 ml solution) at room temperature and at a potential of 20 V. The anodised specimens were then examined using polarised light techniques.

3.6.2. Scanning Electron Microscopy (SEM)

A JEOL T-200 scanning electron microscope fitted with a qualitative energy dispersive x-ray micro-analysis (EDX) system and a JEOL JSM -35CF SEM fitted with LINK 860 fully quantitative EDX microanalysis system were used in both Secondary Electron Imaging (SEI) and Back Scattered Electron Imaging (BEI) modes to characterise the as cast material and the fractured surfaces of the failed tensile and fracture toughness test specimens.

3.6.3. Transmission Electron Microscopy (TEM)

Thin foils for transmission electron microscopy were prepared by spark cutting 3 mm discs from 0.2 mm thick specimens. Before electropolishing, the discs were lightly ground on 1200 grit silicon carbide paper and washed in methanol. The discs were then electrolytically thinned on a Struers Tenupol Jet polishing machine operating at 20 V using a solution of 30 % nitric acid and 70 % methanol (by volume) at -30^{o}C.

TEM was carried out on a Philips EM 301 and JEOL 120 CX TEMSCAN operating at 100 kV, and on a JEOL 2000 FX STEM operating at 200 kV.

3.6.4. Quantitative Chemical Analysis

Quantitative chemical analysis by x-ray EDS (energy dispersive spectroscopy) was carried out on bulk samples using JEOL JSM-35CF SEM and on thin foils using a JEOL 2000 FX STEM. Both these microscopes were equipped with LINK analytical programme for ZAF [atomic number (Z), absorption (A) and fluorescence (F)] corrections on bulk and ZA corrections on thin foils respectively. Additionally, to ensure accuracy and consistency of the EDS analysis all scanning electron imaging and bulk sample analysis were carried out on polished but unetched samples. Also, compositions are always given in weight percentage.

3.6.5. Secondary Ion Mass Spectrometry (SIMS)

Conventional investigation techniques (e.g. light microscopy, electron probe micro analysis) are limited in their applications to commercial Al-Li alloys, because of the low optical contrast of several phases and their strong tendency to oxidise, as well as the inability of EPMA to perform analysis of lithium. These limitations can be overcome by using secondary ion mass spectrometry which allows chemical analysis with low detection limits in addition to the capability of direct imaging of all elements ($1 < Z < 92$) on the surface of bulk samples.

SIMS studies were carried out on a CAMECA IMS 4F Ion Microanalyser. The samples were sputtered with a mass filtered primary ion beam of 16 O_2^+ with an incident energy of 10.5 kV. The primary beam was focussed in a 50 μm spot which was rastered over the surface in order to produce a uniform current density. Ion micrographs, showing elemental distributions were produced over a 250 μm wide area on polished surfaces.

3.7. Mechanical Testing

3.7.1. Hardness Tests

For rapid approximate property determination for example in establishing the ageing behaviour of the alloy, hardness measurements were taken using the Vickers hardness testing machine operating with a 10 kg. weight. The heat treated test pieces were mechanically polished via silicon carbide papers to remove the lithium depleted surface layers before the hardness tests were made. Typically ten indentations were made for each test. For the extruded material, hardness measurements were always taken at the core of the extrudes and along its length.

3.7.2. Tensile Tests

To characterise the strength and ductility of the as extruded, naturally aged and artificially aged extrudes standard Hounsfield -13 and Hounsfield -12 (for the extrudes performed at extrusion ratio greater than 50:1) test pieces were machined from the extrudes and tested on an Instron Universal Testing Machine using a cross head speed of 0.2 mm/minute (corresponding initial strain rate being 1.8×10^{-4} sec^{-1}).

3.7.3. Fracture Toughness Tests

A modified Terratek (159) short rod fracture toughness indicator test proposed by Aluminium Company of America (ALCOA) was used to assess the fracture toughness properties of the heat treated extrudes. The fracture toughness specimens were machined from the longitudinal sections of the round bar extrusions to the specifications shown in Figure 3.1. The specimens were loaded in the special mechanism designed as a "Frackjack". The lines of contact in the Frackjack grip groove are so designed that the effective load does not change as the specimen mouth is forced open under load; in all cases load was applied at 90^{o} to the extrusion direction. The fracture toughness was then calculated using the following equation:

$k_V = A \times F \times B^{-3/2}$, where,

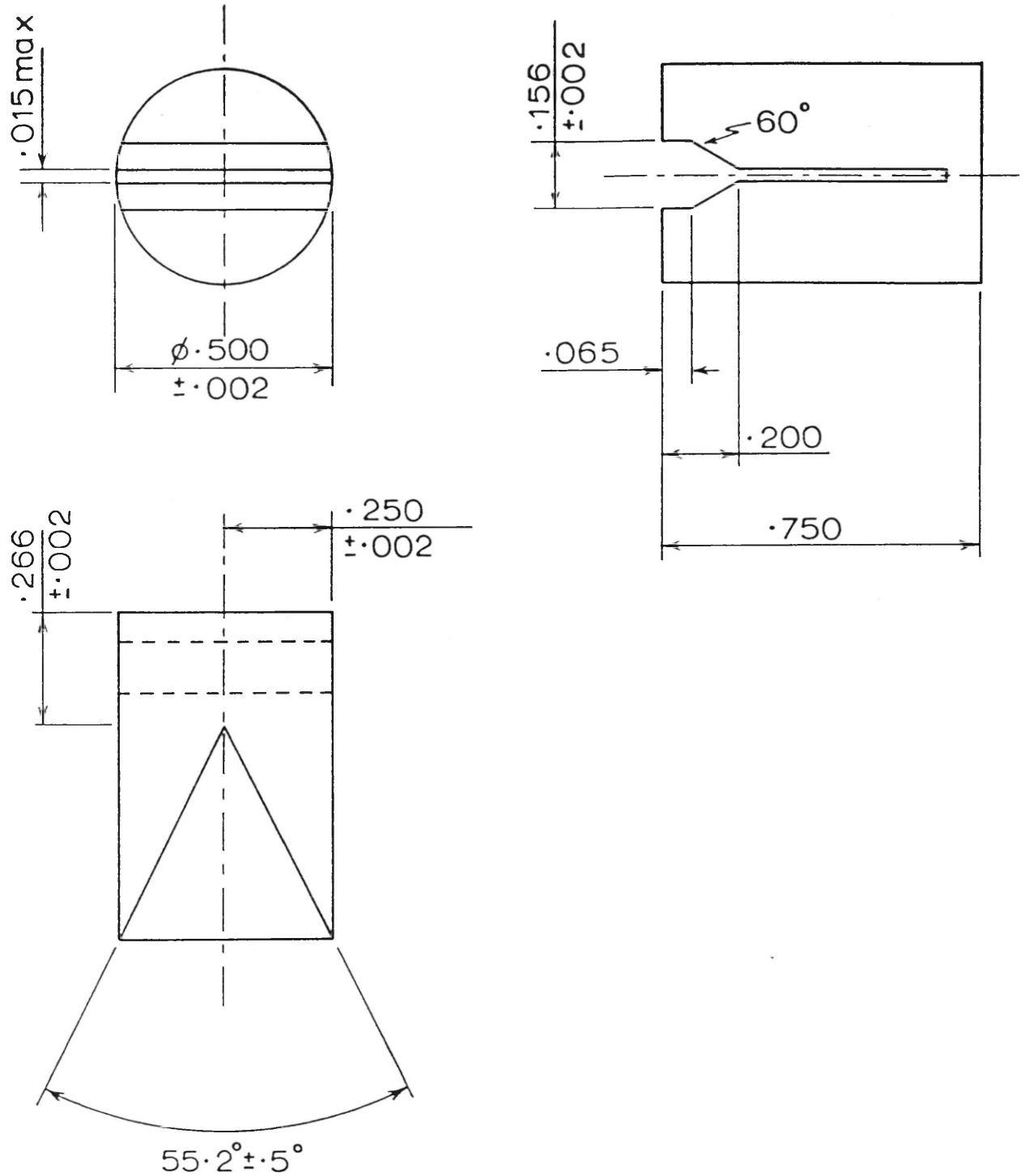


Figure 3.1. Fracture toughness test piece dimensions; all dimensions in inches.

A = calibration constant = 22, a value unique to the specimen geometry and the Frackjack grip design, F = maximum load, and B = specimen diameter (viz. 0.5 inch).

All the tests were carried out on an Instron Universal Testing Machine using a cross head speed of 0.2 mm/minute.

CHAPTER FOUR

DEVELOPMENT OF MICROSTRUCTURE AND PROPERTIES THROUGH SUITABLE CONTROL OF HEAT TREATMENT CONDITIONS.

4.1. Introduction

The work presented in this chapter is concerned with the effect of variation in solution heat treatment temperature combined with natural ageing treatment upon the precipitation of S(Al_2CuMg) phase within an Al- 2.5 Li - 1.2 Cu - 0.68 Mg - 0.12 wt % Zr system viz. alloy A 2 (see Figure 3.1). The aim is to develop heat treatment schedules producing uniform distributions of S as an alternative to a preageing stretch.

The effect of quench bath temperature upon the precipitation of S phase is also discussed. The age hardening characteristics of the alloy are discussed in terms of microstructural changes which take place.

4.2. Results

4.2.1. Age Hardening Behaviour

The Al-Li based alloys rely upon precipitation hardening to develop their high strength potential; it was, therefore, necessary to characterise their ageing response. The effects of variation in ageing times and solution treatment temperatures with a constant typical ageing temperature of 190^{o}C were investigated using hardness testing as this is a rapid method for characterising alloy behaviour. Figure 4.1 shows the artificial ageing response of the alloy due to three solution treatment temperatures viz. 540, 560 and 580^{o}C. In all cases care was exercised to minimise the time lag between quenching and ageing. The form of the ageing curves, and positions of the ageing peaks were essentially the same in all cases such that the maximum hardness was attained after 24 hours of artificial ageing. However, the hardness value due to a particular ageing time increased slightly with an increase in the solution treatment temperature.

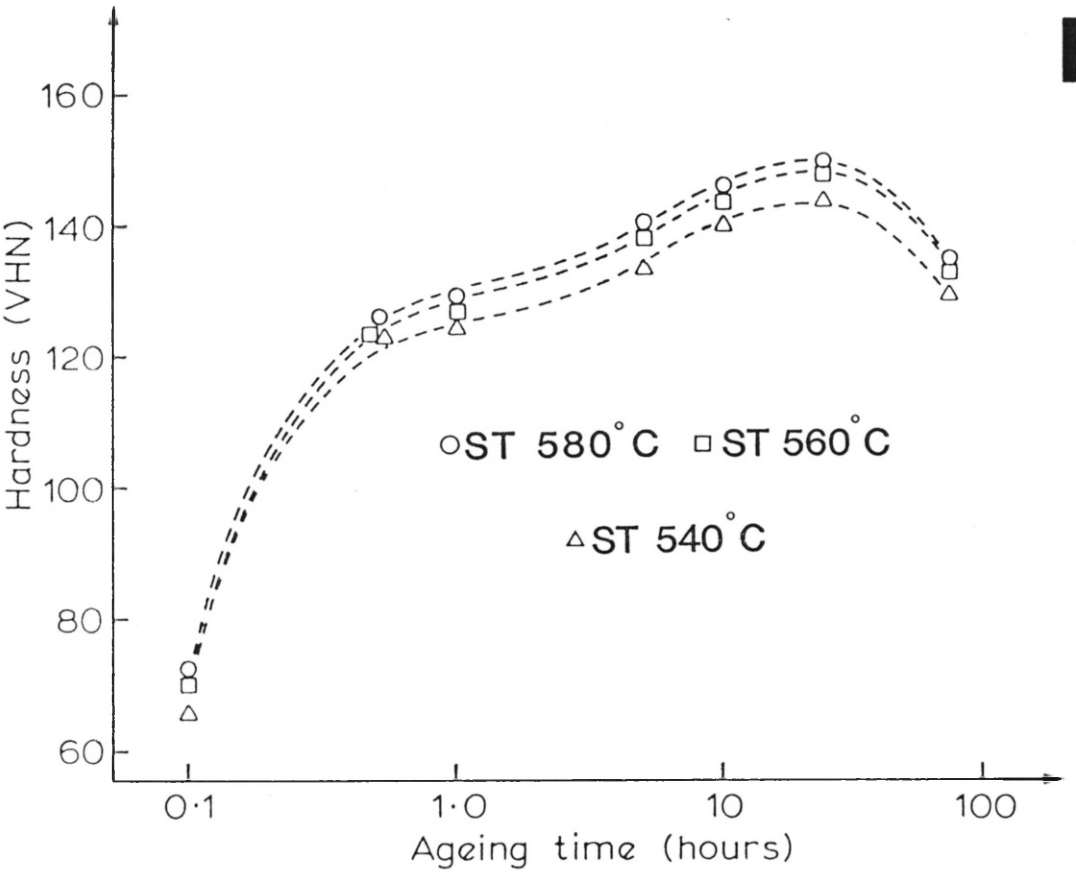


Figure 4.1. Effect of variation in solution treatment temperature on the artificial ageing response of alloy A2 at 190°C.

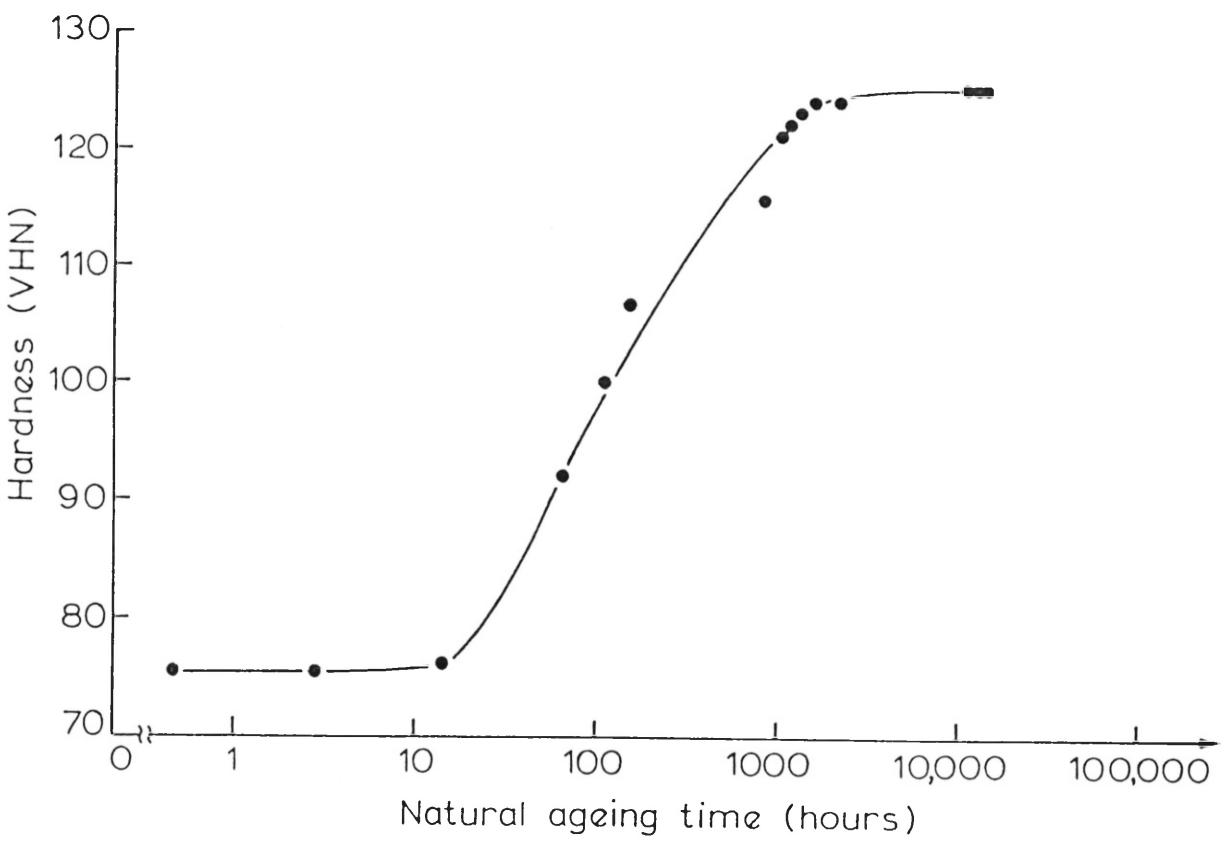


Figure 4.2. The natural ageing response of alloy A2 after solution treatment at 530°C and water quench at room temperature (RT).

Since, the natural ageing response of many age hardening aluminium alloys has been found (160) to bring about interesting modifications in their precipitation mechanisms, the next step of this investigation was to examine the natural ageing characteristics of the alloy. Figure 4.2. shows the natural ageing response of the alloy. The Figure clearly demonstrates the ability of the present alloy to respond to the natural ageing treatment but only after an incubation period of about 24 hours; beyond that point the hardness data increased very rapidly up to a plateau within 4000 hours.

In order to determine the effects of natural ageing upon subsequent artificial ageing, the alloy was subjected to a natural ageing treatment for 24 hours between the quenching operation after solution heat treatment and the final artificial ageing heat treatment. Figure 4.3 shows such ageing curves of the alloy. Comparison of Figures 4.1 and 4.3 shows that with this short natural ageing time the initial ageing response at 190^{o}C is unaltered; however, the natural ageing inhibited the onset of overageing otherwise observed after 24 hours at 190^{o}C such that prolonged artificial ageing for 100 hours lowered the hardness values only very slightly.

All these results suggest that some modifications in the precipitation mechanisms must have been occurring due to the introduction of natural ageing treatment which, in turn, delayed the onset of overageing in this system. In order to study the corresponding modifications, a detailed microstructural examination of the alloy was necessary; the results of the microstructural studies are reported in the following sections.

4.2.2. Microstructure of the Alloy Without Natural Ageing Treatment

4.2.2.1. As Quenched Microstrucutre

Transmission electron microscopy (TEM) of freshly solution treated and water quenched material revealed a very clean microstructure. Figures 4.4 (a), (b) and (c) show the as quenched microstructures of the alloy after three different solution heat treatment temperatures viz. 540, 560 and 580^{o}C respectively. The figures show that in all cases the alloy remained unrecrystallised with subgrain size

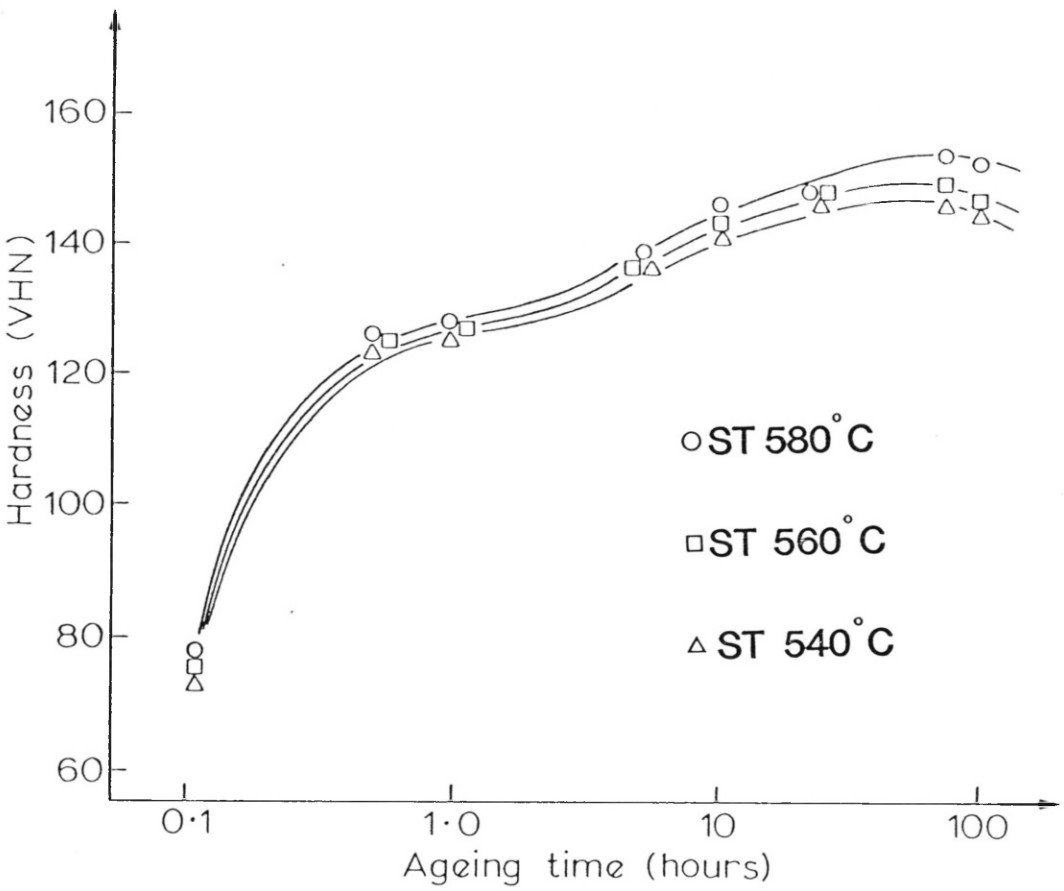


Figure 4.3. Effect of variation in solution treatment temperature, and 24 hours natural ageing on subsequent artificial ageing response of alloy A2 at 190°C.

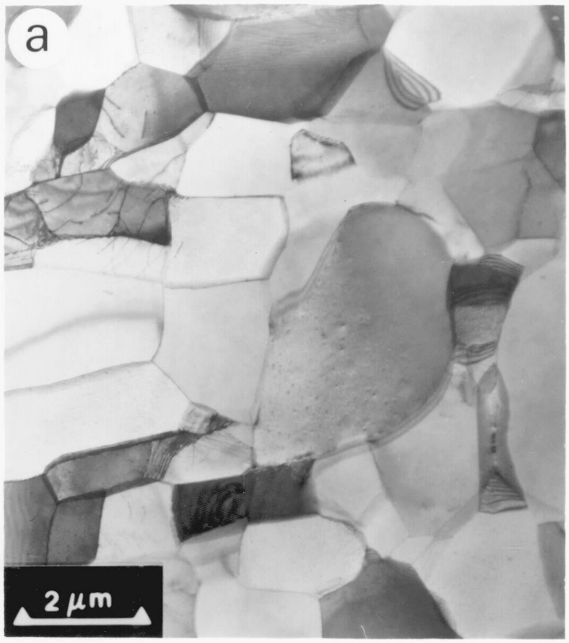
Figure 4.4. TEM micrographs of the as quenched material

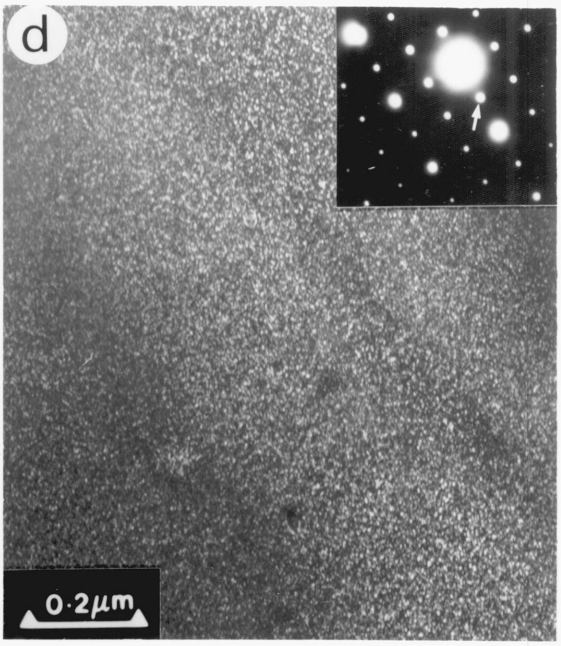
(a)-(c) BF images showing variation in subgrain size due to variation in solution treatment temperature viz. 540, 560 and 580^{o}C respectively.

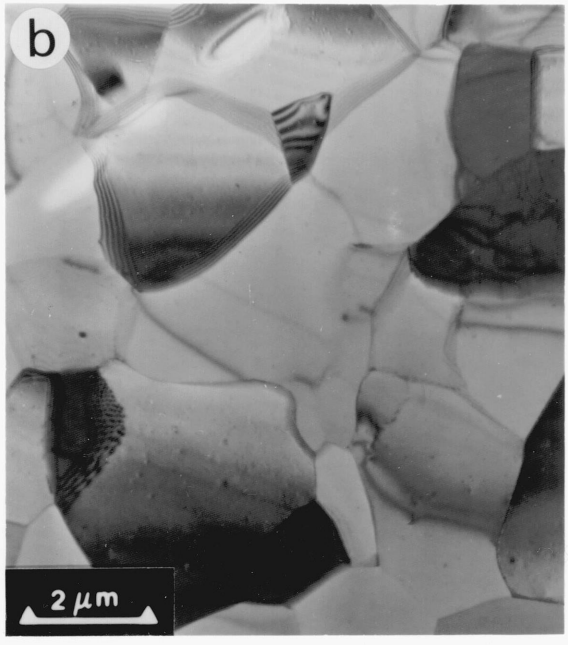
(d) DF image showing δ' precipitation; imaged using (100) superlattice reflection; <100> Al orientation.

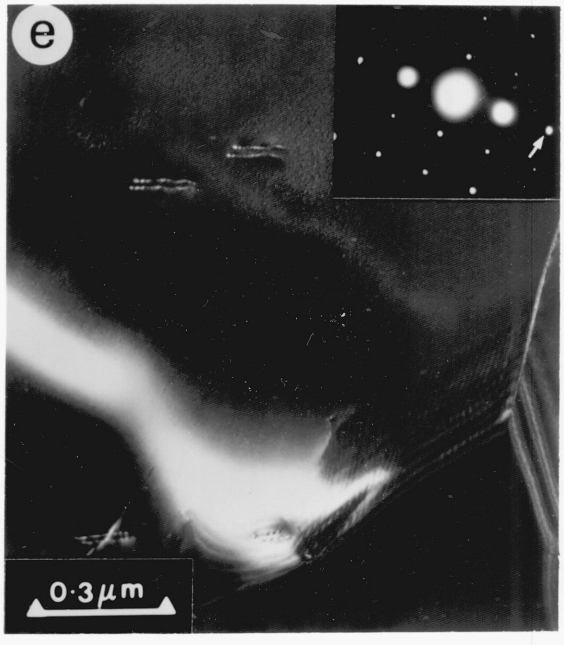
(e) DF image showing superdislocations; g = 222. <112>Al orientation.

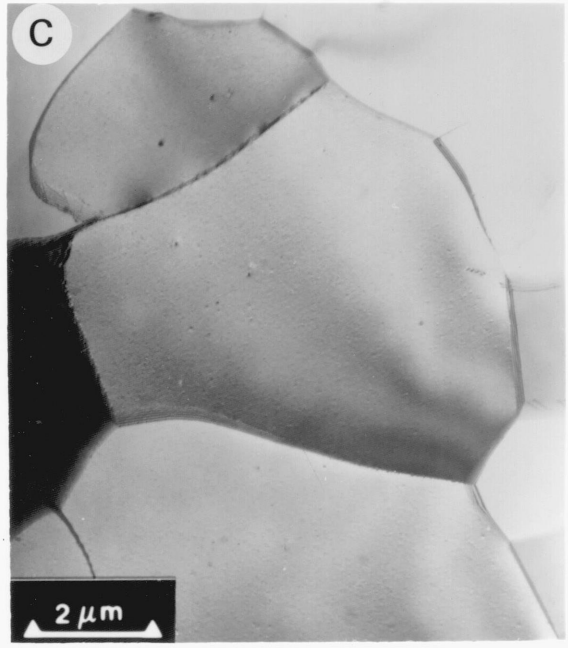
(f) BF image showing inhomogeneous distribution of β' precipitates; close to <100>Al orientation.

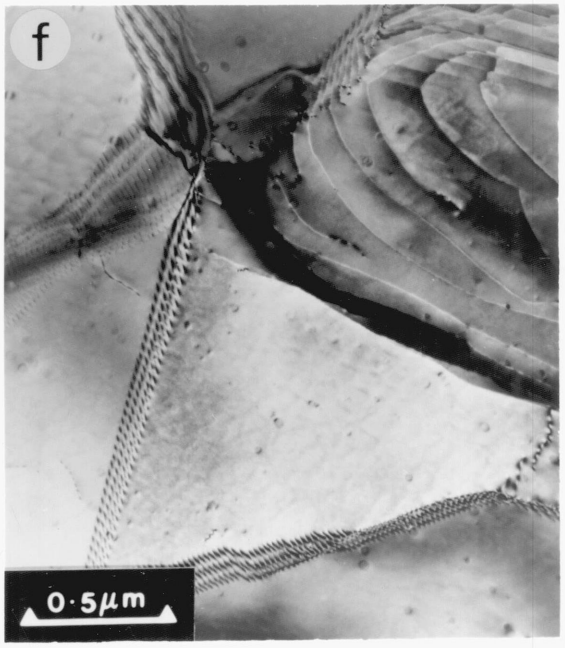

a
2 μm


d
0·2μm


b
2 μm


e
0·3μm


c
2 μm


f
0·5μm

increasing with solution treatment temperature. Any sign of precipitation under bright field imaging conditions was difficult to obtain, but, dark field images using superlattice reflections clearly showed an extremely fine homogeneous dispersion of metastable δ'(Al_3Li) precipitates. Figure 4.4 (d) shows such δ' precipitation. The mottled background of Figure 4.4 (e) indicates the presence of very finely distributed δ' particles and additionally the Figure shows the presence of superdislocations associated with the coherent ordered metastable δ' dispersion. Apart from the δ' particles, the only other particles were in the form of an uneven distribution of Al_3Zr particles (Figure 4.4 (f)). In contrast to many other aluminium alloys, the as quenched microstructure of the present alloy did not show any trace of quenched-in dislocation defects such as dislocation loops or helices.

4.2.2.2. Artificially Aged Microstructure

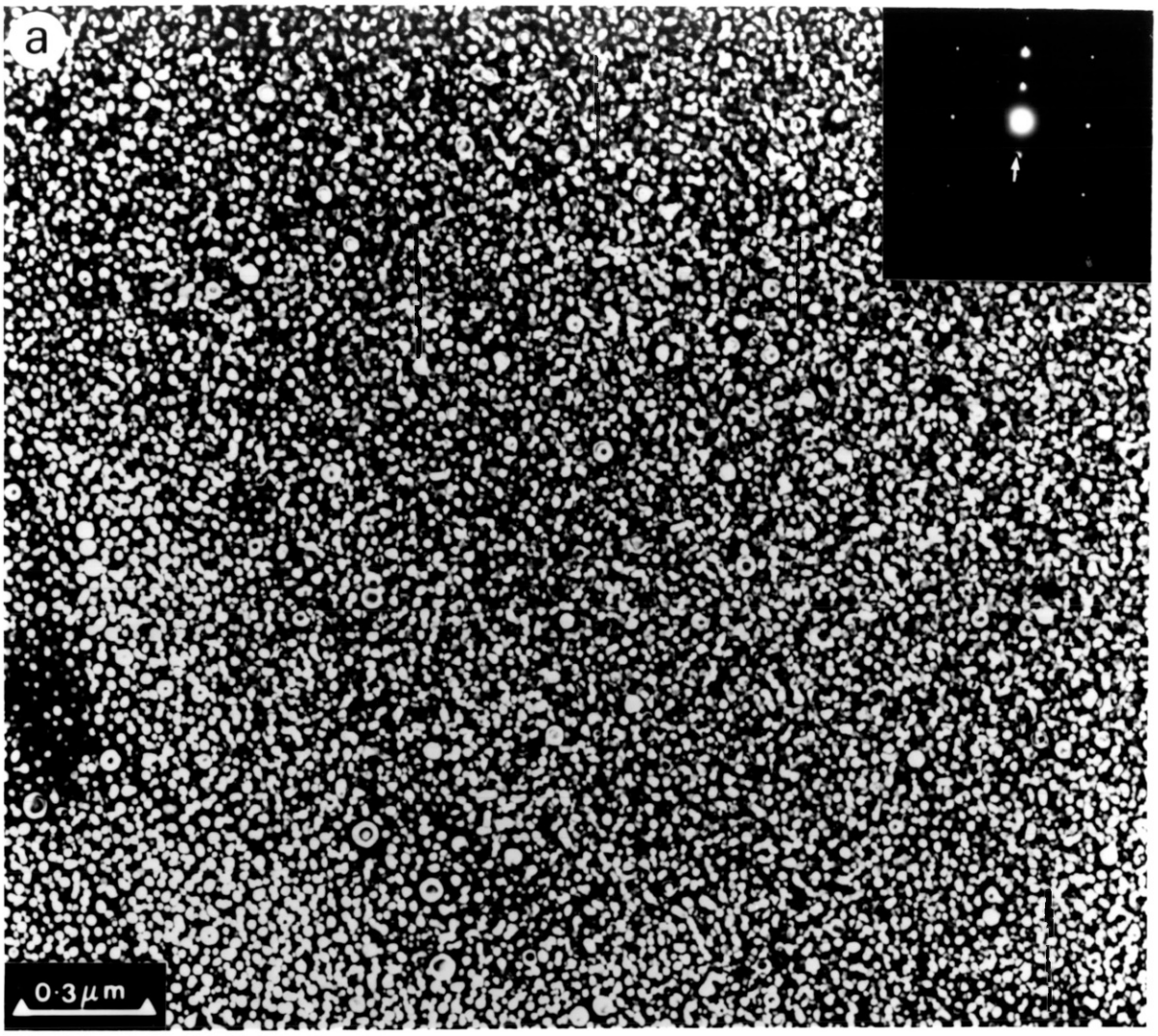
Subsequent heat treatment, initially caused a general growth of the individual δ' particles. However, prolonged ageing heat treatments brought about further microstructural changes in terms of additional precipitation. In the peakaged material the precipitate phases were clearly imaged using TEM. Figure 4.5(a) shows the δ' distribution in the peakaged material. Unlike the δ' distribution, the distribution of additional phases was far from being homogeneous. A few T_1 (Al_2CuLi) phases, as shown in Figure 4.5 (b), were observed adjacent to the subgrain boundaries; also, the precipitation of S phase was very limited, taking place heterogeneously along subgrain boundaries (Figure 4.5 (c)). Prolonged ageing for 72 hours coarsened the precipitates previously observed and additionally revealed the existence of finely distributed homogeneously nucleated S precipitation. Homogeneously nucleated S precipitation was evident after all three different solution heat treatment temperatures; however, the precipitate density decreased with decreasing solution heat treatment temperature. Figures 4.6 (a-c) and (d-f) show the homogeneous S precipitation in [110] and [100] Al orientation respectively.

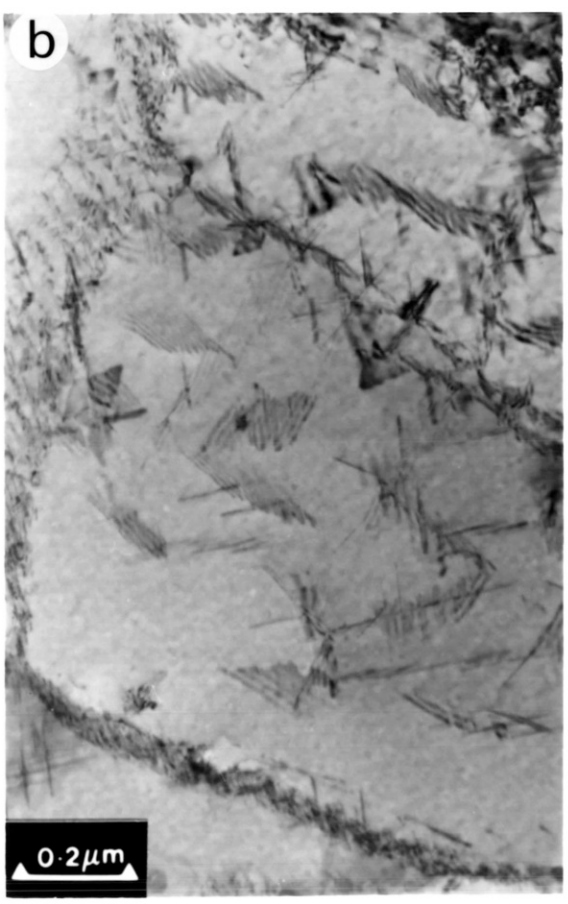
Figure 4.5. TEM micrographs showing precipitate phases in the peakaged material. Material treatment: ST 530°C, WQ(RT), and AA 24 hours at 190°C;

(a) DF image showing δ' precipitation; imaged using (100) superlattice reflection

(b) BF image showing heterogeneous T_1 and S precipitation; <110> Al orientation

(c) BF image showing heterogeneous S (and a few T_1) precipitation; <110> Al orientation.


a
0·3μm


b
0·2μm

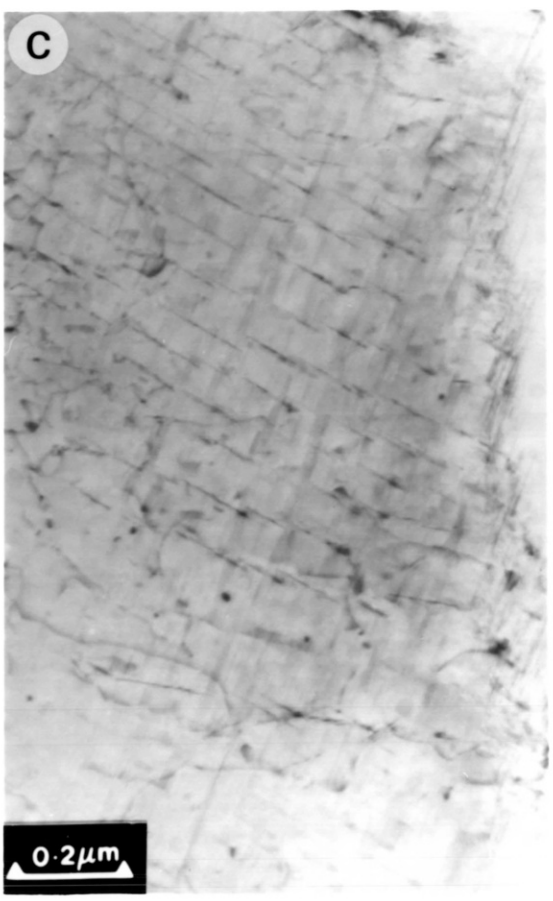
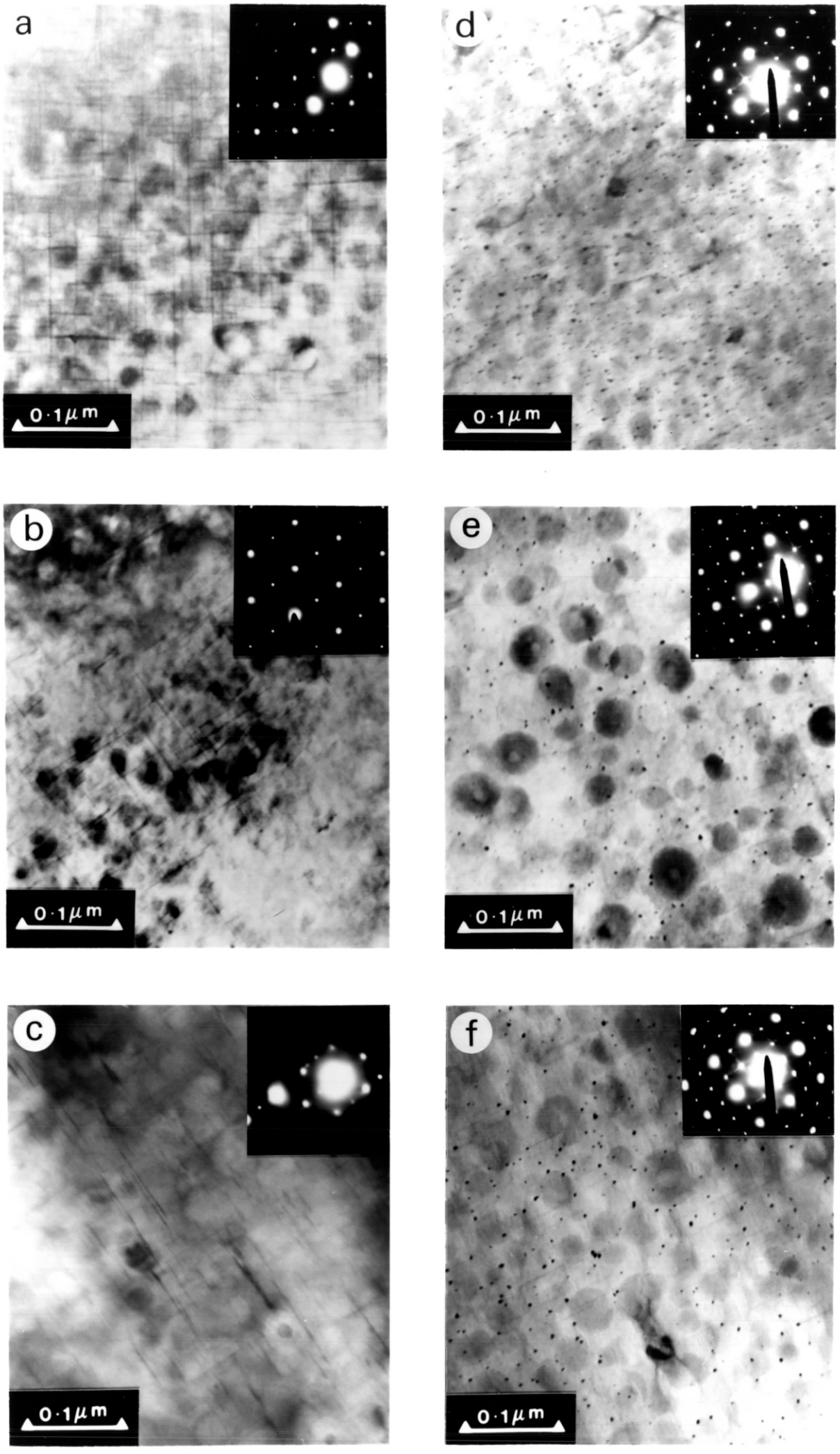

c
0·2μm

Figure 4.6. TEM BF micrographs showing homogeneous S precipitation. Material treatment: solution treated (ST) at 580[(a) and (d)], 560 [(b) and (e)] and 540^{o}C[(c) and (f)], water quenched (WQ) at room temperature (RT) and artificially aged (AA) 72 hours at 190^{o}C. (a) -(c) <110> Al orientation and (d) - (f) <100> Al orientation.


a
0·1μm
d
0·1μm
b
0·1μm
e
0·1μm
c
0·1μm
f
0·1μm

4.2.3. Effect of Natural Ageing

4.2.3.1. Quenched Microstructure

In order to examine the effect of natural ageing upon the quenched material, specimens were solution heat treated, water quenched and were allowed to age at room temperature for 24 hours. No detectable change in the δ' density or size was observed; but, in contrast to the as quenched microstructure, precipitation of a few loops and helices (Figure 4.7 (a)) was observed. In a specimen naturally aged for 120 hours, larger numbers of loops and helices were detected (Figure 4.7 (b)). In order to follow this trend specimens were allowed to age for 1440 hours at room temperature after solution heat treatment. The corresponding microstructure as shown in Figure 4.7 (c) clearly revealed an increased numbers of dislocation loops and helices, thus indicating vacancy precipitation at room temperature.

4.2.3.2. Artificially Aged Microstructure

The quenched samples aged for 24 hours at room temperature were subjected to elevated temperature artificial ageing. Holding the quenched samples for 24 hours at room temperature produced a significant change in the precipitation behaviour within the artificially aged microstructure. After 24 hours at 190^{o}C samples solution treated at 580^{o}C revealed an inhomogeneous distribution of dislocation loops (Figure 4.7 (d)) with broad loop-free zones near subgrain boundaries. In addition, a dispersion of homogeneously nucleated S phase was observed to be well developed (Figure 4.8 (a)), the S phase laths being larger than those produced by ageing for 72 hours without the prior natural ageing treatment. Prolonged artificial ageing for 72 hours almost doubled the density of homogeneously nucleated S phase and revealed a well developed picture of homogeneous S precipitation (Figures 4.8 (b)).

The effect of prolonged natural ageing was worth noting; the microstructure of a specimen, solution treated at 580^{o}C and naturally aged for 1440 hours, when subsequently aged for 24 hours at 190^{o}C revealed a clearer picture of homogeneously nucleated S phase; the S phase density being nearly double that produced by 24 hour natural ageing (Figure 4.8 (c)). Additionally, the artificially

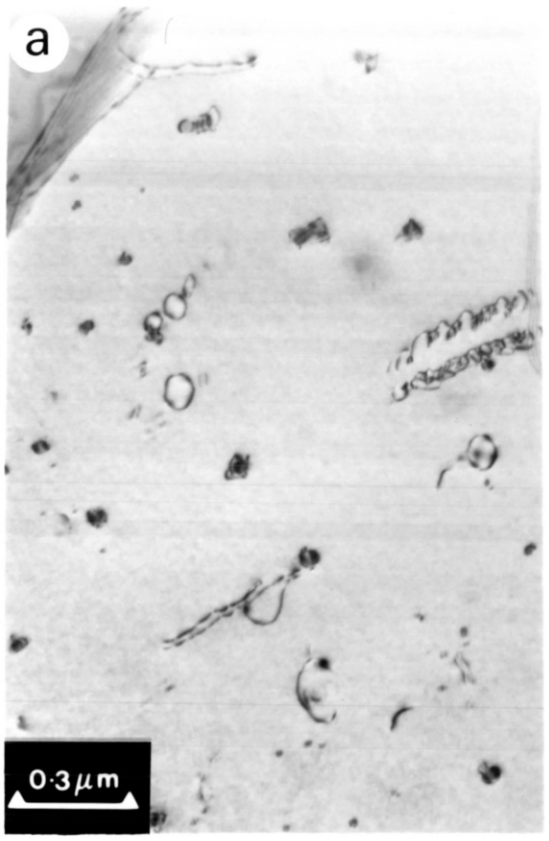
Figure 4.7. TEM BF micrographs showing precipitation of dislocation loops and helices; <110>Al orientation. Material treatment:

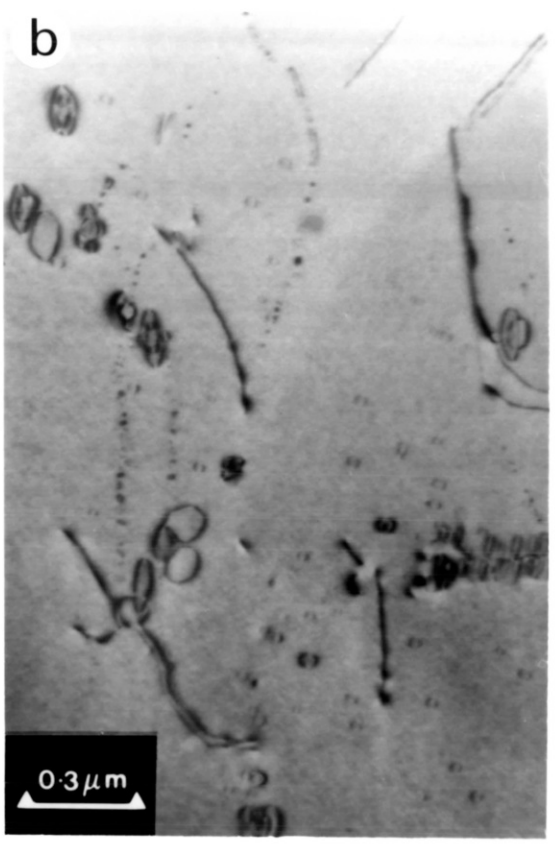
(a) ST 580°C, WQ(RT), NA 24 hours

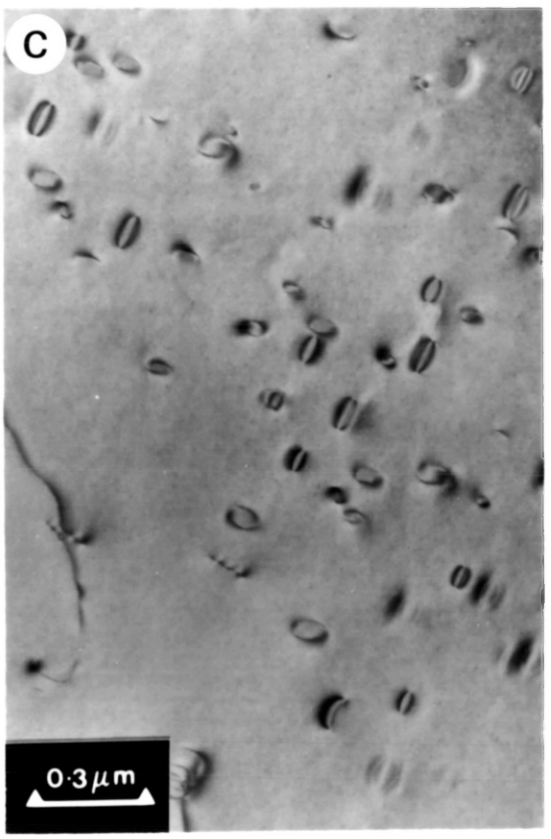
(b) ST 580°C, WQ(RT), NA 120 hours

(c) ST 580°C, WQ(RT), NA 1440 hours

(d) ST 580°C, WQ(RT), NA 24 hours and AA 24 hours at 190°C.


a
0·3μm


b
0·3μm


c
0·3μm

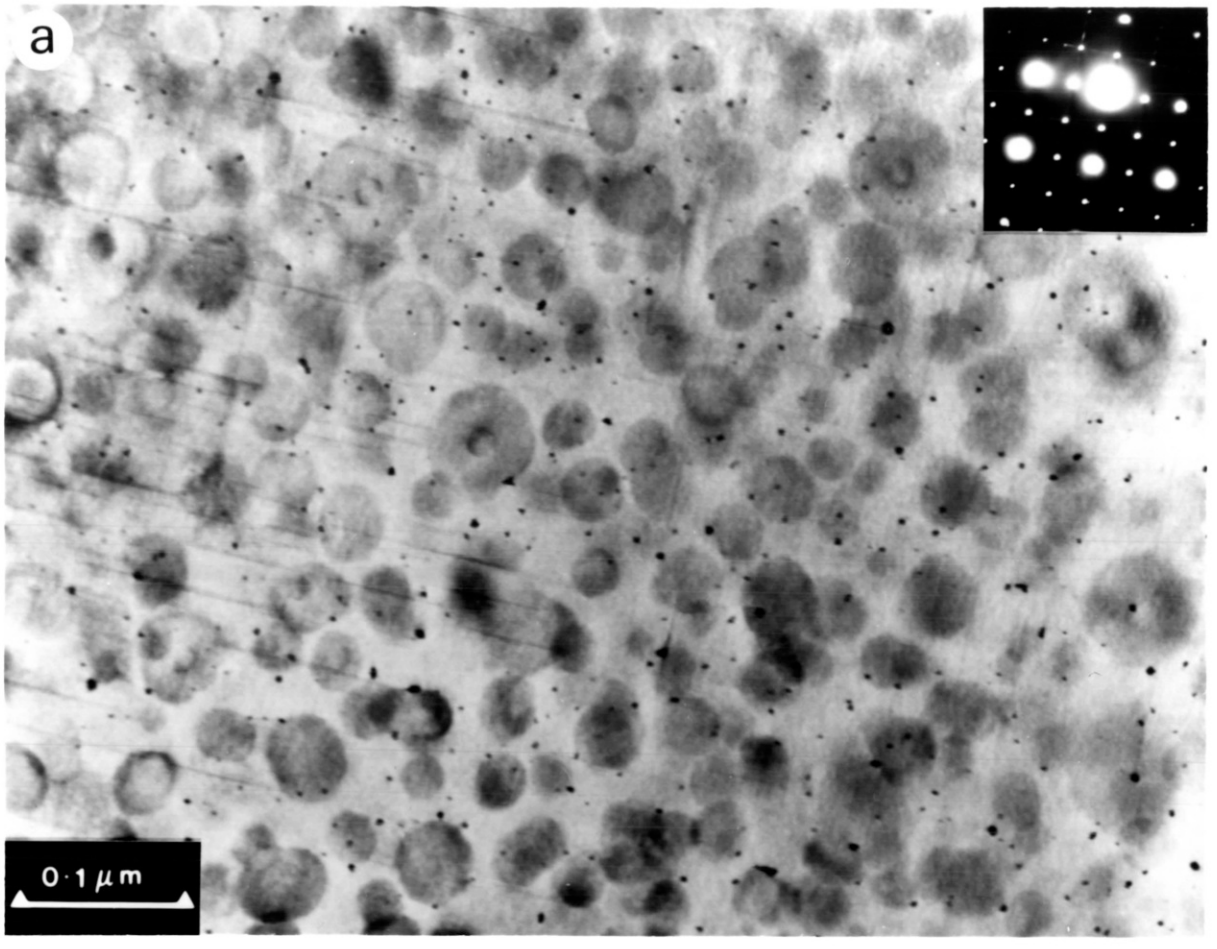

d
0·5μm

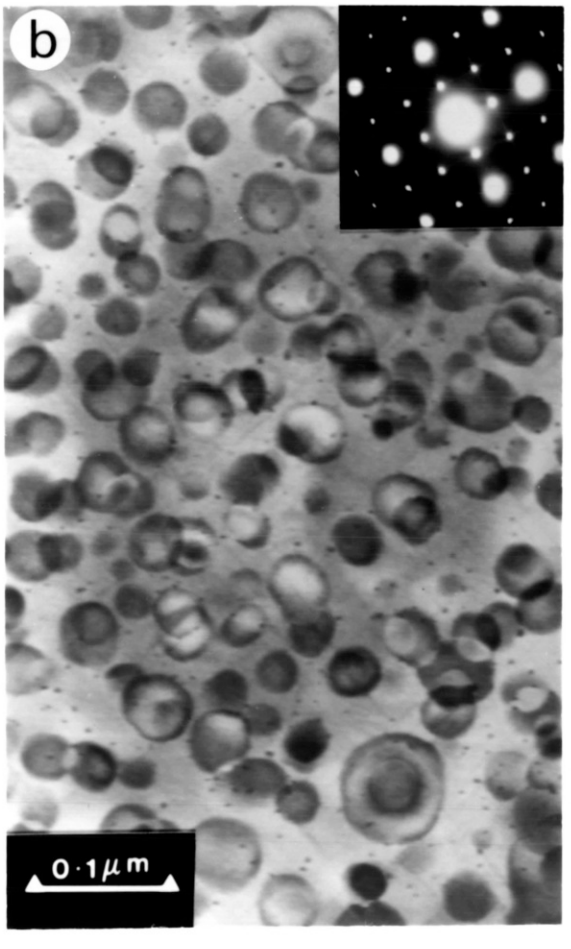
Figure 4.8. TEM BF micrographs showing homogeneous S precipitation; <100>Al orientation. Material treatment:

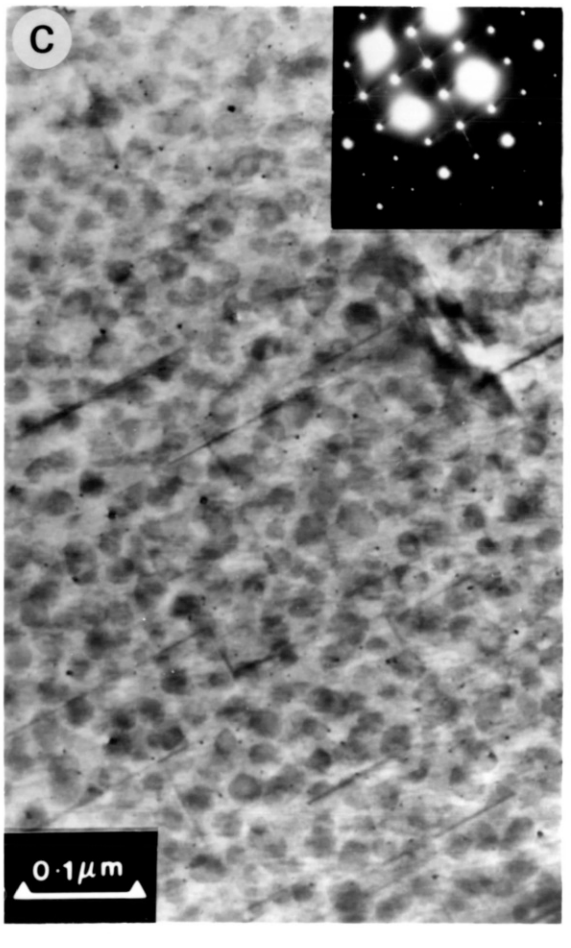
(a) ST 580°C, WQ(RT), naturally aged (NA) for 24 hours and AA 24 hours at 190°C.

(b) ST 580°C, WQ(RT), NA 24 hours and AA 72 hours at 190°C.

(c) ST 580°C, WQ(RT), NA 1440 hours and AA 24 hours at 190°C.


a
0·1 μm


b
0·1μm


c
0·1μm

aged microstructure showed a more uniform distribution of dislocation loops and revealed heterogeneous nucleation of S phase upon the quenched in defects (Figure 4.9 (a)). The aged microstructures after solution treatment at 560 and 540^{o}C also revealed a well developed picture of homogeneous S precipitation and heterogeneous S precipitation upon dislocation loops (Figures 4.9 (b) & (c)). However, the S phase density increased with increasing prior solution heat treatment temperature.

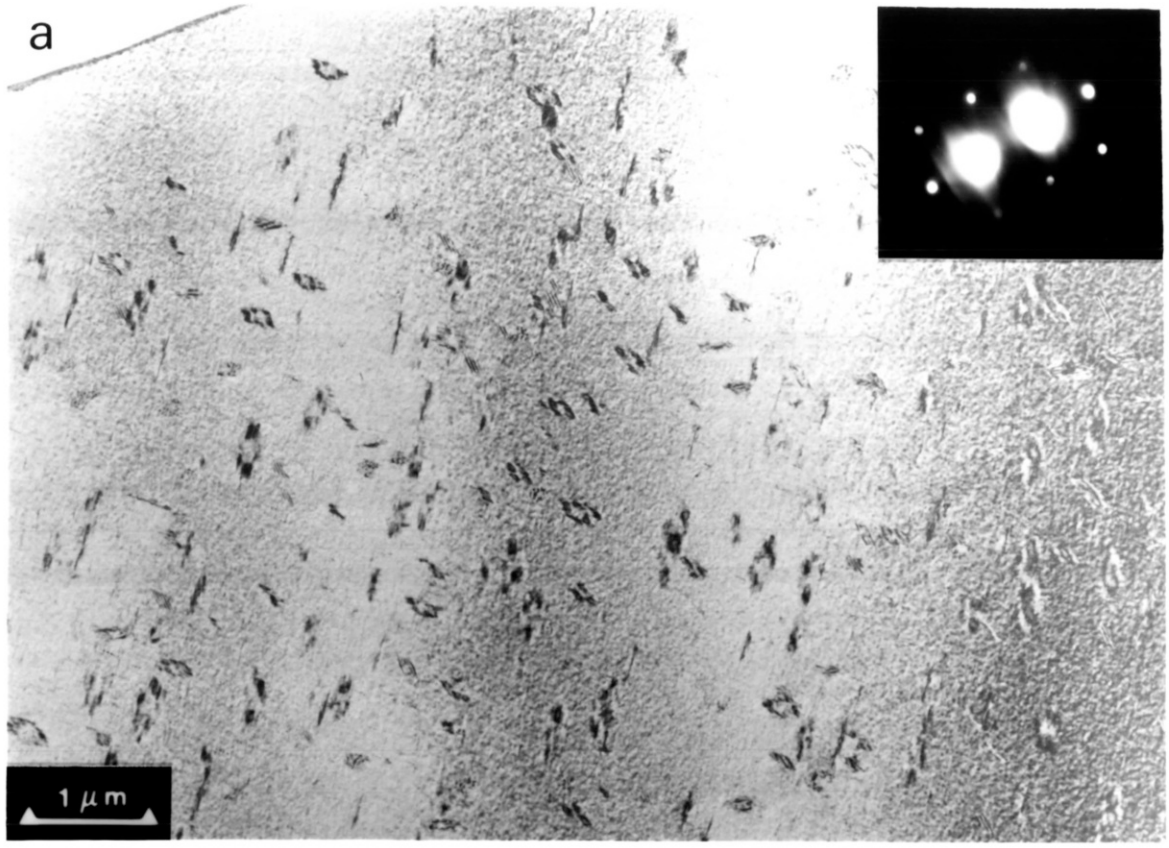
4.2.4. Effect of Quench Bath Temperature

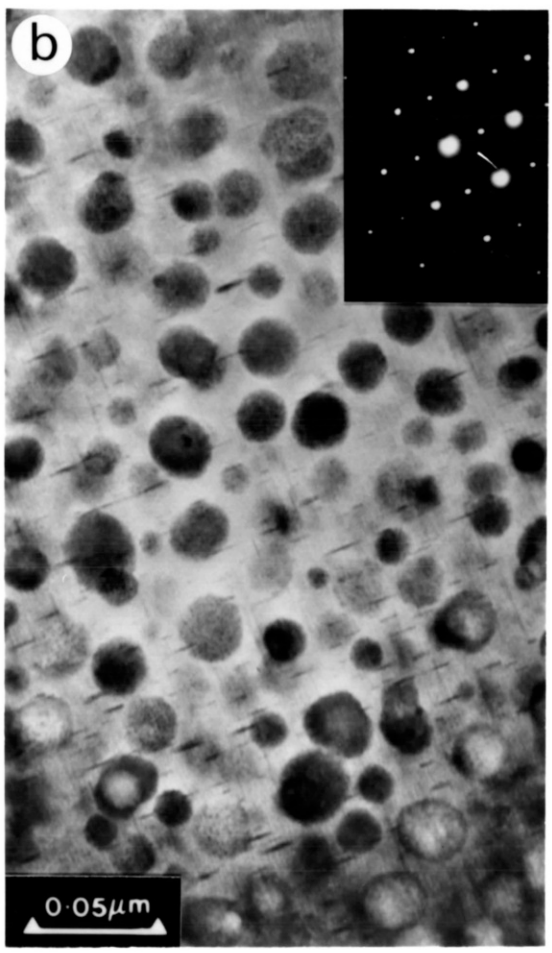
It was reported earlier in section 4.2.2.1. that the present alloy system is not capable of precipitating vacancies in the form of quenched in dislocation defects within the as quenched microstructure. An attempt was thus made to facilitate the release of vacancies through raising the quench bath temperature. For this purpose five different quench bath temperatures viz. 30, 45, 60, 80 and 100^{o}C were used (quenching medium being water). In five different experiments, specimens were solution heat treated, directly quenched to a particular quench bath for one minute, water quenched to room temperature (~23^{o}C) and finally artificially aged at 190^{o}C for 24 hours.

The necessary microstructural details were then characterised using TEM. Up to 45^{o}C, no change was detected within the aged microstructure compared to that of a specimen quenched to room temperature and subsequently aged. But, when the temperature was raised to 60^{o}C, the corresponding artificially aged microstructure clearly revealed homogeneously nucleated S precipitation. Figure 4.10 (a) shows such homogeneous S precipitation. Further, when the temperature was raised to 100^{o}C, the microstructure showed a very high density of homogeneously nucleated S precipitation (Figure 4.10 (c)). The presence of homogeneous S precipitation was evident within the aged microstructures due to all three different solution treatment temperatures and again the precipitation density was found to decrease with decreasing solution heat treatment temperature. Precipitation of dislocation loops and subsequent heterogeneous precipitation of S phase upon them were also observed within the microstructure to a limited extent. In order to investigate further the effect of prolonged prior annealing at 100^{o}C upon the S phase precipitation, the material was solution treated, directly quenched to 100^{o}C for 14 hours and aged at 190^{o}C for 24 hours. The corresponding aged microstructure (Figure 4.10 (b)) clearly revealed homogeneous S precipitation but the density of S

Figure 4.9. TEM BF micrographs; <110>Al orientation.
(a) Distribution of dislocation loops
(b) Homogeneous S precipitation
(c) Heterogeneous S precipitation upon dislocation loops

Material treatment: ST 580^{o}C [ST 560^{o}C for 4.9(b) and (c)], WQ(RT), NA 1440 hours and AA 24 hours at 190^{o}C.


a
1 μm


b
0·05μm

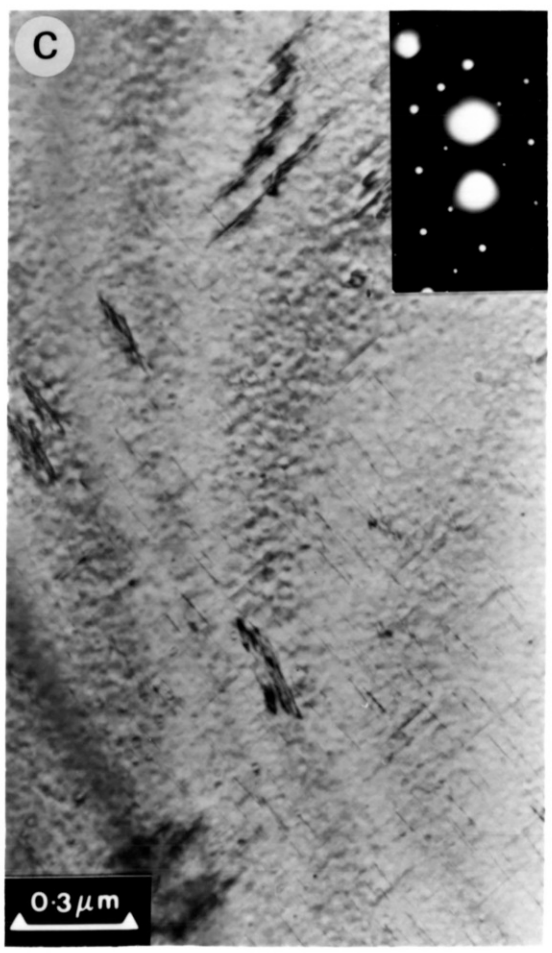
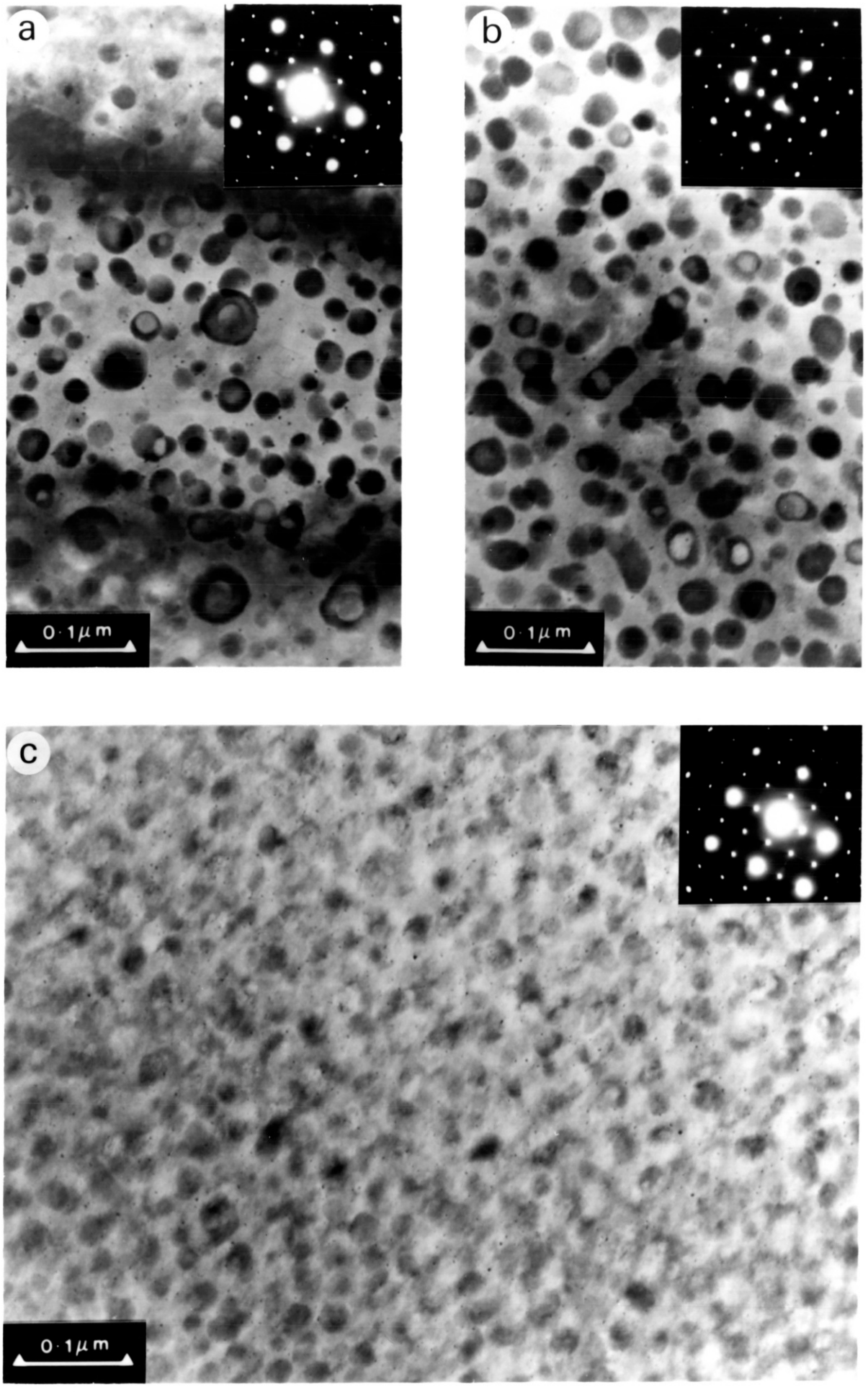

c
0·3μm

Figure 4.10. TEM BF micrographs showing homogeneous S precipitation; <100> Al orientation. Material treatment:

(a) ST 580°C, WQ (60°C for 1 minute), WQ(RT) and AA 24 hours at 190°C.

(b) ST 580°C, Oil quenched (100°C for 14 hours), WQ(RT) and AA 24 hours at 190°C.

(c) ST 580°C, WQ (100°C for 1 minute), WQ (RT) and AA 24 hours at 190°C.


a
0·1μm
b
0·1μm
c
0·1μm

precipitate was no different from that obtained with a 24 hour natural age prior to artificial ageing for the same time and showed a 250 % decrease compared to that obtained in a 1 minute/100^{o}C sample. Additionally, the microstructure showed no trace of quenched in defects. For comparison, the data on the homogeneous S precipitate density and δ' particle size due to some typical heat treatments used in this study are given in Table 4.1. The details of various solution heat treatments and low temperature ageing heat treatments used in this study are additionally shown in Figure 4.11.

4.3. Discussion

4.3.1. Ageing Curves

The general shape of the curves, as shown in Figure 4.1, clearly shows the classical ageing behaviour for a system producing metastable coherent precipitates. The early stages of ageing are characterised by a rapid initial hardness increase. This is due to the interaction of glide dislocations with the δ' precipitates by a shearing mechanism. Continued ageing leads to coarsening and a gradual loss of coherency with the matrix, together with an increase in the interparticle spacing, which changes the hardening mechanism from shearing to one of dislocation looping. The latter stage is accompanied by a gradual loss of hardness. In contrast to the simple nature of the curves of Figure 4.1., Figure 4.3 revealed some interesting features. At the very initial stage, slightly increased values of hardness suggests that the material is able to respond to the 24 hours natural ageing treatment; other than this 24 hours of artificial ageing produced no noticeable difference between the two sets of curves. The onset of overageing, otherwise observed after 24 hours at 190^{o}C, was however, inhibited. This may be attributed to the rapid homogeneous S precipitation in the material with a prior natural age. Natural ageing accelerated homogeneous S precipitation which resulted in the hardness peak due to S phase moving to shorter times and possibly increasing in magnitude: it overlapped the peak due to δ' and thus inhibited the onset of overageing. The continuing increase in hardness values up to 72 hours of prolonged artificial ageing may be again attributed to the increased precipitation of homogeneous S throughout the matrix, (see Table 4.1 for comparison). Finally, after 72 hours, the overageing began to dominate accompanied by a gradual loss in hardness.

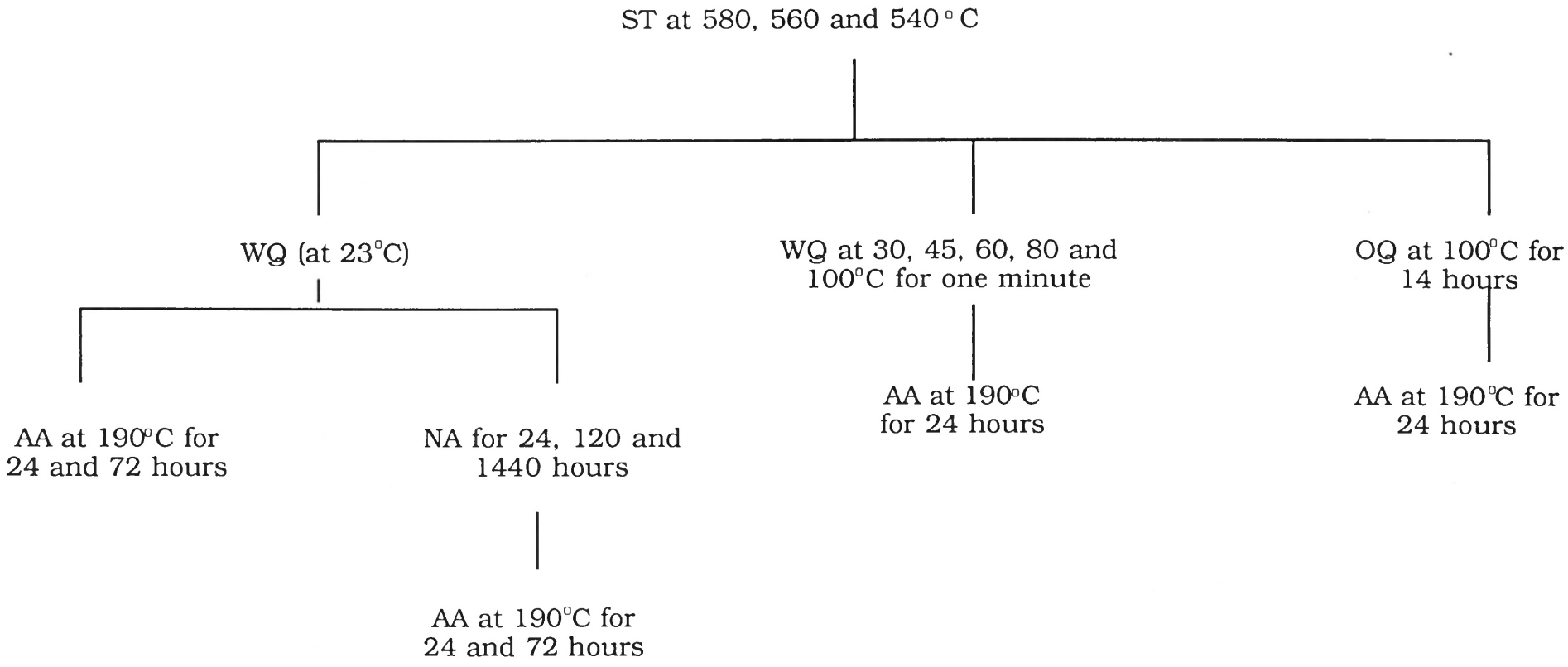
Table 4.1. Average $\delta'(Al_3Li)$* particle diameter and homogeneous $S(Al_2CuMg)$ precipitate density

Details of Heat Treatment	Average δ' particle diameter (nm)	Homogeneous S precipitate density (x 10^4 per sq. cm.)
ST at 580°C, WQ at 23°C and AA at 190° C for 24 hours	24	Homogeneously nucleated S precipitate could not be detected.
ST at 580°C, WQ at 23°C and AA at 190 °C for 72 hours	28	231
ST at 560°C, WQ at 23° C and AA at 190°C for 72 hours	29	146
ST at 540°C, WQ at 23°C and AA at 190°C for 72 hours	34	119
ST at 580°C, WQ at 23°C, NA for 24 hours and AA at 190°C for 24 hours	26	122
ST at 580°C, WQ at 23°C, NA for 1440 hours and AA at 190°C for 24 hours	26	252

ST at 580°C, WQ at 23°C, NA for 24 hours and AA at 190°C for 72 hours	30	252
ST at 580°C, WQ at 60°C (for 1 minute), WQ at 23°C and AA at 190°C for 14 hours	26	145
ST at 580°C, WQ at 100°C (for 1 minute), WQ at 23°C and AA at 190°C for 24 hours	27	314
ST at 580°C, OQ at 100°C (for 14 hours), WQ at 23°C and AA at 190°C for 24 hours	28	120
ST at 560°C, WQ at 23°C, NA for 1440 hours and AA at 190°C for 24 hours	26	144
ST at 540°C, WQ at 23°C, NA for 1440 hours and AA at 190°C for 24 hours	26	106

* Coarse δ' particles nucleated heterogeneously on zirconium rich particles were not included for the diameter measurement

Figure 4.11 Details of Heat Treatments



ST : Solution Treated, WQ : Water Quenched, OQ : Oil Quenched,

AA : Artificially Aged, NA : Naturally Aged

The most consistent feature common to both sets of ageing curves shown in Figures 4.1 and 4.3 was that the hardness values in any stage of the ageing curves increased with increasing solution heat treatment temperatures; such an event may be explained primarily on the basis of higher vacancy supersaturation contributing towards more δ' nuclei forming in association with higher solution treatment temperatures. Although no detectable changes were observed in the δ' density or size in the quenched microstructures due to different solution treatment temperatures, measurement of δ' particle diameter in the corresponding artificially aged microstructures revealed that the δ' particle diameter decreases with increasing prior solution heat treatment temperature (see Table 4.1). The present observation is in close agreement with that of Suzuki et al (21). The authors studied in detail the role of excess vacancies in δ' precipitation in binary Al-Li alloys; it was shown that the density of δ' phase precipitates after quenching and in the initial stages of ageing increases with increasing solution treatment temperatures. The authors suggested that the excess vacancies not only initially increase the dispersion of the lithium atoms in the parent phase, but also by temporarily occupying lithium atom positions in the $L1_2$ structure, facilitate δ' nuclei formation. However, in Al-Li-Cu-Mg alloys additional precipitation reactions are feasible and the results of the present study clearly showed that the influence of solution heat treatment temperature on the formation of homogeneous S phase is significant such that the S precipitate density increases with increasing prior solution treatment temperatures. It is, therefore, suggested that the increase in strength with increasing prior S.H.T. temperatures in the peakaged (Figure 4.3) and beyond the peakaged (Figures 4.1 and 4.3) conditions is additionally due to the increased and widespread precipitation of homogeneous S within the microstructure.

The role of excess vacancies in homogeneous S precipitation within the present alloy system is discussed in the following section. However, discussion on Figure 4.2, the natural ageing curve of the alloy will be reserved until Chapter 5.

4.3.2. Effect of Natural Ageing, Solution Treatment Temperature and Quench Bath Temperature

In the solution treated condition the lithium free Al-Cu-Mg alloys exhibit a widespread distribution of dislocation loops and helices typical of aluminium and many of its alloys (161). During ageing S phase precipitates heterogeneously on

these sites and spreads autocatalytically throughout the microstructure. In contrast, the lithium bearing aluminium alloys do not contain any quenched in dislocation defects in the solution treated conditions after quenching at room temperature from the temperatures ranging 540 to 580^{o}C (see section 4.2.2.1). This implies that the vacancies are bound by lithium, and this is consistent with the high lithium to vacancy binding energy (0.25 - 0.26 eV) previously reported (64, 162) and the analogous behaviour of addition of silicon (which has a similar binding energy) to Al-Cu-Mg alloys (161).

Weatherly (161) reported that within an alloy composition Al - 2.72 Cu - 1.34 wt % Mg. the addition of 0.2 wt % silicon converted the age hardened microstructure from one containing entirely heterogeneously nucleated laths of S phase to one consisting of a widespread distribution of homogeneously nucleated laths. The results of the present investigation also showed that in lithium containing Al-Cu-Mg alloys, where the heterogeneous S precipitation is suppressed, homogeneous nucleation of S phase can occur; but the process is extremely sluggish and homogeneous S precipitation was only detected after prolonged artificial ageing for 72 hours. Clearly prolonged ageing heat treatment cannot be practiced commercially when the δ' particles become appreciably coarsened. However, the present results also showed that when the material was subjected to a natural ageing treatment for 24 hours prior to artificial ageing, precipitation of homogeneous S phase took place only after 24 hours at 190^{o}C; the aged microstructure additionally showed an inhomogeneous distribution of dislocation loops with broad loop free zones near subgrain boundaries.

The results imply that the suppression by lithium of vacancy condensation on quenching inhibits heterogeneous S precipitation by removing the dislocation loops and helices upon which it normally forms in Al-Cu-Mg alloys and the resultant high vacancy concentration in solution would in turn, be expected to promote homogeneous S precipitation. However, the process is extremely slow, although, the increase in vacancy concentration by increasing solution treatment temperature does result in the formation of more S nuclei. Natural ageing eventually produces dislocation loops in the material. This implies that vacancy condensation can take place at room temperature as the vacancies become unbound (the wide loop free zones present after ageing at 190^{o}C result from vacancy loss to subgrain boundary sinks). This interpretation is supported by the concomitant

rapid homogeneous precipitation of S phase. This implies that as δ' precipitates grow the vacancies are released back into solution. Such a process is unlikely to be associated with binding to individual lithium atoms, since the concentration of lithium remaining in solution after ageing is orders of magnitude greater than the vacancy concentration inherited from solution treatment at 580^{o}C, and this suggests that the vacancies are most strongly bound to the lithium atom clusters which form the δ' nuclei. Rejection from these during their growth increases the concentration of free vacancies in solution. The effect of natural ageing may thus be to release vacancies back into solution as δ' grows, which can either cause S phase nuclei to form at room temperature and subsequently grow at 190^{o}C or simply enhance direct nucleation from solution at the ageing temperature.

Small-angle neutron scattering (SANS) studies (163) have shown that the δ' present after quenching from the solution treatment grows at room temperature and achieves volume fractions in excess of those attainable at 190^{o}C within 1700 hours of natural ageing. The TEM observations show the growth of δ' but it was not possible to determine the increase in δ' volume fraction as indicated by the SANS technique. If, therefore, vacancies become freed during precipitation of δ', it would be expected that prolonged natural ageing should increase the free vacancy concentration available for formation of S phase during subsequent ageing at 190^{o}C (unless the δ' redissolves on heating to 190^{o}C, but recent studies (164) indicate that this would not be the case at this lithium concentration). The present results clearly show that the homogeneous S precipitate density (see Table 4.1 for comparison of the S precipitate density) in a material after a prior natural age of 1440 hours was double that observed in material with a short natural age of 24 hours. These results again imply that either the earlier availability of the maximum concentration of free vacancies promotes the formation of homogeneous S phase or GP zones of the Al-Cu-Mg system, produced (but not detected) at room temperature, might survive on heating to 190^{o}C and act as S nucleation sites. In either case, it is a prerequisite that formation of free vacancies must take place during natural ageing; it is essential because formation of any precipitate phase during natural ageing is also dependent on the availability of such free vacancies, which, in turn control the diffusion process at room temperature. The distinctive feature of the present alloy system is, therefore, the vacancies initially bound to the lithium atom clusters which form the δ' nuclei are freed as δ' grows and can then

influence S phase formation. The sluggish nature of homogeneous S precipitation in lithium containing Al-Cu-Mg alloys, may, therefore, be explained.

The results on the use of higher quench bath temperatures and promotion of homogeneous S precipitation during subsequent artificial ageing heat treatments additionally reflect the critical role of vacancies in homogeneous S phase formation in this material. Homogeneous S precipitation could not be detected within the material with a prior quench bath temperature of less than $60^{o}C$; it implies that the vacancies are most strongly bound to the δ' particles and also a critical concentration of free vacancies is clearly required in order to encourage the matrix precipitation of S phase. Further investigations showed that homogeneous nucleation of S phase was significantly enhanced when the material was directly quenched to $100^{o}C$ for 1 minute compared to that in a material quenched to $100^{o}C$ for 14 hours. This may be explained as follows: vacancy liberation and condensation is rapid at $100^{o}C$. Holding for only one minute results in substantial liberation but little condensation, hence S phase is greatly promoted upon subsequent artificial ageing. In contrast, holding for 14 hours permits more condensation to occur. Also observations show loops and helices only in the central regions of subgrains suggesting that long range diffusion at $100^{o}C$ results in vacancy loss to subgrain boundary sinks. Consequently the concentration of free vacancies within the matrix is reduced and less promotion of S precipitation can occur. All these results indicate that the effects of solution treatment variation, natural and low temperature ageing upon S precipitation behaviour at $190^{o}C$ must involve alterations in the concentration of free vacancies in solution.

4.4. Summary

1. Lithium bearing alloy A 2 when solution treated and quenched from the range 540 to $580^{o}C$ contains no loops and helices which is otherwise typical of aluminium and its alloys. The evidence suggests that many of the nonequilibrium excess vacancies are confined to the δ' phase (Al_3Li) particles produced during or immediately after quenching rather than being bound to individual lithium atoms still remaining in solution. Besides homogeneously distributed δ' particles TEM revealed only an uneven distribution of Al_3Zr particles within the as quenched microstructures.

2. In the peakaged condition (24 hours at 190°C), precipitation of additional phases viz. S(Al_2CuMg) and T_1(Al_2CuLi) takes place; but unlike δ', their distribution is far from homogeneous. Precipitation of S phase which relies on heterogeneous nucleation is necessarily sparse in this system due to the supression of vacancy condensation on quenching which prevents formation of the dislocation loops and helices. However, the resultant high vacancy concentration in solution, in turn, encourages homogeneous S precipitation within the material. Although, the process is extremely slow an increase in vacancy concentration resulting from increasing prior solution treatment temperature is observed to refine the homogeneous S phase dispersion. It is suggested that during age hardening processes as δ' grows, vacancies are released back to solution and promote homogeneous S precipitation.

3. Homogeneous S precipitation can be achieved and it is attributed to the attainment of a critical concentration of free vacancies in solution. During natural ageing, δ' grows and the release of bound vacancies clearly occurs as evidenced by the dislocation loop and helix formation. Consequently natural ageing increases the numbers of free vacancies present at the start of artificial ageing and accelerates homogeneous S precipitation; alternatively, S embryos are created during natural ageing and survive heating to 190°C. On the basis of the present results, it is not feasible to distinguish between these two possibilities.

4. Natural ageing prior to artificial ageing induces rapid homogeneous S precipitation and inhibits the onset of overageing, otherwise observed after 24 hours at 190°C in a sample without a prior natural age. It is suggested that the accelerated homogeneous S precipitation results in the hardness peak due to S phase moving to shorter times and possibly increasing in magnitude: it overlaps the peak due to δ' and thus inhibits the onset of overageing.

5. With increasing prior solution heat treatment temperatures, the strength of the material always increases. It is suggested that this is primarily due to the high vacancy supersaturation contributing towards more δ' nuclei

forming in association with higher solution heat treatment temperatures. The increase in strength in the peakaged and beyond the peakaged conditions (depending on the preaging heat treatment) is additionally due to the increased precipitation of homogeneous S; increasing prior solution heat treatment temperature increases the total vacancy concentration which in turn contributes towards more S nuclei forming.

6. Controlled low temperature ageing releases bound vacancies resulting in their condensation as dislocation loops. The presence of loops provides heterogeneous nucleation sites in the absence of stretch. Also, if the released vacancies can be held in sufficient concentration in solid solution they promote homogeneous S precipitation. However, treatments which involve loss of vacancies to sinks limit homogeneous precipitation of S and almost completely inhibit heterogeneous S precipitation.

CHAPTER FIVE

THERMAL ANALYSIS STUDY OF THE PRECIPITATION REACTIONS IN Al-Li-Cu-Mg-Zr ALLOY

5.1. Introduction

The work presented in this chapter is concerned with the characterisation of the precipitation reactions within the Al-Li-Cu-Mg-Zr alloy of AA 8090 specifications (viz. alloy A2) by differential scanning calorimetry (DSC). The precipitation reactions within the quaternary system are complex. To avoid confusion, some selected binary and ternary systems (viz. Al-Li, Al-Li-Zr and Al-Cu-Mg system) are initially examined via DSC following examination and interpretation of the DSC data for the quaternary system.

In the previous chapter, the effect of natural ageing upon the precipitation reaction within the quaternary system was discussed in detail. It was suggested that during natural ageing formation of S embryos (might well be in the form of GP zones of the Al-Cu-Mg system) is possible. However, TEM could not detect development of any such phase within a naturally aged material; it may be due to very low solute (Cu + Mg) supersaturation in the present material. The present work, therefore, additionally investigates the modifications in precipitation reactions, if any, within the naturally aged material via high sensitivity differential scanning calorimetry. In light of the DSC results, the natural ageing response of the quarternary system is also discussed.

5.2. Results

5.2.1. Aluminium-Lithium (Alloy A3)

Specific heat (S) measurements on the binary Al-Li alloy in the as quenched (AQ), naturally aged (NA) and artificially aged (AA) conditions are shown in Figure 5.1. The as quenched specimens were unavoidably delayed for between 30 and 150 minutes at room temperature prior to thermal analysis. In Figure 5.1, the dotted line is an estimation of the base line, representing the alloy's specific heat (ΣCp) as a

a function of temperature using the Neumann-Kopp prediction (165). When S > ΣCp, an endothermic reaction is taking place, and when S < ΣCp an exothermic process is occurring. In the case of age hardening alloys formation of precipitate phases is normally an exothermic process whilst their dissolution is an endothermic reaction.

In the as quenched condition in Figure 5.1, the specific heat appears to move in an exothermic direction during the earliest stages of heating (A). This behaviour is terminated by the endothermic reaction at 130°C (B) which has previously been interpreted in terms of the dissolution of GP zones of Al-Li system (17) or retrogression of fine δ' (18) which form rapidly at room temperature or during the quenching process. The subsequent exotherm at 170°C is similar to those observed in previous work (10, 17, 18) and is generally considered to be associated with δ' formation, but the magnitude of thermal fluctuation depends critically upon the exact position of the Neumann-Kopp baseline (ΣCp) which is difficult to determine accurately. The endotherm "peaking" at 300°C (D_2) is again consistent with previous thermal analysis studies on binary Al-Li alloys and it is attributed to δ' dissolution.

TEM studies of the as quenched material revealed the presence of superlattice reflections in electron diffraction patterns prior to any heating in the DSC; however, no δ' particles could be clearly imaged in dark field at this stage. Previous workers have imaged particles of δ' and quoted sizes variously as 1.5 or 3 nm in similar alloys (20, 164). This suggests that the rate of quenching is very important in determining the room temperature δ' size and distribution. After being heated to 250°C in the DSC and quenched, samples contained a homogeneous distribution of δ' particles (~ 10 nm in diameter). Similar TEM studies after heating to 300°C revealed fewer δ' particles of 35 nm in diameter and also very fine δ' (< 4 nm) distributed throughout the matrix, presumably having formed from supersaturated solution during the quench from 300°C. These observations are consistent with endotherm D_2 being due to δ' dissolution.

Microscopic observations of the naturally aged alloy revealed similar features to the as quenched material but the δ' could now be clearly imaged (~ 5 nm particles). The DSC traces showed some notable differences. The endotherm at 130°C became more pronounced and contained two maxima (B_1 and B_2) as shown in

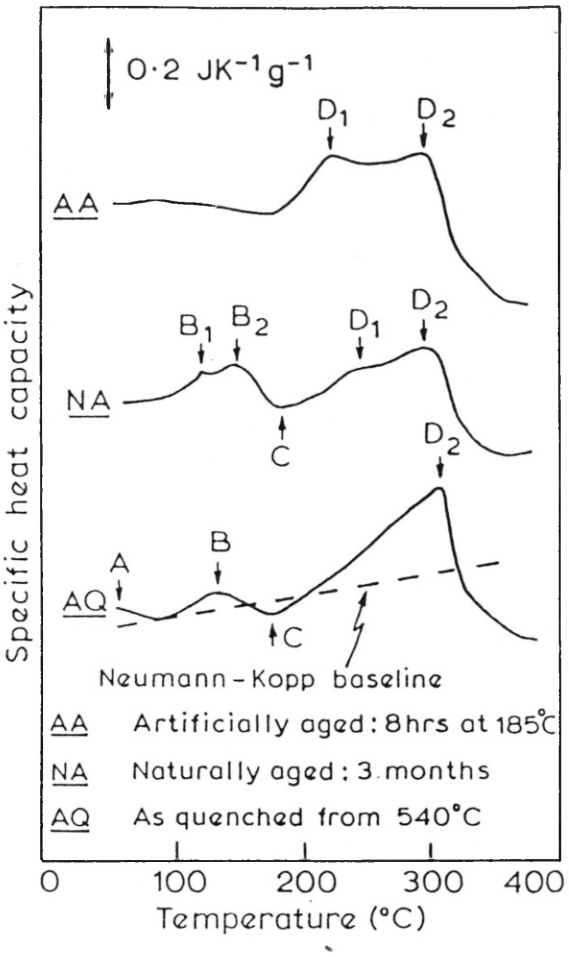


Figure 5.1. Specific heat capacity vs. Temperature curves for binary Al-Li system (alloy A3).

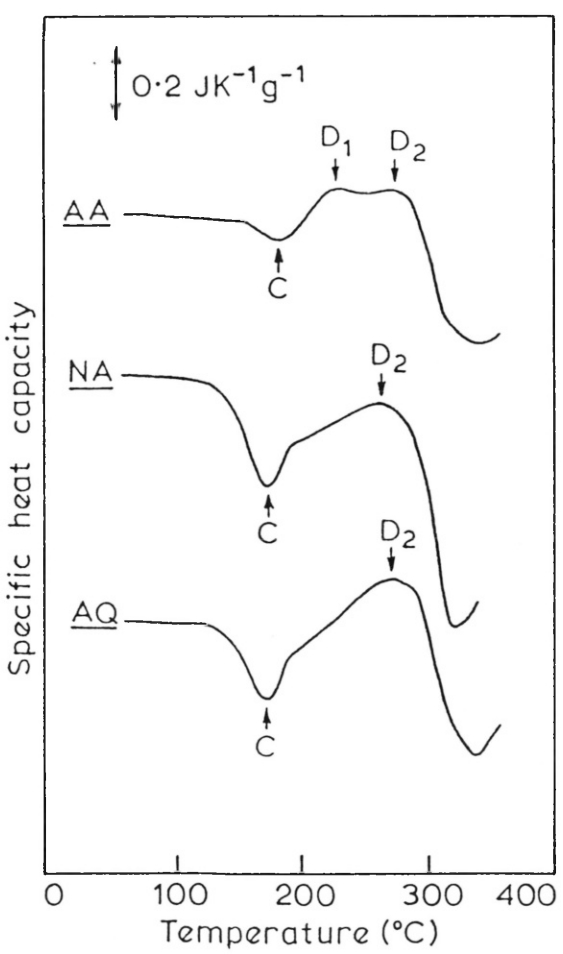


Figure 5.2. Specific heat capacity vs. Temperature curves for ternary Al-Li-Zr system (alloy A4).

Figure 5.1. In a similar fashion the δ' dissolution peak is broadened by the appearance of a shoulder on the curve at about 250°C (D_1). These curves are similar in form to those of Nozato and Nakai (10). They attribute B_1 to the dissolution of an additional GP zone phase and D_1 to the dissolution of δ' particles having short range order. This interpretation will be discussed later in the discussion section.

Artificial ageing prior to thermal analysis results in the disappearance of the dissolution reactions occurring early in the continuous heating cycle (B_1 and B_2 <150°C) whilst the endothermic peak is more prominent and extends down to ~220°C (i.e. between D_1 and D_2). The change in shape of the endotherm from that of the as quenched material (D_2) on artificial ageing is also clearly evident in the previous studies of binary alloys. It is generally associated with the δ' dissolution although the reasons for the change in the peak shape have not been satisfactorily resolved. TEM observation showed that the δ' present after age-hardening remained essentially unchanged in size (~ 20 nm) during continuous heating up to 250°C in the DSC, although the volume fraction may have been reduced.

5.2.2. Aluminium-Lithium-Zirconium (Alloy A4)

The addition of 0.1 % Zr to the binary alloy gives rise to substantial changes in the thermal analysis traces (Figure 5.2). In the as quenched condition the low temperature exotherms and endotherms (< 150°C) seen in the binary alloy are no longer evident, but the exothermic reaction (C) at 170°C is much more pronounced. The endothermic reaction (D_2) associated with δ' dissolution is more symmetrical with the peak moving below 300°C to about 270°C. Again this δ' dissolution endotherm broadens with natural ageing and develops a plateau between D_1 and D_2 after artificial ageing extending down in temperature to ~220°C as observed in the binary alloy. Artificial ageing also substantially reduces the δ' formation exotherm (C) at 170°C.

The microstructural effects of zirconium are two fold. The solution treated microstructure is changed from the recrystallised equiaxed form of the binary alloy to an unrecrystallised structure containing subgrains and coherent $ZrAl_3$(β') particles. The latter act as excellent heterogeneous nucleation sites for δ' precipitation upon natural and artificial ageing (166). Other than that there were no

obvious differences in the δ' distribution compared to the binary alloy on artificial ageing at 185°C. However, TEM of samples heated in the DSC to 300°C and water quenched revealed that while much of the homogeneously nucleated δ' had dissolved and then reformed as a very fine dispersion during the quench, the δ' nucleated on the β' particles was retained.

5.2.3. Aluminium-Copper-Magnesium (Alloy A5 & A6)

Thermal analysis data from the Al-Cu-Mg system (having the same copper and magnesium content as AA 8091) is simpler in form (Figure 5.3). In the as quenched condition the alloy initially shows limited instability but then remains stable during continuous heating up to 200°C; the initial instability was found to be more evident in alloy A6 (having the same copper and magnesium content as AA 8090). An endotherm (E) peak at 220°C is followed by a substantial exotherm at 270°C (F). Similar observations have previously been interpreted (167) in terms of dissolution of GP zones and the subsequent precipitation of S' and S phases.

In the naturally aged condition the GP zones endotherm (E) is more pronounced as a result of the increased GP zone formation occurring during natural ageing (and association with substantial hardening of the alloy). Artificial ageing (8 hours at 185°C) completely suppresses further reaction during continuous heating to just under 400°C; complete precipitation of S phase had occurred during the ageing treatment. TEM observations (see Figure 5.4) were consistent with the DSC results. Alloy A6, having equivalent copper and magnesium concentrations to AA 8090 but without any lithium, showed identical features to alloy A5.

5.2.4. Aluminium-Lithium-Copper-Magnesium-Zirconium (Alloy A2)

Thermal analysis data from the quaternary alloy A2 of AA 8090 compositions are shown in Figure 5.5. In the as quenched condition the alloy showed signs of exothermic reactions at ~90°C (G) and 170°C (H) followed by an endothermic reaction having two maxima at 230°C (I) and 250°C (J). The dominant exothermic reaction (K) occurs at 320°C.

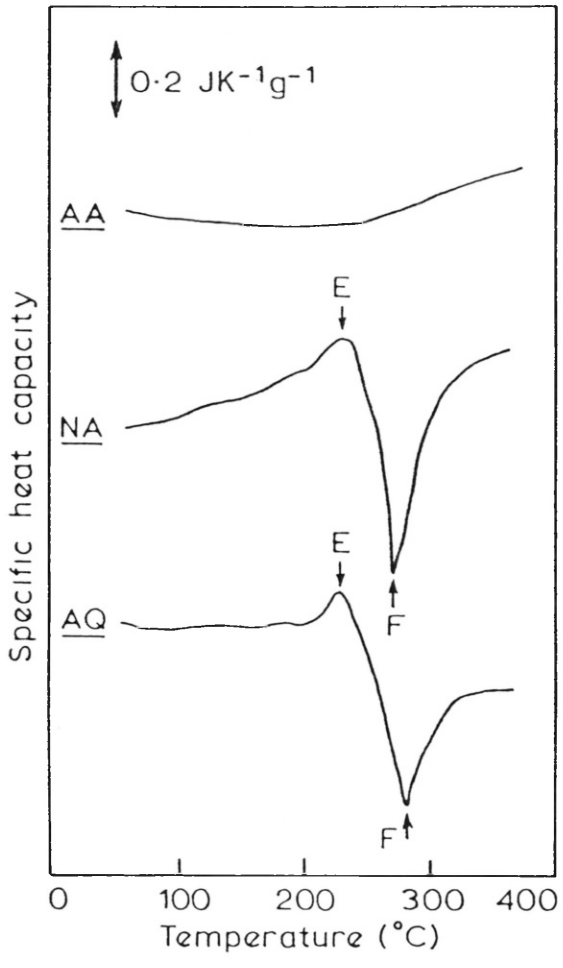
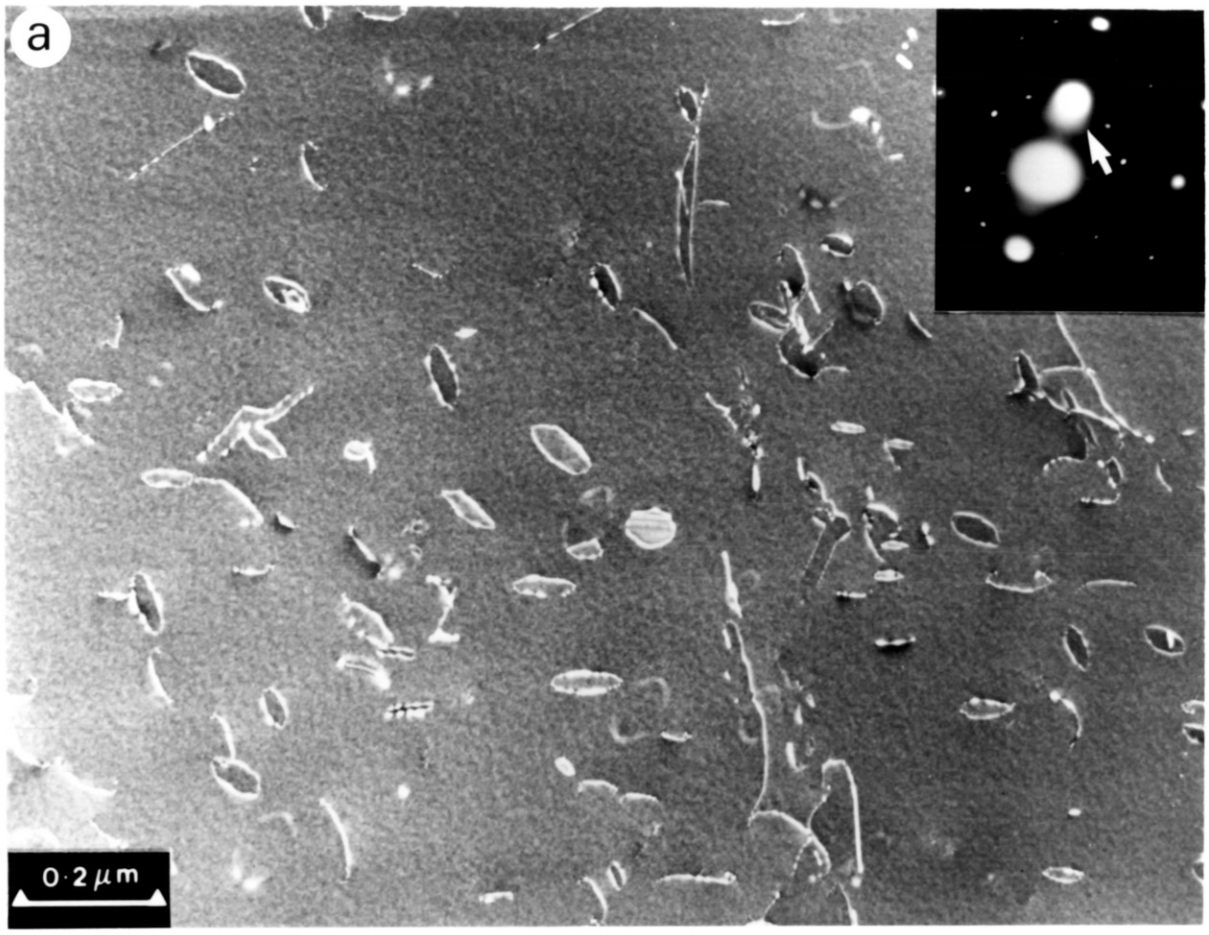
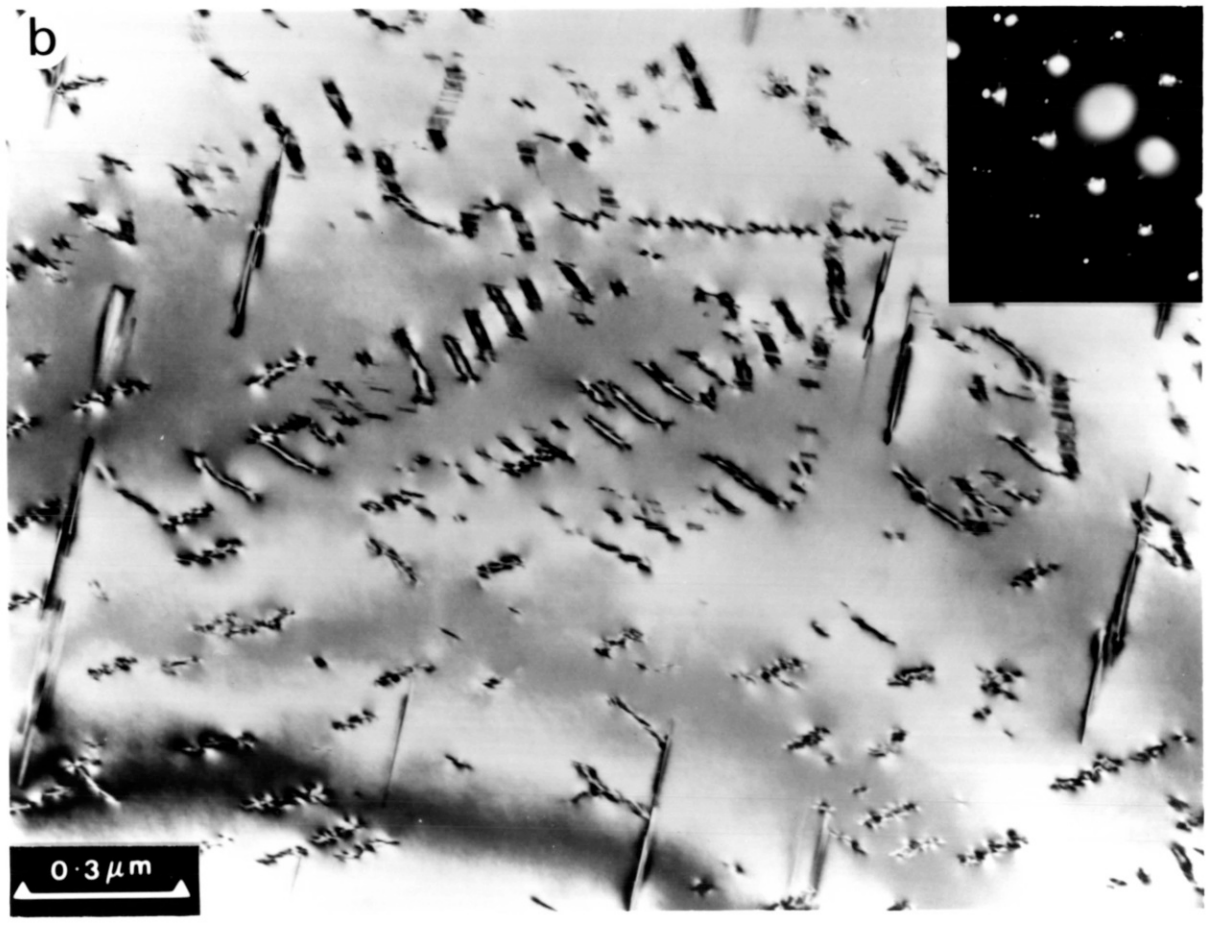


Figure 5.3. Specific heat capacity vs. Temperature curves for ternary Al-Cu-Mg system (alloy A5).

Figure 5.4. (a) TEM DF micrograph showing precipitation of dislocation loops in alloy A5. Material treatment: ST 540^{o}C and WQ(RT).

(b) TEM BF micrograph showing heterogeneous S precipitation in alloy A5; <110> Al orientation. Material treatment: ST 540^{o}C, WQ(RT), NA 1 month and AA 24 hours at 190^{o}C.


a
0·2 μm


b
0·3 μm

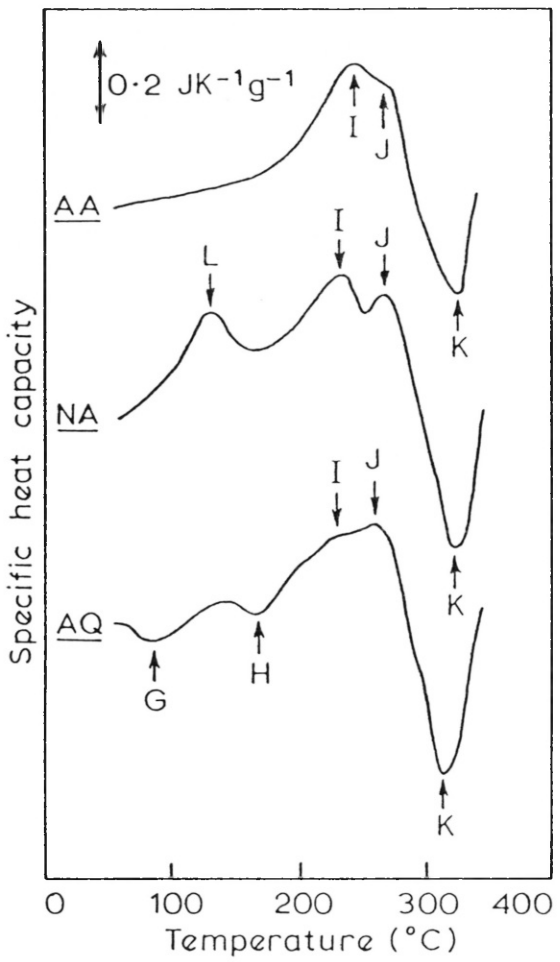


Figure 5.5. Specific heat capacity vs. Temperature curves for quaternary Al-Li-Cu-Mg-(Zr) system (alloy A2).

In the naturally aged condition the low temperature exothermic reaction (G) is replaced by a pronounced heat absorption process at 130°C (L). The endotherm labelled I is similar to that in the as quenched material, but the second peak (J) occurs at a position of lower specific heat. The exothermic reaction (K) is unaltered.

TEM studies revealed the presence of superlattice reflections in the as quenched material, and the individual δ' particles could be resolved in the naturally aged condition (as in the Al-Li-Zr alloy). During continuous heating up to 250°C, the δ' particles coarsened and the numbers of loops and helices increased, particularly in the previously naturally aged samples. At 270°C, there was an evidence of some δ' dissolution (this being delayed at the β' sites) together with S phase precipitation at dislocation sites and homogeneously throughout the matrix.

After artificial ageing low temperature reactions are suppressed but the endothermic reaction has a greater magnitude. 'J' is reduced to a point of inflection but the major exothermic reaction (K) remains unaltered by artificial ageing, even up to 72 hours at 190°C.

5.3. Discussion

5.3.1. Al-Li System

The exothermic shift in the specific heat at the start of the heating (A) of the as quenched materials indicates instability within the alloy. This would be consistent both with GP zone formation at room temperature proposed by Nozato and Nakai (10) and with δ' growth which is observed to occur in this alloy. The endotherm at 130°C (B) has previously been attributed to δ' dissolution (18) or GP zone dissolution (10, 17). Referring to the work of Baumann and Williams (164) shows, in agreement with Papazian et al (17), that even the small (~ 1 nm) δ' observed at room temperature will be stable against reversion to much higher temperatures (estimated to be ~170°C for a 2.5 wt % Li alloy). This view is reinforced by the observation of the same 130°C endotherm in naturally aged samples when the δ' is much larger (5 nm) for which reversion is predicted at a temperature close to the δ' solvus (~290°C). Therefore, it must be concluded that there is indeed a second metastable precipitate phase present in addition to the δ'. This may well be in the form of GP zones which are not imaged in TEM because of

the presence of the very fine δ' which dominates the microstructure. The results imply that δ' and GP zones grow competitively at room temperature since natural ageing enlarges the 130°C endotherm and is observed to produce larger δ' particles. The absence of the 130°C endotherm in artificially aged material implies that the GP zones have been completely replaced by δ'. This is consistent with the calculated GP solvus which lies well below 185°C (17).

The 170°C exotherm (C) has previously been attributed to δ' precipitation and the current results are in agreement with this view. Baumann and Williams proposed that δ' grows from that present as quenched: if so this should be a continuous process on heating. As the temperature rises the driving force for continued precipitation (i.e. the supersaturation) falls but the diffusivity rises; 170°C must represent the temperature at which these two factors result in a maximum precipitation rate.

The δ' dissolution peak at D_2 is above the δ' solvus, as expected for continuously heated material, and is possibly truncated at the high temperature end by the exothermic δ(AlLi) formation reaction. On ageing (natural or artificial) the peak broadens to a plateau between D_1 and D_2. As noted earlier, Nozato and Nakai attribute this to dissolution of δ' with short range order at D_1 and dissolution of more fully ordered δ' at D_2. Balmuth (18) implies that the dissolution temperature range reflects a range of particle sizes. Neither explanation is satisfactory. There is no evidence for differing degrees of order within δ' particles and in any case order should be increased by ageing. The calculation of Baumann and Williams (164) show that only very small δ' particles could dissolve at the temperature of D_1 (which is below the δ' solvus) as a result of capillarity and the particles present after ageing greatly exceed this value. Hence arguments based on a range of δ' sizes cannot be sustained.

The explanation for δ' dissolution moving to lower temperatures on ageing can be found by considering the concentrations of lithium remaining in solution compared with the position of the δ' solvus. In as quenched material a lower volume fraction of δ' is present on heating in the DSC above 185°C than in either of the other two cases. Hence the average concentration of lithium in solution is greater and closer to that of the δ' solvus: the driving force for dissolution of δ' is least. In the

artificially aged condition, the volume fraction of δ' should decrease by a factor greater than 2 between 200 and 250°C to maintain the equilibrium concentration of lithium in solution so there is the greatest driving force for dissolution in this condition. The TEM observations suggest a decrease in δ' fraction although remaining particles retain their size or even coarsen.

5.3.2. Al-Li-Zr system

The most surprising observation in this alloy is the total absence of the 130°C GP zone dissolution endotherm. If GP zone formation is competitive with δ' precipitation it is possible that either (i) the quench rate in this case was slow and more δ' formed on quenching, or (ii) more δ' formed on quenching as a result of nucleation on the β' and the supersaturation of lithium was thereby reduced sufficiently to inhibit GP zone formation at room temperature. However, no definite TEM observations have been made to support this suggestion. The more obvious δ' exotherm (C) is consistent with the growth of a larger number (or larger size) of δ' particles present as quenched. The remaining endothermic and exothermic behaviour is essentially similar to that reported and discussed for the binary alloy.

5.3.3. Al-Cu-Mg system

The results are broadly in agreement with those of Howe (167). The endotherm (E) observed and attributed to GP zone dissolution implies that their formation must have taken place during the quench. The slight exothermic instability observed in the present work below 100°C suggests continued formation of zones in this temperature range and this was, in fact, more significant with lower solute supersaturation.

5.3.4. Al-Li-Cu-Mg-Zr system

A notable feature in the quaternary system containing zirconium is the presence of an exotherm (G) at ~90°C. It would appear that this is an extension of the exothermic trend observed in the same temperature range in the Al-Cu-Mg alloys. It has no parallel in the Al-Li-Zr alloy system and it is presumably associated with the formation of the GP zones of the Al-Cu-Mg system. The results imply that the presence of lithium inhibits the formation of these zones during

quenching. The high vacancy-lithium binding energy (166) may reduce the free vacancy concentration and thus slow down the diffusion of solutes required for zone formation. Natural and artificial ageing eliminate this exotherm, presumably since GP zone formation is complete.

In the as quenched condition, the δ' exotherm observed in other lithium containing alloys is still present. It is followed by an endotherm (I) at ~230°C which corresponds to the lower temperature range δ' dissolution and GP zone dissolution in the Al-Cu-Mg alloys. The thermal fluctuation labelled J cannot be interpreted in the terms of a single reaction but must instead be considered as the result of the superposition of δ' dissolution and S precipitation reactions. Over the range of the exothermic peak (K), the S precipitation exotherm also overlaps at higher temperatures with the δ formation exotherm observed at about 330°C in the Al-Li-Zr alloy.

In the naturally aged condition, the most notable feature besides the disappearance of the exotherm (G) is the formation of the endotherm (L) at about 130°C. This is similar in form and position to that occurring in the Al-Li alloys and attributed to the dissolution of GP zones. Given the presence of Zr in the quaternary alloys, it is surprising that this peak is present since the zirconium removes it in the binary system. In that instance it was suggested that it might be due to preferential δ' formation during the quench reducing the driving force for GP zone formation. Magnesium is reported to reduce lithium solid solubility in aluminium and to restore the lithium supersaturation needed for GP zone formation in the quaternary alloy. However, it seems unlikely that the magnesium addition could effect a sufficiently large change. The role of zirconium in supressing the 130°C endotherm and of copper and magnesium in restoring it remains a matter of speculation.

Artificial ageing destroys the low temperature reactions leaving the dissolution peak (I); this must be associated with δ' dissolution and is unlikely to also involve GP zones of the Al-Cu-Mg system since artificial ageing is observed to promote the formation of S. However, after 8 hours at 185°C, TEM indicates that S precipitation is incomplete; further precipitation of S phase, is therefore, possible during DSC heating as evidenced by the continued presence of thermal fluctuation

(J) rather than the broad D_1-D_2 plateau of the Al-Cu-Mg alloys in which a similar artificial ageing has resulted a complete precipitation of S phase. The DSC results, therefore, provide additional evidence for the view that the presence of lithium delays the formation of S phase.

5.3.5. Natural Ageing Response of Al-Li-Cu-Mg-Zr Alloy

The natural ageing curve for alloy A2 (AA 8090 specifications) was shown in the previous chapter (see Figure 4.2). However, the characteristics of the ageing curve could not be explained because of lack of information on the exact precipitation reactions which occur within the material during natural ageing. The interpretation of the DSC data for the quaternary alloy A2 suggests that a number of factors contribute to the hardening of the material during natural ageing and they are as follows: growth of δ' particles, growth of GP zones of the binary Al-Li system and, nucleation and growth of GP zones of the ternary Al-Cu-Mg system.

Comparison of the natural ageing curve for binary Al-Li (alloy A3) with that due to quaternary alloy A2 suggests that during natural ageing the increment in strength due to the growth of δ' and that due to the GP zones of binary Al-Li system is insignificant. The superior natural ageing response of Al-Li-Cu-Mg system must be largely due to the development of GP zones of the Al-Cu-Mg system during room temperature ageing.

It should be recalled that within the as quenched microstructures of lithium containing aluminium alloys the vacancies are confined to the δ' particles and these vacancies are eventually freed as δ' grows during subsequent natural ageing treatment. These free vacancies are then available to promote the formation of GP zones of the Al-Cu-Mg system as well as the growth of the existing phases within the microstructure. The vacancy liberation is a sluggish process and this constitutes the incubation period being shown in the Figure 4.2. With continuing natural ageing more bound vacancies are released and as a result, formation and growth of GP zones of the Al-Cu-Mg system are accelerated. The rapid increase in strength after the incubation period demonstrates such a process. However, after about 1000 hours the hardness increases very slowly in Figure 4.2. This can be explained as follows. The number of free vacancies in solution will increase initially and will promote formation and growth of GP zones. However, because of the presence of

large numbers of sinks (in terms of loose dislocations, grain and subgrain boundaries) within the microstructure, together with the process of condensation of vacancies forming dislocation loops, the numbers of free vacancies will gradually decrease and so will the rate of diffusion. The latter is evidenced by the plateau after about 4000 hours.

5.4. Summary

1. Interpretation of DSC data for the quaternary Al-Li-Cu-Mg-Zr system is not possible in the absence of data for the constituent binary and ternary systems as a consequence of the overlapping of several exothermic and endothermic peaks.

2. DSC results are consistent with previous studies indicating the formation of GP zones in binary Al-Li alloys. The GP zones are formed simultaneously with the δ' during the quenching process and grow competitively with δ' during natural ageing. Upon artificial ageing at 190^{o}C, the GP zones are replaced by δ'; this is consistent with the GP zone dissolution temperature (~130^{o}C) obtained in this investigation together with the calculated GP zone solvus previously reported (17). It appears that zirconium supresses, and copper and magnesium restore Al-Li GP zone formation. The reasons for this are not clear.

3. Lithium slows down both the precipitation of Al-Cu-Mg GP zones during quenching and heterogeneous S phase during ageing compared with that in Al-Cu-Mg alloys. In the quaternary system, the formation and growth of Al-Cu-Mg GP zones can occur during natural ageing. However, the process is slow because the free vacancies required for rapid diffusion only become available as a result of growth of δ' particles which release the bound vacancies.

4. The natural ageing response in the quaternary Al-Li-Cu-Mg-Zr system is due to a combination of growth of δ' particles, growth of Al-Li GP zones, and formation and growth of GP zones of the Al-Cu-Mg system. Unlike the lithium free Al-Cu-Mg system, the natural ageing curve for the quaternary system is accompanied by an incubation period of about 24 hours; this is

attributed to the absence of a free vacancy supersaturation initially in solution to allow rapid diffusion. However, in common with the natural ageing curves for other aluminium alloys, the present ageing curve also terminates to a plateau (after ~4000 hours). This is attributed to the loss of free vacancies via annihilation in sinks together with vacancy condensation forming dislocation loops.

CHAPTER SIX

AS CAST MICROSTRUCTURE AND HOMOGENISATION

6.1. Introduction

Materials for extrusion work were received in the form of DC cast billets. Initially, it was therefore, necessary to characterise the cast microstructure and to develop a homogenisation schedule for the cast material.

Under industrial conditions, equilibrium crystallisation of solid solution is never achieved and this results in non-equilibrium changes within the materials viz. dendritic segregation (coring) and crystallisation of excess phases from the melt (whilst, no such phases exist under equilibrium conditions) with the structure of the alloy changing from single phase to multiphase. These non equilibrium changes, unless removed from the material, can cause serious problems during thermal or mechanical processing of the material and the inevitable result is poor mechanical properties of the products. Clearly, elimination of the structural defects present within the cast material is necessary and this is usually carried out via the process of homogenisation. Homogenisation involves dissolution of non equilibrium excess phases together with equilisation of concentration inside grains of solid solution. The selection of homogenisation temperatures depends on the solidus point of the material whilst the annealing time required for complete homogenisation depends on the size of the excess phase particles and that of dendritic cells. The annealing time may be reduced by suitably raising the temperature for homogenisation. From the commercial point of view, accordingly, a compromise between the homogenisation temperature and time is always made. In lithium containing aluminium alloys where lithium loss by oxidation at high temperature is a crucial factor, optimisation of the homogenisation schedule appears to be extremely important.

The work presented in the following sections is initially concerned with the morphology, composition and the crystallographical details of the phases present within the cast material (i.e alloy A1) following determination of the solidus point of the alloy via thermal analysis and design of an optimum homogenisation schedule for the cast material.

6.2. Results

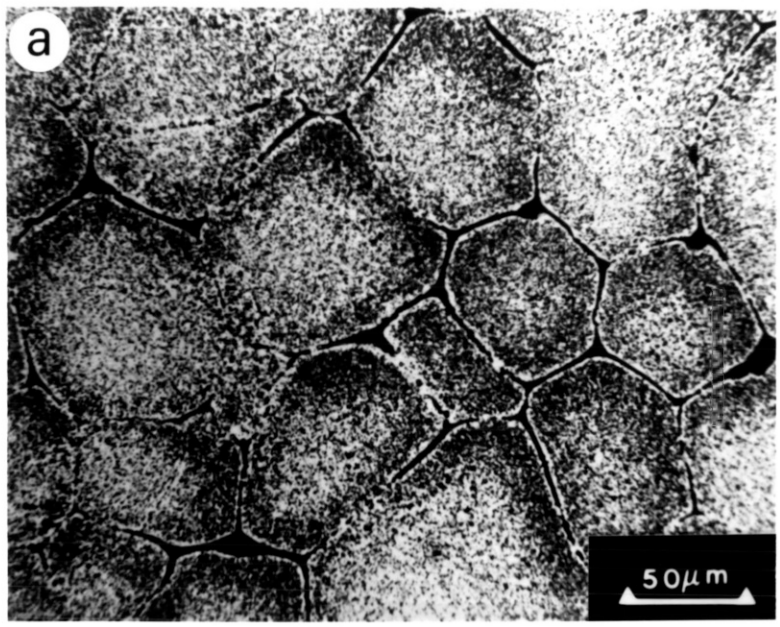
6.2.1. Characterisation of As Cast Microstructure

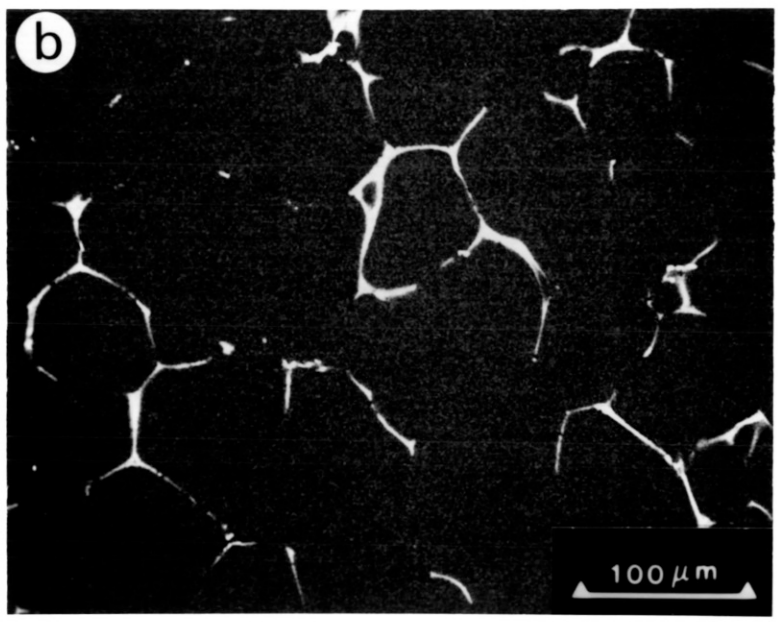
Figure 6.1(a) shows a light micrograph of the cast material. The Figure reveals that the material has an equiaxed grain structure and during solidification elemental partitioning has occurred resulting in second phase precipitation within the grains as well as at the boundaries between the grains. The striking feature of the microstructure is the absence of a dendritic structure which is typically observed in most of the cast microstructures. It implies that the particular rapid cooling practice adopted during casting controlled the grain size principally by causing dendrites to break up thus multiplying the numbers of seed crystals giving rise to an equiaxed grain structure. The average grain size was found to be ~90 microns. The precipitate size within the grains is much finer. On the other hand, second phase precipitation has occurred forming a continuous thick precipitate layer along the grain boundary. In the following subsections, the precipitates present at the intergranular sites (designated as "Grain Boundary Phases") and those within the grains (designated as "Matrix Phases") are described separately.

6.2.1.1. Grain Boundary Phases

Figures 6.1(b) and (c) show scanning electron micrographs of the cast microstructure in the secondary electron mode and in the back scattered electron mode respectively. Figure 6.1(b) shows the extent of intergranular precipitation of the second phase particles whilst Figure 6.1(c) reveals that there are two distinct phases at the grain boundary (labelled P1 and P2). The first phase P1 (the larger of the two and which appears mottled) is always present in the form of a divorced eutectic along the grain boundary interfaces but at the triple point junctions the phase is contained in what resembles a lamellar eutectic. A similar eutectic structure is better illustrated in Figure 6.2(a). Recently Smith (168) suggested that the dark features (of lamellar eutectic appearance) at the triple point junctions might possibly be mere surface depressions produced due to preferential dissolution of specific particles during etching. However, in the present investigation, as-polished samples were examined and the presence of features like lamellar eutectic at the triple point junctions was common. Comparison of Figure 6.2(a) with the

Figure 6.1. Microstructures of the as cast material (alloy A1)
(a) Light micrograph
(b) An SEM micrograph imaged in the secondary electron mode
(c) An SEM micrograph imaged in the back scattered mode.


a
50μm


b
100μm

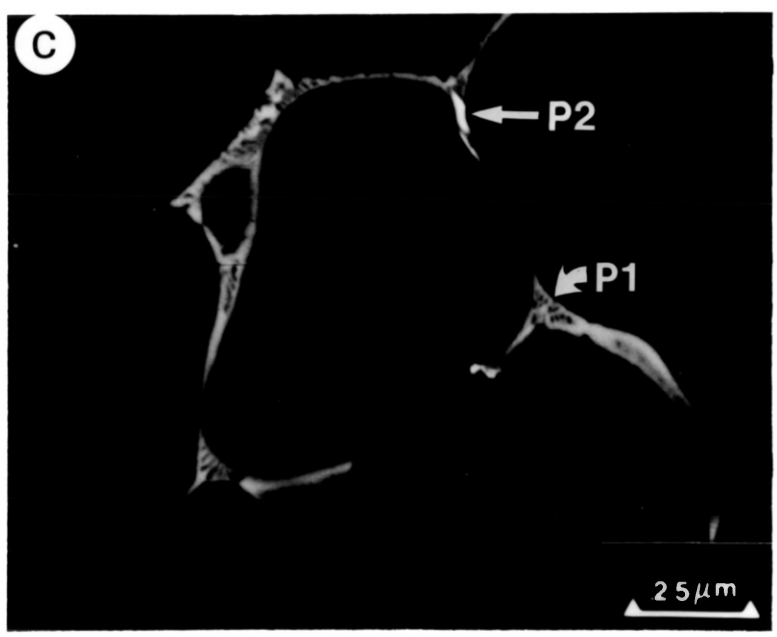
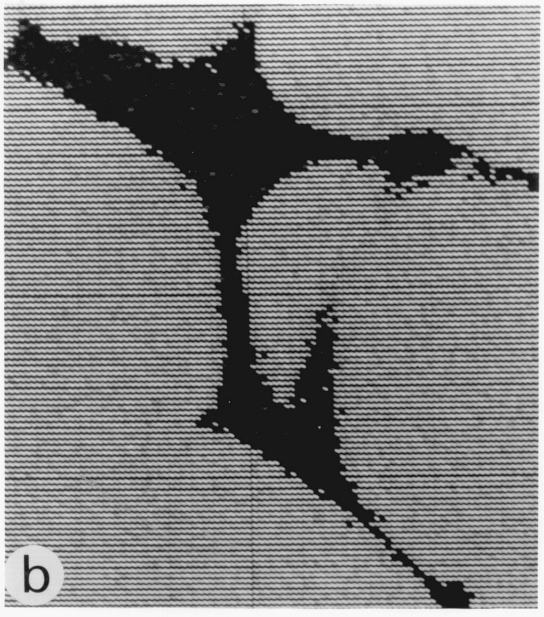
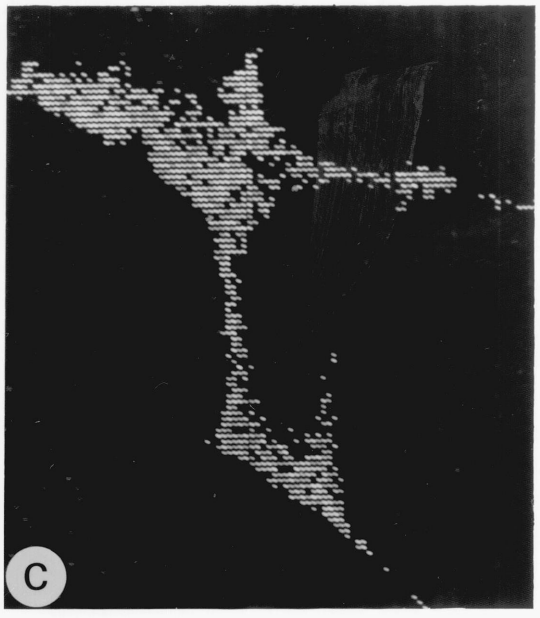
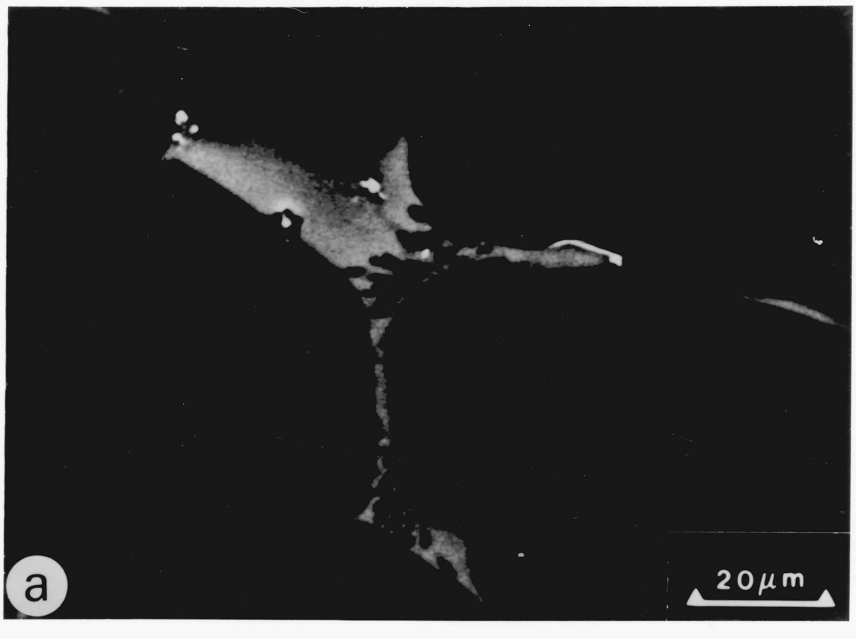
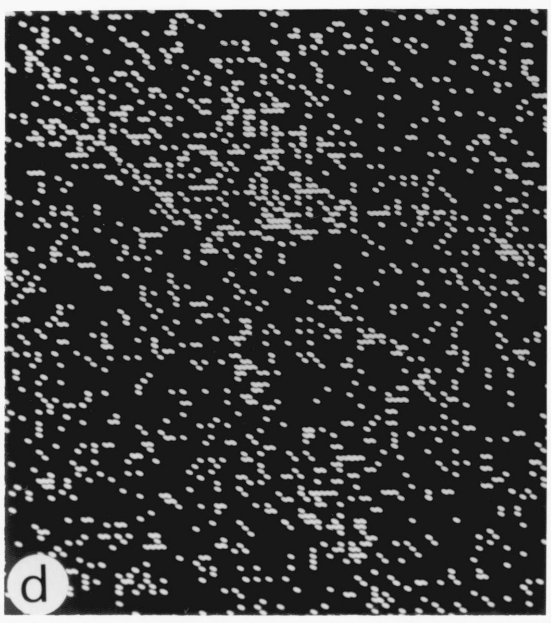

c
P2
P1
25μm

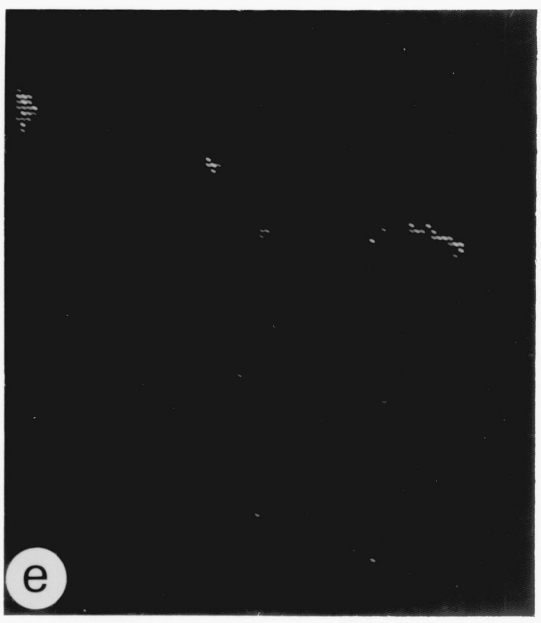
Figure 6.2. (a) An SEM micrograph in the back scattered mode showing the phases at the grain boundary triple point junctions.
(b) - (e) Element X-ray maps of 6.2(a); (b) Aluminium, the count level is adjusted to show only the matrix aluminium distribution, (c) copper (d) magnesium and (e) iron.


b


c


a
20μm


d


e

SEM micrograph of the same area in the secondary electron mode together with the element digimapping of the same region [shown in Figures 6.2(b) - (e)] revealed that the oval shaped dark features at the triple point junctions are not due to surface depressions; the lamellar eutectic at the triple point junctions may, therefore, be considered to consist of α(aluminium) and P1 phase.

The other grain boundary phase P2 which appears bright in the back scattered mode (see Figures 6.1(c) and 6.2(a)) was found to be unevenly distributed and was always present in small volumes; the P2 phase mainly possessed a plate like morphology although it was also present in the form of a small round precipitate.

Element digimapping together with x-ray EDS analysis of P1 and P2 phases revealed that P1 is a copper rich Al-Cu-Mg based phase whilst P2 is an iron rich Al-Fe-Cu based phase. The composition of P1 phase was found to be two fold: along the grain boundary interfaces P1 phase had a composition range of 16-18 % copper, 4-5 wt % magnesium and balance aluminium whilst at the triple point junctions P1 had an average composition range of 24-26 % copper, 6-8 % magnesium, ~1 wt % silicon and balance aluminium. The composition range for P2 was found to be 15-16 % iron, 7-9 % copper, 3-4 % magnesium, ~1 wt % silicon and balance aluminium. In the literature, no reference of any iron rich phase containing magnesium is available; it is suspected that the smaller volume of P2 phase in this material together with its presence in association with Al-Cu-Mg based P1 phase made the analysis erroneous; the exact composition of P2 phase remained, therefore, unknown.

It may be recalled that using energy dispersive x-ray analysis facility, detection of elements having atomic number less than 11 can not be made. Lithium (atomic number 3) is, therefore, undetectable using this equipment and hence the compositions specified above exclude this element, although a normalised (100 %) read out was always given. The next step of this investigation was, therefore, concerned with the detection of lithium, if present within the grain boundary phases via secondary ion mass spectroscopy (SIMS). Line scan data of the cast material are presented in Figure 6.3. The Figure shows that all the major alloying elements including lithium are segregated at the grain boundary with copper being present in the highest concentration (compare the relative peak intensity).

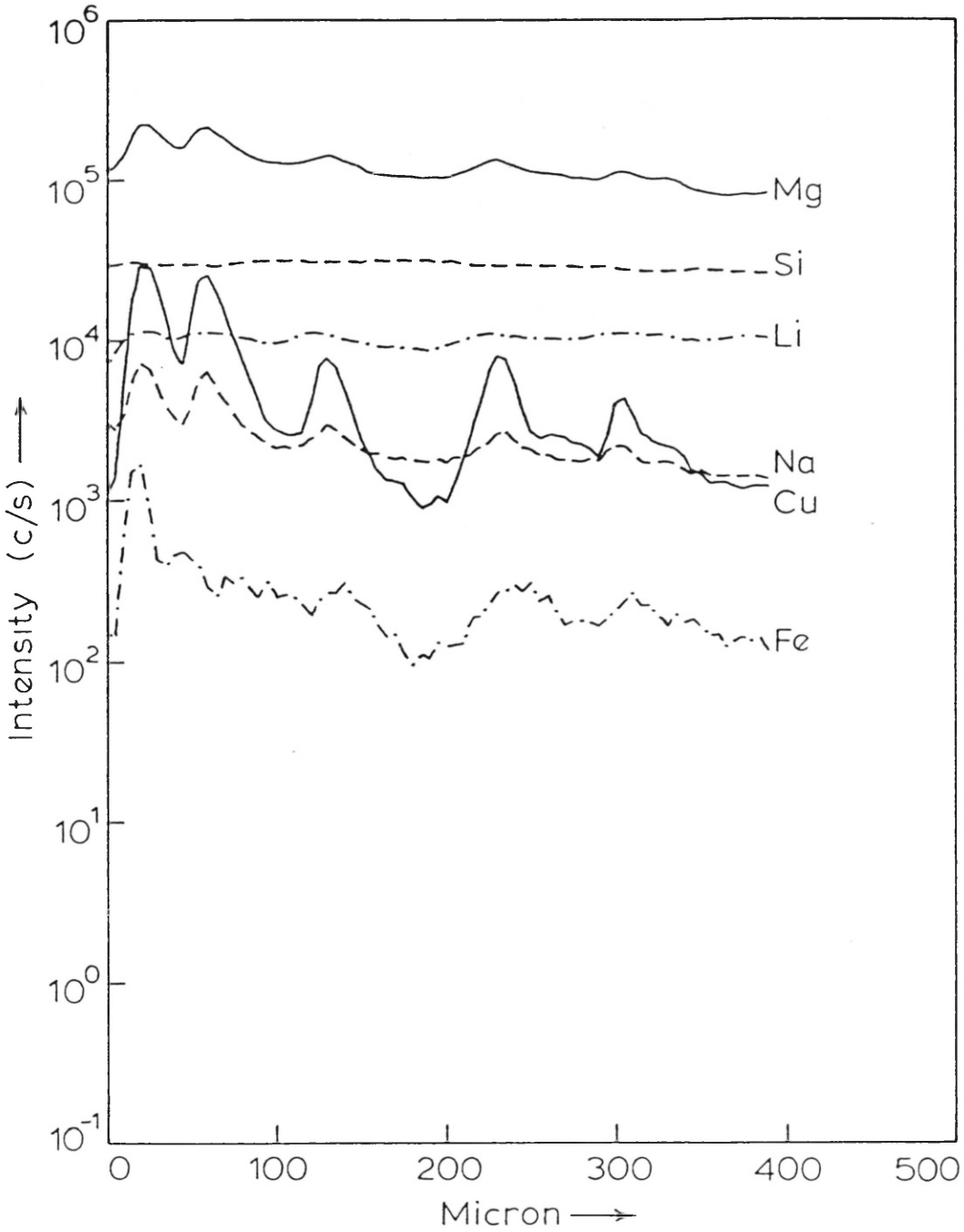


Figure 6.3. Secondary Ion Mass Spectrometry (SIMS). Line scan traces showing the distribution of elements at the grain boundaries of the cast material A1.

Figure 6.4. Element SIMS maps of the grain boundary phases in cast material A1. All images are from the same area.

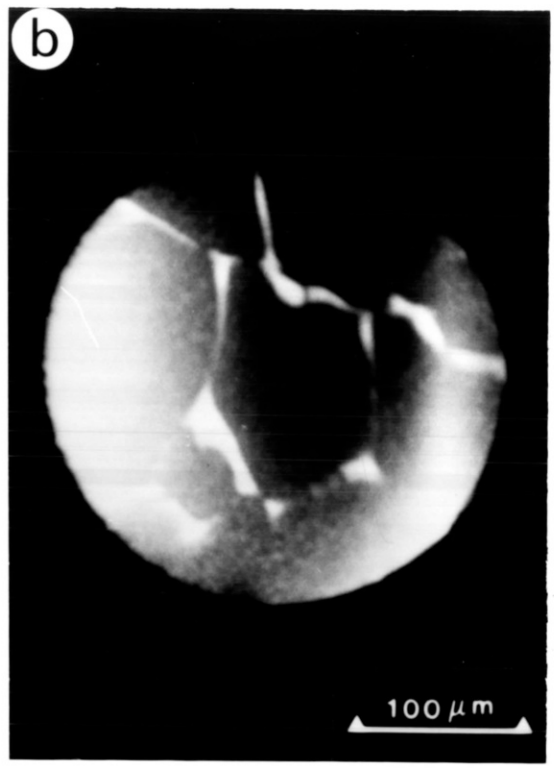
(a) Copper, 63 $_{Cu}^{+}$

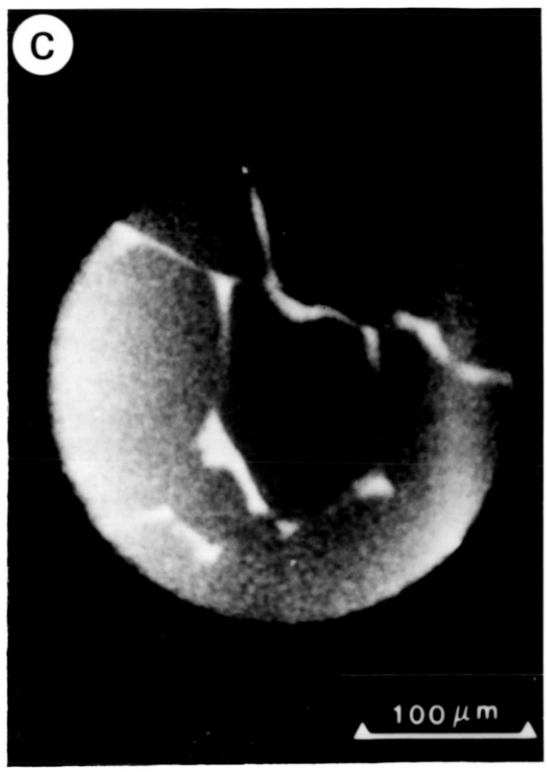
(b) Lithium, 7 $_{Li}^{+}$

(c) Magnesium, 24 $_{Mg}^{+}$

(d) Iron, 56 $_{Fe}^{+}$


a
100 μm


b
100 μm


c
100 μm


d
100 μm

Amongst the impurities, iron was evident, whilst the horizontal intensity line due to silicon ruled out the presence of any major silicon rich phase at the grain boundary as well as limiting the possibility of its association with other grain boundary phases; such an inference is justified in view of a low level of silicon present in the cast material together with the x-ray EDS analysis of the grain boundary phases reported earlier in this section. The line scan data also revealed the large scale segregation of tramp elements to the boundaries. Figure 6.3 demonstrates that even within a clean alloy such as the present material, sodium segregation to grain boundaries can be readily detected using this technique. SIMS ion micrographs due to the major alloying elements (viz. lithium, copper and magnesium) together with iron are presented in Figure 6.4; the Figure shows the distribution of alloying elements within the grain boundary phases. In accordance with the line scan data (Figure 6.3), Figure 6.4 reconfirmed the presence of lithium at the grain boundary implying that the P1 phase contains substantial amounts of lithium and is a quaternary Al-Cu-Li-Mg phase. Examination and comparison of the SIMS ion micrograph of iron with that due to lithium and magnesium suggested that the iron rich phase P2 contains neither of these two elements.

In order to establish the crystallography of the grain boundary phases thin foils of the cast material were prepared for examination by transmission electron microscopy (TEM). Figure 6.5(a) shows two grain boundary particles (labelled G_1 and G_2) sitting close to one another. Quantitative x-ray EDS analysis from these particles showed that both are Al-Cu-Mg based phase having composition as follows: 17.0 % copper, 3 wt % magnesium and balance aluminium (G_1), and 16 % copper, 4 wt % magnesium and balance aluminium (G_2). A typical diffraction pattern due to particle G_1 is shown in Figure 6.5(b); the diffraction pattern was found to be consistent with a face centered cubic structure with a lattice parameter a_o = 19 Å. Figure 6.5(c) shows another pair of intergranular particles. Quantitative x-ray EDS analysis from the particle G_3 suggested that it is also an Al-Cu-Mg based phase having 15 % copper, 5 wt % magnesium and balance aluminium. A typical diffraction pattern from G_3 is shown in Figure 6.5(d); the diffraction pattern was consistent with a face centered cubic structure with a lattice parameter a_o = 26.0 Å. In the present investigation, a few more grain boundary precipitates were examined. The composition range of these precipitates were found to be 15-18 % copper, 3-5 wt % magnesium and balance aluminium, and it was found that all these precipitates could be indexed as F.C.C. with lattice parameter a_o ranging from 19 to 26 Å;

Figure 6.5. TEM micrographs of the grain boundary phases in cast material A1

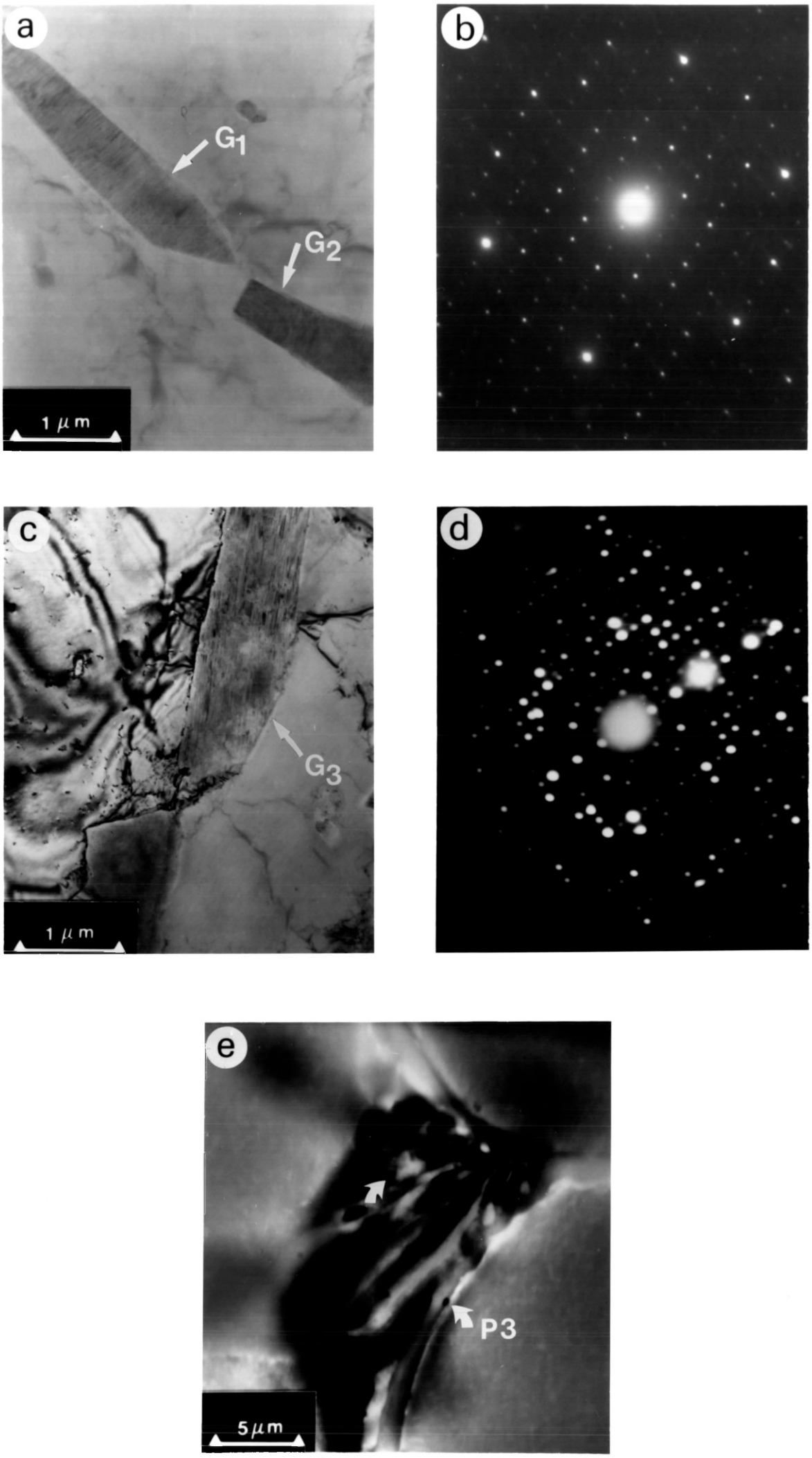
(a) BF micrograph showing grain boundary particles (labelled G_1 and G_2)

(b) SADP from particle G_1; close to [013] FCC. $L\lambda$ = 42.44 mm Å.

(c) BF micrograph showing grain boundary particles (labelled G_3).

(d) SADP from G_3; close to [100]FCC. $L\lambda$ = 398 mm Å.

(e) BF micrograph showing lamellar eutectic and silicon rich phase, P3 (shown by arrows) at the grain boundary triple point junctions.


a
G1
G2
1 μm
b
c
G3
1 μm
d
e
P3
5μm

although, no two different diffraction patterns due to the same particle could be indexed both as F.C.C. A regular feature of all the grain boundary particles was that they always contained planar defects running normal to the length of the particles. The nature of such defects (which was also observed later within the matrix precipitates) is illustrated in section 6.2.1.2.

Figure 6.5(e) represents a TEM micrograph of the triple point junctions. The lamellar eutectic at the triple point junctions may clearly be noted. Quantitative x-ray EDS analysis suggested that this region has an average composition of 24 % copper, 8 % magnesium, ~3 % silicon and 66 wt % aluminium. The analysis carried out at the same area using bulk samples on SEM (reported earlier in this section) was identical to the present analysis except that the present analysis shows relatively higher percentage (3 wt % compared to ~ 1 %) of silicon. Close examination of Figure 6.5(e) revealed that very small dark precipitates (shown by arrows) are present at the triple point junctions. X-ray EDS microanalysis suggested that these precipitates (P3) had an average composition of 18 % copper, 8 % silicon, 3 wt % magnesium and balance aluminium. The precipitates were smaller in volume and were sitting in the thicker region of the foil in association with the lamellar eutectic at the triple point junctions; it is suspected, therefore, that due to phase overlap the analysis might be erroneous and the actual silicon content may be very high within these precipitates. Attempts to obtain suitable diffraction patterns from these particles were also not successful due to the reasons specified above.

It may be recalled that lithium could not be analysed using x-ray EDS; but, in view of the SIMS analysis on the grain boundary phases presented earlier in this section it is clear that all the grain boundary phases (except P2 phase) contain various amounts of lithium.

6.2.1.2. Matrix Phases

Within the matrix of the as cast material, a fine dispersion of particles was found (Figure 6.6(a)). The precipitates possessed either a plate or a rhombohedral morphology. Figure 6.6(b) shows a typical rhombohedral shaped particle. As with the grain boundary particles one of the most regular and striking feature was that all particles displayed gross structural inhomogeneity. High resolution images

Figure 6.6. Details of matrix phases in cast material A1.

(a) BF micrograph showing distribution of matrix phases.

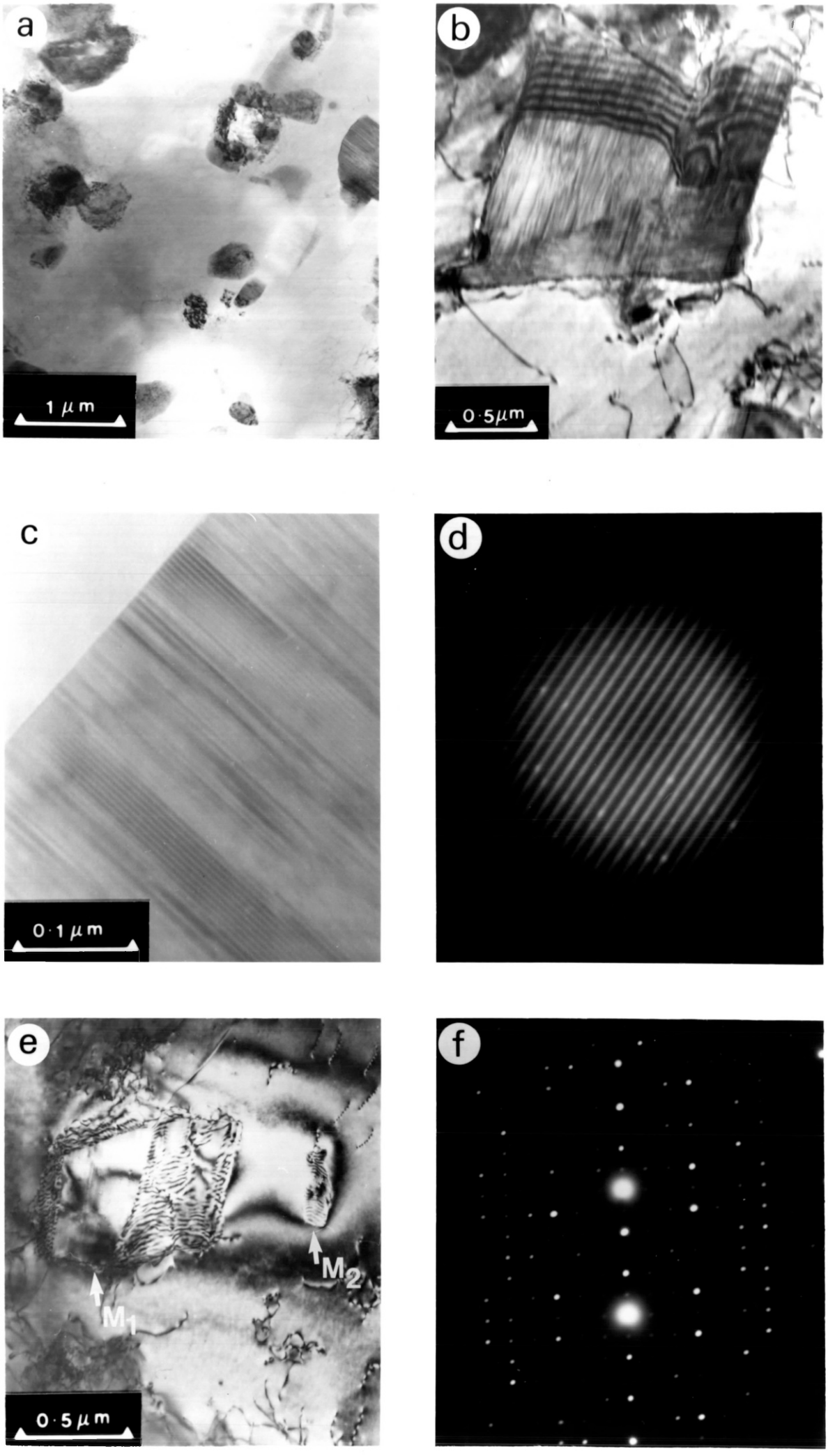
(b) BF micrograph showing a typical rhombohedral shaped particle.

(c) High resolution image revealing modulation of planar defects normal to the length of a particle.

(d) SADP of 6.6 (c); streaking about the diffraction spots due to planar defect structure.

(e) Matrix Particles (labelled M_1 and M_2)

(f) SADP from M_1 of 6.6(e); close to [100] FCC. $L\lambda$ = 42.44 mm Å


a
1 μm
b
0·5μm
c
0·1 μm
d
e
M2
M1
0·5 μm
f

(Figure 6.6(c)) showed a modulation of planar defects running normal to the length of the precipitates. The period of the planar defect was found to be of the order of 24 Å. Selected area diffraction patterns such as that in Figure 6.6(d) detail the defect structure, which is displayed as a series of parallel streaks normal to defect planes in the particle. Quantitative x-ray EDS analysis, suggested that these precipitates were Al-Cu-Mg based phases having a composition range of 15-19 % copper, 2-5 wt % magnesium and balance aluminium. No other type of precipitate phase was recognised within the matrix which had a composition beyond this specified range. Figure 6.6(e) shows a pair of plate shaped particles (labelled M_1 and M_2). A typical diffraction pattern from M_1 is shown in Figure 6.6(f); the diffraction pattern was consistent with a face centered cubic structure with a lattice parameter a_o = 19.33 Å. A series of other diffraction patterns were produced by tilting the particle M_1, but the patterns were not found to be consistent with the F.C.C. structure. Diffraction patterns from a few other particles were examined and it was found that these could be indexed as F.C.C. with lattice parameters ranging from 18.5 to 20.0 Å. The diffraction patterns could not be indexed conclusively as cubic or hexagonal and hence it would appear that these particles have either a tetragonal, orthorhombic or other low symmetry structure.

6.2.1.3. Homogenisation

Figure 6.7 shows the thermal analysis curve for the present cast material as determined by differential scanning calorimetry. The Figure reveals a pronounced dissolution peak at about 547^{o}C. Up to 600^{o}C no further change was observed in the DSC curve. Unfortunately, from the safety point of view, the particular DSC equipment could not be used beyond 600^{o}C. In order to examine the thermal behaviour of the cast material above 600^{o}C, the material was examined in a DTA (differential thermal analysis) unit. The DTA curve (not presented here) showed a pronounced dissolution peak at about 622^{o}C implying that the material starts to melt at this temperature. These results imply that although the actual melting point (i.e. the equilibrium solidus point) of the material is high, the material has a non equilibrium solidus point at about 547^{o}C; consequently, the homogenisation temperature for the cast material cannot exceed 547^{o}C if partial melting within the material is to be avoided. In order to check this theory, the cast material was annealed at 550^{o}C for a few hours. The corresponding light microstructure is

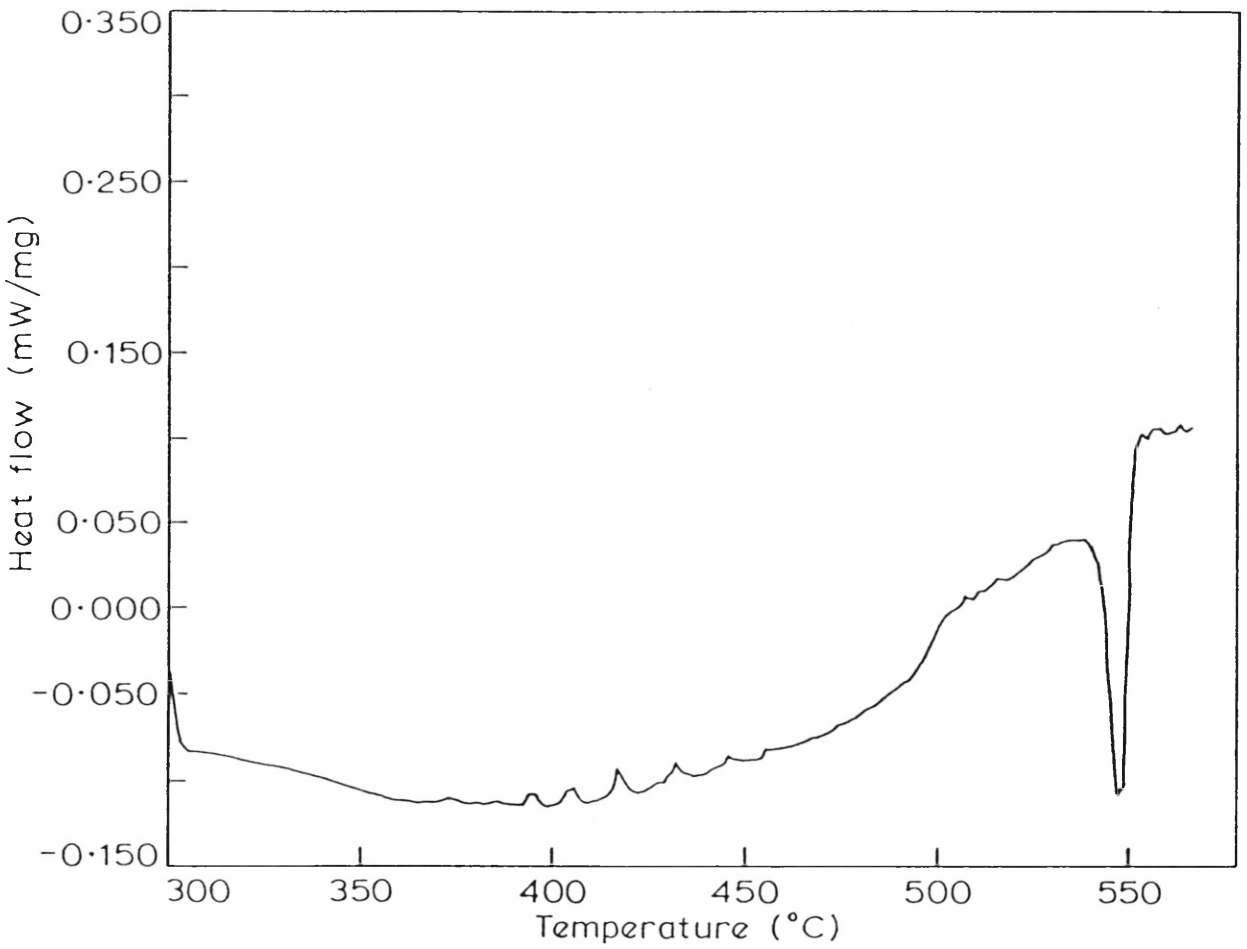


Figure 6.7. DSC trace of the cast material A1.

presented in Figure 6.8(a). The Figure clearly reveals that partial melting has occurred within the material but an interesting observation is that the melting is confined only to the triple point junctions of the cast microstructure. The significance of such an observation will be discussed later in the discussion section.

Light micrographs of the cast material when annealed at different temperatures and times are presented in Figures 6.8(b-d). The Figures demonstrate the change in microstructure of the material during homogenisation treatments; a gradual reduction in the volume of the intergranular phase fraction with increasing homogenisation temperature and time may clearly be noted. Figure 6.8(d) suggested that the material becomes almost completely homogenised when annealed at 537^{o}C for 24 hours. The corresponding TEM micrograph in Figure 6.9(a) reveals a very clean microstructure showing grain boundaries free of any precipitation and the absence of intergranular cast phases. Only an uneven distribution of very fine β' (Al_3Zr) particles is present within the grains.

Although Figure 6.9(a) did not show the presence of any grain boundary precipitation, detailed microstructural studies of the wrought (extruded) material carried out later in this investigation showed that the iron bearing phases P2 survived the homogenising annealing treatment and remained mainly at the original grain boundaries. Figure 6.9(b) shows such an iron bearing phase within the wrought material. A typical diffraction pattern due to this particle is also shown in Figure 6.9(c). Quantitative x-ray EDS analysis indicated that the particle had a composition of 22 % iron, 7 wt % copper and balance aluminium. The diffraction pattern was found to be consistent with an orthorhombic structure.

6.3. Discussion

6.3.1. Grain Boundary Phases

Table 6.1 summarises the composition of all the phases found in the present cast material. The summary reveals that the composition of P1 phase is two fold such that along the grain boundary interfaces the phase contains much less copper and magnesium compared to that present at the triple point junctions; it is evident, therefore, that the Al-Cu-Li-Mg based phases present along the grain boundary interfaces (viz. P1(I)) and that at the triple point junctions (viz. P1(T)) are not the same phase.

Figure 6.8. Light micrographs showing the effect of annealing temperatures and times on the cast material A1. The heat treated materials were air cooled. Material Treatment:

(a) 8 hours at 550°C

(b) 10 hours at 525°C

(c) 8 hours at 537°C

(d) 24 hours at 537°C

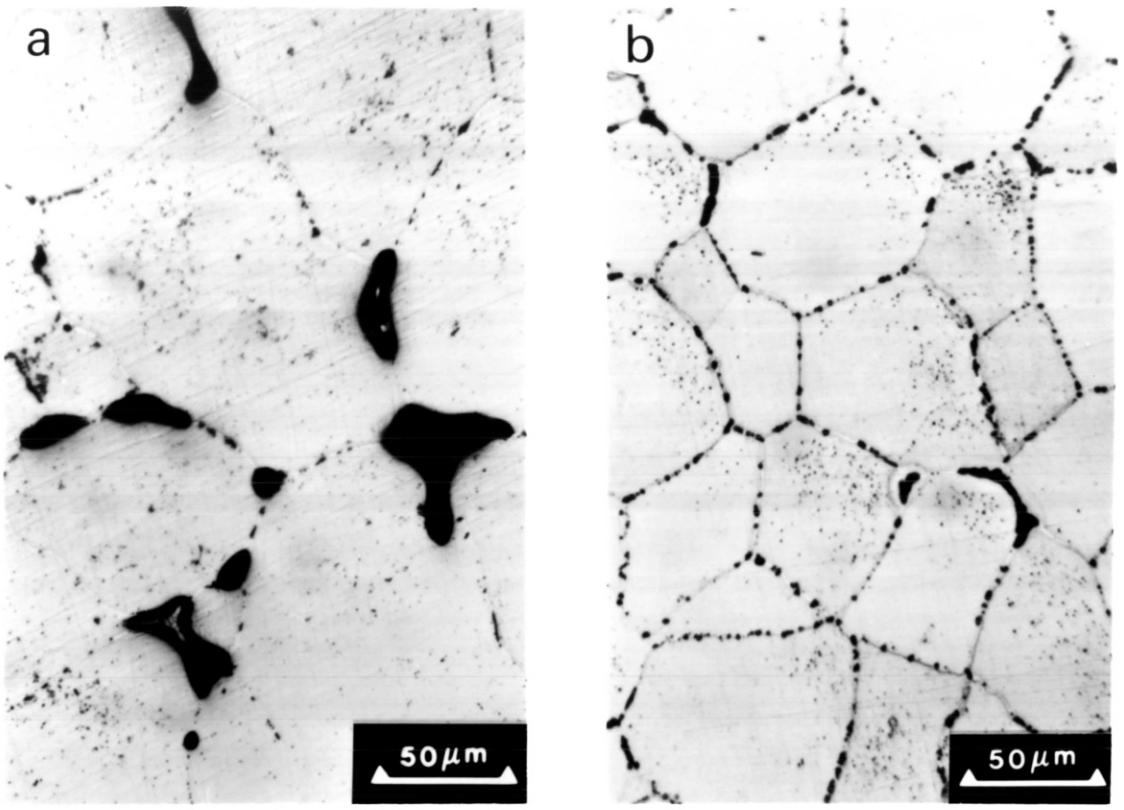

a
50μm
b
50μm
c
50μm
d
100μm

Figure 6.9. (a) BF micrograph of the homogenised material
(b) BF micrograph showing an Al-Fe-Cu based particle at the grain boundary of the wrought structure.
(c) SADP from the Al-Fe-Cu based particle of 6.9(b); close to [001] orthorhobmic; $L\lambda = 47.75$ mm Å.
(d) BF micrograph showing matrix particles in cast material A1.
(e) SADP from particle M3 of 6.9(d); close to [034] orthorhombic. $L\lambda = 42.24$ mm Å.
(f) SADP from particle M3 of 6.9(d); close to [001] orthorhombic; $L\lambda = 42.24$ mm Å.

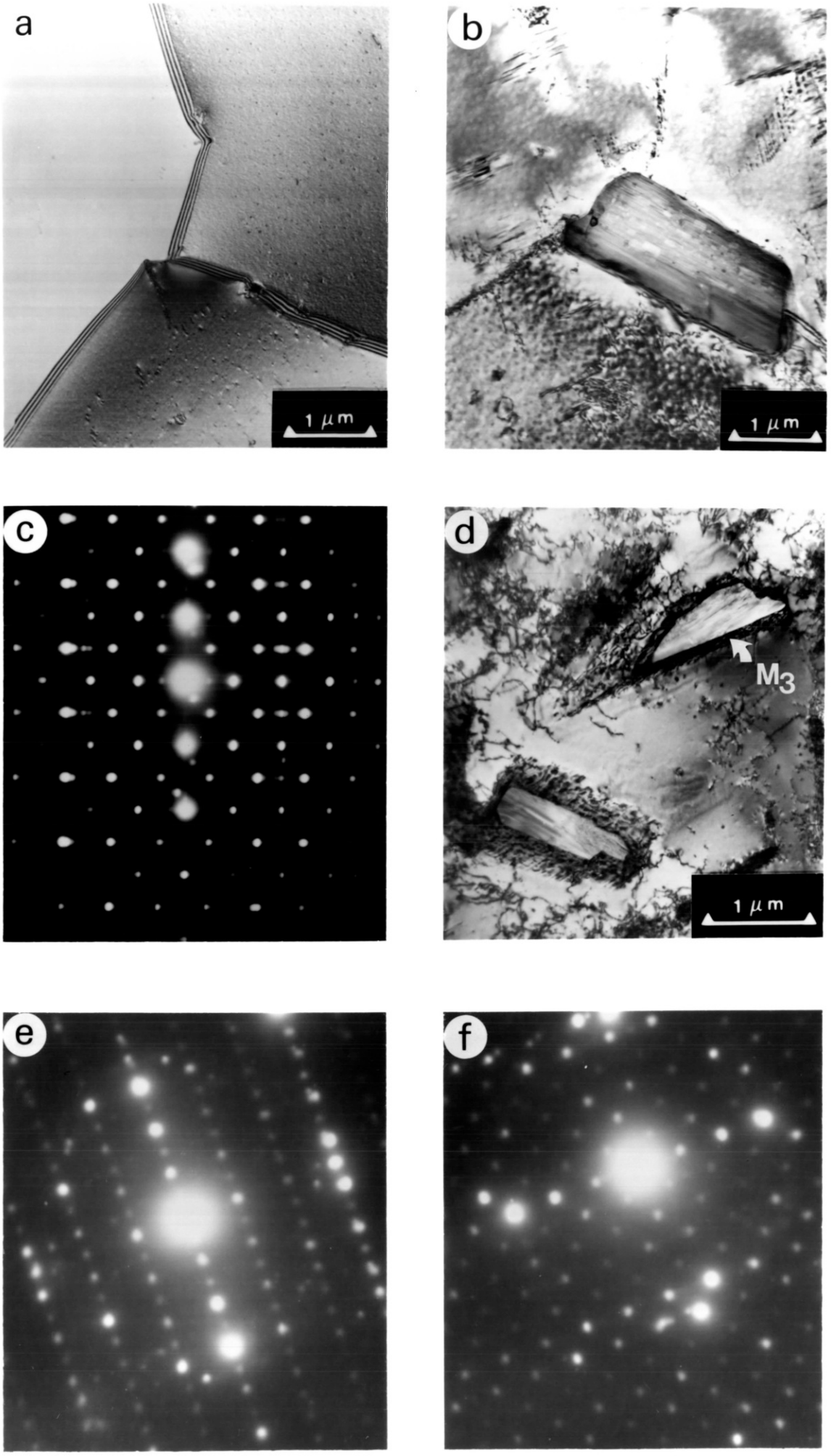

a
1 μm
b
1 μm
c
d
M3
1 μm
e
f

Table 6.1. Phases Detected in the Cast Material A1

Phases present at the Grain Boundary	Composition, wt % (balance aluminium)				
	Copper	Magnesium	Iron	Silicon	Lithium
1. P1 (i) P1 (T) At the triple point junctions	24-26	6 - 8	Nil	1 - 3	Not determined
(ii) P1 (I) Along the grain boundary interfaces	15-18	3 - 5	Nil	~ 1	Not determined
2. P2	7 - 9	3 - 4	15-16	~ 1	Not present
3. P3	18	3	Nil	8	Not determined
Phases Present in the Matrix					
1. P4	15-19	2 - 5	Nil	Nil	Not determined

The P1(T) phase observed in this investigation is identical in morphology and chemical composition to that examined by Owen et al (113) using backscattered electron analysis and x-ray EDS microanalysis. The analysis for the P1(T) phase bears a striking resemblence to the T_2 (Al_6CuLi_3) phase (26.9 % copper, 8 % lithium and balance aluminium) as identified by Hardy and Silcock (39). A similar analysis has been performed on an as cast alloy (Al-2.5 Cu - 3 Li - 1.4 wt % Mg) by Dubost et al (169); their alloy contained an interdendritic phase of composition 29 % copper, 6.5 wt % magnesium as determined by EPMA. SIMS analysis revealed traces of lithium in the compound and so they considered it to be an extension of the ternary T_2 phase (28.8 % copper, 9.6 % lithium) with magnesium atoms substituting for lithium up to the compound formula T_2 ($Al_6CuLi_{3-x}Mg_x$) with $x \leq 1$. Owen et al (113) used x-ray EDS and a backscattered electron image contrast technique to analyse this phase in an AA 8090 alloy; the authors measured the atomic number of the phase and found it to be 17.0 and found the phase to contain 29 % copper and 9 wt % magnesium. The computed atomic number of the T_2 phase (based on the composition of T_2 phase reported by Hardy and Silcock) is 16.0, and that of T_2 phase (reported by Dubost et al) with magnesium atoms substituted for lithium is between 16.0 and 17.0. Therefore, the P1(T) phase found in this investigation could be considered as an extension of the T_2 phase. Such an interpretation is further supported by the DSC results of the cast material reported earlier in section 6.2.1.3. The present cast material has a non equilibrium solidus point at ~547^{o}C such that partial melting occurred within the material when the material was heated above 547^{o}C; but melting was only confined to the triple point junctions [Figure 6.10(a)] which is coincident with the sites for the P1(T) phase. Rao and Sekhar (170) have recently reported that the T_2 phase (27.9 % copper, 6.07 % Lithium and balance aluminum) undergoes melting at 545^{o}C. It would, therefore, appear from the three independent analysis techniques viz. x-ray EDS, SIMS and DSC that the P1(T) phase closely resembles the T_2 phase with magnesium atoms subsituting for lithium atoms in varying amounts up to a concentration of 8 %. The microstructural form of the P1(T) phase additionally suggests that it forms together with α aluminium and the Si rich phase by a ternary eutectic reaction in these Al-Li-Cu-Mg alloys; the solidification path clearly misses the eutectic reactions of the ternary Al-Cu-Mg system at this lithium concentration.

The chemical composition, thermal behaviour and the crystallographic nature of the P1(I) phase particles formed along the grain boundary interfaces, on the other hand, suggest that the P1(I) phase has no parallel with the established phases in the cast Al-Li-Cu-Mg based alloys. The crystallographic nature of the P1(I) phase is as follows: no two P1(I) particles had the same lattice parameter; this may be attributed to the variation in composition from one particle to another implying that formation of these particles is as a result of non equilibrium crystallisation and P1(I) is a non equilibrium phase. The P1(I) particles may be indexed as a F.C.C. structure but no two diffraction patterns from the same particle could both be indexed as F.C.C.; it implies that P1(I) phase does not have a F.C.C. structure. The diffraction patterns could not be indexed conclusively as cubic or hexagonal and it would, therefore, appear that the particles have either tetragonal or orthorhombic or other low symmetry structure. It may be noted that a diffraction pattern (Figure 6.5(b) due to a P1(I) particle (viz. G_1 in Figure 6.5(a) could be also indexed as orthorhombic. However, the exact crystal structure of P1(I) phase remained unknown due to the inadequate data here and further work is clearly required to ascertain its true form.

The other major grain boundary phase P2 was found to have a composition range of 15-16 % iron, 3-4 % Mg, 7-9 % copper, ~1 % silicon and balance aluminium. In view of the SIMS analysis and reported iron bearing phases in the literature, it is understood that the analysis is inaccurate and the P2 phase does not contain magnesium. An error in the analysis is expected because the iron bearing P2 phase in this material is present in very small volumes and in association with the copper rich P1(T) and P1(I) phases. It is reasonable, therefore, to consider that the actual copper content will be less whilst the actual iron content within the particles will be much higher. Table 6.2. provides an account of the established iron bearing phases in various cast and homogenised aluminium alloys containing varying amounts of copper (as an alloying element) and iron (as an impurity). It may be noted that the presence of Al_3Fe phase in the cast microstructure is decided by the iron content of the material whilst formation of Al_6CuFe phase or Al_7Cu_2Fe phase during ingot cooling (and homogenisation) depends on the available copper i.e. the copper content of the material as well as the cooling rate during solidification. In the case of the present material the cooling rate was very high and also where both the iron (0.04 wt %) and copper (1.0 wt %) contents of the material are low, none of the phases like Al_3Fe, Al_6FeCu or Al_7Cu_2Fe can be present in the cast microstructure. It is

Table 6.2. A summary of Iron Bearing Phases Formed in the Cast and Homogenised Aluminium Based Alloys as Functions of Alloy Composition and Cooling Rate

Alloy Composition (weight %)		Phases Present		Copper: Iron ratio (Obtained from the Alloy Composition)	Reference
Copper	Iron	Cast Material	Homogenised Material		
2.90	0.10	Al_6CuFe	Al_7Cu_2Fe	29	168
1.61	1.10	Al_3Fe	$FeAl_6(Cu)$	1.46	168
1.20	0.36	Al_3Fe	~Al_6CuFe	3.33	90
1.20	0.06	~ Al_6CuFe	Al_6CuFe	20	90
4.90	0.29	Al_3Fe + Al_6CuFe + Al_7Cu_2Fe (cooling rate : 10° C/minute)	Al_7Cu_2Fe	17	171
4.50	0.16	Not mentioned	Al_7Cu_2Fe	28	110

suggested that the P2 phase in the present cast material is an intermediate form of the $FeAl_3$ phase (which always dissolves some amount of copper) and the stable Al_6CuFe phase; in other words, the P2 phase may be described as an unstable version [$FeAl_6$(Cu)] of the Al_6CuFe phase, which (P2 phase) contains less copper but a higher or equal amount of iron to that present within the stable Al_6CuFe phase [7-8 % copper, 22-25 % iron and balance aluminium (172)].

Very little data has been gathered on the silicon bearing phase (P3) which would appear to contain substantial amounts of silicon. The fact that it appears in association with P1(T) phase suggests that it may precipitate via a ternary eutectic reaction following the binary $\alpha + P_1$ (T) eutectic reaction. In view of the presence of P1(T) phase in the background of P3 phase, it is suspected that this phase does not contain magnesium; also, in the literature since no Al-Si-Cu based phase is reported, it is likely that P3 is an Al-Si-Li-(Cu) based phase.

6.3.2. Matrix Phase

The composition range and the structural features of the matrix phase particles (P4) bear a striking resemblence to that of the P1(I) particles formed along the grain boundary interfaces; only the morphology of these two types of precipitates were different and this may be attributed to the two different sites at which they form. It may be noted (Figure 6.6(f)) that the matrix particles maintain an orientation relationship with the matrix. No two matrix particles had an identical composition and hence, as would be expected, no two particles had the same lattice parameter either. Also, since no two diffraction patterns from the same particle could both be indexed as F.C.C., it is conclusive that these particles do not have a F.C.C. structure; rather a tetragonal or an orthorhombic or a lower symmetry structure would be its true crytallographic form. A series of diffraction patterns due to orthorhombic and tetragonal structures were, therefore, generated using a programme developed and modified by Aeberli (173) and Khataee (174) respectively and the patterns were then compared with those obtained from the matrix particles. Figure 6.9(d) shows matrix particles and, Figures 6.9(e) and (f) show two different diffraction patterns obtained from the particle M_3. It was found that the diffraction pattern in 6.9(e) could be indexed roughly as F.C.C. with lattice parameter a_o = 19.92 Å or tetragonal with lattice parameters a = b = 14.0 Å and c = 16 Å; however, the diffraction pattern in 6.9(f) could be indexed neither as F.C.C. nor

tetragonal. However, both of these diffraction patterns were found to be quite consistent with an orthorhombic structure with lattice parameters a = 8.04 Å, b = 10.56 Å and c = 19.86 Å. Recently, Loiseau and Lapasset (176) characterised the phases present within an Al - 2.5 Li - 1.3 Cu - 1 wt % Mg wrought alloy annealed at 400^{o}C for different times. The authors examined in detail a previously undocumented crystalline phase viz. C-phase present in the annealed material. The authors suggested that the C phase has an average composition of 15 % copper, 4 % magnesium, ~10 % lithium and balance aluminium and the phase has a face centered tetragonal structure with lattice parameters a = b = 14 Å and c = 20 Å. The authors also observed that the C phase could be roughly indexed as F.C.C. with a lattice parameter a_0 = 20 Å. The C phase was found to be present at the grain boundaries as well as within the matrix; the precipitates present in the matrix were found to maintain an orientation relationship with the matrix and all the precipitates contained a modulation of planar defects.

In view of the findings of Loiseau and Lapasset (175, 176) it appears that in the present cast material the matrix phase (P4) and the P1(I) phase formed along the grain boundary interfaces are very similar to the crystalline C-phase. It also implies that the matrix phase P4 contains substantial amounts of lithium and is a quaternary Al-Cu-Li-Mg phase. Additionally, the fact that the lattice parameters of C phase and that of P4 phase (when indexed as tetragonal) are very similar also suggests that it may be that initially the P4 particles have an orthorhombic structure and then the structure changes to high symmetry tetragonal structure accompanied by a change in composition. Verification of this theory would clearly require examination of a slowly cooled cast structure or a heat treated cast material where a change from an orthorhombic to a tetragonal structure is likely to occur.

6.3.3. Homogenisation

In view of the presence of eutectics within the cast material, the upper limit of the homogenisation temperature is restricted to below 547^{o}C (the melting temperature of the ternary eutectic). It was found that the material could be almost completely homogenised without any sign of incipient melting due to annealing at 537^{o}C for 24 hours. However, later studies involving examination of the extruded material showed that the P2 phase survived such homogenising annealing treatment. The iron bearing phases present in the wrought structure were found to

have an orthorhombic structure with an average composition of 22 % iron, 7 % copper and balance aluminium. The composition and the structural form of these phases suggest that these are stable Al_6CuFe phase which is orthorhombic having a composition range of 22-24 % iron, 7-8 % copper and balance aluminium. The presence of Al_6CuFe phase in the wrought microstructure of the present material is consistent with the findings of other workers (see Table 6.2) together with the interpretation on the nature of P2 phase in the cast material discussed in section 6.3.1.

6.4. Summary

1. The as cast material Al (Al - 2.5 Li - 1.0 Cu - 1.1 Mg - 0.12 wt % Zr) had an equiaxed grain structure and the average grain size was found to be about 90 microns. Light microstructure of the cast material revealed that elemental partitioning occurred during solidification resulting in second phase precipitation within the grains as well as at the boundaries between the grains.

2. The thermal behaviour of the cast material was characterised by differential scanning calorimetry and differential thermal analysis studies. It was found that although the equilibrium solidus point of the material is at a considerably higher temperature (~622^{o}C), the material has a non equilibrium solidus at about 547^{o}C implying that a eutectic has formed during solidification as a result of non equilibrium crystallisation.

3. At the intergranular sites four phases (viz. P1(T), P1(I), P2 and P3) were found whilst in the matrix only one type of phase (viz. P4) was present. The phases were characterised as follows:

   (a) <u>P1(T) phase</u>: it was present at the triple point junctions in the form of a lamellar eutectic [the other phase being α (aluminium)]. It had a composition range of 24-26 % copper, 6-8 wt % magnesium and balance aluminium. SIMS analysis showed that it contains substantial amounts of lithium and the thermal characteristics of this phase were found to be such that it melts at 547^{o}C. These results suggest that P1(T) phase may be

considered to be an extension of T_2 (Al_6CuLi_3) phase (having a composition of 26.9 % copper, 8 wt % lithium and balance aluminium, and a melting temperature of 545^{o}C) with magnesium atoms substituting for lithium atoms up to a concentration of 8 %.

(b) P1(I) phase: This phase was present along the grain boundary interfaces having a composition range of 15 - 18 % copper, 3-5 % magnesium and balance aluminium. SIMS analysis revealed the presence of lithium at the grain boundaries and hence it is suggested that P1(I) is a quaternary Al-Cu-Li-Mg based phase. It was found that the P1(I) particles may be indexed as F.C.C. (although not conclusively) with lattice parameters a_o ranging from 19 to 26 Å. The compositional and the structural characteristics of P1(I) phase bear a strong resemblence to the crystalline C-phase observed in the heat treated AA 8090 alloys.

(c) P2 phase: This phase was present in small volumes in association with P1(T) and P1(I) phases. The P2 phase had an average composition of 15-16 % iron, 7-8 % copper, 3-4 % magnesium and balance aluminium. Elemental SIMS mapping revealed that the P2 phases do not contain magnesium and lithium implying that this is an Al-Fe-Cu based phase. It is suggested that the P2 phase is a metastable version of Al_6CuFe phase. The P2 phase particles were difficult to find in a thin foil for TEM study and hence the crystallographic details of this phase remained unspecified.

(d) P3 phase: This phase was present in association with the P1(T) phase at the triple point junctions in very small volumes. It had an average composition of 18 % copper, 3 % magnesium, 8 % silicon and balance aluminium. It was suggested that P3 might be an Al-Si-Li-(Cu) based phase. Mainly in view of very small volumes of these particles the exact composition as well as its crystallographic form remains unknown.

(e) P4 phase: This was the only phase present in the matrix of the cast material. It had a composition range of 15-19 % copper, 2-5 % magnesium, and balance aluminium. The particles contained a modulation of planar defects and they may be indexed as F.C.C. (although not conclusively) with lattice parameter a_o ranging from 18.5 to ~20 Å. One matrix particle was

conclusively indexed as orthorhombic with a = 8.04 Å, b = 10.56 Å and c = 19.86 Å.

4. An optimum homogenisation schedule was established for the present cast material. Annealing for 24 hours at 537^{o}C resulted in complete dissolution of all the as cast phases (except P2) without any sign of incipient melting. The Al-Fe-Cu based particles present at the grain boundaries of the wrought material had an average composition of 22 % iron, 7 wt % copper and balance aluminium. The particles had an orthorhombic structure and it is suggested that they are the Al_6CuFe phase.

CHAPTER SEVEN

CHARACTERISATION OF THE AS EXTRUDED MICROSTRUCTURE AND MECHANICAL PROPERTIES

7.1. Introduction

The present chapter is concerned with the extrusion processing of homogenised alloy A1. Extrusion was performed over a wide range of processing variables which produced extrudates having a variety of grain and subgrain structures. Variation in grain and subgrain morphology is interpreted in terms of the various processing parameters employed and the mechanisms responsible for recrystallisation in this alloy system are discussed in detail. The mechanical properties of the as extruded material are correlated with the extrusion processing conditions. The natural and artificial ageing responses of the as extruded materials are also discussed.

7.2. Results

7.2.1. Extrusion Processing

Figure 7.1 defines the variation in maximum extrusion pressure required at varying initial billet temperatures viz. 400, 450 and 500^{o}C, and extrusion ratios ranging from 20:1 to 80:1. The data may be fitted linearly: the pressure requirement decreases with increasing temperatures for a particular extrusion ratio and increases with increasing extrusion ratios for a particular temperature. Variation in extrusion pressure required at varying ram speeds viz. 3, 7 and 15 mm/sec. is shown in Figure 7.2. It may be noted that increasing ram speed has the effect of raising the required pressure at any extrusion ratio and temperature.

The temperature rise during extrusion was calculated using a programme developed by Cooper (177). The temperature rise during extrusion due to the initial billet temperatures of 400, 450 and 500^{o}C (and the extrusion ratio of 20:1 and a ram speed of 3 mm/sec) was determined to be 90, 66 and 45^{o}C respectively. The highest processing temperature was, therefore, restricted to the use of an initial billet

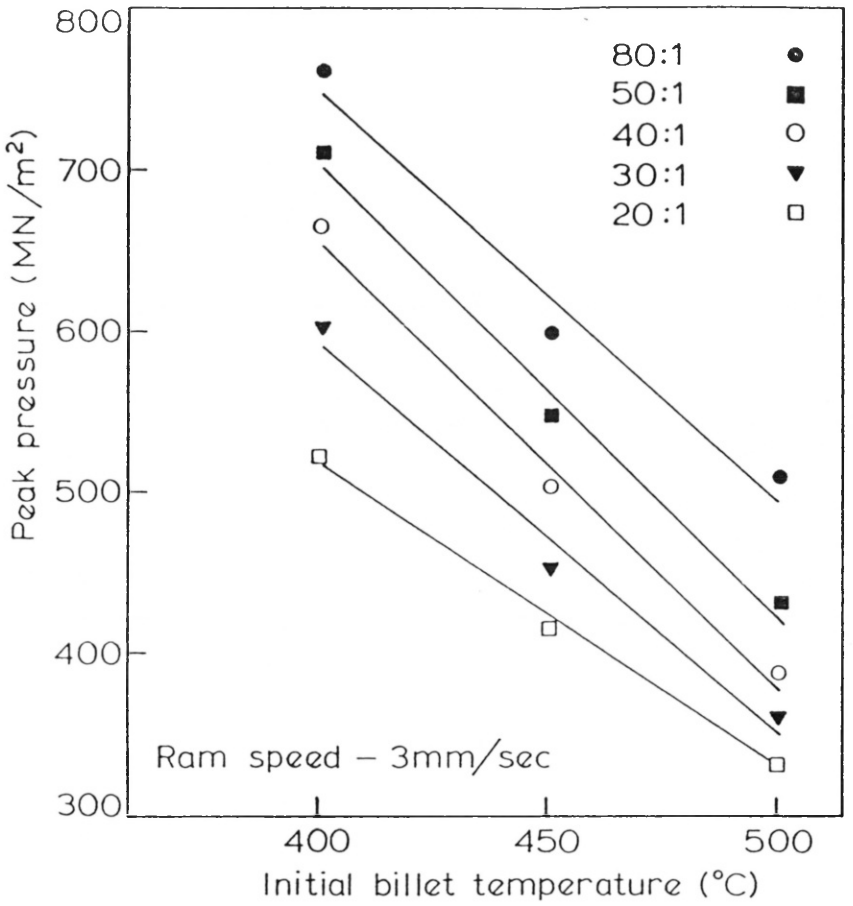


Figure 7.1. Variation in peak pressure as functions of initial billet temperature and extrusion ratio.

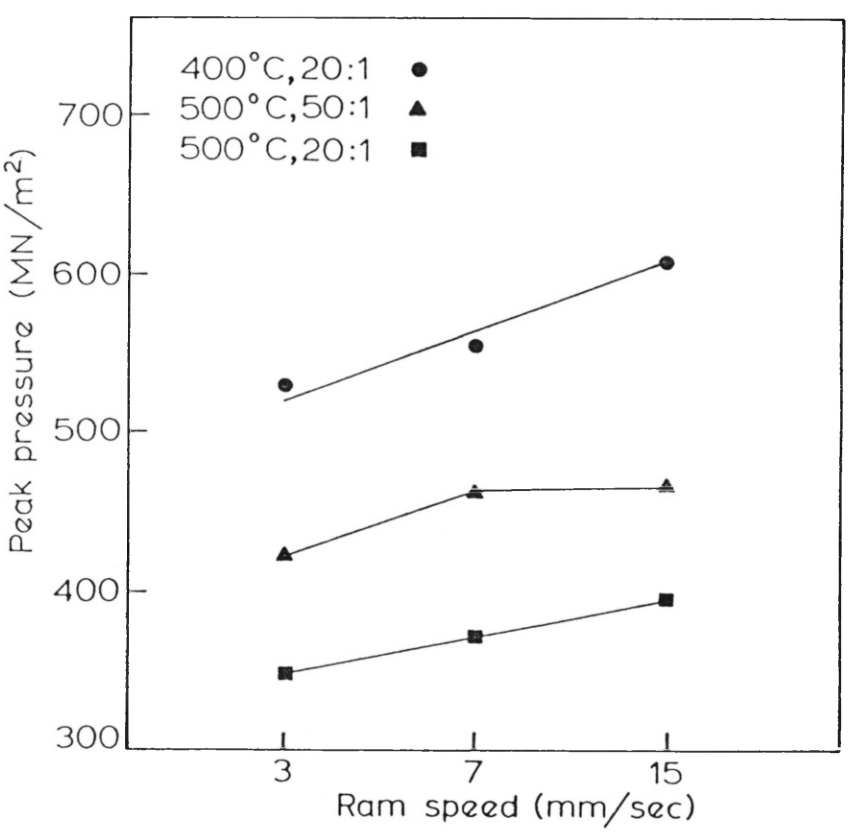


Figure 7.2. Variation in peak pressure as a function of ram speed.

temperature of 500^{o}C in order to avoid the risk of incipient melting. On the other hand the material could not be extruded within the load capacity of the press employed below 350^{o}C, using an extrusion ratio of 20:1 and the lowest ram speed. It was also found that the surface quality of all the extrusions produced over the processing range was very good implying that the homogenisation treatment given to alloy A1 before extrusion was appropriate.

7.2.2. Extrudate Grain Structure

7.2.2.1. Effect of Extrusion Processing Variables

Under all processing conditions, extrusions produced microstructures which varied through the extrude section: the layer immediately adjacent to the surface was fully recrystallised and the mid radius location was partially recrystallised merging in with the core structure which was essentially unrecrystallised. The periphery of the extrudates recrystallised under all imposed process conditions: a result of the high strain and strain rate experienced by the surface material as it traverses the deformation zone. Both the grain morphology of the surface layers as well as the depth of the recrystallised periphery varied with the extrusion processing conditions: at extrusion temperatures above 450^{o}C, a very fine equiaxed structure [Figure 7.3(a)] was produced with a grain size of about 5-10 microns whilst at lower temperatures this coarsened [Figure 7.3(b)] resulting in considerable variations in the grain size. Increasing the extrusion temperature, extrusion ratio or ram speed increased the depth of the recrystallised surface layer and the core increasingly exhibited partial recrystallisation (Figures 7.3 and 7.4). Increasing the ram speed from 3-15 mm/sec only slightly increased the amount of recrystallisation. Changing the reduction ratios from 20:1 to 80:1, however, produced a bigger change in the amount of recrystallisation. Using the approximate equation (124) for strain rate, $\dot{\varepsilon} = (6v \ln R)/D$ (where, v is the ram speed, R is the extrusion ratio, and D is the initial billet diameter), it is clear that recrystallisation is not sensitive to strain rate changes but rather to strain change via the variation in R, the extrusion ratio; it may be noted that the strain rate increases by a factor of 5 when the ram speed increases from 3mm/sec to 15 mm/sec, whilst, by increasing the extrusion ratio from 20:1 to80:1, the strain rate increases by a factor of only about 1.5. Consideration of Figures 7.3 and 7.4 suggest that the extrusion ratio has a strong influence on the extrudate structure. The extrusion temperature, however,

Figure 7.3. Light micrographs of the as extruded grain structure (Longitudinal section);

(a) Near surface; 500°C (initial billet temperature), 20:1 (extrusion ratio), 3 mm/sec (ram speed).

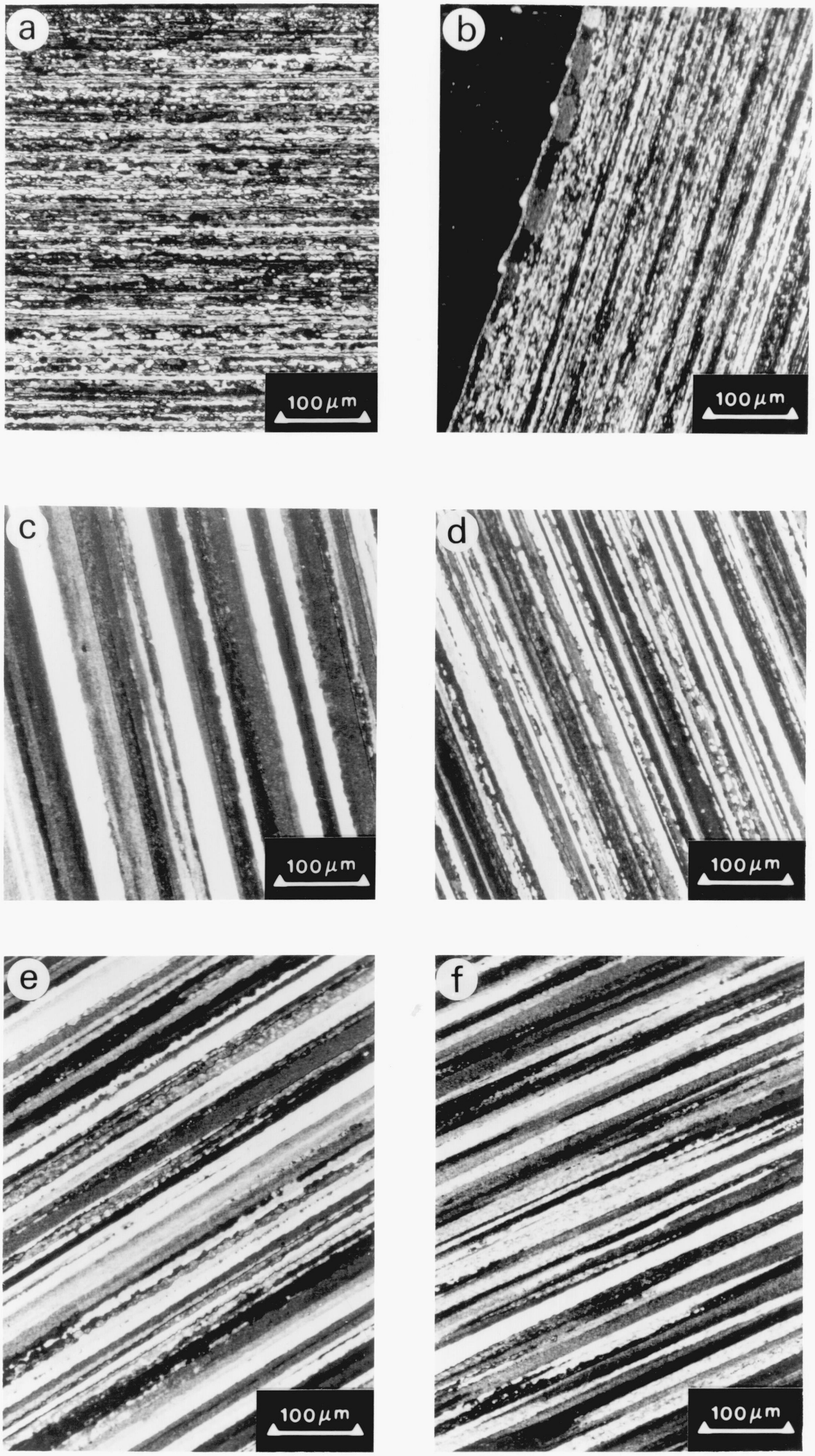
(b) Near surface; 400°C, 20:1, 3 mm/sec.

(c) Core, 500°C, 20:1, 3 mm/sec.

(d) Mid-radius, 500°C, 80:1, 3 mm/sec.

(e) Core, 500°C, 80:1, 3 mm/sec.

(f) Core, 400°C, 50:1, 3 mm/sec.


a
100μm
b
100μm
c
100μm
d
100μm
e
100μm
f
100μm

always had the effect of increasing the total amount of recrystallisation under any deformation condition. In other words, the influential role of the extrusion ratio was much more evident at higher processing temperatures, implying that recrystallisation in the present alloy system is strain induced and is, of course, thermally activated.

A consistent feature of the recrystallisation was its banded nature and the proximity of the nucleation points to original grain boundaries (as shown in Figures 7.3 - 7.4) implying that high angle boundaries of original grains are the places of greatest inhomogeneity. However, it may be noted that apart from the presence of a recystallised annulus at the surface, recrystallisation always occurred nonuniformly within the other areas of the extrudes. The level of recrystallisation was not systematically measured as a function of the process parameters. In the extreme case of 80:1 extrusion ratio and the highest processing temperature the volume fraction recrystallised was not found to exceed 30 %.

7.2.2.2. Effect of Isothermal Annealing

The press quenched extrudates were annealed at 530^{o}C under argon atmosphere for 5 hours. The resultant microstructures as shown in Figures 7.4 (a)-(c) illustrate the effect of isothermal annealing upon the extrudate grain structures. The extruded structures were very stable and extremely resistant to further static recrystallisation. The only noticeable changes that occurred were mainly at the surface and at the mid-radius location, such that the fine grains present after extrusion underwent grain growth. Prolonging the annealing time or increasing the annealing temperature (up to 580^{o}C) caused only further growth of the existing small grains but the core structure remained unrecrystallised. An interesting feature is that even the extrusions performed at lower temperatures did not exhibit any tendency to undergo static recrystallisation during the solution soak.

7.2.2.3. Effect of Variations in Cooling Rate Post Deformation

In a further experiment, at the end of hot deformation the extruded material was allowed to cool in air. The resultant microstructures were generally very similar to those of the press quenched extrudates produced under similar

Figure 7.4. Light micrographs of the extruded material (Longitudinal sections)

(a) Mid-radius; 450°C, 20:1, 3 mm/sec; annealed at 530°C for 5 hours under argon atmosphere.

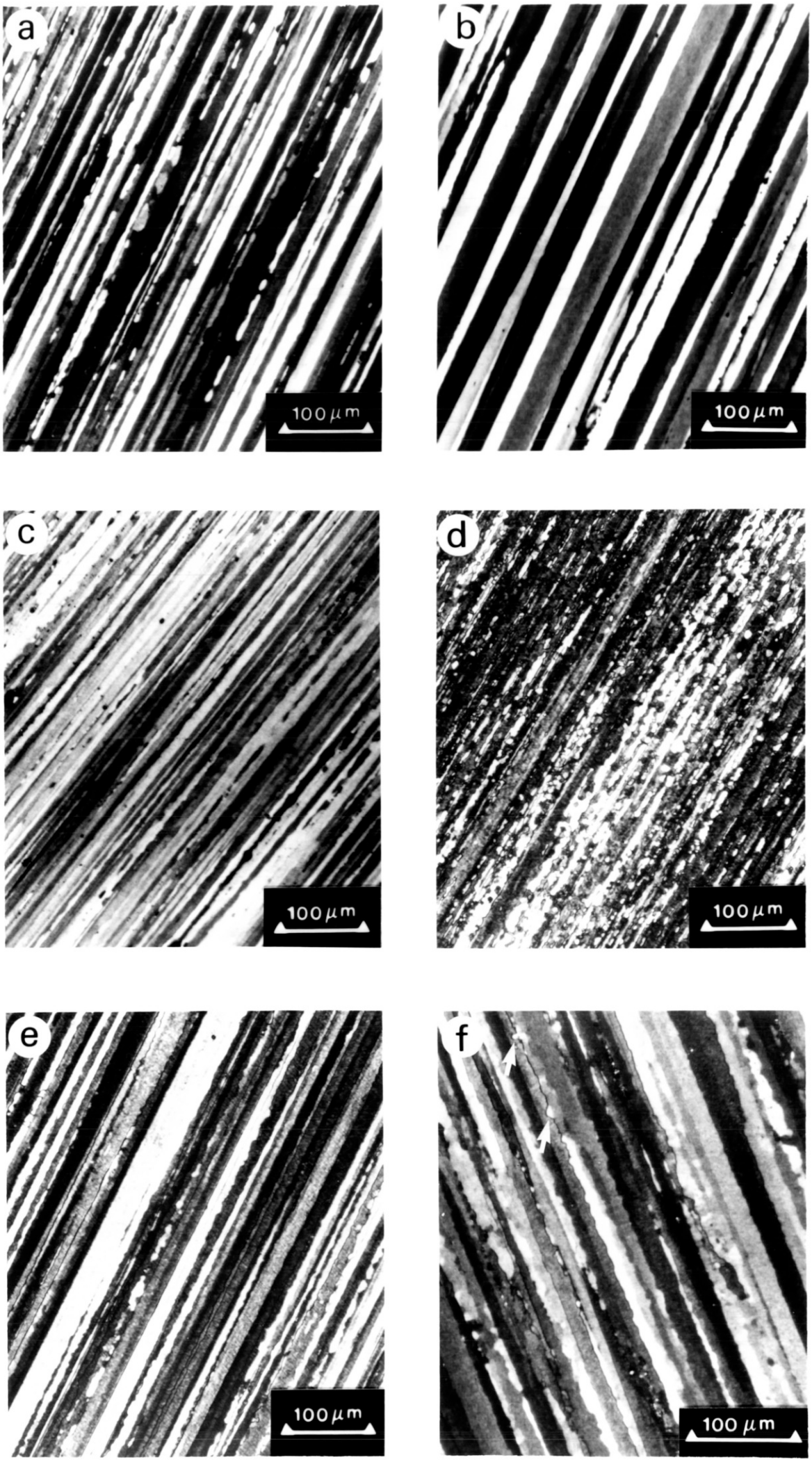
(b) Core; 450°C, 20:1, 3 mm/sec; annealed at 530°C for 5 hours under argon atmosphere.

(c) Mid-radius; 400°C, 20:1, 3 mm/sec; annealed at 530°C for 5 hours under argon atmosphere.

(d) Mid-radius; 500°C, 20:1, 15 mm/sec.

(e) Core; 500°C, 20:1, 15 mm/sec.

(f) Core structure of an air cooled extrudate; 500°C, 20:1, 3 mm/sec.


a
100 μm
b
100 μm
c
100 μm
d
100 μm
e
100 μm
f
100 μm

deformation conditions, the only change being the formation of a few new grains within the core structure as shown in Figure 7.4(f). As noted earlier, the original high angle boundaries were frequently serrated: these serrations acted as nucleation sites for those grains. Apart from the limited numbers of new grains, the core structure remained unrecrystallised.

7.2.3. Grain Structure Produced in Torsion

In extrusion processing, there is inevitably a short delay between the end of deformation and the quenching of the material. To check whether such a delay affects the press quenched microstructures, the homogenised material was deformed in torsion at 500^{o}C at a strain rate of 0.3 sec^{-1}. The deformation was stopped in the steady state regime at a strain value of 2.5 and the material was immediately quenched. The resultant microstructures are shown in Figure 7.5. The Figure clearly shows the presence of small recrystallised grains in the near surface and mid-radius locations whilst the core is completely unrecrystallised. In common with the as extruded microstructures, it is worth noting that the nucleation sites of the new grains were always confined to the regions adjacent to the original grain boundaries. Figure 7.5 also indicates the formation of serrated high angle boundaries and nucleation of small grains at those sites (see Figure 7.5(a)). However, no recrystallised surface layer was produced in torsion implying that this is a result of the severe surface strains in extrusion. In a further experiment, under similar deformation conditions, the hot deformed material was quenched first and then the deformation was stopped. The resultant microstructures were found to be identical to those shown in Figure 7.5., implying that the observed recrystallation is indeed dynamic.

7.2.4. Development of Subgrain Structure

Under all extrusion conditions the as extruded microstructures exhibited well recovered subgrain structures. Development of such subgrain structures at the core of the extrudates is presented in Figure 7.6. The Figure shows the effect of extrusion temperature indicating a decrease in subgrain size with decreasing temperature and illustrates the dramatic effect of extrusion ratio. The subgrains are equiaxed at an extrusion ratio of 20:1 [Figure 7.6(a)] becoming more closely spaced and elongated in the extrusion direction at a ratio of 80:1 [Figure 7.6(e)].

Figure 7.5. Light micrographs showing grain structure produced in torsion (deformed at 500°C; total strain = 2.5).
(a) Near surface
(b) Near surface
(c) Mid-radius
(d) core

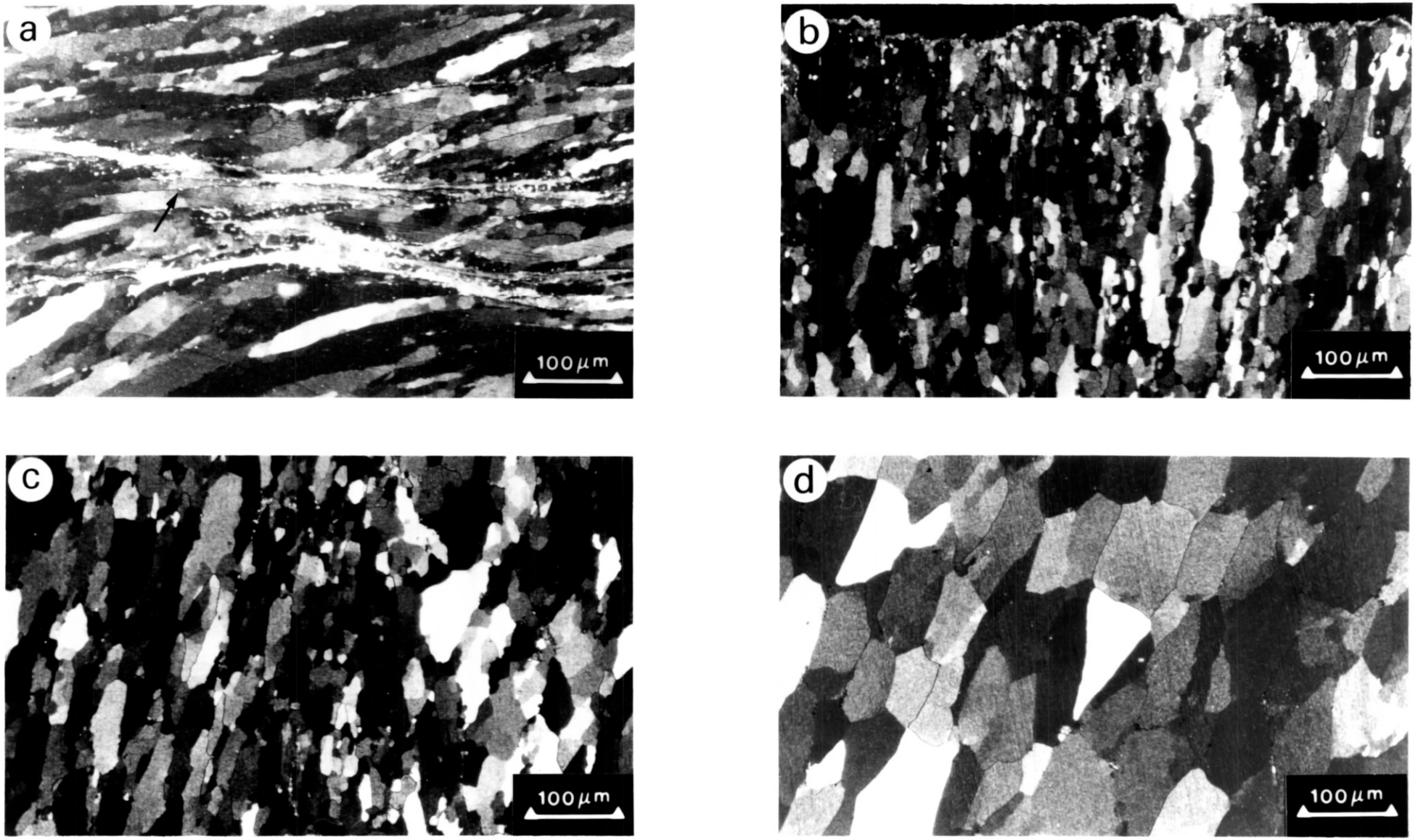

a
100μm
b
100μm
c
100μm
d
100μm

Figure 7.6. BF micrographs showing development of subgrain structures at the core of the as extruded material.

(a) 500°C, 20:1.

(b) 450°C, 20:1.

(c) 400°C, 20:1.

(d) 500°C, 50:1.

(e) 500°C, 80:1.

Ram speed being 3 mm/sec. TEM micrographs of longitudinal sections.

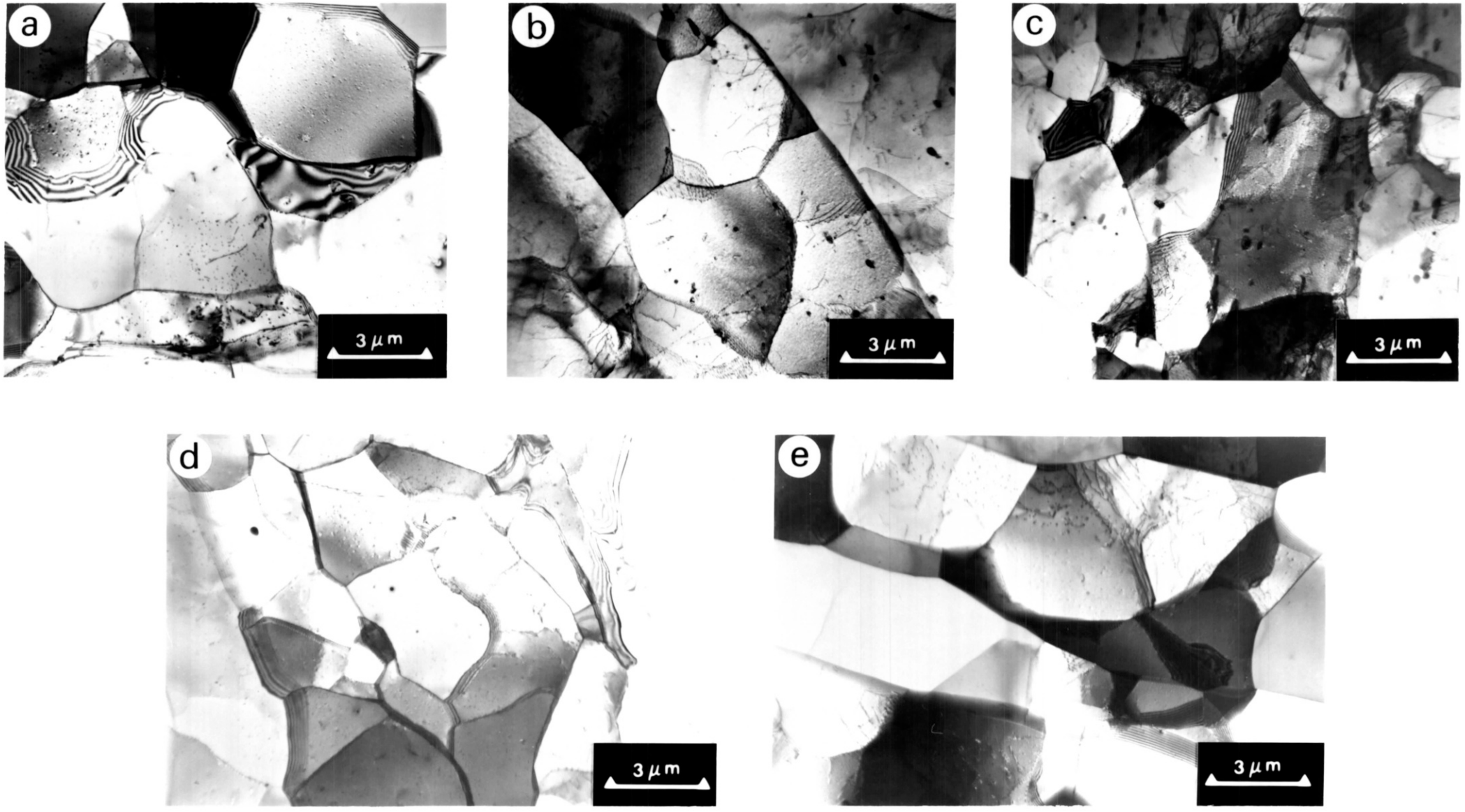

a
3 μm
b
3 μm
c
3 μm
d
3 μm
e
3 μm

Figure 7.7(a) illustrates the variation in subgrain morphology across the extrude section; thin foils for TEM were made from the mid-radius location of an extrudate produced at 500^{o}C and 20:1 extrusion ratio. The resultant microstructure revealed that the subgrains were smaller in size, more closely spaced and elongated along the extrusion direction compared to those present at the core of the same extrudate [compare Figure 7.6(a) with Figure 7.7(a)]. Figure 7.7(b) shows the subgrain structure at the mid-radius location of an extrudate produced at 400^{o}C and 50:1 extrusion ratio. The combined effect of higher strain and lower temperature on the subgrain morphology may clearly be noted: the subgrains are more closely spaced, elongated and smaller in size. Variation in subgrain morphology across the extrude section is clearly a result of the presence of a strong strain gradient across the extrude section where the strain is maximum at the surface and minimum at the core. The effect of strain on subgrain morphology is not generally recognised although Hollinshead and Sheppard (132) have reported such an effect during the rolling on an Al-1 Mg - 1 wt % Mn alloy.

Detailed examination of the subgrain structures revealed that unlike pure aluminium and many of its alloys, the subgrain boundaries in this material were not, in general, of low angle type; rather, the angle of misorientation across many of these boundaries were often found to exceed 5-10^{o}. Also, with increasing strain the subgrains were found to be increasingly misoriented. Figure 7.7(c) shows the subgrain structure at the mid-radius location of an extrudate produced at 500^{o}C and at 50:1 extrusion ratio. As evidenced by the selected area diffraction patterns the angle of misorientation across some of the boundaries of subgrain P is as high as 18^{o}. Further examination of the subgrain structures revealed that under any deformation condition the subgrains formed adjacent to the original high angle boundaries were more misoriented than those formed away from the original boundaries. The mechanisms involved in the formation of these highly misoriented subgrains are detailed in the discussion section.

7.2.5. Recrystallisation Mechanisms

Press quenched extrudates were examined by TEM in order to determine the mechanisms responsible for recrystallisation in this alloy system. Inspection by TEM revealed that under all extrusion conditions, but notably at lower extrusion ratios, recrystallisation occurred by local migration of original grain boundaries.

Figure 7.7. BF(a,b) & DF(c) micographs showing development of subgrain structures, in the as extruded material.

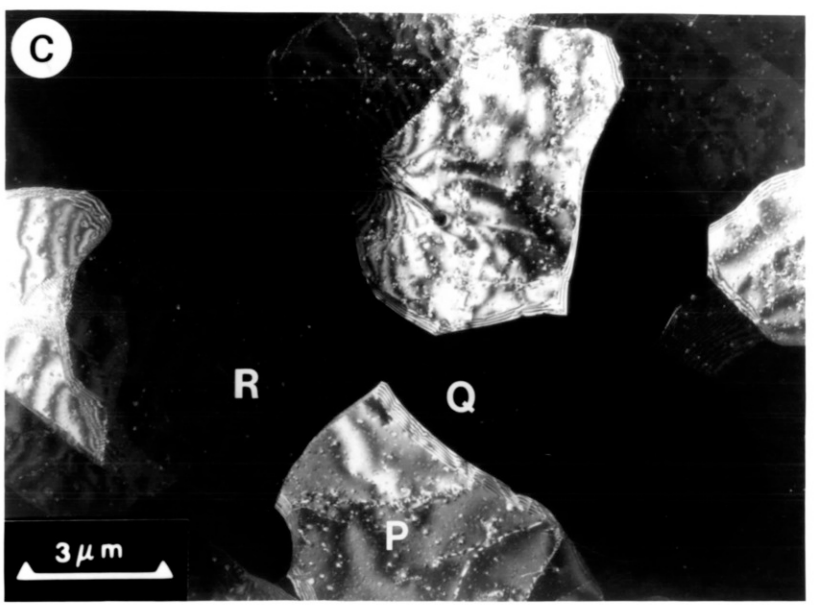
(a) Mid-radius 500^{o}C, 20:1, 3 mm/sec.

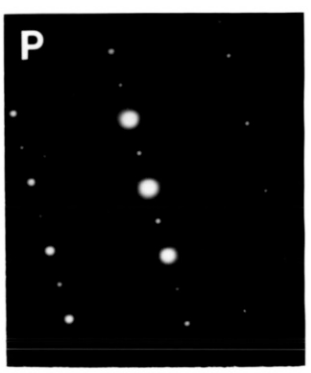
(b) Mid-radius 400^{o}C, 50:1, 3 mm/sec.

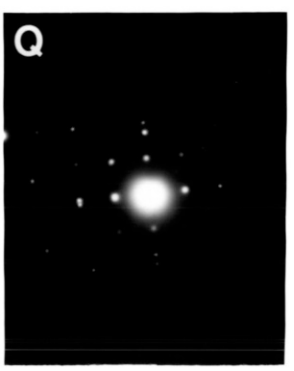
(c) Mid-radius, 500^{o}C, 50:1, 3 mm/sec.


a
2 μm


b
3 μm


c
R
Q
P
3 μm


P


Q

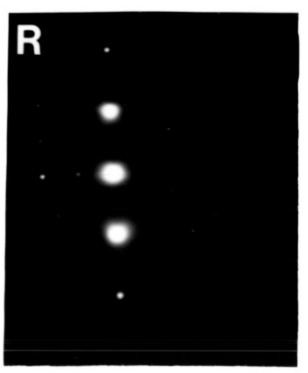

R

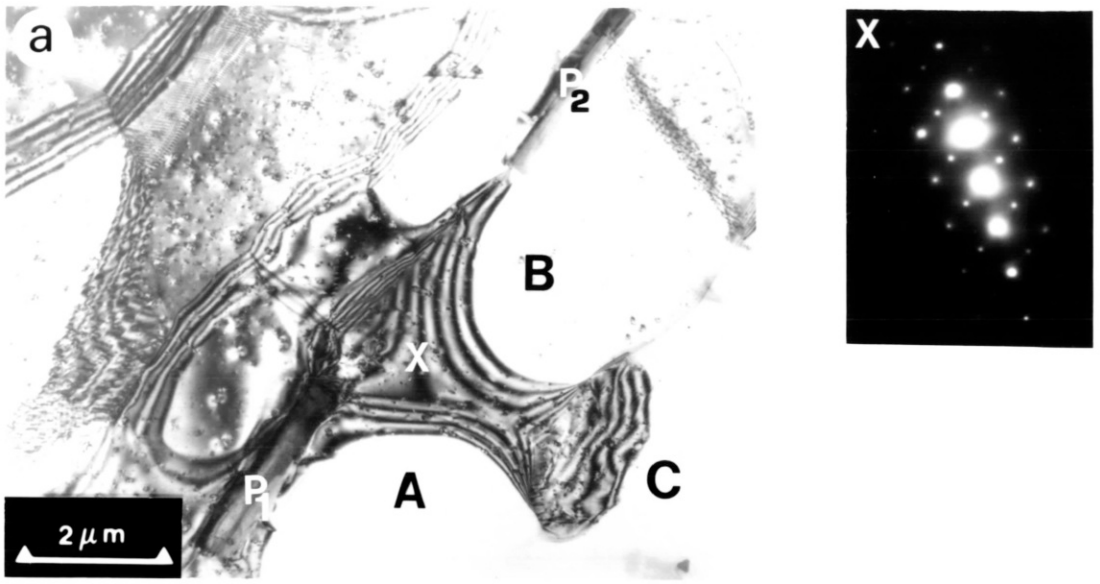
Figure 7.8(a) illustrates this mechanism in which the portion of the high angle boundary limiting the bulge is pinned by the second phase (viz. Al-Fe-Cu based phase) particles (labelled P_1 and P_2). Selected area diffraction patterns covering the periphery of the bulge region (from A,B, C) confirmed the high misorientation of its interface with the surrounding matrix. Figure 7.8(b) shows nucleation of what appears to be a small grain adjacent to an original grain boundary by the same mechanism; the bulging of the original grain may be viewed to be occurring from below the plane of view of the micrograph. Selected area diffraction patterns covering the periphery of the bulge (labelled X) region confirmed the high misorientation of its interface with the surrounding matrix.

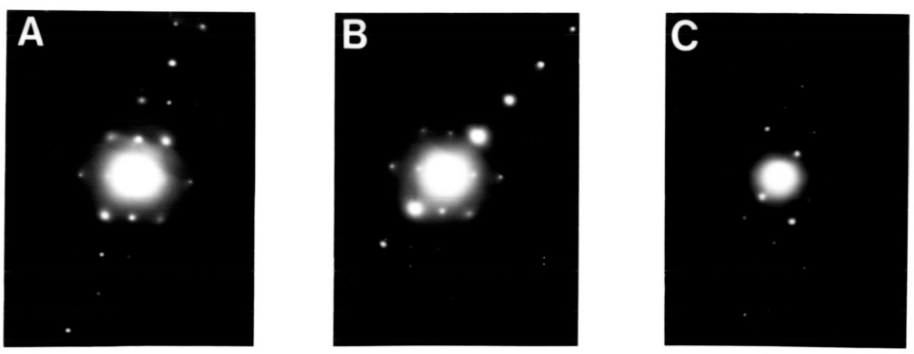
TEM revealed that this bulging mechanism was supplemented by a second process at higher deformation rates and temperatures. Figure 7.9(a) illustrates the mechanism involved. Subgrains located in the vicinity of an original high angle grain boundary (the original boundary is not shown in the micrograph) exhibit a very high degree of misorientation with neighbouring subgrains as indicated by the selected area diffraction patterns. This implies that rotation recrystallisation is also occurring. In this mechanism, these subgrains must rotate to accommodate the inhomogeneous strain at the original boundary thus forming a new high angle boundary with both original grains. These new grains were frequently observed to contain substructures (e.g. the sub-boundary within subgrain S; see Figure 7.9(a)) indicating the process to be dynamic and similar to that recently shown to be responsible for recrystallisation during hot deformation in Al-Mg alloys (143).

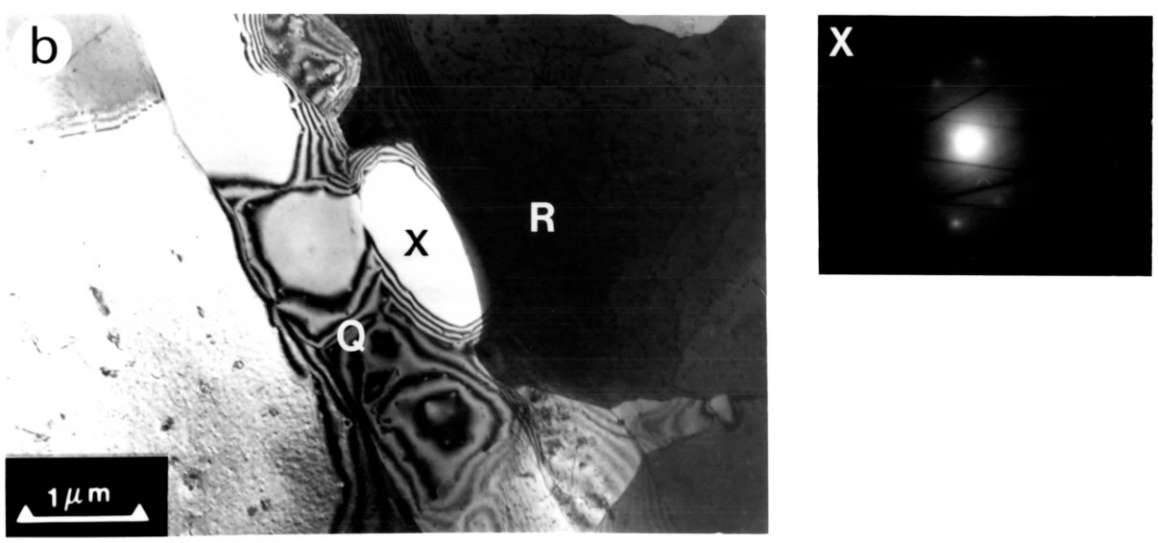
At higher deformation rates and temperatures, TEM also revealed the formation of some very large subgrains (having average diameters of ~20 μm compared to the typical subgrain size of the order of 1-10 μm in the present material) adjacent to transition bands (viz. deformation bands). Figure 7.9(b) shows one such subgrain (labelled A). Formation of such subgrains is common in aluminium and many of its alloys (178) during annealing of the hot deformed material and is attributed to the growth (via coalescence) of the subgrains by the rotation mechanism (rather than by migration of sub-boundaries) in preferentially deformed regions of the material such as deformation bands. The result is that the large coalesced subgrains become recrystallisation nuclei. In view of the reluctance of the present material to undergo static recrystallisation (see section 7.2.2.2), together with the fact that subgrain rotation is the principal mechanism

Figure 7.8. (a) TEM BF micrograph illustrating recrystallisation by grain boundary bulging mechanism in the as extruded material; 500°C, 20:1, 3 mm/sec.

(b) TEM BF micrograph illustrating recrystallisation by grain boundary bulging mechanism in the as extruded material; 500°C, 20:1, 3 mm/sec.

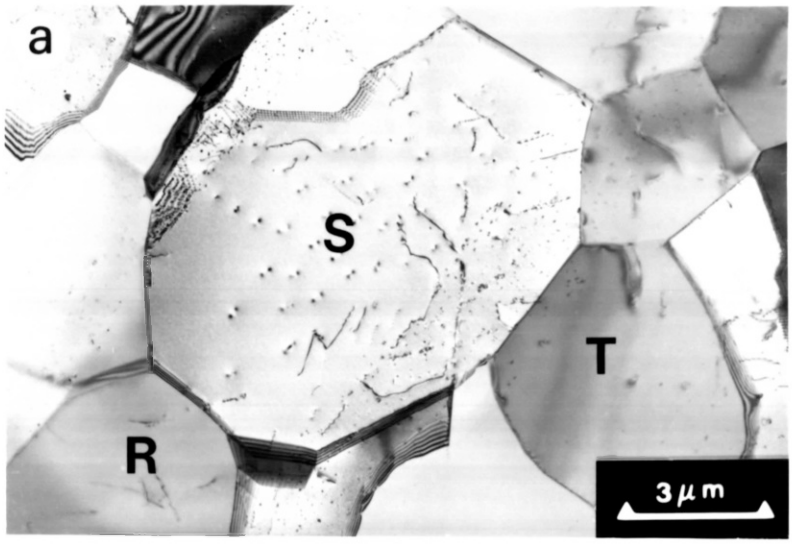

a
P2
B
X
P1
A
C
2μm
X

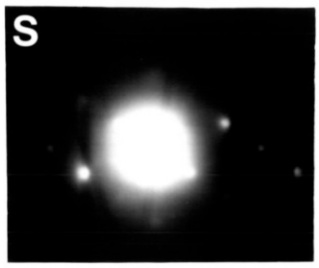

A
B
C


b
R
X
Q
1μm
X

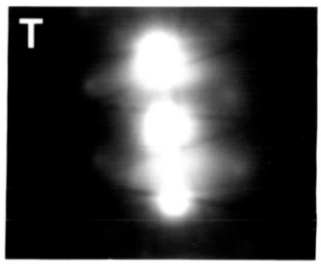

Q
R

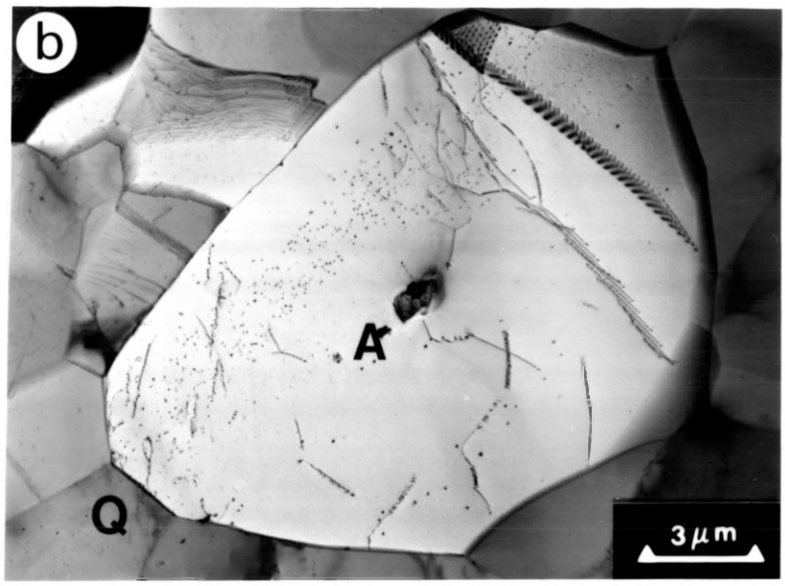
Figure 7.9. (a) TEM BF micrograph illustrating development of highly misoriented subgrains adjacent to the original boundaries; 500°C, 50:1, 15 mm/sec.
(b) TEM BF micrograph showing a large subgrain (labelled A) in the as extruded material; 500°C, 50:1, 15 mm/sec.

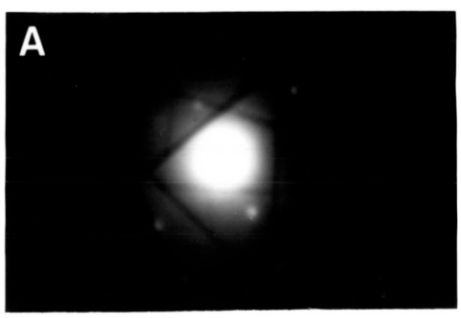

a
S
T
R
3μm

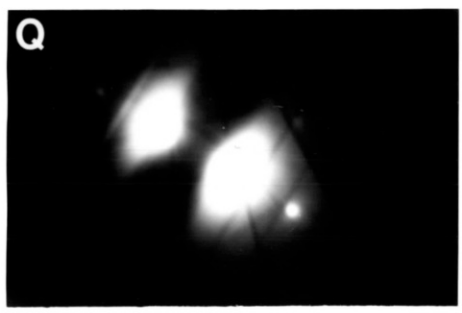

S


R


T


b
A
Q
3μm


A


Q

responsible for recrystallisation in this material at higher deformation rates and temperatures, it is suggested that formation of these large subgrains took place during the deformation process proper. This is further evidenced by the presence of well knit sub-boundaries and loose dislocations within subgrain 'A' which should have been removed had the rotation of the subgrains, following coalescence, taken place after hot deformation. Selected area diffraction patterns across the interfaces of subgrain 'A', Figure 7.9(b), confirmed its high misorientation with respect to its neighbours. However, detailed examination of the extrudate microstructures by TEM revealed that recrystallisation by this mechanism was not a regular phenomenon in this material.

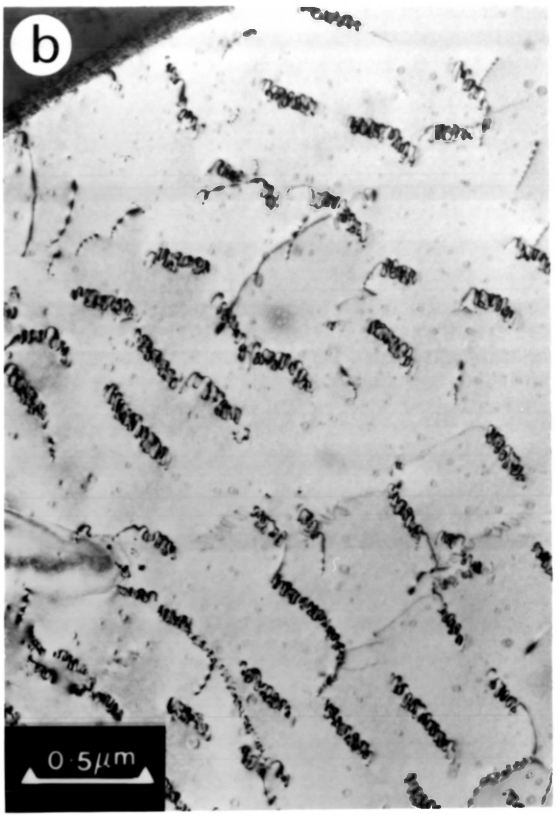
Materials hot deformed via torsion were also examined. TEM revealed well recovered subgrain structures. It was found that recrystallisation primarily occurred by the grain boundary bulging mechanism. Additionally, TEM revealed the presence of highly misoriented subgrains adjacent to the original grain boundaries and the deformation bands indicating that recrystallisation also occurred by rotation recrystallisation. These observations suggest that the recrystallisation in torsion is esentially similar to that in extrusion.

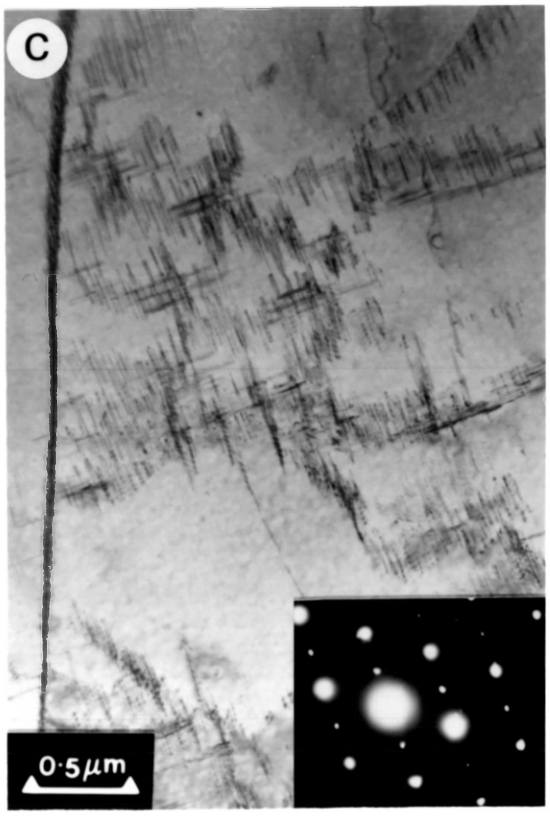
7.2.6. Precipitation within the As Extruded Microstructure

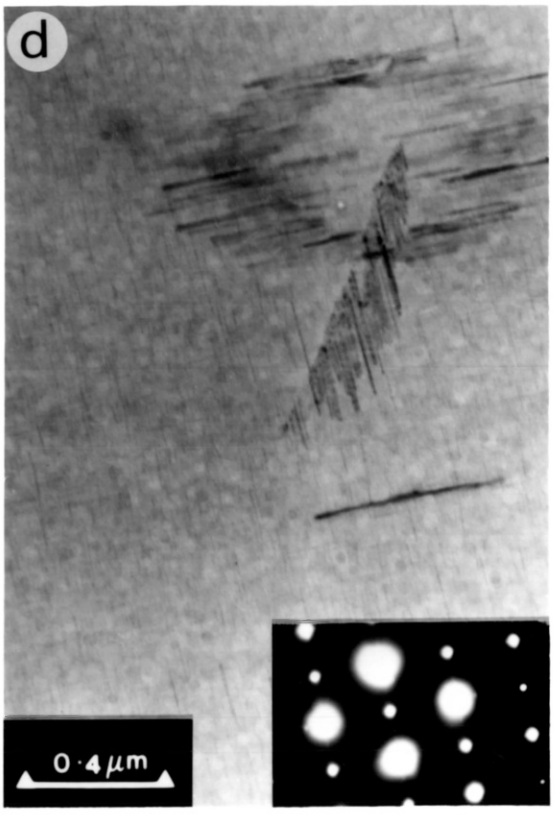
Microstructural studies were carried out on extruded material which had been held at room temperature for 1 month prior to examination; some natural ageing will therefore have taken place. TEM revealed that under all process conditions a very fine distribution of δ' phase particles was present within the microstructures. Within the extrudates produced at the highest processing temperature, no other precipitate phase could be detected. However, within the extrudates processed at lower temperatures, TEM revealed additionally a heterogeneous distribution of coarse second phase particles (Figure 7.10(a)). In general, the particles were aligned along the extrusion direction. The particles had an average size of about 1 micron and qualitative x-ray EDS analysis suggested they were copper rich Al-Cu-Mg based phase particles. The particles were present within the matrix as well as at the grain and subgrain boundaries of the material. It was also found that formation of these precipitates was a strong function of the processing temperature such that the number density of these particles was maximum at the lowest processing temperature.

Figure 7.10. TEM BF micrographs showing
(a) precipitation of second phase particles in the as extruded material; 400°C, 20:1, 3 mm/sec.
(b) Precipitation of helices in the material extruded at 500°C and NA 1 month; <112> Al orientation.
(c) Heterogeneous S (and T_1) precipitation in the material extruded at 500°C, NA 2 months, AA 24 hours at 190°C.
(d) Homogeneous, and heterogeneous (on dislocation loops) S precipitation in the material extruded at 500°C, NA 2 months, AA 24 hours at 190°C.


a
1 μm


b
0·5μm


c
0·5μm


d
0·4μm

TEM additionally revealed precipitation of dislocation loops and helices within the naturally aged microstructures (Figure 7.10(b)). However, except within the extrudates produced at the highest extrusion temperature, the presence of dislocation loops was a rare event. It is suggested that the reasons for this are two fold: firstly, the total numbers of vacancies decreased with decreasing extrusion temperatures and, secondly, the loose dislocations which were present in greater numbers in the extrudates produced at lower temperatures acted as sinks for the vacancies released during natural ageing.

7.2.7. As Extruded Mechanical Properties

7.2.7.1. Tensile Properties

Tensile testing was performed on extrudates processed at varying temperatures and extrusion ratios and a ram speed of 3 mm/sec. in order to evaluate the contribution of the processing variables to the final properties without this being masked by the effects of heat treatment. Although, before the tensile tests were made, the specimens were unavoidably naturally aged for 2 weeks. The tensile data are presented in graphical form in Figure 7.11 and in tabular form in Table 7.1.

The results indicate that the tensile strength increased with increased temperature and extrusion ratio. Also, it may be noted that improvements in the ultimate tensile strength (UTS) due to increasing temperature and extrusion ratio were most marked at lower extrusion ratios and lower extrusion temperatures respectively. For example, at 20:1 extrusion ratio, the UTS increased by 100 MPa over the extrusion temperature range as compared to an increase by about 40 MPa at 80:1; similarly, at an initial billet temperature of 400^{o}C, the UTS increased by 60 MPa over the extrusion ratio range as compared to an increase of only 5 MPa at 500^{o}C.

The processing variables had a similar effect on the proof stress except at the highest processing temperature where the properties were observed to decrease with increasing extrusion ratio.

In contrast to UTS and proof stress, ductility was relatively insensitive to the processing variables; although, up to 50:1 extrusion ratio, a general trend of

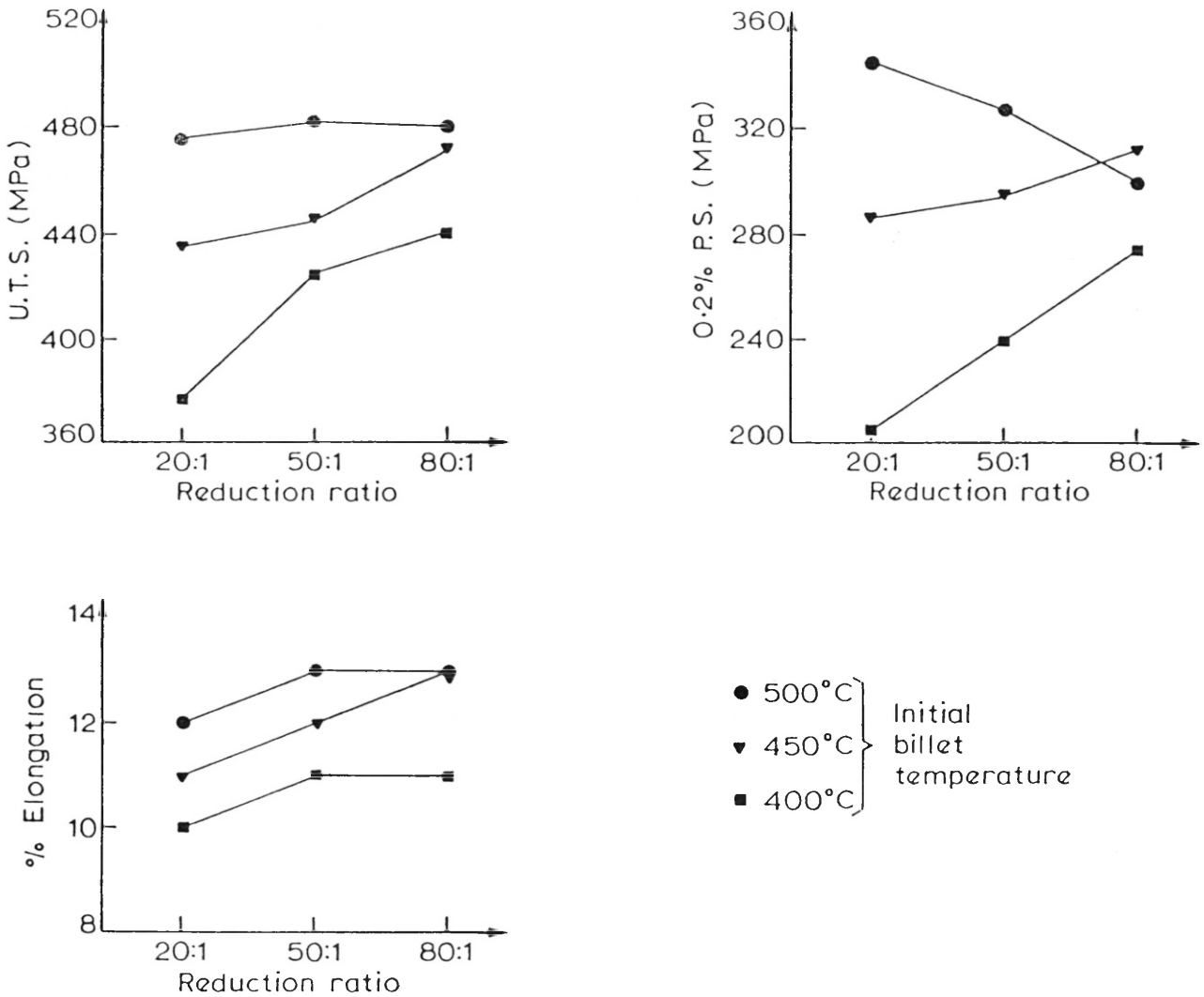


Figure 7.11. Variation in as extruded tensile (longitudinal) properties as functions of extrusion temperatures and extrusion ratios.

Table 7.1. As Extruded Tensile Properties*(Longitudinal)

Extrusion Ratio	Initial Billet Temperature		
	500°C	450°C	400°C
20:1	UTS : 476 (MN/m^2)	435	377
	0.2 % PS : 345 (MN/m^2)	295	205
	% Elongation : 12	11	10
50:1	UTS: 482	445	425
	0.2 % PS : 327	287	240
	% Elongation : 13	12	11
80:1	UTS : 481	472	441
	0.2 % PS : 300	312	274
	% Elongation : 13	13	11

* Each value is the average of two values obtained from two identical tests

Table 7.2 As Extruded Hardness (VHN_{10}) Data

Initial Billet Temperature (°C)	Extrusion Ratio 20:1	30:1	40:1
400	69	75	102
450	72	78	115
500	77	113	116

increasing ductility with increasing extrusion ratio and temperature may be noted. Also, the results indicate that the ductility was least where the volume fraction of the Al-Cu-Mg based phase particles was greatest and the degree of recrystallisation was least after extrusion at 400^{o}C.

7.2.7.2. Hardness Data

Before the tensile tests were made, the specimens were unavoidably naturally aged for about 2 weeks. For that reason, hardness measurements were also taken later in the as extruded condition within 2 hours of the extrusions being performed. The hardness data are presented in Table 7.2. It may be noted that a very consistent trend of increasing hardness values of the extrudates with increasing temperature and extrusion ratio was obtained. The hardness value of any press quenched extrudate is principally due to the following factors: the substructure of extrude, formation of precipitate phases on quenching and, solid soluion hardening due to the elements (e.g. in this material mainly due to magnesium) present. The present observations clearly indicate that the contributions due to the latter two factors are more significant in the present material.

7.2.7.3. Artificial Ageing Response

The age hardening curves for the extrudates produced at 400^{o}C and 500^{o}C respectively are shown in Figure 7.12. The extrudates were naturally aged for two months before they were artificially aged at 190^{o}C. Figure 7.12 indicates that the 400^{o}C extrudate always had inferior properties compared to the 500^{o}C extrudate. The initial hardness values of the extrudates before ageing at 190^{o}C were also quite different suggesting an inferior natural ageing response of the 400^{o}C extrudate. The results also show that in the case of the 400^{o}C extrudate, the maximum hardness (i.e. 147 V.H.N.) was obtained after 10 hours at 190^{o}C beyond which up to 24 hours the hardness values remained almost constant followed by a rapid decrease in hardness with increasing ageing times. In contrast the 500^{o}C extrudate showed a much higher peak hardness value (i.e. 158 V.H.N.) after 24 hours at 190^{o}C, the hardness remained almost constant up to 72 hours and overaging was only gradual beyond that time. Within the peakaged microstructure of the 500^{o}C extrude, TEM

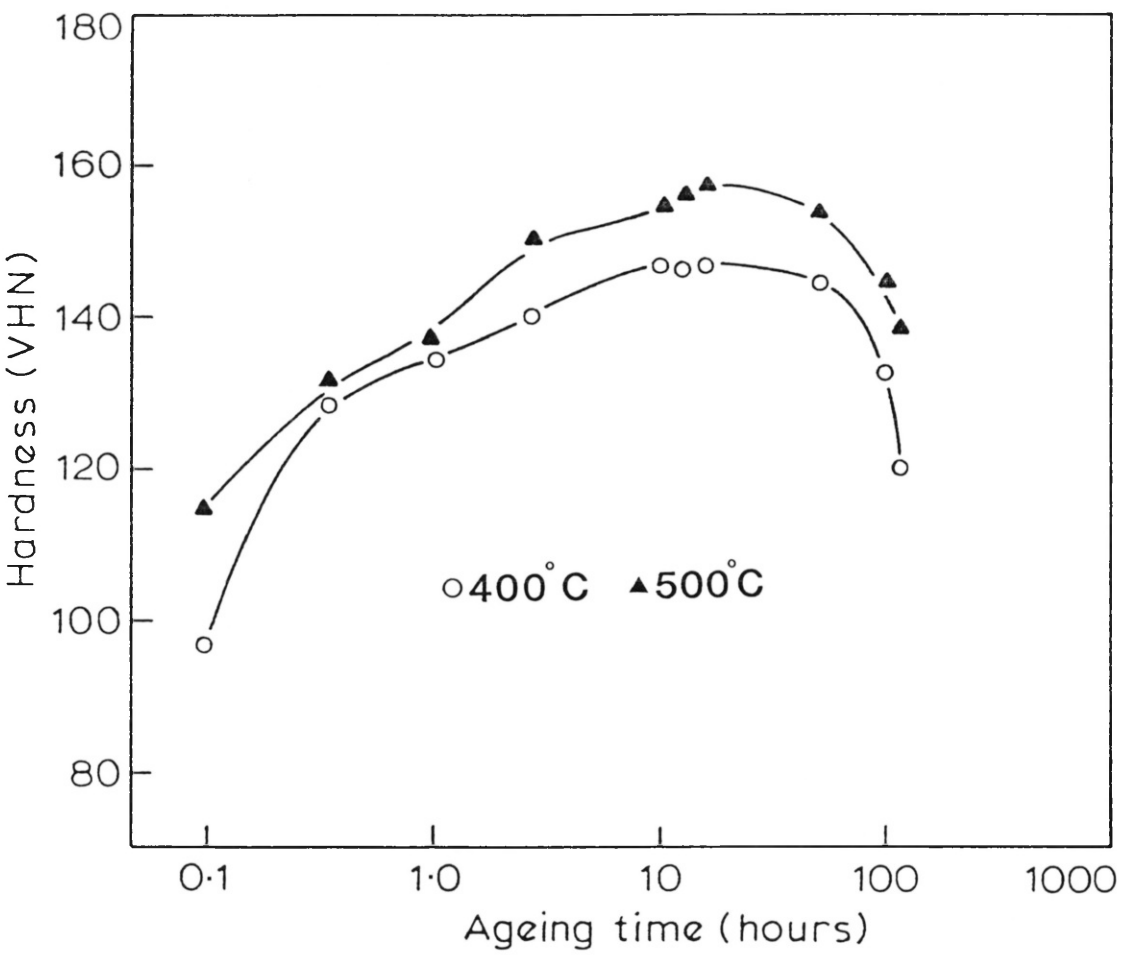


Figure 7.12. Artificial ageing response at 190°C of the extrudates produced at 400 and 500°C, 20:1, 3 mm/sec and NA 2 months.

revealed co-precipitation of δ' and S phases homogeneously distributed within the microstructure; additionally, S phase was found to nucleate heterogeneously at the loose dislocations within the subgrains, at the subgrain boundaries and upon the dislocation loops [Figures 7.10(c) and (d)].

7.3. Discussion

7.3.1. As Extruded Mechanical Properties

The general increase in ultimate tensile strength (and the hardness values) with increasing extrusion temperature and extrusion ratio is suggested to be due, principally, to the solutionising effect of the temperature of the emergent extrude. This is increased due to either increased thermal energy or conversion of work to heat during the process. TEM revealed that extrudates produced at 500^{o}C remained single phase during extrusion whilst at lower temperatures the press quenched microstructures were found to contain coarse Al-Cu-Mg based phase particles. Also, it was found that the number density of these particles was maximum within the extrudates produced at the lowest processing temperature and extrusion ratio. It would be, therefore, expected that with increasing process heating the strength of the extrudates processed at lower temperatures would increase rapidly as more of the Al-Cu-Mg based particles would go into solution. Such an interpretation is consistent with the present observations. These results also indicate that any strengthening due to reduction in subgrain size at lower temperatures is clearly outweighed by the solutionising effect of higher process temperatures.

The increase in proof stress values with extrusion ratio at lower temperatures may again be attributed to the solutionising effect. At the highest processing temperature on the other hand, the volume fraction recrystallised continued to increase with increasing extrusion ratio and is associated with a decreasing proof stress. At lower temperatures (viz. at 450^{o}C) the volume fraction recrystallised also increased over the extrusion ratio range but the increase in proof stress due to the solutionising effect clearly dominated and it was most significant at the lowest temperature where the recrystallisation was minimum.

Unlike the ultimate tensile strength and the proof stress, ductility was not found to be sensitive to the processing variables. The results indicate that ductility decreased with increasing volume fraction of the Al-Cu-Mg based particles (and with decreasing recrystallisation), and it increased with increasing volume fraction of recrystallised grains within the microstructure (as at the same time the volume fraction of the Al-Cu-Mg based particles decreased). It is suggested that the role of the coarse Al-Cu-Mg based particles situated at the grain and subgrain boundaries was to facilitate the crack nucleation process, whereas, the role played by the small recrystallised grains nucleated adjacent to the original boundaries was to direct the crack path, thereby inhibiting the crack propagation process. In the latter case, the result was an increase in ductility.

7.3.2. Natural and Artificial Ageing Response

As indicated in Figure 7.12, the 400^{o}C extrudate exhibited a much smaller natural ageing response than the 500^{o}C extrudate. It may be explained as follows: the superior natural ageing response of an Al-Li-Cu-Mg alloy is largely dependent on the formation and growth of GP zones of the Al-Cu-Mg system during room temperature ageing (see section 5.3.5). Also, formation of such GP zones necessarily depends on the solute (viz. Cu + Mg) supersaturation and the vacancy supersaturation. In the latter case, the vacancies must be "free" i.e not bound at trap sites, if they are to enhance GP zone formation kinetics. In the case the of 400^{o}C extrudate, TEM revealed the presence of Al-Cu-Mg based coarse particles throughout the microstructure (see section 7.2.6) such that the solute supersaturation is limited. Also, the total vacancy concentration decreased with decreasing process temperatures. Moreover, the dislocation density was higher within the 400^{o}C extrudate (see section 7.2.6) and the dislocations act as sinks for the vacancies released during natural ageing. These observations imply that the poor natural ageing response of the 400^{o}C extrudate was due to the low solute and vacancy supersaturation in the material.

The artificial ageing characteristics of the naturally aged extrudates may be interpreted as follows. In the case of the 500^{o}C extrudate, both $\delta'(Al_3Li)$ and $S(Al_2CuMg)$ phase precipitates contributed to the hardening of the material, whilst, in the case of the 400^{o}C extrudate the contribution of S phase to overall hardening of the material was negligible. The result was a much higher peak hardness value in

the case of the 500°C extrudate. However, as would be expected for a material with a prior natural age (see Chapter 4) the hardness values did not increase after 24 hours at 190°C. In the naturally aged material TEM revealed the presence of large numbers of helices implying that the loose dislocations present in the press quenched extrudates acted as sinks for the unbound vacancies and this reduced the numbers of free vacancies available to assist homogeneous S precipitation. Therefore, although, TEM indicated the presence of homogeneous S in the peakaged microstructure of the 500°C extrudate, the number density of homogeneous S precipitates formed in this material was clearly reduced and the result was that the onset of averaging observed after 24 hours in solution treated and artificially aged material was inhibited but no further hardness increase was observed [c.f. solution treated, naturally aged and artificially aged material (see Chapter 8 for details)].

These results additionally imply that the extrudates produced at temperatures below 500°C cannot be artificially aged directly without prior solution heat treatment.

7.3.3. Recrystallisation

The mechanisms responsible for recrystallisation described in section 7.2.5 were a clear indication that recrystallisation occurred under the influence of higher deformation rates and temperatures during the deformation process. This is strongly supported by the fact that during torsion tests even when the deformation was stopped after quenching, the resultant microstructures clearly revealed recrystallisation. Furthermore, the extrusion performed at lower temperatures did not subsequently recrystallise during the solution soak and even when the extrudates were allowed to cool in air, the structures remained essentially unchanged. This inhibition of static recrystallisation in Zr containing Al-Li alloys has previously been observed by Makin and Stobbs (156) who attributed the phenomenon to the solute drag of lithium on grain boundaries together with boundary pinning by Al_3Zr precipitates (see section 2.3.3. for details).

Examination of the extrudate grain structures revealed that high angle boundaries of original grains were the nucleation sites for recrystallised grains, often forming a banded structure as was also observed by Parson and Sheppard (152)

in Al-Li-Mg alloys. At lower deformation rates recrystallisation occurred via a grain boundary bulging mechanism i.e. by local boundary migration driven by dislocation density differences across the grain boundaries. Recrystallisation by this mechanism could occur either during or immediately after deformation without any incubation period. The present observations indicate that nucleation of recrystallised grains by this mechanism occurred mostly during the deformation process proper.

At higher deformation rates recrystallisation occurred by rotation recrystallisation. Humphreys and Drury (143) showed this mechanism to be responsible for recrystallisation in Al-Mg alloys. The authors attributed this phenomena to the low grain boundary mobility in Mg containing Al alloys; a magnesium solute drag mechanism is understood to be responsible for this. In this mechanism, the subgrains formed adjacent to the original high angle boundaries are the potential nuclei for recrystallisation. These subgrains undergo progressive lattice rotations during the deformation process giving rise to the formation of highly misoriented subgrains or altogether new grains, the driving force for rotation being the inhomogeneous deformation accumulated at the original grain boundary. The authors (143) suggested that in pure aluminium the grain boundaries are highly mobile such that they will migrate rapidly and consume the adjacent regions of high dislocation density, thus preventing the build up of the inhomogeneous deformation at the boundary. Like magnesium, lithium is also reported to segregate to the grain boundaries (156) and hence the occurrence of rotation recrystallisation in the present alloy system may be attributed to the solute drag effect of both magnesium and lithium on grain boundaries.

The present observations showed that recrystallisation in this material increased with increasing strain and temperature. This is consistent with the recent report by Skillinberg and Ashton (179) who also observed an increase in recrystallisation with increasing strain and temperature in AA 8090 alloys. These observations may be explained as follows: with increasing strain, the amount of inhomogeneous deformation at the original grain boundary region increases providing the driving force for subgrain rotation. Also, tilting or rotation of the subgrains involves dislocation climb which is enhanced by increasing temperature leading to the formation of recrystallisation nuclei more rapidly.

7.4. Summary

1. The homogenised alloy A1 was extruded over a wide range of processing conditions (viz. the initial billet temperatures varied from 400 to 500^{o}C, the round bar extrusion ratios varied from 20:1 to 80:1 and the ram speeds utilised were in the range of 3-15 mm/sec). The material could not be extruded (within the load capacity of the press employed) below 350^{o}C using an extrusion ratio of 20:1 and the lowest ram speed. Also, the highest processing temperature was restricted to the use of an initial billet temperature of 500^{o}C in order to avoid incipient melting. Data on variation in extrusion pressure requirement with the process parameters indicates that the overall pressure requirement increases with increasing extrusion ratios and ram speeds, and decreases with increasing extrusion temperatures.

2. Under all processing conditions, extrusion produced microstructures which vary through the extrude section: the surface was fully recrystallised whilst the core was essentially unrecrystallised. Increasing the extrusion ratio, extrusion temperature and ram speed increased the depth of the recrystallised surface layer and the core increasingly exhibited partial recrystallisation. It is suggested that recrystallisation is most sensitive to extrusion ratio such that recrystallisation at higher temperatures is enhanced only at higher strain.

3. It is proposed that recrystallisation is dynamic and occurs by a grain boundary bulging mechanism and by rotation recrystallisation.

4. The extruded structure is extremely resistant to static recrystallisation during subsequent heat treatment.

5. Under all processing conditions, the as extruded microstructures exhibited well recovered subgrain structures. The subgrain size decreased with decreasing temperature whilst with increasing extrusion ratio, the subgrains became more closely spaced and elongated along the extrusion

direction. A change in the subgrain morphology across the extrude section was also observed as a result of the presence of a strain gradient across the extrude section. The subgrain size varied from 1-10 μm and the subgrains were found to be more misoriented with increasing strain. Additionally, under any extrusion condition, the subgrains formed adjacent to the original boundary were more misoriented. It is suggested that these subgrains are the potential nuclei for recrystallisation and are consequently responsible for the banded nature of the recrystallised grains in this alloy system.

6. Extrudates produced at 500^{o}C remained single phase during extrusion whilst at lower temperatures coarse ($\lesssim$ 1 μm) copper rich Al-Cu-Mg based particles were produced as a result of the thermal exposure. The presence of these particles influences the mechanical properties of the as extruded material.

7. The tensile properties of the as extruded material are affected by the processing variables. The tensile strength increases with increasing temperature and extrusion ratios and this is attributed to the solutionising effect as the process temperature increases during extrusion. The variables have a similar effect on proof stress except at the highest processing temperature where the proof stress values decrease with increasing extrusion ratios. This is consistent with the increased volume fraction recrystallised in the microstructures. Ductility is relatively insensitive to the processing variables but is least where the volume fraction of Al-Cu-Mg based particles is greatest and the degree of recrystallisation is least after extrusion at 400^{o}C. It is suggested that the Al-Cu-Mg based particles situated at the grain boundaries facilitates the crack nucleation process, whereas, the small recrystallised grains nucleated adjacent to the original boundaries divert the crack path and therefore, inhibit the crack propagation process. In the latter case, the result is the increased ductility.

8. The press quenched extrudates respond to natural ageing; however, the extrudates processed at the lowest temperature exhibit a much smaller natural ageing response. It is suggested that this is due to the low solute (i.e. Cu + Mg) and vacancy supersaturation in the material.

9. Press quenched extrudates, naturally aged and subsequently aged at 190^{o}C, showed artificial ageing characteristics which varied with extrusion temperatures: extrudates produced at the lowest temperature always had inferior mechanical properties. It is suggested that in the case of 500^{o}C extrudate, both $\delta'(Al_3Li)$ and $S(Al_2CuMg)$ phase precipitates contributed to the hardening of the material, whilst, in the case of 400^{o}C extrudate the contribution of S phase to the overall hardening of the material is negligible. In the case of the 500^{o}C extrudate, the hardness values did not increase after 24 hours at 190^{o}C as would be expected for a material with a prior natural age. It is suggested that this is due to the reduced homogeneous S precipitation in the material: the loose dislocations present in the press quenched extrudates act as sinks for the unbound vacancies and thus reduce the numbers of free vacancies available to assist homogeneous S precipitation.

CHAPTER EIGHT

HEAT TREATED EXTRUDATES - THEIR MICROSTRUCTURE AND MECHANICAL PROPERTIES

8.1. Introduction

The work presented in this chapter is concerned with the microstructure and mechanical properties of the heat treated extrudates. Initially, the artificial ageing response of the extrudates is established in the T6 condition, for various extrusion parameters and ageing temperatures. The effect of prior natural ageing on the artificial ageing characteristics of the extrudates is also discussed. The age hardening characteristics of the materials are discussed in terms of the microstructural changes which take place.

The tensile properties viz. the strength and ductility of the heat treated (underaged, peakaged and overaged) extrudates are evaluated for a wide range of extrusion processing variables. The fracture toughness properties of the heat treated extrudates as functions of extrusion temperatures are presented. The effects of variation in heat treatment involving natural ageing, stretching, and combination of natural ageing and stretching on the strength, ductility and fracture toughness are also discussed in relation to the microstructural changes produced.

The fractured surfaces of failed tensile and fracture toughness specimens are characterised in detail and variations in the failure modes are correlated with the development and morphology of typical precipitate phases in the material and the deformation mechanisms involved.

8.2. Results

8.2.1. Ageing Response

The artificial ageing curves for the 20:1 extrudates produced at 400^{o}C and 500^{o}C respectively are presented in Figure 8.1. The extrudates were solutionised for 20 minutes at 530^{o}C prior to ageing at 190^{o}C. The Figure reveals that extrusion at

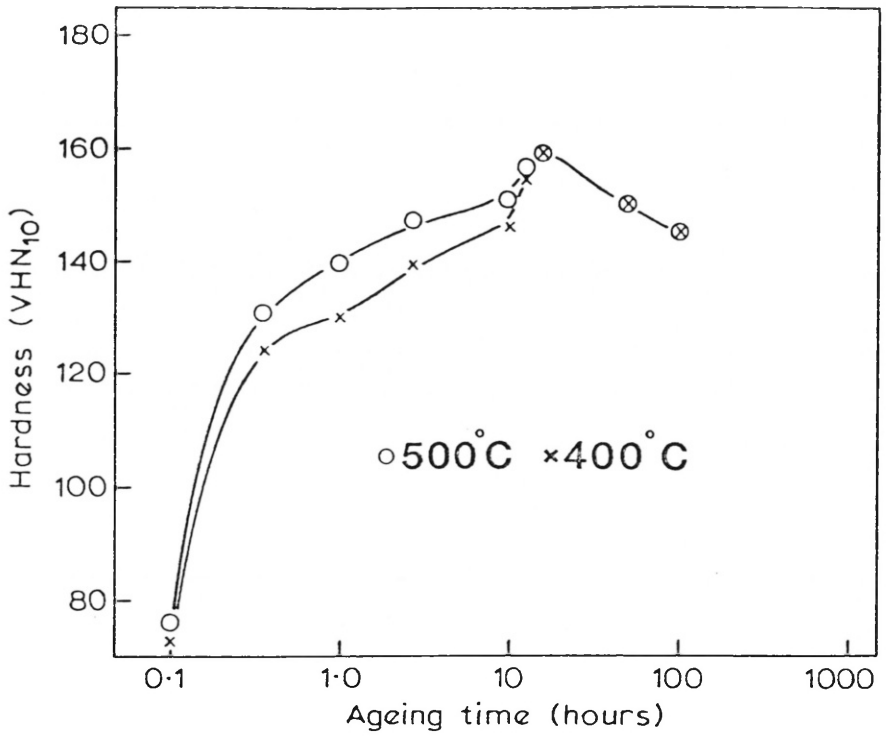


Figure 8.1. Ageing response of the extrudates (produced at 400°C and 500°C, 20:1, 3 mm/sec) at 190°C with prior solution treatment at 530°C for 20 minutes.

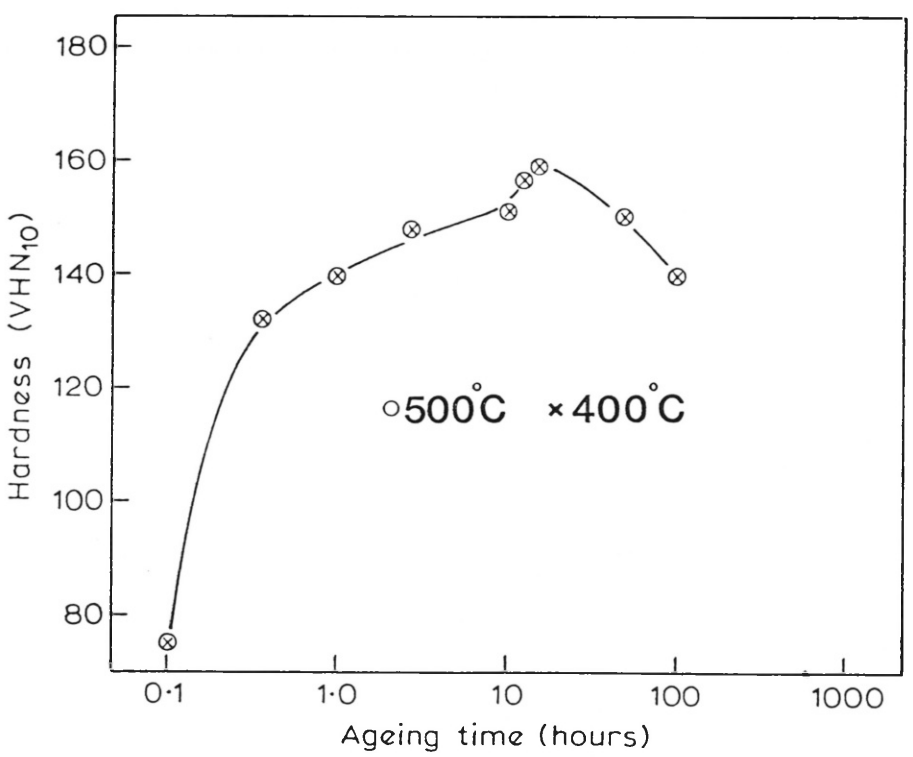


Figure 8.2. Ageing response of the extrudates (produced at 400°C and 500°C, 20:1, 3 mm/sec) at 190°C with prior solution treatment at 530°C for 40 minutes.

either 400°C or 500°C resulted in the same peak hardness (viz. 159 V.H.N) but the 400°C extrudate had inferior properties prior to peak (viz. 24 hours at 190°C). Figure 8.2 shows the artificial ageing curves for the extrudates produced at similar extrusion condition but solutionised for 40 minutes at 530°C before ageing. It may be noted that increasing the solutionising time to 40 minutes did not affect the ageing curve of the 500°C extrudate (compare Figure 8.2 with Figure 8.1) but brought the response of the 400°C extrudate up to that of the 500°C extruded material. Later, in this investigation, 40 minutes at 530°C was, therefore, adopted as the standard solution treatment for extrudates produced below 500°C.

Figure 8.3 shows the artificial ageing response at 170°C. As would be expected, a higher peak hardness value (e.g. 168 V.H.N. for the 500°C extrudate) was obtained after 72 hours of ageing. However, Figure 8.3 revealed that the 400°C extrudate had slightly inferior properties in the peakaged and immediately post peak conditions. Figure 8.4 shows the artificial ageing response of the extrudates produced at different extrusion ratios (50:1 and 80:1) and at the highest processing temperature. Comparison of Figure 8.4 with Figure 8.2 suggests that in the T6 condition, the artificial ageing response of the present alloy at 190°C as evaluated by the hardness measurements is essentially the same under all extrusion conditions.

Since the natural ageing response of alloy A 2 was found to bring about interesting modifications in the precipitation mechanisms (see Chapter 4 and 5), the next step of this investigation was to examine the natural ageing characteristics of the extruded alloy A1. The extruded materials produced at 500°C were solution treated, water quenched and were subjected to natural ageing. The natural ageing response of alloy A1 was recorded over a period of six months and it was found that the resultant natural ageing curve was identical to that for alloy A 2. In a further experiment, in order to determine the effects of natural ageing upon subsequent artificial ageing, the alloy was solution treated, water quenched and naturally aged for 24 hours prior to ageing at 190°C. The results are shown in Figure 8.5. The initial ageing response (i.e. up to the peak aged condition) at 190°C remained unaltered but the onset of overageing otherwise observed after 24 hours at 190°C in a material without a prior natural age (compare Figure 8.5 with Figure 8.2) is inhibited. However, Figure 8.5 revealed that the 400°C extrudate had slightly inferior properties in the peak and post peak aged conditions compared to the 500°C

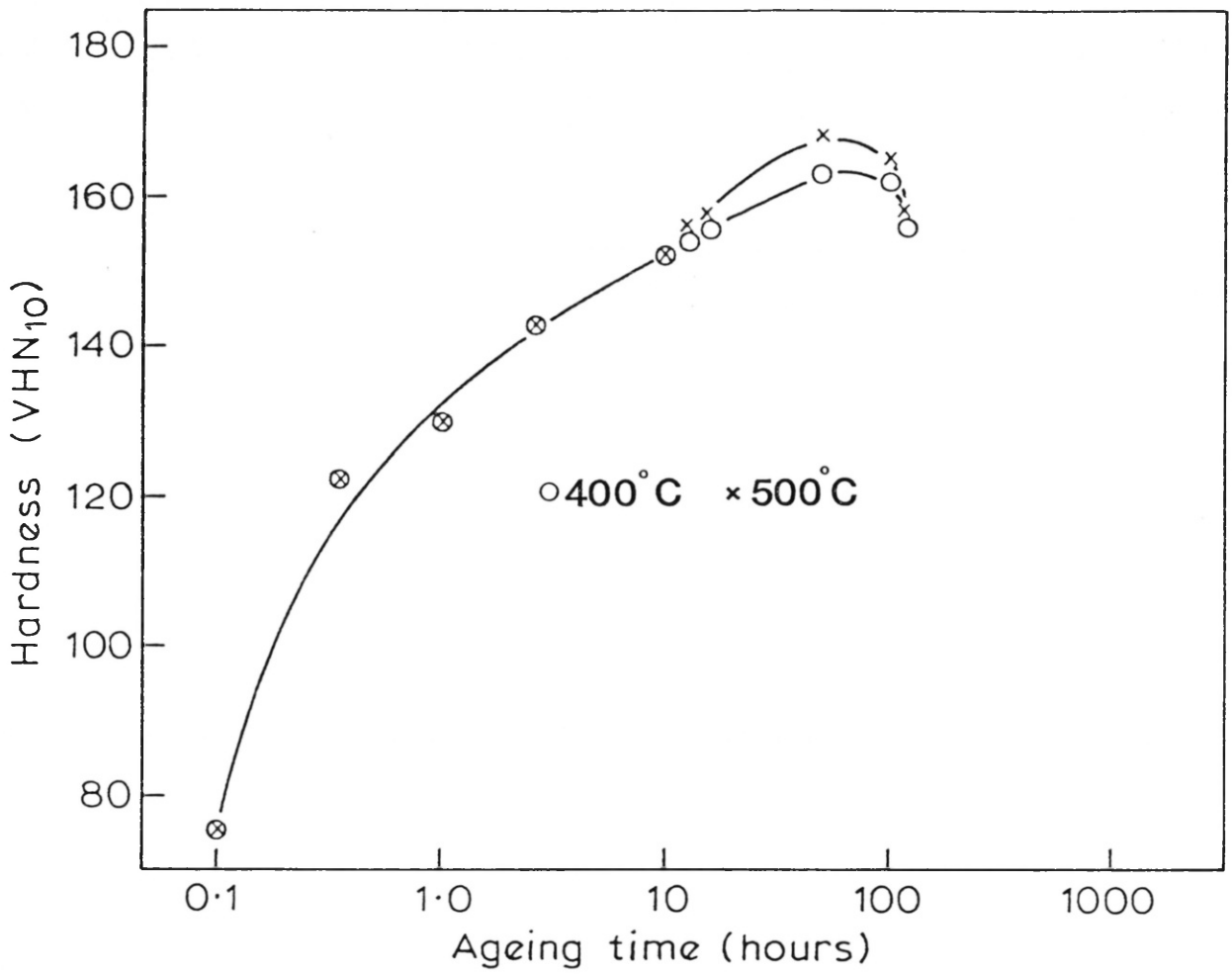


Figure 8.3. Ageing response of the extrudates (produced at 400 and 500°C, 20:1, 3 mm/sec). at 170°C (T6 temper).

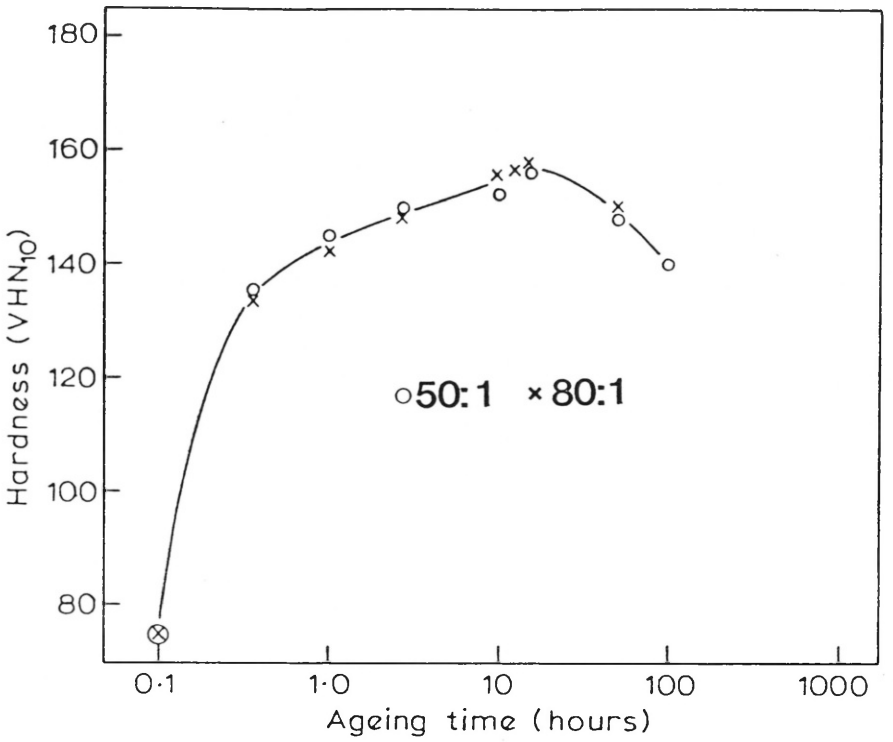


Figure 8.4. Ageing response of the extrudates (produced at 500°C, 50:1 and 80:1, and 3 mm/sec) at 190°C (T6 temper).

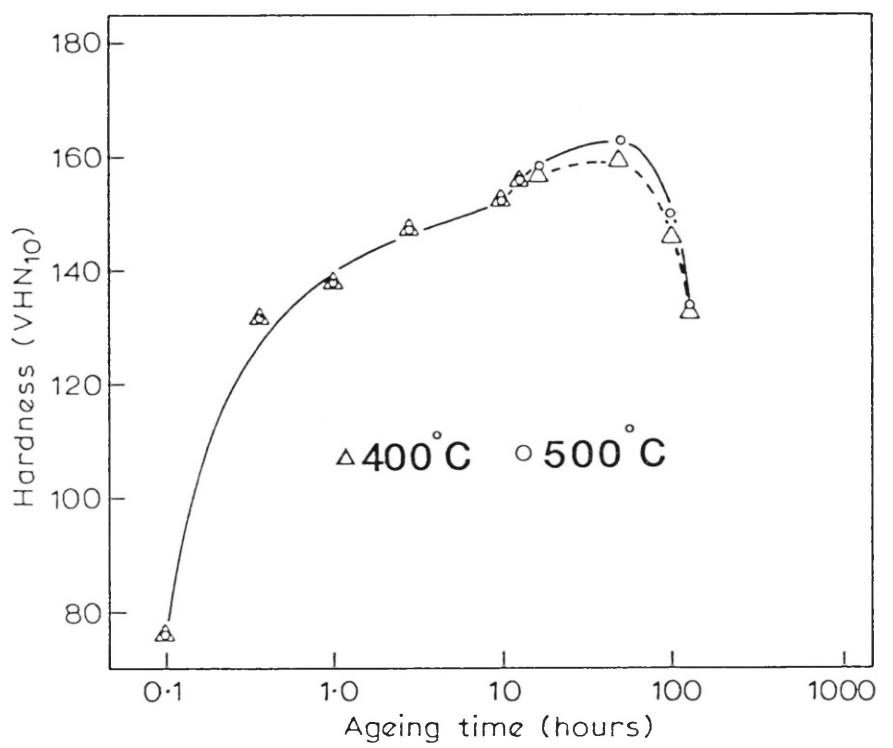


Figure 8.5. Ageing response of the extrudates (produced at 400 and 500°C, 20:1, 3 mm/sec) at 190°C with a prior natural age of 24 hours.

extrudate.

A detailed microstructural examination was carried out to characterise the precipitation reactions and the results of the microstructural studies are reported in the following sections.

8.2.1.1. Microstructure of the Alloy without Natural Ageing

Freshly solution treated and water quenched material revealed a very clean microstructure similar to the as quenched microstructure of alloy A1 described in section 4.2.2.1. Subsequent heat treatment initially caused a general growth of the individual δ' particles; even after 5 hours at 190°C, no heterogeneous precipitation of S and T_1 phase could be detected at the subgrain boundaries. Figure 8.6 (a) shows the δ' precipitation and Figure 8.6 (b) shows the absence of any S or T_1 precipitate phase at the subgrain boundaries in material aged for 5 hours at 190°C. Prolonged ageing at 190°C, however, brought about further microstructural changes in terms of additional precipitate phases. In the peakaged condition (i.e. after 24 hours at 190°C), besides well developed δ' particles, heterogeneous precipitation of S and T_1 phase at the subgrain boundaries were clearly imaged using TEM [Figure 8.6(c)]. Additionally, TEM revealed a homogeneous distribution of S phase within the microstructure (Figure 8.6(d)); this contrasts with alloy A 2 where, in the peakaged condition homogeneously nucleated S phase precipitates could not be detected. Prolonged ageing for 72 hours coarsened the δ' precipitates and increased the homogeneous S precipitate density in the microstrucutre.

8.2.1.2. Effect of Natural Ageing

In order to examine the effect of natural ageing upon the quenched material, specimens were solution treated, water quenched and aged at room temperature. TEM revealed that the major change in structural morphology was the growth of δ' particles; no loop formation could be detected in the material with a prior natural age of up to 2 weeks. However, in a material naturally aged for about a month, TEM clearly revealed the presence of dislocation loops and helices (Figure 8.6(e)). These results clearly contrast with the observations made earlier in this investigation for alloy A 2 (see chapter 4), where loop formation was detected in the material within 24 hours of natural ageing. It may be noted that the alloy A 2 was also solution

Figure 8.6.

(a) TEM DF image showing δ' precipitation imaged using (100) superlattice reflection; <110> Al orientation. Material treatment: ST 530°C, WQ, AA 5 hours at 190°C.

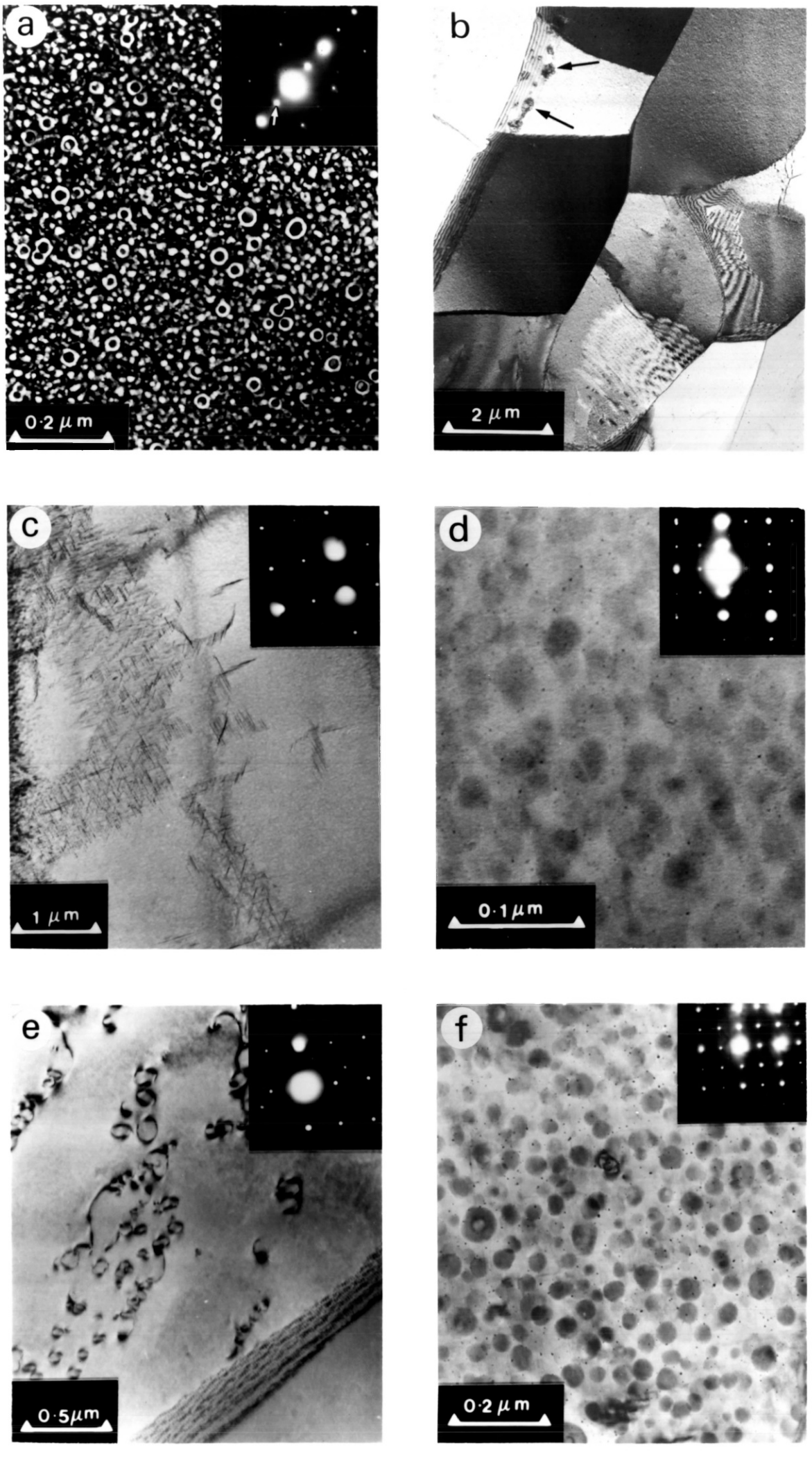
(b) BF image showing subgrain boundaries free of any S and T_1 precipitate. The arrows show precipitation of coarse grain boundary precipitates. Material treatment: ST 530°C, WQ and AA 5 hours at 190°C.

(c) BF image showing heterogeneous S and T_1 precipitation; close to <112> Al orientation. Material treatment: ST 530°C, WQ, AA 24 hours at 190°C.

(d) BF image showing homogeneous S precipitation; <100> Al orientation. Material treatment: ST 530°C, WQ, AA 24 hours at 190°C.

(e) BF image showing precipitation of dislocation loops; Close to <112> Al orientation. Material treatment: ST 530°C, WQ, NA 1 month.

(f) BF image showing homogeneous S precipitation; <100> Al orientation. Material treatment: ST 530°C, WQ, NA 24 hours and AA 24 hours at 190°C.


a
0·2 μm
b
2 μm
c
1 μm
d
0·1μm
e
0·5μm
f
0·2 μm

treated at 530°C.

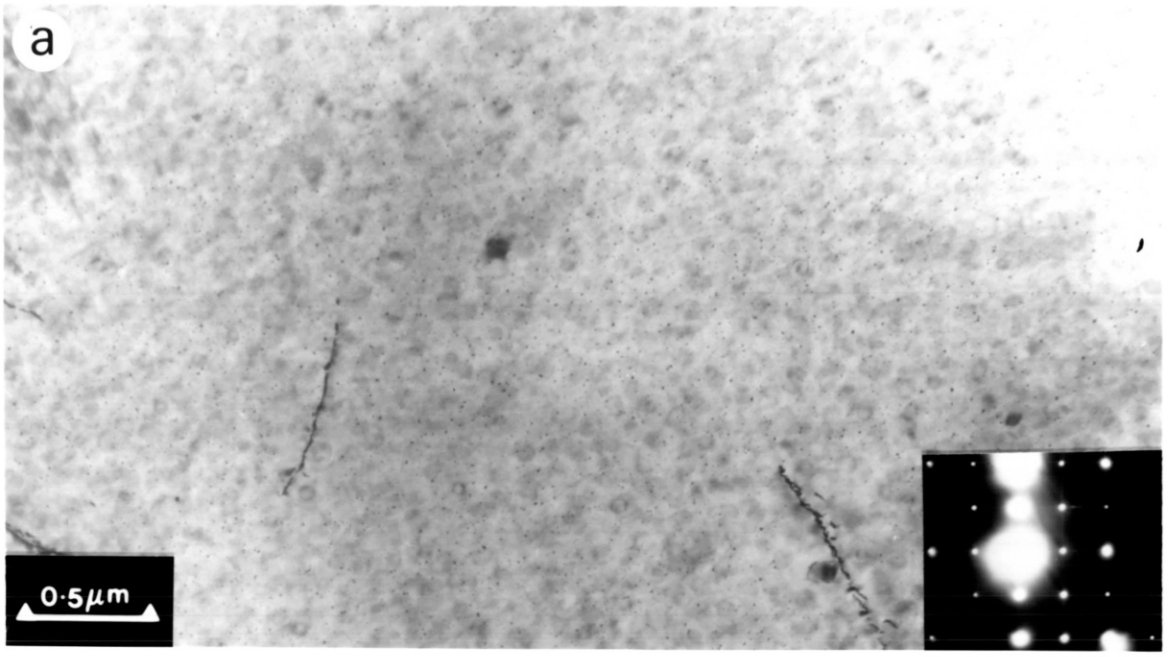
The quenched samples of alloy A1 aged for 24 hours at room temperature were subjected to artificial ageing at 190°C for 24 hours. The resultant microstructure (Figure 8.6(f)) clearly revealed an increased density of homogeneous S precipitates compared to that in the material without a prior natural age. In a further experiment, the quenched samples were naturally aged for a month and subsequently aged at 190°C for 24 hours. The corresponding microstructure revealed a well developed picture of homogeneous S precipitation (Figure 8.7(a)].

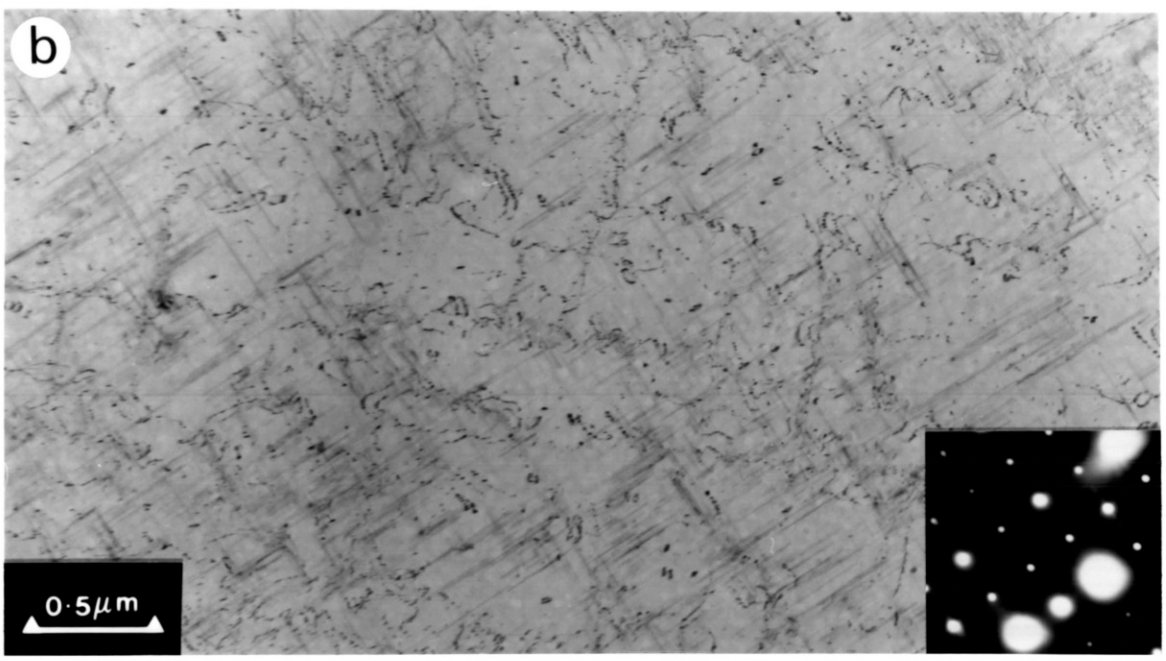
8.2.2. The Effect of a Preageing Stretch, and Combination of Natural Ageing and a Preageing Stretch on S Phase Precipitation.

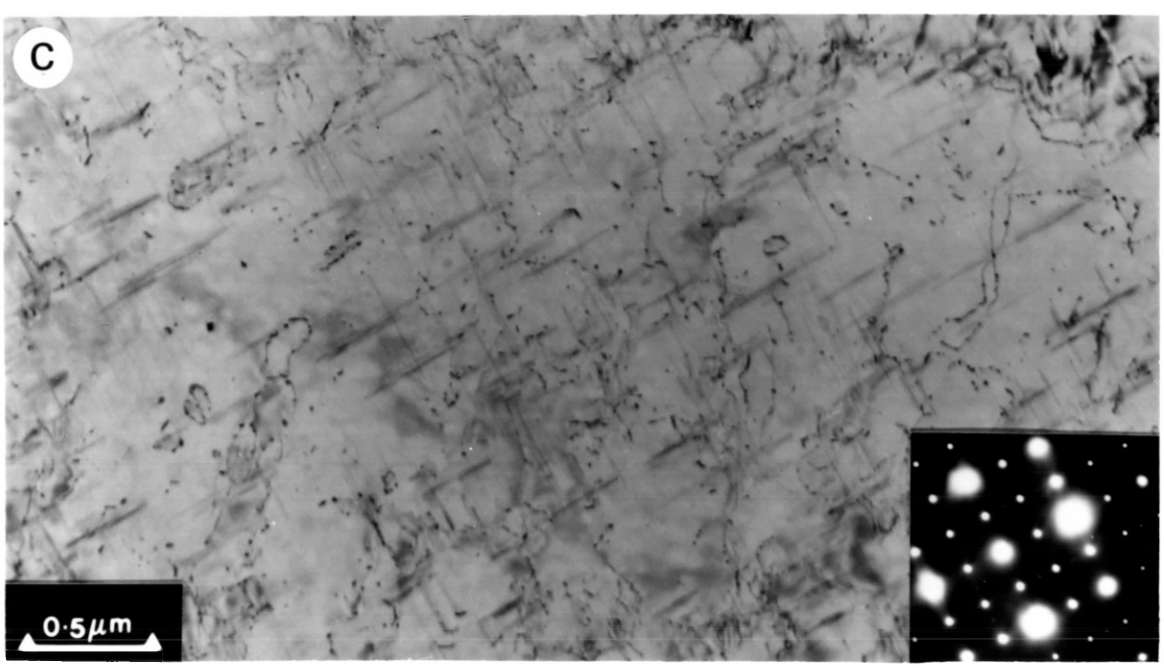
In the absence of quenched in defects in lithium containing aluminium alloys, a preageing stretch has the effect of accelerating the nucleation of S phase precipitation by providing nucleation sites in the form of dislocation defect structures (66). In the present investigation, the extruded materials were solution treated, water quenched, stretched (2 %) and then artificially aged at 190°C for 24 hours. The resultant microstructures revealed that S phase has formed heterogeneously on dislocations introduced by the stretch; Figure 8.7(c) shows the laths of S phase in [100] Al orientation. In a further experiment, the quenched materials were naturally aged for a month, stretched (2 %) and then aged at 190°C for 24 hours. The resultant microstructures [Figure 8.7 (b)] revealed that the introduction of natural ageing did not alter the heterogeneous mode of S precipitation in the presence of a preageing stretch; this is evidenced by the end on laths of S on the dislocation loops as shown in Figure 8.7 (b). However, comparison of Figure 8.7 (b) with Figure 8.7 (c) clearly indicated that the presence of natural ageing in the heat treatment cycle had the effect of producing more uniform and much finer precipitation of S upon ageing at 190°C.

These micrographs additionally revealed that at the present alloy composition, T_1 precipitation is very limited and S is the dominant precipitating phase of the two.

Figure 8.7. TEM BF images showing
(a) Homogeneous S precipitation; <100> Al orientation. Material Treatment: ST 530°C, WQ, NA 1 month, AA 24 hours at 190°C.
(b) Heterogeneous S precipitation, <100> Al orientation. Material Treatment: ST 530°C, WQ, NA 1 month, 2 % stretch and AA 24 hours at 190°C.
(c) Heterogeneous S precipitation; <100> Al orientation. Material treatment: ST 530°C, WQ, 2% stretch, and AA 24 hours at 190°C.


a
0·5μm


b
0·5μm


c
0·5μm

8.2.3. Coarse Grain Boundary Precipitates in the Heat Treated Material

In the solution treated material, TEM revealed that at the grain boundaries the only second phase particles were rich in iron (viz. Al-Fe-Cu based phase; see Chapter 6). During subsequent artificial ageing heat treatment at 190°C, TEM detected the formation of additional small precipitates at the grain and subgrain boundaries; x-ray EDS analysis suggested that all of them contained substantial amounts of copper. In the underaged condition, the number density of these precipitates was, in general, low and the precipitates had an average diameter of about 0.1 μm. These particles (as shown by arrows in Figure 8.6(b)) were often surrounded by dislocation structures. Ageing the material up to peak strength caused these precipitates to grow in size and also caused the formation of many more coarse copper rich precipitates at the grain boundaries. These precipitates were always surrounded by δ' free zones. Prolonged ageing beyond the peak aged condition caused further growth of these precipitates and the width of the PFZs was found to increase.

Figure 8.8(a) shows the presence of coarse grain boundary precipitates in a peakaged 80:1 extrudate. The corresponding dark field image as shown in Figure 8.8 (b) illustrates clearly the absence of δ' particles surrounding the precipitates. It may be noted that δ' particles on either side of the boundary were clearly imaged; this implied that the coarse precipitates have formed along a subgrain boundary. Quantitative X-ray EDS analysis of these particles suggested that the precipitates were rich in copper and had a composition range of 13-17 % copper, 2-5 wt. % magnesium and balance aluminium. It would appear that these particles also contain lithium, as local depletion of lithium containing phase δ' (Al_3Li) has occurred in the region surrounding these particles. Figure 8.8 (c) also shows formation of coarse grain boundary precipitates in a peakaged material. Quantitative X-ray EDS analysis for these precipitates suggested a similar composition to that obtained for the precipitates shown in Figure 8.8 (a). Figure 8.8 (c) also shows an intragranular Al-Fe-Cu based particle. In the present investigation many more grain boundary precipitates were examined and it was found that the precipitates associated with dislocation structures were very difficult to image using bright field imaging conditions unless carefully tilted (Figure 8.8 (d)). The grain boundary precipitates also gave in general a very poor contrast.

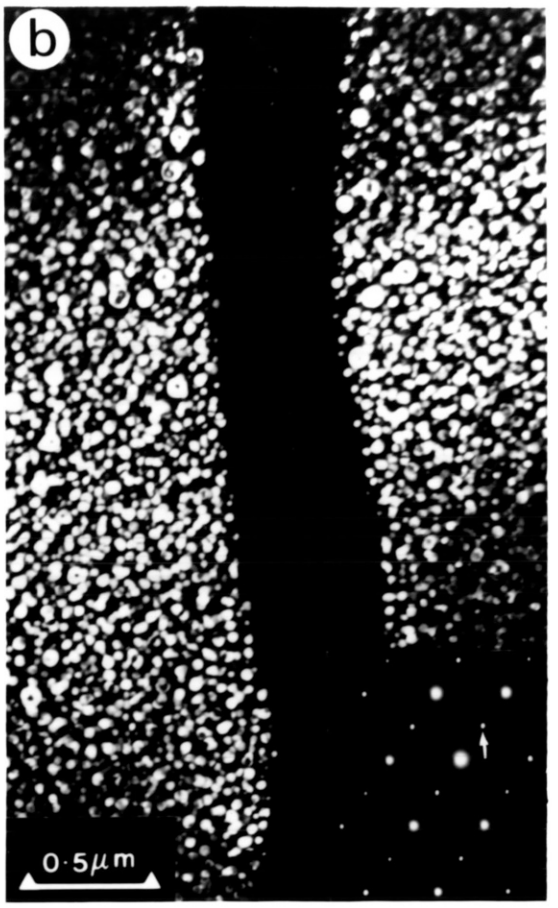
Figure 8.8. (a) BF image showing coarse grain boundary precipitates; <110> Al orientation. Material treatment: ST 530°C, WQ, AA 24 hours at 190°C.

(b) DF image of 8.8(a) showing δ' PFZs; imaged using (100) superlattice reflection.

(c) BF image showing coarse grain boundary precipitates. Material treatment: ST 530°C, WQ, AA 24 hours at 190°C. The micrograph also shows an intragranular Al-Fe-Cu based particle.

(d) BF image showing coarse grain boundary precipitates associated with dislocation structures. Material treatment: ST 530°C, WQ, AA 24 hours at 190°C.


a
0·5μm


b
0·5μm


c
1 μm


d
0·3μm

Earlier in this investigation, it was reported that many of the subgrain boundaries in this material are not of low angle tilt boundary type;rather often they had misorientations in excess of 5-7^{o}; they may be better classified, therefore, as medium angle grain boundaries (180). Earlier work in this investigation (see chapter seven) also showed that the subgrains become more misoriented with increasing extrusion ratio. Inspection of the fully heat treated materials by TEM revealed that formation of the copper rich coarse precipitates at the subgrain boundaries depends on the angle of misorientation across the sub boundaries. In a fully heat treated 80:1 extrudate, it was found that majority of the sub boundaries acted as nucleation sites for the coarse precipitates rather than the S or T_1 precipitates. The result was that these coarse precipitates almost formed a continuous precipitate film along those subgrain boundaries. TEM revealed that nucleation of coarse precipitates could take place at sub-boundaries having angles of misorientation as low as 3^{o} whereas formation of S and T_1 precipitation was detected only at the lower angle tilt boundaries.

8.2.4. Mechanical Properties of Heat Treated Material

8.2.4.1. Tensile Properties

The tensile properties were measured along the longitudinal direction of the heat treated extrudates. The variation in tensile properties in the underaged (UA), peakaged (PA) and overaged (OA) conditions (T6 temper) are presented as functions of three extrusion ratios (viz. 20:1, 50:1 and 80:1) and two extrusion temperatures viz. 400^{o} and 500^{o}C in Figures 8.9 and 8.10. The tensile data are also presented in tabular form in Tables 8.1 and 8.2.

The tensile data revealed that variations in extrusion ratio had only a minor effect on the ultimate tensile strength (UTS) and the proof stress (PS) values of the extrudates in any ageing condition; the 80:1 extrudates exhibited slightly inferior UTS and PS values, this effect being more notable at the highest processing temperature and in the underaged condition. Variations in extrusion temperature affected the strength values: decreasing extrusion temperature had the effect of raising the UTS and PS values in all ageing conditions. The tensile data also revealed that ductility values always increased from the underaged to the overaged

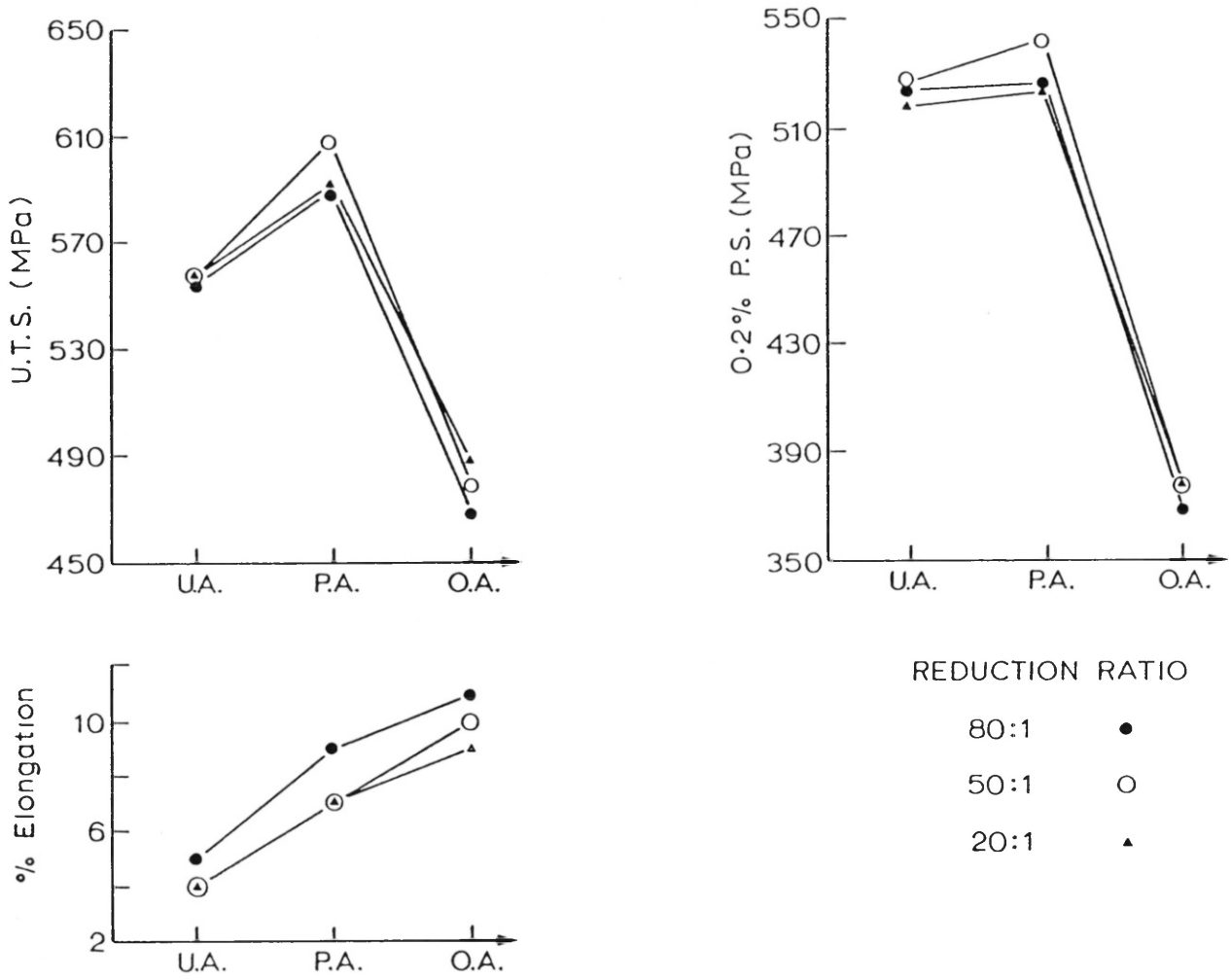


Figure 8.9. Longitudinal tensile properties of the heat treated extrudates (T6 condition) extruded at 400°C.

Table 8.1 : Longitudinal Tensile Properties* of the Heat Treated (T6 Condition) Extrudates (Initial Billet Temperature = 400°C)

Extrusion Ratio	Ageing Condition		
	Under Aged (5 Hours at 190°C)	Peak Aged (24 Hours at 190°C)	Over Aged (100 Hours at 190°C)
20:1	UTS (MN/m^2) : 557	591	487
	0.2 % PS (MN/m^2) : 518	523	377
	% Elongation : 4	7	9
50:1	UTS : 557	608	478
	0.2 % PS : 527	542	378
	% Elongation : 4	7	10
80:1	UTS : 556	590	468
	0.2 % PS : 525	526	368
	% Elongation : 5	9	11

* Each value is the average of two values obtained from two identical tests.

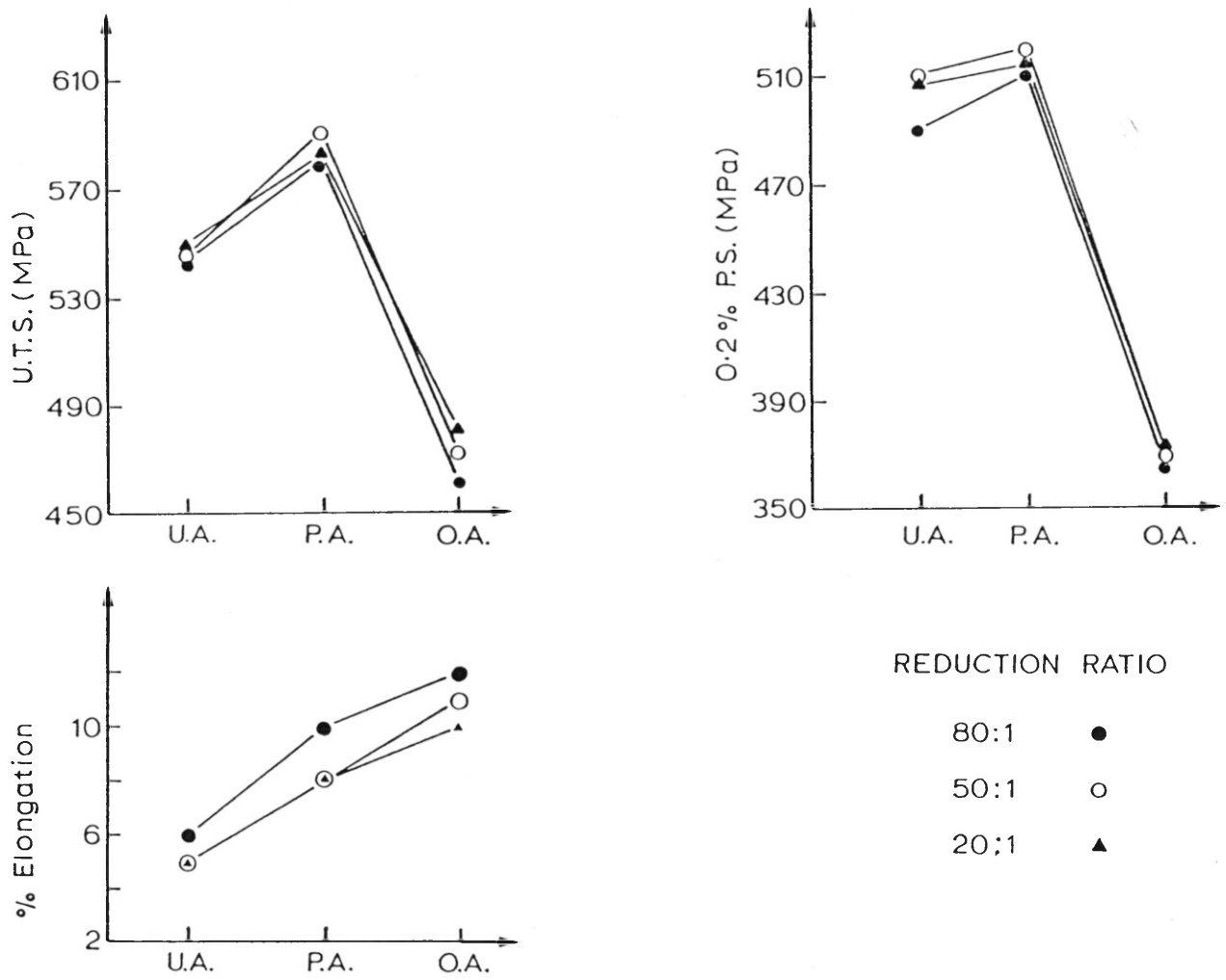


Figure 8.10. Longitudinal tensile properties of the heat treated (T6 condition) extrudates produced at 500°C.

Table 8.2 : Longitudinal Tensile Properties* of the Heat Treated (T6 Condition) Extrudates (Initial Billet Temperature = 500°C)

Extrusion Ratio	Ageing Condition		
	Under Aged (5 Hours at 190°C)	Peak Aged (24 Hours at 190°C)	Over Aged (100 Hours at 190°C)
20:1	UTS (MN/m^2) : 550	583	480
	0.2 % PS (MN/m^2) : 510	518	373
	% Elongation : 5	8	10
50:1	UTS : 547	591	472
	0.2 PS : 515	520	370
	% Elongation : 5	8	11
80:1	UTS : 545	580	461
	0.2 PS : 490	510	365
	% Elongation : 6	10	12

* Each value is the average of two values obtained from two identical tests.

condition and also in general both increasing extrusion ratio and increasing extrusion temperature led to improved elongation values.

Figure 8.11 shows traces of the load-extension curves corresponding to the tensile tests made on the as quenched, underaged and peakaged conditions of the extrudates. The curves clearly show variations in the σ_{UTS} and σ_{PS} with ageing time at 190^{o}C and the associated changes in the work hardening characteristics. They also showed that serrated yielding occurs in these alloys. The serrations are most pronounced in the as quenched condition and gradually decrease with increasing ageing time and no serrated yielding occurs in the peakaged condition.

8.2.4.2. Fracture Toughness

The variation in fracture toughness in the underaged, peakaged and overaged conditions (T6 temper) for the extrudates produced at 500^{o}C is presented in Figure 8.12. The effects of varying heat treatment cycle (involving natural ageing, stretching, and combinations of natural ageing and stretching) on the fracture toughness of the material in the underaged, peakaged and overaged conditions are also shown in Figure 8.12. All the extrusions were performed at 20:1 extrusion ratio, 500^{o}C and at a ram speed of 3 mm/sec. Table 8.3 summarises all the fracture toughness results in tabular form. Table 8.3 also includes the toughness values in different ageing conditions for the extrudates produced at 400^{o}C.

The results listed in Table 8.3 suggest that the toughness in general decreases from the underaged to the overaged condition. Also, variation of the extrusion temperature has essentially no effect on the fracture toughness of the material. However, the variations in preageing heat treatment conditions have a remarkable effect on the fracture toughness. The fracture toughness in all three ageing conditions were improved by natural ageing before the 190^{o}C treatment: compared to the T 6 condition, the toughness values in the underaged condition increased by 35 % and in the peakaged condition the toughness values showed a 30 % increase. However, poor toughness values were associated with any cycle which included the 2 % stretch. The material with a preageing stretch showed inferior fracture toughness properties in all three ageing conditions, but when the material was naturally aged in addition to stretching, the fracture toughness in the peakaged condition was slightly improved.

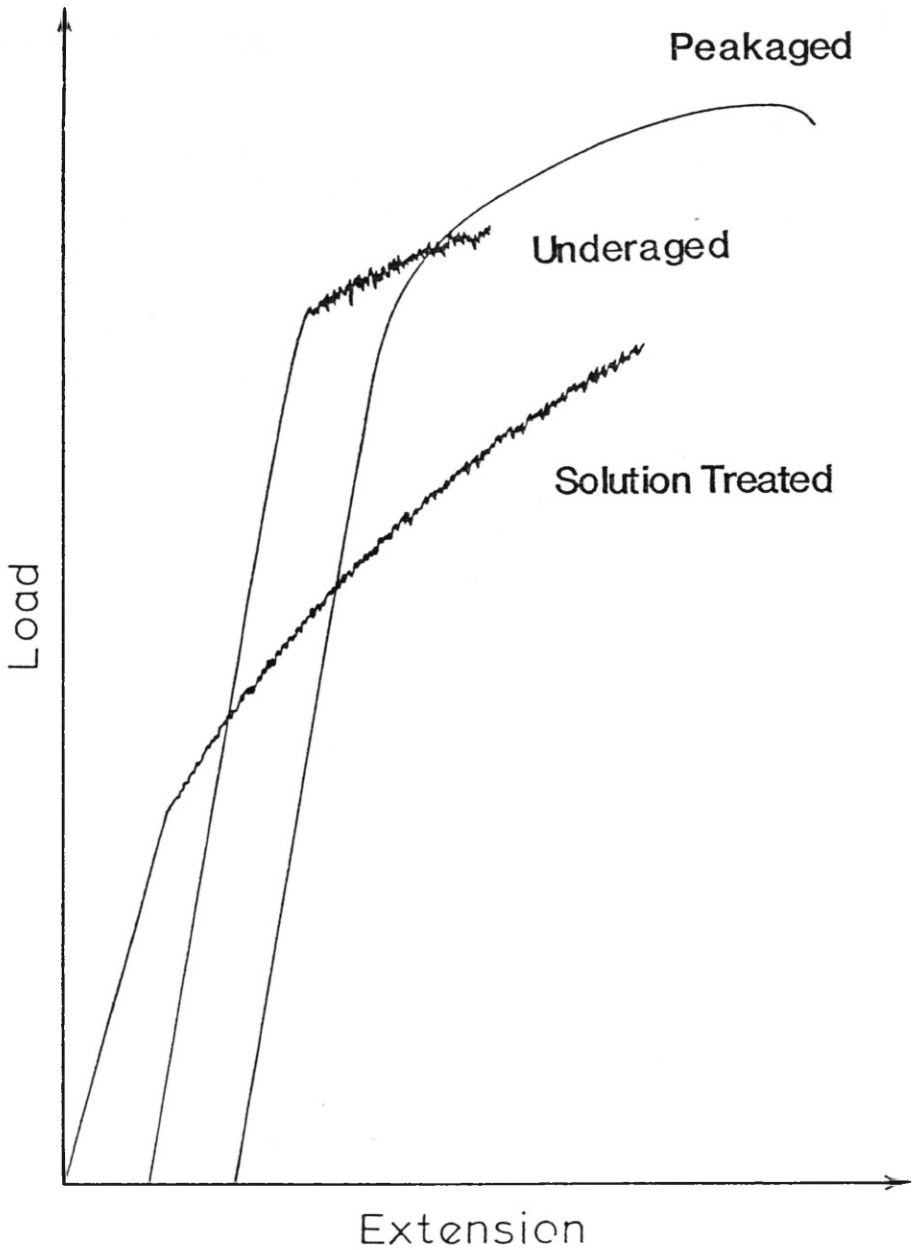


Figure 8.11. Traces of load-extension curves obtained from longitudinal tensile tests made on the solution treated, underaged and peakaged material.

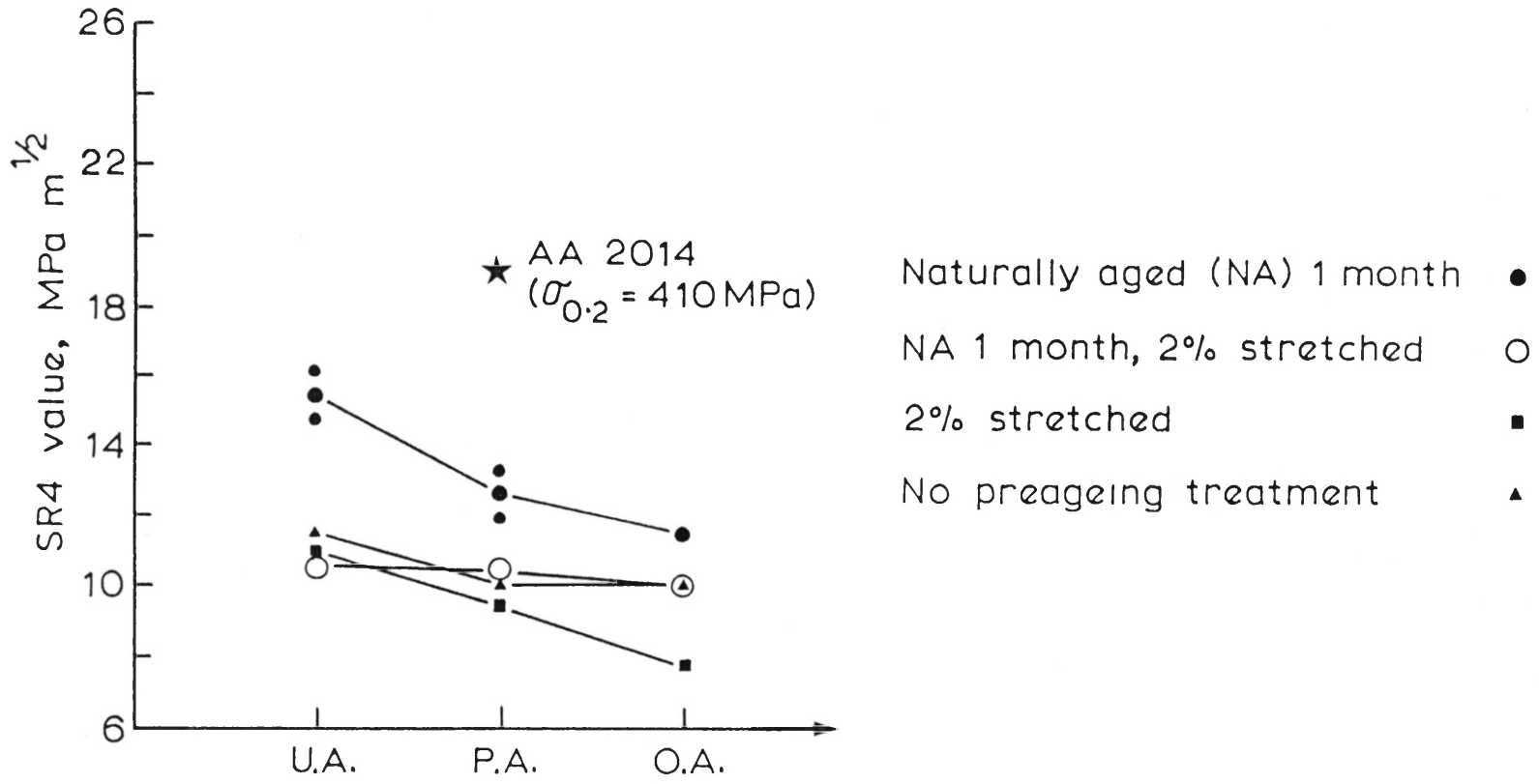


Figure 8.12. Transverse fracture toughness properties of the heat treated extrudates produced at 500°C, 20:1, 3 mm/sec. Details of treatments prior to artificial ageing at 190°C are included in the figure. SR → Short Rod

Table 8.3. Fracture Toughness (SR4, MPa $m^{\frac{1}{2}}$) of the Heat Treated Extrudates

Details of Heat Treatment	Ageing Conditions at 190°C		
	Under-aged (5 Hours)	Peak aged (24 Hours)	Over aged (100 Hours)
T6 Condition, Initial Billet Temperature = 400°C	12 12	10.5 10.2	10 10
T6 Condition, Initial Billet Temperature = 500°C	12 11.6	10 10.2	10.4 10
ST 530°C, WQ 23°C, NA 1 month and AA 190°C	16.27 14.6	13.27 11.9	11.5 11.5
ST 530°C, WQ 23°C, 2 % stretch and AA 190°C	11.35 11	9.5 9.5	8.3 7.68
ST 530 C, WQ 23 C, NA 1 month, 2 % stretch and AA 190°C	10.5 10.5	11 10.4	10.27 10

8.2.5. Fractography

8.2.5.1. Tensile samples

Detailed fractography of the failed tensile specimens indicates that the fracture modes of the specimens were affected by the ageing conditions and were not influenced by variations in the extrusion conditions.

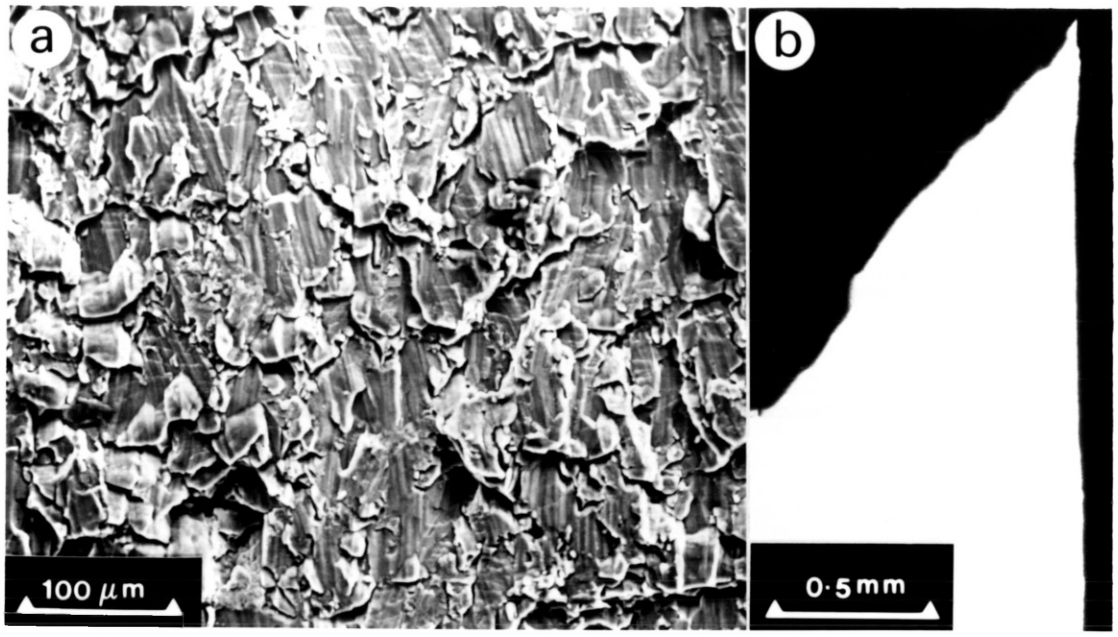
In the underaged condition,the fracture plane was inclined approximately 40^{o} to the stress axis for the specimen. The SEM examination of the fracture surfaces revealed (Figure 8.13 (a)) that the specimens failed via a shear fracture mode. The fracture surfaces were covered with a step like topography. These steps correspond to slip bands and are better illustrated in Figure 8.13(c); the fractograph shows the presence of slip bands adjacent to the grain boundaries along which the cracks propagated. The steep shear lips typically observed in the fracture surfaces are also shown in Figure 8.13 (d).

In the peakaged condition, the samples revealed a dramatic change in the fracture surface from one dominated by shear type fracture in the underaged condition to one consistent with the intersubgranular type fracture (Figure 8.14(a)). Crack propagation along the subgrain boundaries is better illustrated in Figure 8.14(c); the fractograph additionally shows the presence of fine shallow dimples along the subgrain boundaries suggesting a microscopic ductile type fracture. Figure 8.14 (c) also shows that the dimples are sometimes associated with precipitate particles (as shown by the arrows).

In the overaged condition, the fracture surfaces also showed an intersubgranular type fracture (Figure 8.14 (d)). The fractograph indicates that the cracks propagated along the subgrain boundaries by a microscopic ductile type fracture (as evidenced by the dimples on the subgrain and its boundaries).

Figures 8.15 (a) - (c) show the fracture surfaces of the peakaged specimens with varying preageing heat treatment conditions viz. natural ageing (Figure 8.15 (a), and a combination of natural ageing and stretching (Figure 8.15 (b)). The fractographs show that in all cases crack propagation occurred along the subgrain

Figure 8.13. SEM micrographs of fracture surfaces (a, c and d) and accompanying light micrograph (b) of longitudinal tensile profile in the underaged condition (5 hours at 190^{o}C).


a
100 μm
b
0·5mm


c
25μm


d
25μm

Figure 8.14. SEM micrographs of fracture surface (a and c) and accompanying light micrograph of longitudinal tensile profile (b) in the peakaged condition (24 hours at 190°C); Figure 8.14(d) shows the fracture surfaces in the overaged condition (100 hours at 190°C).

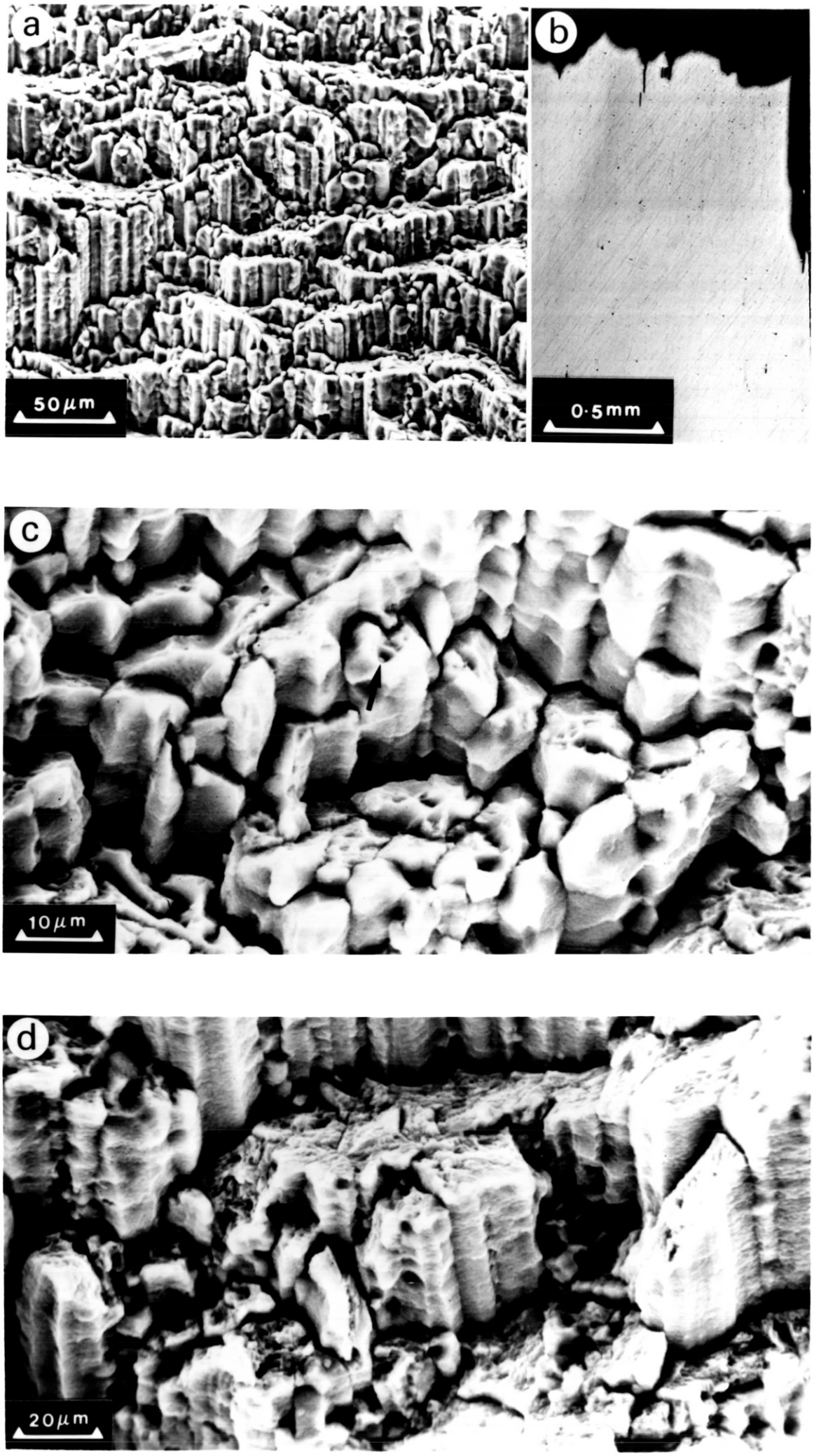
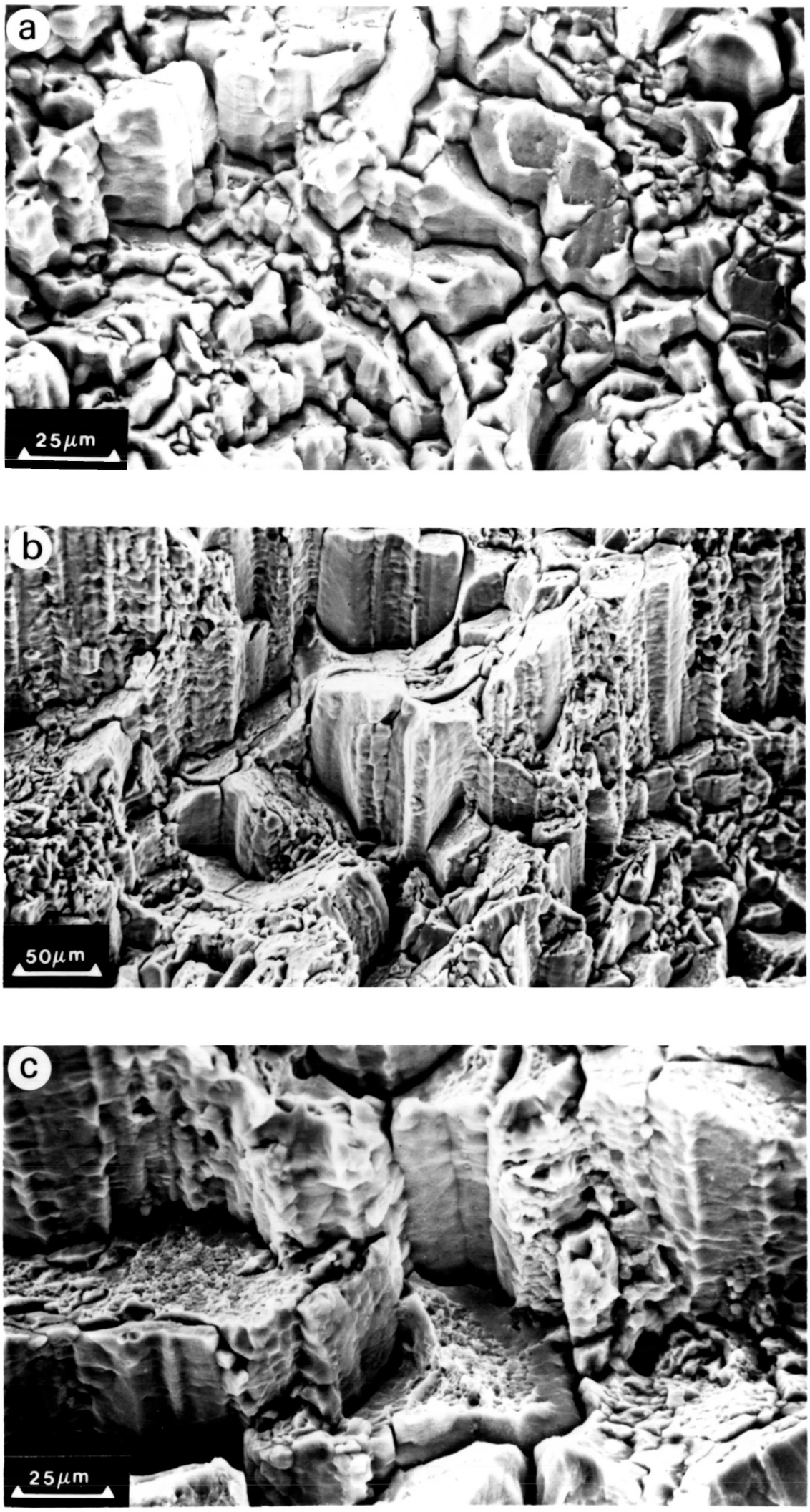

a
50μm
b
0·5mm
c
10μm
d
20μm

Figure 8.15. SEM micrographs showing the fracture surfaces of the failed tensile specimens. Material treatment: (a) ST 530^{o}C, WQ, NA 1 month, AA 24 hours at 190^{o}C; (b)& (c) ST 530^{o}C, WQ, NA 1 month, 2 % stretch and AA 24 hours at 190^{o}C.


a
25μm
b
50μm
c
25μm

boundaries by a microscopic ductile type fracture as indicated by the fine dimples on the subgrains and its boundaries. The fine details of the dimples are better illustrated in Figure 8.15 (c).

8.2.5.2. Fracture Toughness Samples

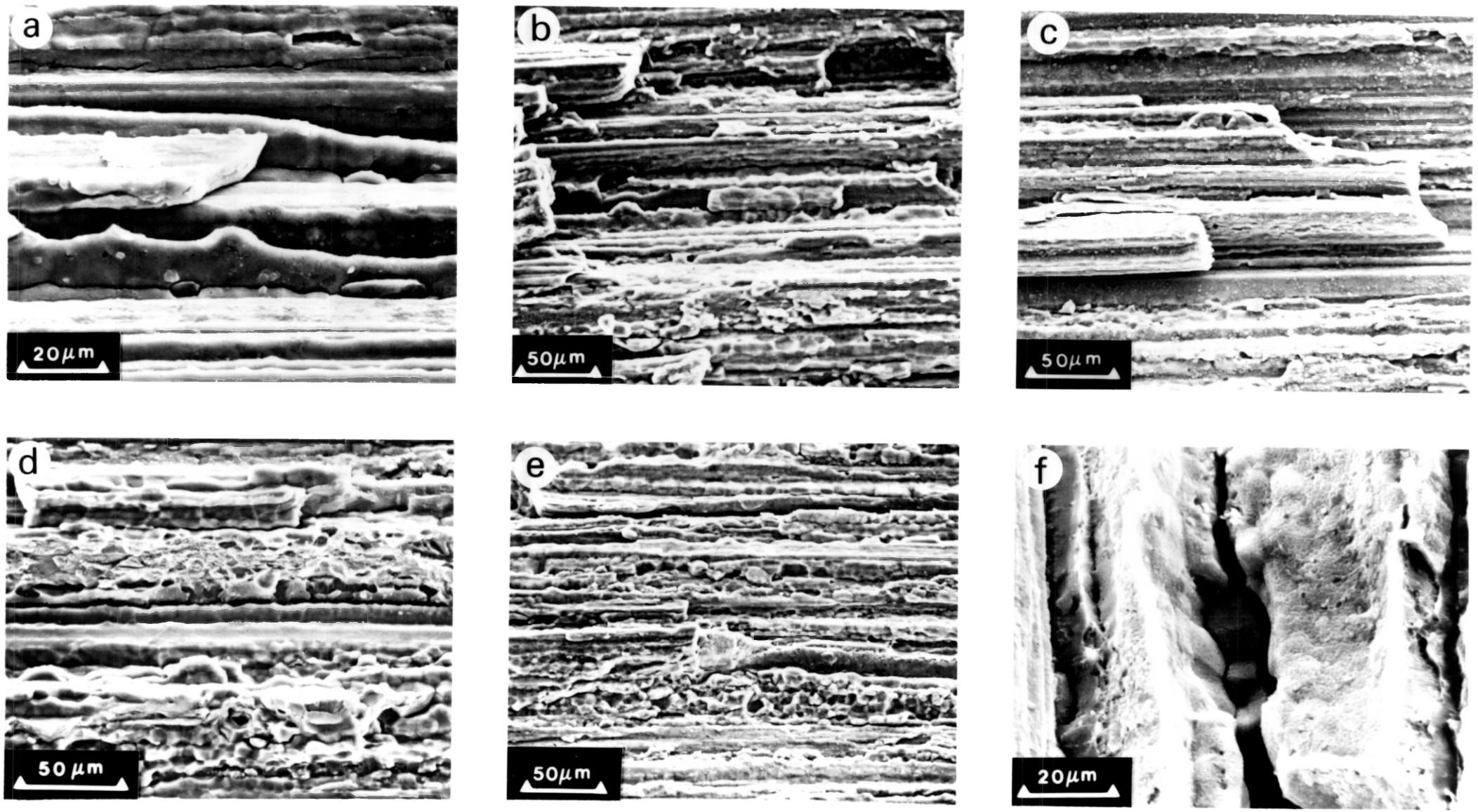
Figures 8.16 (a), (b) and (c) show the fracture surfaces in the underaged, peakaged and overaged conditions (T6 temper) respectively. In all three cases, cracks propagated along the grain boundaries. The underaged samples exhibited large areas of featureless grain boundary fracture surface whilst, the fracture surfaces in other two conditions contained shallow dimples. Figure 8.16 (d) and (e) show the fracture surfaces of the underaged and peakaged samples with a prior natural age. Comparison of Figure 8.16 (a) with Figure 8.16 (d) suggests that although there was no noticeable change in the crack path, substantial microscopic ductility has been introduced into the material by the insertion of natural ageing: in the underaged condition, the fracture surface was no longer featureless rather it was populated with a fine dimple like structure. The microscopic dimples on the fracture surface of the peakaged sample are shown in Figure 8.16 (f).

8.3. Discussion

8.3.1. Ageing Curves

The age hardening curves for the alloy solutionised for 20 minutes at 530°C indicate that the 400°C extrudate has inferior properties prior to peak hardness compared to the 500°C extrudate. TEM investigation revealed incomplete solutionising of the copper rich Al-Cu-Mg based particles produced by 400°C extrusion. Increasing the solution treatment time to 40 minutes results in complete dissolution of these particles and in identical age hardening behaviour in the 400°C and 500°C extrudates. It is suggested that in the presence of coarse Al-Cu-Mg based particles the formation of age hardening S(Al_2CuMg) phase is limited and this is responsible for the inferior ageing response of the 400°C extrudate. These results also indicate that the artificial ageing response of the 500°C extrudate in the T 6 condition is identical to that of the as extruded material, whilst the extrusions produced below 500°C cannot be aged directly and require extended solution treatment at 530°C.

Figure 8.16. SEM micrographs showing the fracture surfaces of the transverse fracture toughness specimens. Material treatment: (a) underaged (5 hours at 190°C), (b) peakaged (24 hours at 190°C), (c) overaged (100 hours at 190°C) (d) ST 530°C, WQ(RT), NA 1 month and AA 5 hours at 190°C; (e) and (f) ST 530°C; WQ(RT), NA 1 month, and AA 24 hours at 190°C.


a
20μm
b
50μm
c
50μm
d
50 μm
e
50μm
f
20μm

The general shape of the age hardening curves and also the changes in the age hardening curves due to the insertion of natural ageing prior to ageing at 190°C are identical to those described in Chapter 4 for alloy A 2 and they may be explained in a similar ways. The 400°C extrudate with a prior natural age exhibits slightly inferior properties in the peakaged and beyond the peakaged conditions. This is attributed to the fact that in a 400°C extrudate, the number of sinks (in terms of subgrain boundaries) for the unbound vacancies is greater and this reduces the numbers of free vacancies available to assist homogeneous S precipitation.

8.3.2. Heat Treated Microstructures

8.3.2.1. Microstructure of the Alloy without Natural Ageing

The precipitation reactions in the alloy prior to the peakaged conditions are identical to those of alloy A 2 described earlier in Chapter 4. However, in the peakaged microstructure TEM revealed homogeneously nucleated S precipitation. It is suggested that this is due to the higher Cu + Mg concentration in the material (viz. Alloy A1). This is consistent with the findings of Flower and Gregson (166). The authors (166) showed that at the upper end of the LITAL A specification range the Cu + Mg concentrations are sufficient to cause such precipitation.

8.3.2.2. Effect of Natural Ageing

No loop formation could be detected in the material when solution treated, water quenched and naturally aged for up to 2 weeks. This is attributed to the higher magnesium concentration in the material. During natural ageing as δ' grows the vacancies are released back into solution. The unbound vacancies can then combine with the lithium atoms or magnesium atoms [magnesium to vacancy binding energy being ~0.19 eV (181)]; alternatively, the vacancies can go to the sinks or contribute to the vacancy condensation processes forming dislocation loops. In the presence of higher concentration of magnesium in solution, it is suggested that the numbers of free vacancies available for loop formation will decrease as they will combine preferentially with the magnesium atoms. It may be noted that the extruded material A1 (produced at 500°C) had a similar subgrain size range to that of alloy A 2 and hence the number of vacancy sinks in both cases were the same.

8.3.3. Coarse Grain Boundary Precipitates

In the heat treated material TEM revealed two types of coarse grain boundary precipitates. Firstly, the iron rich Al-Fe-Cu based particles which were also present in the homogenised material and are detailed in Chapter 6, and secondly, the copper rich Al-Cu-Mg based particles which formed upon artificial ageing at 190^{o}C. The second type of precipitate is discussed in this section.

During artificial ageing at 190^{o}C, small precipitates were visible at the grain boundaries after 5 hours. A δ' PFZ also developed in regions adjacent to the precipitates but the width of the PFZs was very small. The PFZs were viewed only under dark field imaging conditions. After 24 hours at 190^{o}C, the particles grew in size and the width of the PFZs also increased. Many of these particles were associated with dislocation structures usually taken to be indicative of the stable δ phase (91). However, quantitative X-ray EDS analysis indicates that they are not δ phase but particles rich in copper (~ 13-17 wt. %). The particles are surrounded by a δ' PFZ which implies that they contain lithium. They may be considered to be quaternary Al-Li-Cu-Mg based phase particles. The average composition of all the copper rich grain boundary precipitates examined was found to be the same and is similar to that of crystalline C phase observed earlier in the as cast material (see Chapter 6), and in the heat treated Al - 2.5 Li - 1.3 Cu - 1 wt % Mg alloy by Loiseau and Lapasset (175).

Many workers have recently made observations of grain boundary precipitation in AA 8090 alloys (see section 2.1.3 for details). The present observations are consistent with recent work by Owen (90). Using electron diffraction and quantitative X-ray EDS analysis, Owen (90) presented evidence showing that I phase and not δ phase forms at the grain boundaries of the heat treated Al - 2.5 Li - 1.2 Cu - 0.7 Wt% Mg alloy (viz. alloy A 2) and these particles are consequently responsible for PFZ formation. In the present investigation, δ phase was not detected at the grain boundary and C phase rather than I phase, was detected.

Table 8.4 summarises the established grain boundary phases in AA 8090 alloys containing varying amounts of copper and magnesium. It may be noted that formation of I phase (containing about 25 wt % copper) in the material depends not

Table 8.4. Grain Boundary Phases Detected in the Heat Treated Al-Li-Cu-Mg alloys

Li : Cu	Cu: Mg	Grain Boundary Phases	Reference
2.4	0.94	C Phase	Present Investigation
1.96	1.3	C Phase and I Phase	[175]
2.0	1.72	I phase	[90]
1.26	2.52	T_2 phase	[192]

only on the low Li:Cu ratio but also on a high Cu:Mg ratio. In the present material (viz. alloy A1) where the Li:Cu ratio is high and the Cu:Mg ratio is low, formation of C phase (containing 15 wt % copper) rather than I phase was promoted. Also, in the present alloy after 24 hours at 190^{o}C, homogeneous S precipitation was observed implying that a substantial amount of copper was combined with magnesium to form S phase in the matrix. The result was that less copper was available to form copper bearing grain boundary precipitates.

It was established in section 8.2.4 that formation of coarse precipitates on subgrain boundaries depends on the boundary misorientation. The subgrain boundaries often had misorientations in excess of 7-8^{o}, and a δ' PFZ and accompanying C phase precipitation has been shown to exist at those boundaries. It is suggested that this is a result of enhanced diffusion in regions adjacent to those subgrain boundaries; with increasing boundary angle, the subgrain boundaries act as sinks for the vacancies which are also likely to be associated with the solute atoms. The width of the PFZ and the size of the precipitates may, therefore, be correlated with the boundary angle. The creation of a δ' PFZ at high angle boundaries in an Al-Li-Zr alloy has been documented recently by Jha et al (182). The authors also found that the size of the PFZ depended on the boundary angle. It was shown that the width of the PFZ increases with ageing time and with the misorientation across the boundary.

It is concluded that the grain boundary precipitate of binary Al-Li alloys (δ) is replaced by copper bearing C phase or I phase in AA 8090 alloys. The implication is that there must, therefore, exist a strong interaction between lithium and copper solute atoms. Such an interpretation is consistent with the recent report by Howe (183). The author suggested that in an Al-Li-Cu system the Cu-Li bond energy is substantial because of the high solubility of lithium in copper. The author accordingly explained the nucleation and growth of δ' on θ' since lithium atoms are then adjacent to copper atoms. The author also referred to the formation of Al_2CuLi based T_1 phase on stacking faults as a direct consequence of the strong attraction between copper and lithium atoms. In view of the strong interaction between lithium and copper atoms together with the negligible copper to vacancy binding energy viz. 0.05 eV (181) it also appears that the copper atoms do not go to the sinks directly; rather, copper initially combines with a (Li-vacancy) pair and the resultant (Li-vacancy-Cu) complex then travels to the sink. With increasing copper

content in the material, the numbers of such complexes would be higher and so would be the degree of grain boundary precipitation. These explanations are again consistent with the increased quench sensitivity of the Al-Li-Cu-Mg alloys containing higher amounts of copper and formation of Al-Li-Cu based I phase precipitates at the grain boundaries of a slowly quenched wrought AA 8090 alloy (184).

8.3.4. Tensile Properties

The tensile properties of the heat treated extrudates are dominated by the precipitation processes which occur. Variations in extrusion conditions do not significantly influence the strength properties. However, differences may be detected: the general increase in ultimate tensile strength and proof stress with decreasing extrusion temperature may be attributed to the substructural strengthening associated with a decreasing subgrain size at lower temperatures. In general, and in particular at the highest processing temperature, slightly inferior strength properties of the 80:1 extrudates may be attributed to the increased amount of recrystallisation which occurs in the material.

Unlike the strength properties, ductility is sensitive to the variations in extrusion conditions as well as to the ageing treatments at 190^{o}C. Ductility increases with increasing extrusion ratio and increasing extrusion temperature, and it is associated with an increase in the volume fraction recrystallised in the material. The small recrystallised grains nucleated adjacent to the original boundaries are elongated along the extrusion direction. It is suggested that during tensile straining, since the stress axis lies parallel to their major axis, the grain boundaries do not offer a favourable crack path. Instead, the small recrystallised grains divert the crack path and thereby inhibit the crack propagation process. The result is the increased ductility. Ductility also increases from the underaged to the overaged condition. This is attributed to the increasing work hardening capacity of the material with increasing ageing times. In the underaged condition, where only particle (δ') shearing takes place, the degree of strain localisation is maximum and the work hardening capacity of the material is least; the result is that the material exhibits the lowest ductility of the three ageing conditions. With continuing ageing, as the δ' particles coarsen, for example in the peakaged condition, deformation proceeds by a mixture of shearing and Orowan looping (184). Of more importance,

in the peakaged condition, S phase is present homogeneously in the matrix and this would further increase the local work hardening rate and inhibit the development of bands of coplanar slip (66). In the peakaged condition the combination of these factors leads to improved elongations. In the overaged condition, the number density of homogeneously nucleated S precipitates increases and also Orowan looping becomes the dominant deformation mechanism. Deformation becomes more homogeneous and consequently the ductility further increases. With increasing ageing, the number density, as well as the size of the coarse copper rich grain boundary precipitates, also increases (see section 8.2.4). The presence of these particles would be expected to adversely affect the ductility of the material (90). However, the present results indicate that the deleterious effects of these particles on the tensile ductility of the material (in the longitudinal direction) are offset by the homogeneous deformation which occurs in the material in the presence of homogeneous S phase precipitates.

8.3.5. Serrated Yielding

Serrated yielding in Al-Li-Cu-Mg-Zr alloys has been investigated recently by many workers. This had been shown to be strongly dependent on the test orientation and the associated results are described elsewhere (186). The effect of solute elements on serrated yielding is discussed in this section. Wert and Wycliffe (187) attributed the phenomenon to the presence of copper and magnesium in solid solution. The authors (187) presented evidence showing that the occurrence of serrated yielding of an Al-Li-Cu-Mg-Zr alloy coincides with the absence of Al_2CuMg based S precipitates in the microstructure. Such an interpretation is consistent with the occurrence of Portevin-le Chatelier effect in a variety of aluminium alloys when solutes, such as copper or magnesium are present in solid solution (188). However, the authors did not consider the effect of lithium either in the form of solutes in solid solution or in the form of Al_3Li based δ' particles on serrated yielding. In order to investigate this further, two binary Al-Li alloys viz. Al - 2.8 wt % Li and Al - 1.2 wt % Li were selected. The alloys were solution treated and water quenched before the tensile specimens were machined. The load-extension traces for these solution treated samples are shown in Figure 8.17. The figure shows that serrations are pronounced in Al-2.8 wt % Li alloy where no serrated flow is observed in binary Al - 1.2 wt % Li alloy. In Al - 2.8 wt % Li, δ' particles are present whereas in the other alloy there is no δ' precipitate. It may be, therefore, concluded that in

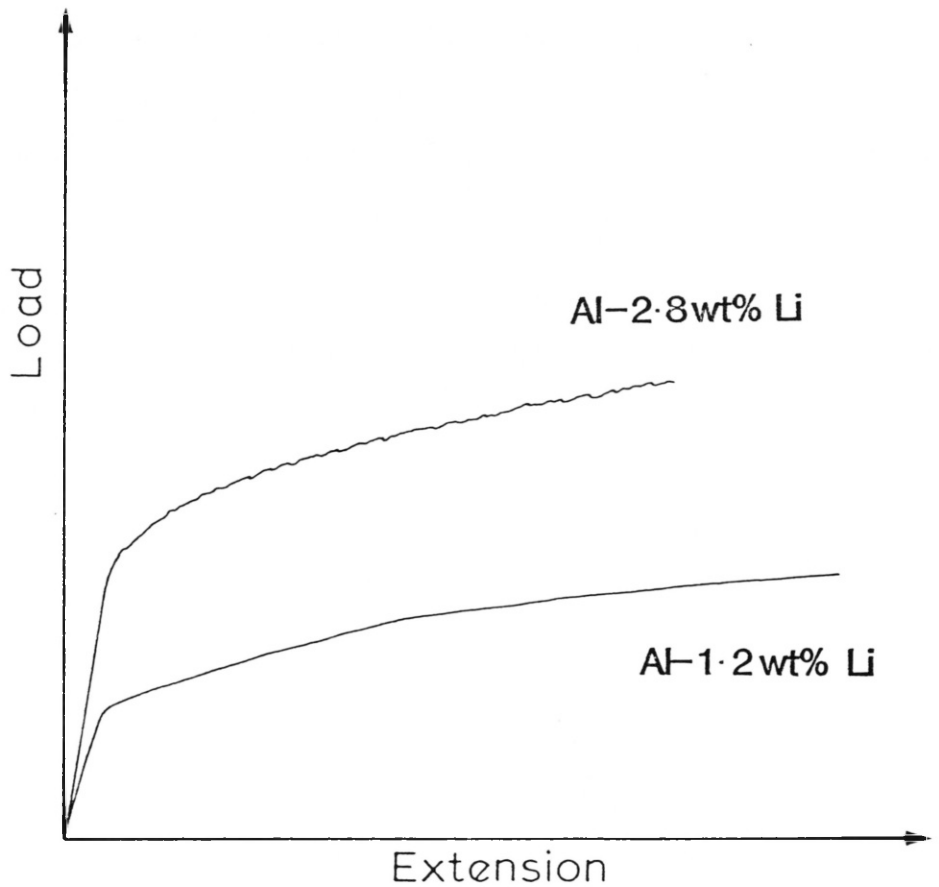


Figure 8.17. Traces of load-extension curves obtained from tensile tests made on the solution treated binary Al--2.8 wt % Li and Al-1.2 wt % Li alloys.

binary polycrystalline Al-Li alloy serrations are caused by the interaction of dislocations with the δ' precipitates. However, Evans (189) reported that lithium atoms can cause serrations but only in moderately concentrated Al-Li solid solutions. The author suggested that solute atoms are repelled by screw dislocations and are generally repelled by edges, although there is a weak attraction near the extra half-plane. Thus dislocation pinning is unlikely in dilute solutions and should therefore, appear only in moderately concentrated Al-Li solid solutions. The present observations may, therefore, be explained on the basis of differences in concentrations of lithium in solution of two binary alloys i.e. in the as quenched Al - 2.8 wt % Li alloy, the concentration of lithium in solution is greater than 1.2 wt %. However, these results do not separate the possible role of δ' particles on serrated yielding.

Tamura et al (190) examined the deformation behaviour of binary Al - 2.6 wt % Li single crystals, and polycrystalline materials. The authors noted serrated flow in binary Al-Li single crystals and it was attributed to work softening associated with dislocations shearing δ' particles. The authors suggested that in polycrystalline material the slip interference due to grain boundaries or due to operation of multiple slip suppress the occurrence of serrations and the serrated flow is observed when a single slip system is active. However, it may be noted that the authors examined the deformation behaviour of a polycrystalline Al - 2.6 wt % Li alloy after it was aged for about 7 hours at 200^{o}C. The absence of serrated flow may, therefore, be explained according to the model proposed by Evans (189) i.e. on the basis of inadequate lithium concentration in solid solution. However, in the aged material, δ' particles have grown to a larger size. So, unless δ' particles of a critical size are responsible for the serrated flow, the model proposed by Evans seems to be appropriate.

In alloy A1, serrations are most pronounced in the solution treated condition. It is suggested that the serrated flow in the solution treated material is due to all three major alloying elements viz. lithium, magnesium and copper. The presence of magnesium and copper in solid solution is known to give rise to this phenomenon in Al-Cu-Mg alloys. On the other hand, lithium also produces this effect in Al-Li alloys, either being present in solid solution or in the form of very fine δ' (Al_3Li) particles which form during or immediately after quenching; on the

basis of the present results it is not feasible to determine the relative importance of each of these and further work is clearly required to clarify this situation.

Finally, in the peakaged material, serrated flow is not observed. This is consistent with the fact that the concentration of lithium in solution is further reduced and also the δ' particles grow to a bigger size. Of more importance, in the peakaged material, most of copper and magnesium come out of solution to precipitate as Al_2CuMg based S phase both homogeneously in the matrix as well as heterogeneously at the low angle subgrain boundaries.

8.3.6. Fractography

8.3.6.1. Tensile samples

In the underaged condition, the specimens failed via a shear fracture mode. In underaged material, the dislocations shear the coherent and ordered δ' particles upon plastic deformation and planar slip is the result. It is suggested that the coarse slip bands lead to strain localisation at the grain boundary region and cause early crack nucleation. In material aged for 5 hours at 190°C, the number density of the grain boundary precipitates is low and also the associated PFZ's are localised to narrow regions surrounding the precipitates and it is unlikely that these play any effective role in the crack nucleation processes in the underaged materials.

In the peakaged condition, the failure mode changes to a mixture of intersubgranular and intergranular type fracture. This is attributed to more uniform strain distribution in the material during deformation. TEM revealed co-precipitation of homogeneously distributed δ' and S phases in the material after 24 hours at 190°C. It is suggested that the presence of homogeneous S phase in the microstructure is responsible for homogeneous deformation in the peakaged condition. Such an interpretation is consistent with the observations of Gregson and Flower (66) who showed that in a wrought Al-Li-Cu-Mg-Zr alloy extensive precipitation of S phase modifies slip behaviour by breaking up the coplanar slip. Recently, Yin et al (185) reported that in an Al - 2.5 Li - 1.2 Cu - 0.7 Mg - 0.12 wt % Zr alloy (viz. alloy A2; see Table 3.1) the material failed via a shear type fracture in the peakaged condition (viz. after 24 hours at 190°C). It may be recalled that unlike alloy A1, S phase is present only heterogeneously at the subgrain boundaries of

alloy A2 after 24 hours at 190°C (see Chapter 4). Clearly, the limited numbers of heterogeneously nucleated S precipitates are not adequate to disperse the coplanar slip associated with shearing of δ' particles; the result is that the material fails via a shear type fracture.

In the peakaged condition, the cracks propagate along the subgrain boundaries implying weakness of the subgrain boundaries. TEM revealed that in a peakaged material, copper rich precipitate particles and δ' PFZs form at the grain and subgrain boundaries. It is suggested that the suggested particles lying along the boundaries act as nucleation sites for void formation and the final fracture proceeds via growth and coalescence of such voids. Such an interpretation is consistent with the observation of dimples (associated with precipitate particles) at the subgrain boundaries of the fracture surfaces.

In the overaged material, the failure mode is similar to that of the peakaged material. With increasing ageing, deformation becomes more homogeneous in the material (see section 8.3.4). At the same time, more coarser precipitates form at the grain and subgrain boundaries providing a path for the cracks to propagate. The ductility however, increases. It is suggested that as a result of homogeneous deformation in the material, the strain concentration at the crack tip is reduced and consequently the crack nucieation processes are delayed and more work is involved in the subsequent crack propagation processes.

8.3.6.2. Fracture Toughness Samples

Materials in all three ageing conditions show the same overall fracture behaviour. Cracks always propagate along the grain boundaries parallel to the extrusion direction. The explanations for grain boundary failure and the typical features (e.g. dimples at the grain boundaries) of the fracture surfaces in the peakaged and overaged conditions are similar to those described in section 8.3.6.1. The fracture surfaces of material with a prior natural age show different features on microscopic scale. In the underaged and peakaged condition the fracture surfaces are populated with a very fine dimple like structure; it is suggested that they are associated with increasing work hardening capacity of the material in the presence of homogeneously nucleated S phase precipitates in the microstructure. The material with a prior natural age exhibits a combination of higher strength,

ductility and fracture toughness (see the section below).

8.3.7. Fracture Toughness

In general the fracture toughness decreases with increasing ageing time at 190°C. This may be explained as follows: it was reported earlier in section 8.3.4 that the work hardening capacity of the material, and hence the ductility, increases from the underaged to the overaged condition. The fracture toughness of the material (which combines both ductility and strength) would, therefore, be expected to be higher in the peakaged material than that in the underaged condition; but the trend is opposite. It may be recalled that during the fracture toughness tests, load was applied at 90° to the extrusion direction whilst, in case of the tensile tests the stress axis was parallel to the extrusion direction. The result is that in the former case, where the stress acts perpendicular to the weak grain boundaries (which are more susceptible to fracture) the fracture strain is limited by the volume fraction of the void nucleating precipitate particles which form at the grain and subgrain boundaries. The equation (191) for fracture toughness (K_{1C}) of particle hardened alloys containing grain boundary precipitates and PFZs may be given as follows:

$$K_{1C} = C.\, n_i\, (Y_i\, \varepsilon_{C_i}\, d/D)^{1/2},$$

where, C is a constant, n_i is the work hardening exponent for the grain boundary PFZ of constant thickness, Y_i is the yield stress of the material in the presence of a PFZ, ε_{C_i} is the critical fracture strain which depends on the volume fraction of the void nucleating grain boundary particles, d is the width of a PFZ and D is the grain size. This equation suggests that in the peakaged condition where the number density of the void nucleating grain boundary particles is greater and also the width of the PFZs is orders of magnitude greater (than that in the underaged condition), the fracture toughness decreases. In the overaged condition, where both the strength of the material decreases and the numbers and size of the void nucleating particles increase, the fracture toughness of the material is least.

The fracture toughness of the material is improved when it is subjected to natural ageing prior to artificial ageing at 190°C. This is explained as follows: natural ageing enhanced nucleation of homogeneous S phase precipitates in the

material; deformation becomes homogeneous and it increases the work hardening capacity of the material. The result is a lower strain concentration at the crack tip for a given stress level and consequently the material achieves a combination of higher strength, ductility and fracture toughness (see Table 8.5). The fracture toughness of the material decreases when the material is stretched before ageing at 190^{o}C. Stretching reduces the residual work hardening capacity of the alloy. Also, stretching encourages heterogeneous S formation at the expense of homogeneous precipitation and thus coarsens the particle dispersion. As a consequence, the strength properties of the material also decrease (see Table 8.5). The results also indicate that the strength and the fracture toughness of the material improve when the material is naturally aged, stretched and subsequently aged at 190^{o}C. The resultant microstructures indicate that the dispersion of heterogeneously nucleated S precipitates is more uniform than that obtained in a material with only a preageing stretch. All these results indicate the critical role of S phase precipitation in determining the mechanical properties. Property improvements in this alloy are associated with the production and refinement of a homogeneous distribution of this phase. Thus natural ageing is beneficial while stretching is detrimental. This may appear to conflict with the conclusion of Gregson and Flower (66) that stretching is beneficial in a dilute LITAL A composition. However, in that work, the only mode of S nucleation achievable in practical heat treatment times, and in the absence of natural ageing, was heterogeneous. Hence, stretching refined the distribution of S and improved the properties. The conclusion in both cases is the same: refinement of the S dispersion results in improved strength and toughness.

The present results also indicate that variation in extrusion temperature i.e. variation in subgrain size does not have any effect on the fracture toughness of the material. The present observations are consistent with the findings of Parson and Sheppard (151) in Al-Li-Mg alloys and of Reynolds and Creed (153) in AA 8090 alloys. These results may be attributed to the fact that subgrain boundaries are ineffective barriers to the planar slip (54). It was shown by Peel et al (54) that in the presence of zirconium, which produces a pronounced grain structure, such planar slip can extend over many subgrains and grains producing long range planar shear bands. Variation in subgrain size is, therefore, unlikely to influence the ductility and toughness of the material.

Table 8.5. Effect of Varying Heat Treatment Cycle on the Longitudinal Tensile Properties**

Details of Pre-ageing Heat Treatment*	Ageing time at 190°C	
	5 Hours (Under Aged)	24 Hours (Peak Aged)
Naturally Aged for one month	UTS (MN/m^2) : 545 0.2% PS : 510 (MN/m^2) % Elongation : 6.2	593 538 8.5
2% Stretched	UTS : 560 0.2 % PS : 518 % Elongation : 5.5	572 528 8.7
Naturally aged for one month and 2% stretched	UTS : 565 0.2 PS : 518 % Elongation : 5.5	580 532 8.5

* All the extrudates (produced at 500°C) were initially solution treated at 530°C and water quenched at room temperature (viz. 23°C)

** Each value is the average of two values obtained from two identical tests

8.4. Summary

1. For the extrusions produced at 500°C, press quenching may be utilised to avoid a separate solution soak before ageing at 190°C, whilst the extrusions produced below 500°C require an extended prior solution treatment (viz. 40 minutes instead of the standard solution treatment time of 20 minutes at 530°C). It is suggested that this is because of the incomplete solutionising of the coarse Al-Cu-Mg based particles produced by lower temperature extrusions.

2. The artificial ageing characteristics of the material are similar to those of alloy A2, except in the peakaged condition where S phase is present homogeneously in the microstructure. It is suggested that this is due to the higher Cu + Mg concentration in the material. Variations in extrusion processing conditions do not influence the artificial ageing response of the material at 190°C.

3. The natural ageing response of the material is identical to that of alloy A2. However, unlike alloy A2, loop formation in the naturally aged material is delayed for up to two weeks. This is attributed to the higher magnesium content of the material. It is suggested that in the presence of a higher concentration of magnesium in solution, the numbers of free vacancies available for loop formation decrease as they are trapped by the magnesium atoms.

4. In the artificially aged material, a copper rich phase (having a composition range of 13-17 % copper, 2-5 % magnesium and balance aluminum + lithium) precipitates at grain boundaries and subgrain boundaries. δ' PFZs surround these particles and, therefore, the particles are expected to contain substantial amounts of lithium. It is suggested that this phase is similar to the C phase observed in as cast material. Formation of this phase is facilitated at low Cu:Mg ratio. δ(AlLi) phase is not observed at the grain boundaries of any heat treated material suggesting a strong interaction between lithium and copper atoms.

5. The mechanical properties of the heat treated material are dominated by the precipitation processes which occur. Variation in extrusion ratio has only a weak effect on the strength properties, whilst, the strength properties slightly improve with decreasing extrusion temperature. This is attributed to the substructural strengthening associated with a decreasing subgrain size at lower temperatures. However, longitudinal ductility increases with increasing extrusion temperature and extrusion ratio, and is associated with increasing volume fraction recrystallised in the material. It is suggested that the small recrystallised grains situated near original grain boundaries (and elongated in the extrusion direction) do not provide a favourable crack path. Instead, they divert the crack path and inhibit the crack propagation process. The ductility is, therefore, improved. Ductility also increases with increasing ageing time at 190^{o}C. This is attributed to the increasing work hardening capacity of the material and is primarily associated with the homogeneously nucleated S precipitates in the microstructure.

6. Serrated yielding occurs in the as quenched and underaged material. It is suggested that the serrated flow is due to the combined effect of all three major alloying elements viz. lithium, magnesium and copper. Magnesium and copper in solid solution give rise to this phenomenon. Lithium contributes to this phenomenon either in the form of solute atoms when present in adequate concentration in the solid solution or in the form of δ' (Al_3Li) particles below a critical size. In the peakaged material, the concentration of lithium is appreciably reduced and the δ' particles grow to a bigger size. Also, most of the copper and magnesium comes out of the solid solution to precipitate as Al_2CuMg based S phase both homogeneously in the matrix as well as heterogeneously at the low angle subgrain boundaries. The combination of these factors leads to the disappearance of serrations in the peakaged material.

7. The fracture surfaces of the tensile specimens change with ageing conditions and this is directly related to the precipitation processes taking place. In the underaged condition, the specimens fail via a shear fracture mode and this is attributed to the strain localisation at the grain boundary region associated with dislocations cutting δ' particles. In the peakaged and overaged conditions, the failure mode changes markedly to a mixture of

intersubgranular and intergranular type. It is suggested that this is primarily associated with the precipitation of homogeneously nucleated S phase in the microstructure and C phase on the boundaries.

8. The fracture surfaces of the failed fracture toughness specimens remain unaffected by the changes in ageing conditions and cracks always propagate along the grain boundaries. However, on a microscopic scale, differences may be detected. The fracture surfaces of the specimens with a prior natural age are populated with shallow featureless dimple like structures suggestive of a ductile intergranular type fracture. The word ductile, in this context, is of course, a relative characteristic.

9. The fracture toughness decreases with increasing ageing time at 190^{o}C. This is attributed to an increase in the volume fraction of void-nucleating coarse grain boundary particles with increasing ageing time. The stress axis acts perpendicular to the weak grain boundaries which are more susceptible to fracture. Variation in extrusion temperature does not have any effect on the fracture toughness of the material. The fracture toughness properties are influenced by variations in the preageing heat treatment conditions: natural ageing prior to artificial ageing improves the fracture toughness in all three ageing conditions. It is suggested that this results from the enhancement of the homogeneous S phase precipitation in the microstructure. Introduction of a preageing stretch (2%) decreases the fracture toughness of the material; stretching prior to ageing promotes heterogeneous formation of S at the expense of homogeneous precipitates and thus coarsens the particle dispersion. This also results a decrease in the strength properties of the material. The implication is that refinement of the S dispersion results in improved strength and toughness.

CHAPTER NINE

CONCLUSIONS AND SUGGESTIONS FOR FURTHER WORK

9.1. Conclusions

Chapter Four.

1. In a solution treated AA 8090 alloy, the evidence suggests that many of the nonequilibrium excess vacancies are confined to the δ' (Al_3Li) phase particles produced during or immediately after quenching rather than being bound to individual lithium atoms still remaining in solution.

2. In AA 8090 alloys, homogeneous precipitation of S phase is feasible; it relies upon the attainment of a critical concentration of free vacancies in solution.

3. During age-hardening, as δ' grows, vacancies are released back into solution; these free vacancies promote homogeneous S precipitation.

4. An increase in vacancy concentration resulting from increasing prior solution treatment temperature refines the homogeneous S phase disperson produced in ageing.

5. Natural ageing releases the bound vacancies (as δ' grows) resulting in their condensation as dislocation loops.

6. Natural ageing induces rapid homogeneous S precipitation on artificial ageing and delays the onset of overaging.

7. Controlled low temperature ageing prior to artificial ageing also induces rapid homogeneous S precipitation. However, treatments which result in the condensation of free vacancies and their loss to sinks, inhibit such S precipitation.

Chapter Five

1. In binary Al-Li alloys, GP zones form simultaneously with the δ' during the quenching process and grow competitively with δ' during natural ageing. The dissolution temperature of the GP zones is 130°C.

2. In AA 8090 alloys, lithium inhibits the precipitation of Al-Cu-Mg GP zones during quenching.

3. The formation and growth of Al-Cu-Mg GP zones occurs during natural ageing.

4. The natural ageing response in AA 8090 alloys is due to a combination of growth of δ' particles, growth of Al-Li GP zones, and formation and growth of GP zones of the Al-Cu-Mg system.

Chapter Six

1. In the as cast Al-2.5 Li - 1.0 Cu - 1.1 Mg - 0.12 wt % Zr alloy, five phases were detected. They are as follows: an Al-Cu-Li-Mg based phase in the form of lamellar eutectic at the grain boundary triple point junctions, an Al-Cu-Li-Mg based phase at the grain boundary interfaces, an Al-Si-Li-(Cu) based phase at the triple point junctions, an Al-Fe-Cu based phase present both at the triple point junctions as well as at the grain boundary interfaces and an Al-Cu-Li-Mg based phase in the matrix.

2. The compositional and the thermal characteristics of the Al-Cu-Li-Mg based phase present at the grain boundary triple point junctions suggest that it is an extension [i.e. $Al_6Cu(LiMg)_3$] of T_2 (Al_6CuLi_3) phase; whilst the matrix phase, and the Al-Cu-Li-Mg based phase present at the grain boundary interfaces are similar to C phase.

3. The equilibrium solidus point of the cast material is at about 622°C; the material also has a non equilibrium solidus at about 547°C.

4. Annealing for 24 hours at 537°C is the optimum homogenisation schedule for the present cast material.

5. The Al-Fe-Cu based phase survives the optimum homogenisation treatment; all other phases dissolve on homogenisation without any sign of incipient melting.

Chapter Seven

1. Extrusion produces microstructures which vary through the extrude section: the surface is fully recrystallised whilst the core is essentially unrecrystallised.

2. The volume fraction recrystallised increases with increasing temperature, extrusion ratio and ram speed. Recrystallisation is most sensitive to extrusion ratio.

3. Recrystallisation is dynamic and occurs by grain boundary bulging and by rotation recrystallisation.

4. The extruded structure is extremely resistant to static recrystallisation during subsequent heat treatment.

5. The as extruded microstructures exhibit well recovered subgrain structures. The subgrain size decreases with decreasing extrusion temperature; with increasing extrusion ratios the subgrains become elongated along the extrusion direction.

6. The subgrains formed adjacent to the original boundary are the potential nuclei for recrystallisation and are responsible for the banded nature of the recrystallised grains.

7. Extrudates produced at 500°C remain single phase during extrusion; at lower temperatures coarse copper rich Al-Cu-Mg based particles are produced as a result of the thermal exposure.

8. The tensile strength of the as extruded material increases with increasing extrusion ratio and temperature. The variables have a similar effect on proof stress except at the highest processing temperature. Ductility decreases in general with decreasing extrusion temperature and extrusion ratio; associated with these are the decrease in volume fraction recrystallised and an increase in the volume fraction of the coarse copper rich Al-Cu-Mg based particles.

9. Natural and artificial ageing characteristics of the press quenched extrudates vary with extrusion temperatures: the mechanical properties always improve with increasing extrusion temperature.

Chapter Eight

1. For the extrusions produced at 500°C, press quenching may be utilised to avoid a separate solution soak before ageing at 190°C. Extrusions produced at lower temperatures require an extended solution treatment if they are to produce aged properties equivalent to those obtained by the 500°C extrudates.

2. Variations in extrusion processing conditions do not influence the artificial ageing response, after solution treatment (T6 condition), of the material at 190°C.

3. In the peakaged material, the matrix precipitate phases are δ'(Al_3Li), S(Al_2CuMg) and T_1(Al_2CuLi). T_1 precipitation is strictly limited, whilst both δ' and S phases are present homogeneously as well as heterogeneously in the material.

4. Natural ageing prior to artificial ageing further enhances homogeneous precipitation of S phase in the material.

5. The grain boundary precipitation of binary Al-Li alloys, δ(AlLi), is replaced by copper bearing C phase. In the material aged up to 100 hours at 190°C, the coarse grain boundary precipitates are the Al-Cu-Li-Mg based C phase. Formation of C phase is facilitated at low Cu:Mg ratio.

6. The mechanical properties (in the longitudinal direction) of the heat treated material are dominated by the precipitation processes which occur. Variation in extrusion ratio has only a weak effect on the strength properties. The strength properties slightly improve with decreasing extrusion temperature. Ductility increases with increasing extrusion ratio and temperature.

7. Longitudinal ductility increases from the underaged to the overaged condition. Associated with this is a change in fracture mode from one of shear type fracture in the underaged condition to one of a mixture of intersubgranular and intergranular fracture in the peakaged and overaged condition.

8. The major change in the fracture mode with ageing is associated with the precipitation of homogeneously nucleated S phase in the matrix and C phase on the boundaries.

9. Serrated yielding occurs in the as quenched and underaged material. The evidence is consistent with a previous interpretation that magnesium and copper in solid solution gives rise to this phenomenon; lithium contributes to this phenomenon either in the form of solute atoms when present in adequate concentration in the solid solution or in the form of δ' particles below a critical size.

10. The fracture toughness (measured in the transverse direction) remains unaffected by variation in extrusion temperature.

11. The fracture toughness decreases with increasing ageing time at 190^{o}C. Cracks always propagate along the grain boundaries.

12. Introduction of a preageing stretch (2 %) decreases the fracture toughness of the material.

13. The fracture toughness of the material is improved when it is subjected to natural ageing prior to artificial ageing. The improvement in properties results from the refinement of the homogeneous distribution of S phase within the microstructure.

9.2. Suggestions for further work

1. In lithium containing Al-Cu-Mg alloys of commercial interest, the vacancies play a very significant role in the development of all the major precipitate phases which in turn decide the mechanical properties of the material. To date, studies concerning solute-vacancy interactions in Al-Li based alloys have been limited. Further work is clearly required for better understanding of the mechanisms involved.

2. In the heat treated AA 8090 alloys, the volume fraction of the coarse grain boundary precipitates is observed to increase with increasing copper content in the material. Copper and magnesium concentrations in these alloys may, therefore, be modified to minimise the grain boundary precipitation while at the same time providing adequate Cu + Mg concentration for matrix S precipitation. Based on the available ternary Al-Cu-Mg phase diagram [See reference (58)] it is suggested that the copper concentration may be lowered to the range of (0.8 - 1.0) wt % and magnesium concentration may be increased to the range of (1.0 - 1.3)wt %; this composition falls into the (α + S) field of the Al-Cu-Mg phase diagram. At this low copper concentration, magnesium, however, cannot be increased beyond 1.3 wt %; because increasing magnesium beyond 1.3 wt %, the composition enters the (α + S + T) phase field and also increasing magnesium further to 2 wt % or beyond would lead to the formation of brittle Al_2LiMg phase. The study of precipitation reactions in the proposed high Mg, low Cu composition should be investigated.

3. Formation of coarse precipitates at the high angle grain boundaries and medium angle subgrain boundaries are a result of enhanced diffusion in regions adjacent to those boundaries. A lower ageing temperature viz. 170^{o}C may be therefore utilised to minimise the grain boundary precipitation. Work is required to investigate such heat treatment and development of

adequate strength.

4. Natural ageing prior to artificial ageing is observed to improve the fracture toughness of the material. Optimisation of the prior natural ageing time is, therefore, required to utilise fully its beneficial effect.

5. Natural ageing prior to artificial ageing enhances the matrix S precipitation; the degree of grain boundary precipitation at the same time is very likely to be influenced because increased matrix S precipitation reduces the available solute required for grain boundary precipitation. Quantitative work is clearly required to investigate these events; the study could be correlated with the mechanical property results.

6. In the extrusion ratio range (viz. 20:1 to 80:1) investigated in this study, the longitudinal ductility is always observed to increase with increasing extrusion ratio. The extrusion ration range of commercial interest varies from 10:1 to 100:1. Therefore, studies involving the effect of variation in extrusion ratio on the fracture toughness of the material is of considerable interest and should be investigated.

ACKNOWLEDGEMENTS

I would like to express my gratitude to my supervisors Dr. H.M. FLower and Professor T. Sheppard for their guidance and encouragement throughout the course of this research work; I am indebted to Dr. Flower, in particular, for his invaluable advice and for all the stimulating discussions during the past three years.

I also owe particular thanks to Mr. G.W. Briers for his advice and guidance on matters involving electron microscopy. Thanks are also due to Dr. P.J. Gregson of the University of Southampton and Dr. F.R. Sale of the University of Manchester for their contributions to the project (in connection with the DSC work).

The technical expertise of Mess rs. M. Andrews, N. Salpadoru and R. Baxter has been gratefully appreciated. I am grateful to Miss Sandra Curley for patiently typing this thesis over an extended period of time and Mr. P. Henry for the reproduction of the plates.

I wish to thank my friends and colleagues, Drs. S. Fox, N. Raghunathan and M.P. Clode, and all others who, knowingly or unknowingly contributed to the compilation of this thesis.

Finally, the provision of a research grant by the Aluminium Company of America (ALCOA) is gratefully acknowledged.

REFERENCES

1. W.E. Quist, G.H. Narayanan and A.L. Wingert, 'Aluminium-Lithium alloys II', (ed. T.H. Sanders and E.A. Starke), Warrandle, Pa., The Metallurgical Society of AIME, 313, (1984).

2. C.J. Peel, B. Evans and D.S. McDarmaid, Metals and Materials, 3, (8), 449, (1987).

3. A.F. Smith, Metals and Materials, 3, (8), 438, (1987).

4. A.J. McAlister, Bull. Alloy Phase Diagrams, 3, 177, 1982.

5. J.M. Silcock, J. Inst. Met., 88, 357, 1959-60.

6. M. Tamura, T. Mori and T. Nakamura, J. Jap. Inst. Met., 34, 919, 1970.

7. T. Yoshi-yama, K. Hasebe and M. Mannami, J. Phys. Soc. Japan, 25, 908, 1968.

8. B. Noble and G.E. Thompson, Met. Sci. J., 5, 114, 1971.

9. L.P. Costas and R.P. Marshall, Trans. Met. Soc. AIME, 224, 970, 1962.

10. R. Nozato and G. Nakai, Trans. J. Inst. Met., 18, 679, 1977.

11. D.B. Williams and J.W. Edington, Met. Sci., 9, 529, 1975.

12. S. Ceresara, G. Cocco, G. Fagherazzi and L. Schiffini, Phil. Mag., 35, 373, 1977.

13. G. Cocco, G. Fagherazzi and L. Schiffini, J. App. Crystal, 10, 325, 1977.

14. F.W. Gayle and J.B. Vandersande, 'Aluminium-lithium alloys III', (ed. C. Baker et al), 376, 1986, London, The Institute of Metals.

15. F.W. Gayle and J.B. Vandersande, Bull. Alloy Phase Diagrams, 5, 19, 1984.

16. C. Sigli and J.M. Sanchez, Acta. Metall. 34, 1021, 1986.

17. J.M. Papazian, C. Sigli and J.M. Sanchez, Scr. Metall., 20, 201, 1986.

18. E.S. Balmuth, Scr. Met., 18, 301, 1984.

19. B. Noble and G.E. Thompson, Met. Sci. J., 6, 167, 1972.

20. S.F. Baumann and D.B. Williams, Met. Trans., 16A, 1203, 1985.

21. H. Suzuki, M. Kanno and N. Hayashi, J. Jap. Inst. Light Metals, 31 (2), 122, 1981.

22. T.H. Sanders, E.A. Ludwiczak and R.R. Sawtell, Mat. Sci. Eng. 43, 247, 1980.

23. D.B. Williams and J.W. Edington, Acta Metall., 24, 323, 1976.

24. T.V. Schegoleva and O.F. Rybalko, Fiz. Met. Metalloved, 3, (42), 546, 1976.

25. P. Niskansen, T.H. Sanders, Jr., J.G. Rinker and M. Marker, Corrosion Science, 22, 283, 1982.

26. D.B. Williams: in 'Aluminium-lithium alloys II', (ed. T.H. Sanders and E.A. Starke), 89, 1984, Warrandle, Pa, The Metallurgical Society of AIME.

27. T.H. Sanders and E.S. Balmuth, Met. Progress, 3, 32, 1978.

28. S.C. Jha, K. Mahalingam and T.H. Sanders: in 'Aluminium alloys - their physical and mechanical properties', (ed. E.A. Starke and T.H. Sanders), Volume II, 677, 1986, Warley, Engineering Materials Advisory Service.

29. W.R. D. Jones and P.P. Das, J. Inst. Met., 88, 435, 1959-60.

30. D.W. Levinson and D.J. McPherson, Translation of the ASM, 48, 689, 1956.

31. E. Schurman and I.K. Geissler: Giessereiforschung, 32, 163, 1980.

32. I.N. Fridylander, V.F. Shamray and N.V. Shiryayeva, Izv. Akad. Nauk, SSSR, Metally, 2, 153, 1965.

33. G.E. Thompson and B. Noble, J. Inst. Met., 101, 111, 1973.

34. T.V. Schegoleva and O.F. Rybalko, Phys. Met. Metalloved, 50, (1), 69, 1980.

35. T.H. Sanders, P.W. Niskansen, Res. Mechanica Letters, 1, 363, 1981.

36. K. Dinsdale, S.J. Harris and B. Noble: in 'Aluminium-lithium alloys I', (ed. T.H. Sanders and E.A. Starke), 101, 1981, Warrandle, Pa, The Metallurgical Society of AIME.

37. S.F. Baumann and D.B. Williams: in Ref. 26, 17.

38. I.N. Fridlyander, S.M. Ambertsumyan, N.V. Shiryayeva and R.M. Gabidullin: Met. Sci. Heat Treat. Met. 3, 211, 1968.

39. H.K. Hardy and J.M. Silcock, J. Inst. Met., 84, 423, 1955-56.

40. M.H. Tosten and P.R. Howell: in Ref. 28, 727.

41. W.A. Cassada, G.J. Shiflet and E.A. Starke: in Ref. 28, 695.

42. E.E. Cherkashin, P.I. Kripyakevich, and G.I. Oleksiv, Kristallografiya, 8, 846, 1963.

43. T.H. Sanders and E.A. Starke: in Ref. 26, 1.

44. T.V. Schegoleva and O.F. Rybalko, Phys. Met. Metalloved, 42, (2), 322, 1976.

45. F.W. Gayle: in Ref. 36, 119.

46. B. Noble, I.R. McClaughlin and G. Thompson, Acta Metall., 18, 339, 1970.

47. H.H. Jo and K. Hirano, Materials Sci. Forum, 13-14, 377, 1987.

48. K.K. Sankaran and J.E. O'Neal: in Ref. 26, 393.

49. R.J. Rioja, and E.A. Ludwickzak: in Ref. 14, 471.

50. J.C. Huang and A.J. Ardell: in Ref. 14, 329.

51. M.H. Tosten, A.K. Vasudévan, and P.R. Howell: in Ref. 14, 483.

52. P.J. Gregson, Ph.D. Thesis: The University of London, 1983.

53. W.S. Miller, A.J. Cornish, A.O. Titchener and D.A. Bennett: in Ref. 26, 335.

54. C.J. Peel, B. Evans, C.A. Baker, D.A. Bennett, P.J. Gregson and H.M. Flower: in Ref. 26, 363.

55. R.J. Kar, J.W. Bohlen and G.R. Chanani: in Ref. 26, 255.

56. K.K. Sankaran and N.J. Grant, Mater. Sci. Engn., 44, 213, 1980.

57. A.T. Little, W. Hume Rothery and G.V. Raynor, J. Inst. Met., 70, 491, 1944.

58. J.M. Silcock and B.A. Parsons, Fulmer Res. Inst. Report, R10/67, 1958.

59. Y. A. Bagaryatski, Dok. Akad. Nauk. SSSR, 87, (3), 397, 1952.

60. H. Perlitz and A. Westgren, Ark. Kemi Miner. Geol., 13, 1943.

61. G.W. Lorimer, "Precipitation Process In Solids", (ed. K.C. Rusell and H.I. Aaaronson), 87, 1978, Warrandale, Pa., The Metallurgical Society of AIME.

62. F. Cuisiat, P. Duval and R. Graf, Scr. Metall. 18, 1051, 1984.

63. J.M. Silcock, J. Inst. Met, 89, 203, 1960-61.

64. S. Cerasara, A. Girada and A. Sanchez, Phil. Mag., 35, 97, 1977.

65. R.N. Wilson and P.G. Partridge, Acta Metall., 13, 1321, 1965.

66. P.J. Gregson and H.M. Flower, Acta Metall., 33, 527, 1985.

67. T.S. Srivatsan, E.J. Coyne and E.A. Starke, J. Mater. Sci., 21, 1553, 1986.

68. B.L. Gu, G.L. Liedl, J.H. Kululicki and T.H. Sanders, Mater. Sci. Engn., 70, 217, 1985.

69. T.S. Srivatsan, J. Mat. Sci. Letters, 6, 948, 1987.

70. P. Niskansen, T.H. Sanders, M. Marek, and J. G. Rinker in Ref. 36, 69.

71. E.A. Starke, T.H. Sanders and I.G. Palmer, J. Metals, 8, (33), 24, 1981.

72. N. Ryum, Acta Metall., 17, 269, 1969.

73. E. Nes, Acta Metall., 20, 499, 1972.

74. L. Angers, Y. Chen, M.E. Fine, J.R. Weertman, and M.S. Zedalis: in Ref. 28, volume I, 321.

75. S. Rystad, and N. Ryum, Aluminium, 53, 193, 1977.

76. F.W. Gayle and J.B. Vandersande, Scr. Metall., 18, 473, 1984.

77. P.J. Gregson and H.M. Flower, J. Mater. Sci. Letters, 3, 829, 1984.

78. P.L. Makin and B. Ralph, J. Mater. Sci., 19, 3835, 1984.

79. W. Stimston, M.H. Tosten, P.R. Howell, and D.B. Williams: in Ref. 14, 386.

80. T. Malis: in Ref. 14, 347.

81. K. Hono, T. Abe, D.R. Hess, H.W. Pickering, P.R. Howell, Y. Hasegawa, T. Sakurai, N. Sano and K. Hirano: in Ref. 28, Volume I, 621.

82. T. Sakurai, A. Kobayashi, Y. Hasegawa, A. Sakai and H.W. Pickering, Scr. Metall., 20, 1131, 1986.

83. K. Hirano, Mater. Sci. Forum, 13/14, 215, 1987.

84. W.S. Miller, J. White and D.J. Lloyd: in Ref. 28, Volume III, 1799.

85. F.W. Gayle, J.B. Vandersande, and O.R. Singleton: in Ref. 28, Volume II, 767.

86. A.K. Vasudévan, A.C. Miller and M.M. Kersker: in Ref. 26, 181.

87. D. Webster: in Ref. 36, 228.

88. D. Webster, G. Wald and W.S. Cremens, Met. Trans., 12A, 1495, 1981.

89. F.S. Lin, S.B. Chakraborty and E.A. Starke, Met. Trans. 13A, 401, 1982.

90. N.J. Owen, Ph.D. Thesis, The University of London, 1987.

91. W.S. Miller, J. White, M.A. Reynolds, D.S. McDarmaid and G.M. Starr, "Aluminium-Lithium Alloys IV", (ed. G. Champier et al), published in J. de Physique, Tome 48, Supple. 9, C3-151, 1987.

92. D.B. Williams: in Ref. 36, 89.

93. A.K.Vasudévan and R.D. Doherty, Acta Metall., 35, 1193, 1987.

94. D. Venables, L. Christodoulou and J.R. Pickens, Scr. Metall. 17, 1263, 1983.

95. S.J. Harris, B. Noble and K. Dinsdale: in Ref. 26, 219.

96. T.H. Sanders: Naval Air Development Centre, Contract No. N62269-76-C-0271, Final report, June 1979.

97. M. Peters, V. Bachmann, K. Welpmann, H. Bellingradt, J. Eschweiler and R. Braun: DFVLR, KOLN Report No. DFVLR-FB86-40, 1986.

98. B. Noble, S.J. Harris and K. Dinsdale, J. Mat. Sci., 17, 461, 1982.

99. B. Noble, S.J. Harris and K. Dinsdale, Met. Sci., 16, 425, 1982.

100. M. Furukawa, Y. Miura and M. Nemoto, Trans. Jap. Inst. Met., 26, 230, 1985.

101. Y. Miura, A. Matsui, M. Furukawa and M. Nemoto: in Ref. 14, 427.

102. L.M. Brown and R.K. Ham, "Strengthening Methods In Crystals", (ed. A. Kelly and R.B. Nicholson), Elsevier, Amsterdam, 9, 1971.

103. J.W. Martin, "Micromechanisms In particle-hardened Alloys", Cambridge, University Press, 1980.

104. T.H. Sanders and E.A. Starke, Acta Metall., 30, 927, 1982.

105. O. Jensrud: in Ref. 14, 411.

106. P. Sainfort and P. Guyot: in Ref. 14, 420.

107. M. Peters and G. Lutjering, Z. Metallkunde, 67, 811, 1976.

108. G. Lutjering: Gleitverteilung und mechamische eigenschafton metallischer werkstoffe: DLR-FB-74-70: DFVLR, KOLN, 1974.

109. I. G. Palmer, R.E. Lewis and D.D. Crooks: in 2nd Int. Conf. on Rapid Solidification Processing, 1980.

110. E.A. Starke and F.S. Lin, Met. Trans., 13A, 2259, 1982.

111. K.V. Jata and E.A. Starke: in Ref. 14, 247.

112. A.K. Vasudévan, P.R. Ziman, S.C. Jha and T.H. Sanders: in Ref. 14, 303.

113. N.J. Owen, D.J. Field and E.P. Butler. Mat. Sci. Tech., 2, 1217, 1986.

114. A.J. Cornish and M.K. B. Day, J. Inst. Met., 99, 377, 1971.

115. J.D. Embury and E. Nes, Z. Metallkunde, 65, 45, 1974.

116. M.O. Speidel: in Proc. 6th Int. Conf. on Light Metals., Leoben, Austria, Aluminium-Verleg, Dusseldorf, 1975.

117. R.F. Ashton, D.S. Thompson, E.A. Starke and F.S. Lin: in Ref. 14, 66.

118. M. Kikuchi, K. Shiozawa and J.R. Weertman, Acta Metall., 29, 1747, 1981.

119. R.E. Crooks, E.A. Kenik and E.A. Starke, Scr. Metall., 17, 643, 1983.

120. S. Fox, H.M. Flower and D.S. McDarmaid: in Ref. 14, 263.

121. J. Waldman, H. Sulinski and H. Markus, Met. Trans., 5, 573, 1974.

122. T.H. Sanders and E.A. Starke, Met. Trans., 7A, 1407, 1976.

123. M.G. Tutcher, Ph.D. Thesis, The University of London, 1979.

124. S.J. Paterson, Ph.D. Thesis, The University of London, 1981.

125. C.M. Sellars and W.J. Mc G Tegart, Met. Rev. 17, 1, 1971.

126. C. Zener and J. Holloman, J. Appl. Physics, 15, 22, 1955.

127. J.J. Jonas, C.M. Sellars and W.J. Mc G Tegart, Met. Rev., 14, 1, 1969.

128. H. McQueen and J. Jonas, 'Treatise on Materials Science', 16, 393, Academic Press, 1975.

129. H. Ormerod and W.J. Mc G Tegart, J. Inst. Met., 89, 94, 1960-61.

130. H. McQueen, Met. Trans., 18A, 807, 1977.

131. J. Cotner and W.J. Mc G Tegart, J. Inst. Met., 97, 1969.

132. P.A. Hollinshead and T. Sheppard, Mat. Sci. Tech., 3, 1019, 1987.

133. D. Sastry, M. Luton and J. Jonas, Phil. Mag., 30, 115, 1974.

134. N.F. Foire and C.L Bauer, Prog. Mat. Sci., 13, 87, 1968.

135. W. Truszkowski, A. Pawlowski and J. Dutkieulicz: in Bull. Acad. Pol. Sci. Ser. Sci. Tech., 19, 55, 1971.

136. H.M. Tensi, P. Dropman and H. Borchers, Z. Metallkunde, 61, 518, 1970.

137. K.J. Gardner and R. Grimes, Met. Sci., 13, 216, 1979.

138. T. Sheppard, N.C. Parson and M.A. Zaidi, Met. Sci., 17, 481, 1983.

139. T. Sheppard and M.G. Tutcher, Met. Sci., 14, 579, 1980.

140. P.N. Kalu and F.J. Humphreys, "Aluminium Technology, 86", ed. T. Sheppard, 197, 1986, London, The Institute of Metals.

141. H.J. McQueen, E.E. Vangelista, J. Bowles and G. Crawford, Met. Sci. 18, 395, 1984.

142. F.J. Humphreys, Acta Metall., 25, 1323, 1977.

143. F.J. Humphreys and M.R. Drury: in Ref. 140, 191.

144. E.C.W. Perryman, "Creep and Recovery", ASM, 111, 1956.

145. H.J. McQueen, Trans. Jap. Inst. Met., 9, 170, 1968.

146. H. McQueen et al., Can. J. Phys., 45, 1225, 1967.

147. C. Gagnon and J.J. Jonas, Trans. Met. Soc. AIME, 245, 2581, 1969.

148. W.A. Wong and J.J. Jonas, Trans. Met. Soc., AIME, 242, 2271, 1968.

149. T. Sheppard: in Proc. 2nd int. aluminium extrusion technical seminar, Atlanta, Ga, Vol. 1, 331, 1977, Washington DC, Aluminium Association.

150. T. Sheppard and M.G. Tutcher, Metals Technology, 8, 319, 1981.

151. N.C. Parson and T. Sheppard: in Ref. 26, 53.

152. N.C. Parson and T. Sheppard: in Ref. 14, 222.

153. M.A. Reynolds and E. Creed: in Ref. 91, 195.

154. I.G. Palmer, W.S. Miller, D.J. Lloyd and M.J. Bull: in Ref. 14, 565.

155. J. Wadsworth, C.A. Henshall and T.G. Nieh: in Ref. 14, 199.

156. P.L. Makin and W.M. Stobbs: in Ref. 14, 392.

157. P.J. Gregson, C.J. Peel and B. Evans: in Ref. 14, 516.

158. R.P. Vierod, Ph.D. Thesis, The University of London, 1983.

159. S.J. Cieslak, 'ALCOA Short Rod Fracture Toughness Indicator Test', Report No. GA-17684.1, ALCOA Application Engineering Division, May 26th, 1985.

160. I. Novikov, 'Theory of Heat Treatment of Metal', Mir Publishers, Moscow, 1974.

161. G.C. Weatherly, D. Phil. Thesis, The University of Cambridge, 1966.

162. K.S. Raman, Scr. Metall., 5, 791, 1971.

163. B. Pike, Private Communication, University of Reading, 1985.

164. S.F. Baumann and D.B. Williams, Acta Metall., 33, 1069, 1985.

165. R.A. Swalin: "Thermodynamics of Solids", 60, Wiley, 1962.

166. H.M. Flower and P.J. Gregson: Mat. Sci. Tech., 3, 81, 1987.

167. J.M. Howe: in Ref. 28, Vol. I, 603.

168. A. F. Smith: in Ref. 14, 164.

169. B. Dubost, J.M. Lang and F. Degreve: in Ref. 14, 355.

170. K.N. Rao and J.A. Sekhar, Scr. Metall. Vol. 21, 6, 805, 1987.

171. P.R. Sperry, Trans A.S.M., 48, 904, 1956.

172. L.F. Mondolfo: "Aluminium Alloys: Structure and Properties", Butterworths, London (1976).

173. K.E. Aeberli, Electron Diffraction Programme Author, Imperial College, London, 1982.

174. A. Khataee, Private Communication, Imperial College, London, 1987.

175. A. Loiseau and G. Lapasset, J. de, physique, colloq. 47, C3-331, 1986.

176. A. Loiseau and G. Lapasset, Submitted to Phil. Mag.

177. P. Cooper, Ph.D. Thesis, The University of London, 1985.

178. J.C.M. Li, J. Appl. Physics, 33, 2958, 1962.

179. M.H. Skillingberg and R.F. Ashton: in Ref. 91, C3-179.

180. P. Cotterill and P.R. Mould, "Recrystallisation and grain growth in metals", Surrey University Press, London, 1976.

181. A.J. Perry and K.M. Entwistle, J. Inst. Met., 96, 344, 1968.

182. S.C. Jha, T.H. Sanders and M.A. Dayananda: Acta Metall., 35, No. 2, 473, 1987.

183. J.M. Howe, J. Metals, 9, 13, 1987.

184. W.S. Miller, J. White and D.J. Lloyd: in Ref. 91, C3-139.

185. Z. Yin, K.T. Aust, G.C. Weatherly and D.J. Lloyd, Can. Met. Quatr., 26, 61, 1987.

186. S. Fox, Ph.D. Thesis, The University of London, 1987.

187. J.A. Wert and P.A. Wycliffe, Scr. Metall., 19, 463, 1985.

188. E.O. Hall, Yield Point Phenomenon in Metals and Alloys, MacMillan, London, 1970.

189. J.T. Evans, Scr. Metall., 21, 1435, 1987.

190. M. Tamura, T. Mori and T. Nakamura, Trans. J.I.M., 14, 355, 1973.

191. E. Hornbogen, Z. Metallkunde, 66, 511, 1975.

192. M. Ahmed and T. Ericsson: in Ref. 14, 509.